Brunel University

Fabrication and Optimisation of SERS Substrates for Medical Diagnostics and Monitoring

A thesis submitted to Brunel University

For the Degree of

Doctor of Philosophy

By

Shavini Wijesuriya

Department of Mechanical, Aerospace & Civil Engineering and

Department of Electronic & Computer Engineering

2016

Abstract

Surface enhanced Raman spectroscopy (SERS) has great potential for design of next generation point-of-care (POC) diagnostic devices. However, its practical application in medical diagnosis is limited due to high cost of SERS substrates. The goal for this thesis was to develop affordable SERS substrates, and demonstrate their efficacy in the detection and assay of a Raman probe and diabetes biomarkers, using 514nm and 1064nm Raman spectrometers. Rapid and less energy intensive methods were optimised for manufacturing three categories of SERS substrates: 1) chemically roughened silver (Ag) metal, 2) Ag and gold (Au) nanoparticles (NPs) prepared using microemulsions, and 3) Ag and Au NPs' coated insoluble electrospun membranes. Immersion of Ag metal for 30 seconds in ammonia (NH_4OH), followed by 10 seconds in nitric acid (HNO_3) produced optimum roughened Ag metal SERS substrates. For synthesis of gold (Au) and Ag NPs, microemulsion compositions were varied, and the use of sodium borohydrate ($NaBH_4$) produced the desired larger sizes and anisotropic shapes of the NPs. Nanostructured planar SERS structures based on insoluble electrospun membranes, were prepared by covalently binding Au or Ag NPs, on electrospun poly acrylic acid-ethylene glycol (PAA-EG) fibres. Ag metal SERS substrates provided the best SERS enhancement for the Raman probe molecule, 4-methylbenzenethiol (MBT), with a detection limit of 1aM, using 514nm Raman spectrometer. The Ag metal SERS substrates were then used to demonstrate proof-of-concept for the use of SERS for assay of diabetes biomarkers. The higher laser intensity of 106nm Raman caused burning of the dry NPs' incorporated SERS substrates; but the thermally conductivity of solid Ag in Ag metal SERS substrate allowed SERS detection of 1nM MBT. To conclude, chemically roughened Ag metal SERS substrates proved cost effective and robust for quantitative SERS detection of MBT and diabetes biomarkers both with 514nm and 1064nm Raman spectrometers.

Acknowledgements

For the completion of this PhD thesis there are many individuals who I have met and have helped me in some way during the past few years. First and foremost I would like to thank my first supervisor Dr. Krishna Burugapalli, who helped direct and develop the skills I have gained within the project. I am also grateful to my second supervisor, Professor Wamadeva Balachandran, who offered advice and solutions when needed. I would also like to thank, Dr Ruth Mackay, with the multidisciplinary nature of the project, her knowledge within the lab and with the work in general, with the fabrication of fluidic chips to testing with interferometry was extremely helpful. I would like to thank Ashley Howkins who helped me with TEM testing as well as my warmest regard for staff from BIB, Wolfson, ETC and DocLab; especially Fiona, Jenny Kume, Roger Paton, Tony Anson, Fatima and Tony Bunce.

There have been many friends who have helped support me, from the 'girls from home'; Lauris, Dhruti, Catherine, Amy and Jen who have always been there for me to people I have had the privilege of getting to know and becoming friends with; Stijn Stuart, Ning Wang, Nicola Pomella, June, Gianpaolo, Pascal, Valeria, Christoph, Nicki, Gijs, Nico, Olimpia, Alessandra, John, Vincent, Nikolay, Angel, Safiya as well as many others, who passed through Brunel making the process more enjoyable.

Last but not least I would like to thank my family; uncles, aunts, grandparents, cousins and my brother all of whom took an interest and wanted to help in any way they could. I would especially like to thank my Mum and Dad. Thanks to my Dad for listening to my experimental issues, providing solutions and even helping to build an electrospinning box for use within the project and to my mum who whenever needed would read through my work and listen to presentations. Without their support this thesis would not have been possible.

Table of Contents   **Page No.**

List of Figures
        Page No.

aration.

Abbreviations & Notations

AA	Ascorbic Acid
ABC	AOT/But/Cyclohexane
ABI	AOT/But/IPM
Ag	Silver
aM	Attomolar
AOT	Dioctyl sulfosuccinate sodium salt
Au	Gold
BSA	Bovine Serum Albumin
C_4H_9OH /But	Butanol
CBC	CTAB/But/Cyclohexane
CME	Chemical Enhancement
CTAB	Hexacetyltrimethyl Ammonium Bromide
Cyclo	Cyclohexane
Cyste	Cysteamine
EDX	Energy dispersive x-ray spectroscopy
EF	Enhancement Factor
EG	Ethylene Glycol
EME	Electromagnetic Enhancement
fM	Femtomolar
FTIR	Fourier transform infrared spectroscopy
H	Hydrazine
Hb	Haemoglobin
HbA_{1c}	Glycated Haemoglobin
HNO_3	Nitric Acid
IPM	Isopropyl Myristate
LOC	Lab-on-a-chip
LOD	Limit of detection
MBT	4-Methylbenzenethiol
M	Molar
mM	Millimolar
N	Sodium Borohydride
$NaBH_4$	Sodium Borohydride
NH_4OH	Ammonium Hydroxide
nM	Nanomolar
NP	Nanoparticles
PAA	Polyacrylic Acid
pM	Picomolar
POC	Point-of-Care
R_a	Average Roughness
R_p	Peak Roughness value
R_q	Root-mean-squared (RMS) average Roughness
R_t	Peak to Valley Roughness

R$_v$	Valley Roughness value
SEM	Scanning Electron Microscopy
SERS	Surface Enhanced Raman Spectroscopy
SP	Surface Plasmons
TEM	Transmission Electron Microscopy
UV-Vis	UV-Visible spectroscopy
μM	Micromolar
aM	Attomolar
zM	Zeptomolar

Chapter 1: Introduction

1.1.   Background & Rationale

There is a clinical need for better diagnostics and monitoring devices within healthcare. One area of increased interest is the use of lab-on-a-chip (LOC) for point of care testing (POCT). Currently only a few LOC-based technologies have gained commercial success, encompassing desired criteria of: low concentrations, ability to quantify, rapid turnover time, low sample volume, multiplexing capability and low cost (Chin, Linder & Sia, 2012).

Surface enhanced Raman Spectroscopy (SERS) is a transduction method which has desirable characteristics for use within a lab on a chip device. It is a molecular spectroscopy technique that provides increased sensitivity and selectivity, with the ability to multiplex, high turnaround time for results, low sample volume required and little to no sample preparation or labelling (Chen & Choo, 2008). As of yet however it has not been implemented within analytical testing (Ramon a. Alvarez-Puebla & Liz-Marzán, 2012). One major bottleneck to the use of SERS within analytical devices is the lack of research with the use of a common SERS substrate design for analytical testing of biomolecules, specifically for disease diagnostic and monitoring purposes. The SERS substrates currently commercially available use fabrication methods that are more time and energy intensive and as such contribute to the high cost of the SERS substrates. The commercial SERS substrates also only work at specific wavelengths for SERS efficacy and as such may exclude a larger library of analytes, due to affinity to the SERS substrate as well as lack of resonance of the molecular bonds within the analyte with the specific laser wavelength.

The use of SERS is to enhance the molecular fingerprint of analytes that typically do not resonate with Raman. Therefore, the preparation of SERS substrate that have SERS efficacy over a larger range of wavelengths 'broadband characteristics' (Zhang et al, 2015), with an affinity for binding to specific analytes, specifically disease biomarkers would be highly desirable for providing proof-of-concept for the implementation of SERS within LOC for analytical testing.

1

Fabrication of such a SERS substrate typically falls under 1 of 3 categories; metallic electrodes, metallic nanoparticles or nanostructured substrates (Le Ru & Etchegoin, 2009; Gómez & Lazzari, 2014); each of which has its own advantages for SERS. The use of less energy and time intensive methodologies for fabrication of SERS substrates within each design category, with a focus on SERS efficacy with two different laser wavelengths and controlled roughness/surface morphology for hot-spot control, would improve the robustness and repeatability of the SERS substrates for testing applications, with particular focus for its implementation within analytical testing research, for disease diagnostics and monitoring and future implementation within LOC devices.

1.2. Aim of Research

The main aim of this thesis was the fabrication of optimised SERS substrates with methodologies that were less energy and time intensive. For the preparation of robust, repeatable morphologies that had desired hot-spot control and therefore repeatable SERS activity. The efficacies of the SERS substrates were tested with two different laser wavelengths, 514nm and 1064nm for broadband characteristics of the SERS substrate. Using firstly a control Raman probe molecule, 4-methylbenzenethiol (MBT) and then secondly diabetes biomarkers; glucose, haemoglobin, HbA_{1c}, albumin and glycated albumin. This was to demonstrate proof-of-concept that SERS can be used for diabetes disease diagnostics and monitoring applications.

1.3. Specific Objectives

The specific objectives of the thesis were firstly to prepare SERS substrates from three design categories using methodologies that were less time and energy intensive. For the 1st category, roughened silver (Ag) wires through the use of chemical etching were prepared. For the 2nd category, Ag and gold (Au) nanoparticles (NPs) using microemulsions were prepared and the 3rd category, Ag and Au NPs on electrospun membranes were prepared.

After fabrication, the Raman-active molecule MBT was attached to SERS substrates and tested with 514nm and 1064nm Raman, qualitative and quantitative characteristics with a specific focus

on enhancement factor (EF) and limit of detection was tested. Two commercial SERS substrates were used for comparison with optimised SERS substrates fabricated to compare SERS efficacy of MBT with the different designs.

An optimised SERS substrate was then used for proof-of-concept work for SERS efficacy of the substrate with diabetes biomarkers, using a direct detection assay approach within relevant control medium. The SERS substrate qualitative characteristics with each diabetes biomarker; glucose, Hb, albumin, HbA$_{1c}$ and glycated albumin were evaluated and quantitative characteristics of the SERS substrates with glucose, Hb and albumin were then addressed. Aims of the thesis were;

- Fabricate and characterise an optimised SERS substrate design using Ag wire through use of NH$_4$OH and HNO$_3$ for chemical etching.

- Fabricate and characterise optimised Au and Ag NPs with specific size (≥30nm) and anisotropic shape, beneficial for SERS using microemulsions.

- Efficiently separate Ag and Au NPs from microemulsions while maintaining their size and shape integrity.

- Fabricate and optimise insoluble electrospun membranes, PAA-EG, for use as a SERS substrate platform.

- Fabricate and characterise an optimised SERS substrate design of Ag or Au NPs on PAA-EG-cysteamine electrospun membrane

- Evaluate the efficacy of the developed SERS substrates, using MBT as the Raman-active molecule with 514nm and 1064nm Raman.

- Compare fabricated SERS substrates from each design category with commercial SERS substrate - SERStrates and P-SERS and calculate EF for the designs with MBT.

- Evaluate the quantitative characteristics of the optimised SERS substrates with MBT.

- Evaluate the qualitative characteristics of 30s NH_4OH+10s HNO_3 chemically etched Ag wire SERS substrate with biomarkers; glucose, Hb, albumin, HbA_{1c} and glycated albumin.

- Evaluate the quantitative characteristics of 30s NH_4OH+10s HNO_3 chemically etched Ag wire SERS substrate with biomolecules; glucose, Hb and albumin.

- Design and fabricate an improved electrospinning setup with improved control over temperature and humidity.

- Fabricate open microfluidic chips for testing of SERS substrates with 1064nm Raman.

1.4.   Summary of Methodology Used

The multidisciplinary nature of the thesis required methodology and a characterisation from a large range of fields. For the 1st SERS substrate design category; chemical etching treatments of Ag wire and resultant characterisations involving scanning electron microscopy (SEM), interferometry, energy dispersive X-ray spectroscopy (EDX) were used. Afterwards as with all SERS substrate design categories 514nm and 1064nm Raman was used for evaluation of SERS efficacy.

For the 2nd SERS substrate design category, a bottom-up, chemical methodology for nanoparticle synthesis through the use of microemulsions was used for synthesis of Ag and Au NPs with controlled size and shape. As well as separation methodologies, centrifugation, anti-solvent and water phase disruption methods to optimise NP separation from microemulsion with maintenance of size and shape integrity. UV-visible spectroscopy and transmission electron microscopy (TEM) were used to evaluate these NP characteristics.

For the 3rd SERS substrate design category, an in-house electrospinning machine with humidity and temperature control was designed and built, with the focus of fabricating insoluble electrospun membranes. Cross-linking methodologies were evaluated for fabrication of insoluble electrospun membranes, with a condensation methodology, with the use of additional heat after electrospinning used to produce cross-linked PAA-EG electrospun membranes. Surface

4

modification methodologies with the use of carbodiimide cross-linking for grafting of cysteamine (cyste) onto PAA-EG fibres was used. Shortlisted Ag and Au NPs from the 2nd category were then used for attachment of the NPs to the thiol groups of cysteamine on the electrospun fibres. Instrumentation used for characterisation was firstly light microscopy, conductivity, thickness and mass for electrospinning parameter optimisation. Afterwards SEM and FTIR were used to evaluate the electrospun fibre morphology and cross-linking efficiency respectively. FTIR was further used to support the grafting of cysteamine onto the surface. TEM was used for morphological observations of the NPs on the electrospun fibre surface.

For assay development, FTIR, 514nm and 1064nm Raman was used for evaluation of the diabetes biomarkers. It was found that with 1064nm Raman, due to the high power the protein biomarkers were burning therefore for SERS substrate efficacy testing, 514nm Raman was predominately used.

For SERS substrate efficacy with MBT, EF was calculated using the analytical EF equation, whereby the intensity of a predominant SERS peak in all substrates was tested against the analyte concentration used and divided by the Raman intensity of the same peak divided by the concentration of the analyte used. For both MBT and diabetes biomarkers, quantitative characteristics were calculated using a peak to peak ratio of two predominant peaks within each analytes spectrum, for calculation of linearity and limit of detection from calibration curves.

1.5. Thesis Organisation

The aim for the rest of the chapters is to firstly introduce the reader to the concepts behind SERS and the current status of the technique with substrates developed and used, with particular focus on diabetes detection and monitoring within the literature review, chapter 2. With further detail on the methods used for the particular SERS substrates fabricated within this thesis. Concepts behind the use of chemical etching, microemulsions for nanoparticle synthesis and electrospinning, particularly towards fabrication of insoluble electrospun membranes were covered, as well as a

larger overview for the need to detect and monitor diabetes biomarkers and their effectiveness within a LOC setting will be covered.

Chapter 3 will cover the materials and methods used for the design and evaluation of the SERS substrates as well as proof-of-concept testing methods used for diabetes biomarkers. The results chapters 4-9, will then introduce the reader to the fabrication methods used for each SERS substrate design category.

With chapter 4 detailing the chemical etching of Ag wire with HNO_3 and NH_4OH with additional heat treatment in some cases as well as characterisation of the Ag wire surface and SERS efficacy with MBT using 514nm and 1064nm Raman.

Chapter 5 evaluates the use of 7 microemulsion parameters; surfactant, co-surfactant, solvent, reducing agent, precursor and reducing agent concentrations, electrolyte and W number for controlling size and shape of Au and Ag NPs, resulting in 7 NP microemulsion systems being shortlisted for further testing to evaluate SERS efficacy.

Chapter 6, details firstly the separation of Ag and Au NPs from microemulsions into water. After which NPs from microemulsions and water are tested within solution and on filter paper with 1mM MBT using 514nm and 1064nm Raman for testing SERS efficacy of the different NP sizes and shapes.

Chapter 7, details the preparation of insoluble electrospun membranes PAA-EG and then the surface modification of the fibres with grafting of cysteamine onto the surface. NPs from microemulsions and NP separated solutions are then covalently attached onto the electrospun membranes and the different SERS substrate designs are evaluated for their SERS efficacy with 1mM MBT using 514nm and 1064nm Raman.

Chapter 8 compares the optimised SERS substrate designs fabricated within each category detailed in previous chapters with two commercial SERS substrates, P-SERS (Diagnostic AnSERS co.)

and SERStrate (Silmeco Ltd) with 1mM MBT, with particular focus on their EF values with 514nm and 1064nm Raman. Quantitative characteristic of an optimised design from each of the SERS substrate design categories is then shown, to evaluate LOD, calibration and linearity with MBT concentrations.

Chapter 9 uses an optimised SERS substrate design, 30s NH_4OH+10s HNO_3 chemically etched Ag wire for proof-of-concept work with diabetes biomarkers; glucose, Hb, HbA_{1c}, albumin and glycated albumin, for SERS substrates qualitative characteristics. Further quantitative characteristics are evaluated using glucose, Hb and albumin with 514nm Raman to provide LOD and linearity with each biomolecule.

Chapter 10 provides the summary and conclusions obtained from the work and future directions are detailed.

1.6. Contribution to New Knowledge

The concept behind the use of SERS for improved analytical testing, specifically for the scope of disease diagnosis and monitoring, is that current transduction methodologies (electrochemical, enzyme-linked immunosorbent assays (ELISA), fluorescence) are restrained for their detection of a wider library of analytes as well as interference of agents within the complex media that would provide false readings. SERS is noted as providing an individual fingerprint for each molecule and as such can provide a selectivity and high sensitivity for a wide library of analytes. The testing requires minimal sample, can be done within a few minutes and is noted as having single molecule detection. All of these characteristics rely predominately on the SERS substrate. Currently SERS substrates have not fully controlled hot-spot uniformity and as such repeatability of SERS signal is not definite. The fabrication techniques typically used are time and energy intensive and the resulting SERS substrates typically work at a narrow wavelength range. Preparation of SERS substrates that use methodologies that are less energy and time consuming

provide the ability for an increased robust design of SERS substrate to be used and tested. Specific aims for control of the surface features, for uniform morphology and increased SERS efficacy with two wavelengths largely different from one another, 514nm and 1064nm Raman would provide the ability to understand the relationship of SERS substrates surface morphology with laser wavelength resonance, as well as preparation of broadband SERS substrates.

Chemical etching treatments of metallic surfaces for SERS substrate design has only been touched upon within the literature, with few articles discussing the preparation and application of these SERS substrates. The use of chemical etching has been shown within this study to produce surface morphologies of controlled roughness that are applicable for SERS enhancement with both 514nm and 1064nm. The chemical etching is done in less than few minutes and the resulting design is robust for use. A range in roughness that shows SERS efficacy and broadband characteristics and therefore novelty in preparation of multiple SERS substrates with this controlled roughness and morphology to provide optimised SERS substrates is shown.

NPs synthesised within microemulsions has been detailed within literature since the 1970s. However, as of yet a standard protocol for the synthesis of Au and Ag NPs within microemulsions, having controlled size and shape is not present within literature. Review articles by Eastoe et al, 2007, Pileni et al, 2003 and Uskokovic et al, 2009, all highlight different microemulsion parameters that can be used to assess NP size and shape control. In this study the 7 main parameters predominately mentioned within literature for alteration of size and shape are systematically tested for the preparation of Au and Ag NPs with controlled size (≥30nm) and anisotropic shape for use as SERS substrates. For additional SERS efficacy the removal of the surfactant that typically coats the NPs within the microemulsion was assessed with a water phase disruption method. Literature in this instance as well does not provide a standard protocol for the separation of NPs from microemulsions (Kowalyczyk et al, 2009). In this study, an optimised NP separation method that involved the addition of water for phase disruption was detailed for their successful separation of NPs from the microemulsion, while maintaining the NPs' size and shape in general.

Despite NPs comprising a large section of the SERS substrate literature, the use of Ag and Au NPs synthesized using microemulsions for use as SERS substrates is not largely detailed within literature. The SERS efficacy evaluation of the NPs' size and shape characteristics, in relation to within solution and on filter paper, is unique to this study, and it highlighted the need for not only size and shape control, but also a nanostructured solid support for SERS efficacy.

SERS signal intensity is dependent on the wavelength of the incident laser light. The longer the wavelength the lesser the intensity. However, shorter wavelengths, typically in the visible region, e.g. 514nm, suffer from interference from the inherent fluorescence signal from the analytes for detection. Use of longer wavelength, in particular 1064nm eliminates interference from fluorescence. There are few reports in literature on the use of 1064nm for SERS detection of clinical analytes. In this study, we report the use of both 514nm and 1064nm Raman spectrometers for SERS detection.

SERS substrates that use electrospun membranes have shown high SERS efficacy up to 50 times higher than other SERS substrate designs (Lee et al, 2011). This is due to the higher surface area per unit volume present through the fibro-porous structure of the electrospun membrane available for SERS scanning. We developed methods to prepare insoluble electrospun membrane and to covalently attach Ag or Au NPs on their fibres' surface.

The use of SERS for testing diabetes biomarkers is yet to be reported in literature, with the exception of that for glucose. In this study, we showed the efficacy of SERS based detection of glucose, Hb and albumin using roughened Ag wire SERS substrates. There is huge scope for application of SERS based detection in medical diagnostics and monitoring.

1.7. List of Publications

1. Wijesuriya S, Burugapalli K, McKay R, Balachandran W. Insoluble Electrospun membranes for analyte pre-concentration in saliva. Proceedings of the 2015 annual meeting of the Electrostatics Society of America, Pomona, CA, USA, 16-18 June 2015. (Won 1st prize for best student paper from Electrostatics Society of America).

2. Wijesuriya S, Burugapalli K, Messias S, McKay R, Balachandran W. The progress of SERS for diagnostics and monitoring. Poster presentation at Optics in Clinical Practice II, Institute of Physics, London, UK, 26th November 2013.

3. Wijesuriya S, Burugapalli K, Balachandran W. Size & Shape Manipulation of Nanoparticles for Surface Enhanced Raman Spectroscopy. Poster presentation at the annual postgraduate research conference, Brunel University, UK, 2013.

4. Wijesuriya S, Burugapalli K, Wang N, Song W, Zheng Y, Ma Y, Moussy F. Electrospun fibro-porous coatings for implantable glucose biosensors. Poster presentation at the Nanofibers to Nanocomposites III conference, Nottingham, 27th February 2014.

5. Wang N, Burugapalli K, Wijesuriya S, Yazdi-Far M, Song W, Moussy F, Zheng Y, Ma Y, Wu Z,Li K. Electrospun polyurethane-core and gelatin-shell coaxial fibre coatings for miniature implantable biosensors. Biofabrication, 6(1):015002, 2014. Paper written from experimental results gained during my Master's thesis.

6. Wijesuriya S, Burugapalli K, Balachandran W. Fabrication of a Multiplex Point-of-Care device, for Better Screening and Monitoring of Diabetes. Poster presentation at the annual postgraduate research conference, Brunel University, UK, 2012.

Chapter 2: Literature Review

2.1. Background Principles

2.1.1. Raman Scattering: Quantum Photonics

Before discussing SERS in more detail, the principles regarding Raman Scattering should be understood. The phenomenon was first observed in 1928 by two independent groups: C.V. Raman and K.F. Krishann who discovered it in liquid and L. Mandelstam and G. Landsberg who discovered it in crystals (Kneipp, 2007; Sur et al., 2008). They both showed that when photons collide with a molecule, two types of scattering can occur: elastic scattering known as Rayleigh scattering and inelastic scattering known as Raman scattering. The inelastic scattering provides the ability for measurement due to loss (stokes) or gain (anti-stokes) of photon energy (Fig. 2.1.) (Sur et al., 2008).
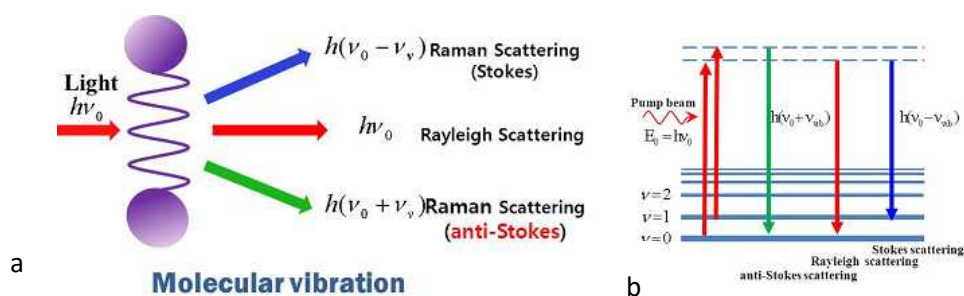
Figure 2.1: Diagrams to show a) the interaction of light with a molecule and the resultant scattering and b) a Jablonski graph for the energy levels that a single photon exhibits with elastic (Rayleigh) and inelastic (Raman) scattering. *h=Plancks constant, v=frequency of vibration, E=energy (frequency)* (Laboratory for ultrafast nonlinear optics, 2015)

The relationship of light with a molecule and corresponding scattering is generally described using electromagnetic radiation, whereby light is an electromagnetic wave (Fig. 2.2), and when the frequency of the wave interacts with the electron cloud of a molecule it can induce a dipole moment. The dipole moment is regulated by the polarizability of the molecular vibration within a molecule (Kneipp et al., 2002). Polarizability is the 'deformability of the electron cloud of the molecule when an external electric field is applied' (Larkin, 2011). Therefore, if an induced dipole oscillation occurs, it is the sum of the incoming light and molecular vibrations, the resulting photons scattered after this interaction have a loss or gain of energy which depicts Raman scattering.
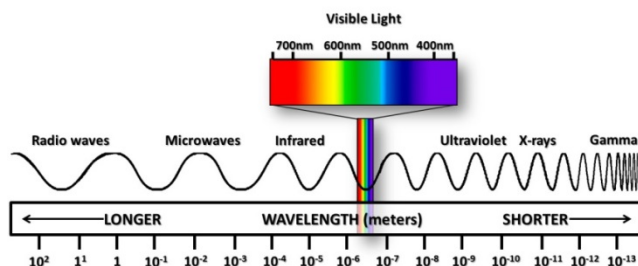
Figure 2.2: Electromagnetic spectrum showing the regions commonly known and the subsequent wavelengths present. (Climate Science Investigations, 2015)

The energy of a vibration, if considered as a classic harmonic oscillator, can be as shown in Equation 2.1. The equation highlights that in theory any value of *r* is possible and therefore a molecule could absorb energy at any wavelength (Stedwell & Polfer, 2013).

$$E = \tfrac{1}{2}\, \kappa \Delta r^2 = h\nu$$

Equation 2.1: Equation to show how the energy (frequency) of a vibration is calculated. E is the energy or frequency, *κ* is the force constant, Δ*r²* is the equilibrium distance, *h* is Planck's constant and *v* is frequency of the vibration.

In Raman scattering laser wavelengths most widely used are; 532nm, 785nm and 1064nm (AZO materials, 2015), however one can use wavelengths in the ultraviolet, visible or near infrared (NIR) regions (HORIBA,2015).

$$P_{scattered} \propto I_o/\lambda^4$$

Equation 2.2: Equation to show the Photons scattered, $P_{scattered}$, is dependent on Intensity, I_o, divided by wavelength, λ to the power of 4.

Equation 2.2 shows that Raman scattering is inversely proportional to the fourth power of the excitation wavelength. Therefore the more energetic the excitation wavelength (shorter the wavelength), the more Raman scattering occurs (higher the frequency) (Atkins & De Paula, 2010; Popp & Kiefer, 2000). There is however a trade-off between intensity of signal and ability to detect the Raman bands for the molecular structure of the target analyte (Fig. 2.3). Whereby a fluorescence region between 275-975nm for molecules (Popp & Kiefer, 2000) causes photons with wavelengths within this range to collide with electrons in the fluorescence region. At shorter wavelengths such as 514nm or 532nm due to the increased Raman scatter highlighted in Equation 2.2, there is a higher amount of fluorescence that will cover the Raman peaks of the molecule.

With wavelengths such as 785nm, which is most widely used for biomedical applications, the fluorescence signal is less powerful with more than 90% of chemicals scanned with this wavelength showing limited fluorescence interference (AZO materials, 2015). However, fluorescence is still present and the longer wavelength produces reduced intensity of Raman peaks.

Another way of overcoming the fluorescence issue is to pick wavelengths outside the fluorescence region such as deep ultraviolet excitation wavelengths (244nm for example) or in the outer regions of near infra-red such as 1064nm. Following the theory behind equation 2.1, both these wavelengths should interact with the molecule and provide vibrational information. However, the problem with the deep ultraviolet wavelength is the intensity of the wavelength is so high it is likely to damage the sample that it is testing. Whereas for the 1064nm, the intensity of the wavelength may be so low that the Raman scattered photons may be too weak to be picked up above the noise.

a   b
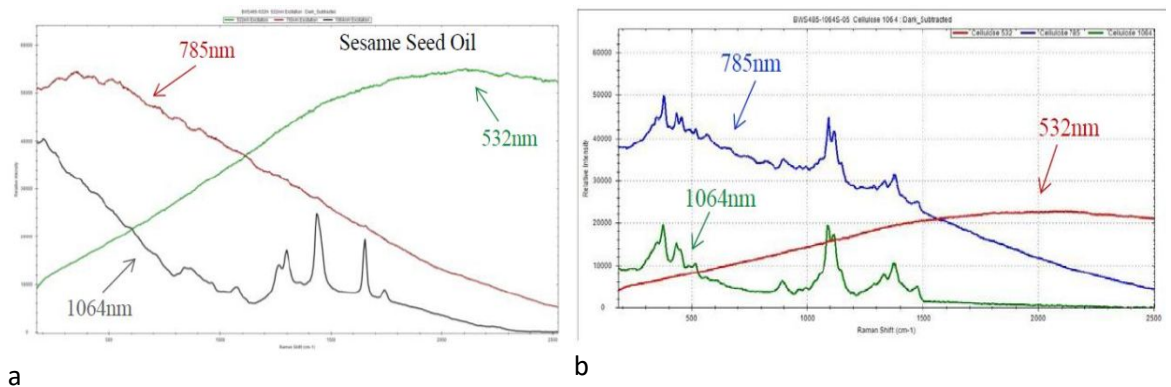
Figure 2.3: Raman spectra for a) relationship of 3 different laser wavelengths; 532nm, 785nm and 1064nm with detection of sesame seed oil Raman spectra and b) three different laser wavelengths corresponding Raman spectra for cellulose. (AZO materials, 2015)

2.1.2. Raman Scattering: Molecular Information

The molecular information that is depicted from the interaction of the photons with the electrons within the molecule produces Raman spectra, which depicts information for vibrational, rotational and other low frequency modes exhibited by a molecule. Raman scattering is defined as a form of molecular spectroscopy, predominately depicting vibrational spectra (Popp & Kiefer, 2000). Raman vibrational bands can be characterised by individual 'frequency (energy), intensity (polar character or polarizability) and band shape (environment of bonds)'(Larkin, 2011), therefore Raman spectra for that molecule provides a molecular 'fingerprint'.

There is a general 'rule of thumb' for the internal degrees of freedom a molecule may exhibit and can be 'resolved into components along the three directions in the Cartesian coordinate system, x, y and z' (Stedwell & Polfer, 2013). These 3 degrees of freedom express a molecule's vibrations, rotations and translations, Figure 2.4, and are depicted as either 3N-6 or 3N-5 for linear or non-linear molecules respectively. N is for the number of atoms within the molecule.
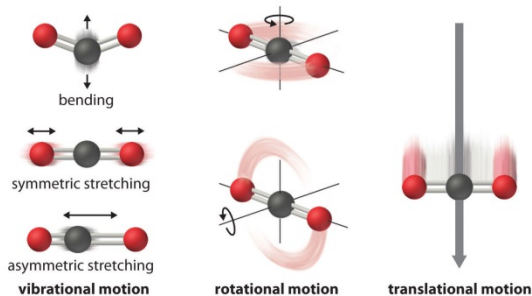
Figure 2.4: Diagram to depict the three general ways by which an atom within a molecule can move (Atkins & De Paula, 2010).

The frequencies of the molecular vibrations, depends on the 'mass of the atoms, geometric arrangement and strength of their chemical bonds' (Larkin, 2011). For vibrations, rotations and translations, these categories are quite broad and Raman is able to typically depict the vibrational type of movement from the spectra obtained (Fig. 2.5).
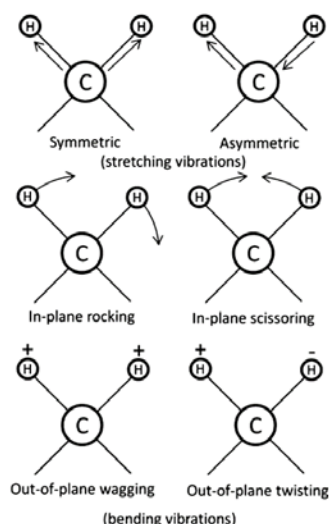
Figure 2.5: Diagram to show the different types of movements that can be determined as molecular vibrations (Stedwell & Polfer, 2013).

Raman scattering is an ideal technique for analytical testing with its ability to qualitatively depict a molecule's individual fingerprint. The type of bonds can be commonly associated with different groups of molecules and these bonds can be categorised as scattering at certain ranges within the Raman spectra (Fig. 2.6). Thus Raman can be used for determining unknown compounds as the peaks present can be associated with peaks present within other molecules.
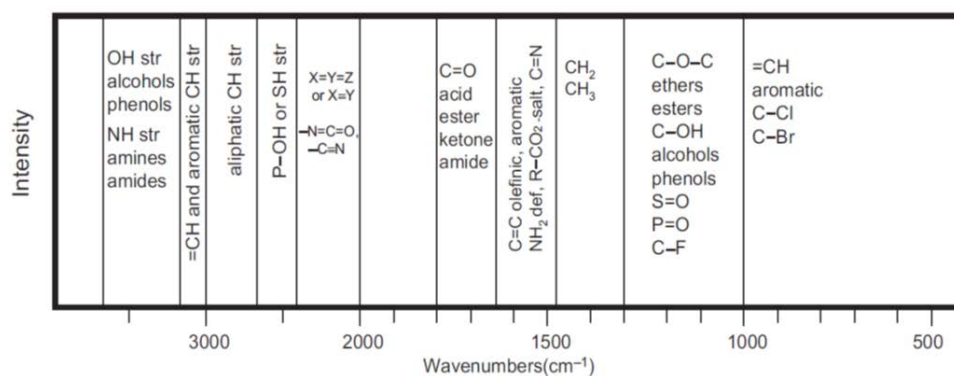
Figure 2.6: Diagram to show the general peaks associated with different groups and their relative ranges within Raman spectra. (Larkin, 2011)

Raman scattering is also capable of quantitative measurement, as shown with Equation 2.3;

$$I_R \propto v^4 I_o N (\delta\alpha/\delta Q)^2$$

Equation 2.3: Equation to show the intensity of Raman scattered radiation in relation to; frequency of excitation laser, v, incident laser intensity, I_o, number of scattering molecules in a given state, N, polarizability of a molecule, α and vibrational amplitude, Q. (Larkin, 2011)

The equation for intensity of Raman scattered radiation highlights three things (Larkin, 2011);

1) The presence of N highlights the fact that intensity of Raman correlates with the number of scattered molecules present, therefore the end value will be concentration dependent and thus quantitation can occur.

2) Using a shorter wavelength as discussed before or increasing laser power would increase Raman intensity.

3) The equation only depicts that molecular vibrations would cause a change in molecular polarizability which would be Raman active.

2.1.3. Raman Scattering: Problem

Although Raman scattering appears quite straightforward, the problem with Raman and the reason why it has not been more commercially used as an analytical technique commonly found within the lab (Cialla et al., 2012), is due to Raman scattering providing weak signals, particularly for molecules with small cross-sections. The Raman scattering phenomenon only occurs in 1 in 10^6–10^{10} of scattered light (Bantz et al., 2011). It was only through the advancements in laser technology and detector systems that Raman was able to move forward from the original experiments done in the 1920s (Sur et al., 2008). The general cross-section for the technique is between 10^{-31} and 10^{-29} cm^2/molecule (Bantz et al., 2011), which is 12-14 orders of magnitude below fluorescence cross-sections. Fluorescence is another optical method which is more commonly used for analytical testing in biomedical applications. However the molecular bands for structural information in fluorescence are quite broad compared to Raman; with Raman spectral widths being 10-100 times narrower (Bantz et al., 2011). Therefore, fluorescence is a less sensitive technique. Equation 2.4 depicts the general parameters that affect the ability of measuring an individual molecule.

$$P=\sigma S_{inc}$$

Equation 2.4: Equation to show the Intensity or Power, P, in relation to the cross section of the molecule, σ and the incident power density at the molecule position, S_{inc}.

Raman spectroscopy, although theoretically capable of having high sensitivity, Equation 2.4 highlights the importance of the molecules' cross-section; as molecules with larger cross-sections provide a higher probability of a collision between a photon and an electron within the molecule

structure. Raman scattering can provide sensitive information for large molecules, however for smaller molecules such as those required for detection within the biomedical field, Raman is too weak a technique for efficient use (Le Ru & Etchegoin, 2009).

Raman was initially used for neat solvents and analytical testing within the petroleum industry (Sur et al., 2008). It underwent many advancements; from the equipment used, with the introduction of lasers, better detection systems and the miniaturisation of these components for the applicability of Raman within a portable device. Currently, Raman is used in multiple fields from; homeland security and law enforcement to pharmaceutical processing and food safety (Grunsby, 2012). However, to further the technique to provide increased sensitivity for trace amounts of molecules and capability to detect smaller molecules, beneficial for the design of LOC devices particularly for disease diagnostics and monitoring in healthcare, Surface enhanced Raman spectroscopy (SERS) was proposed.

2.1.4. Surface Enhanced Raman Spectroscopy: Additional Parameters

SERS was first discovered in the 1970s by Fleischmann and co-workers through the enhanced signal of pyridine on electrochemically roughened silver electrodes (Kneipp et al., 2002). The enhancement of the Raman scattering is as of yet still not fully understood. However, two main mechanisms have been highlighted to provide the enhanced characteristic. Jean-Marie and Van Duyne proposed that the enhancement was due to an electromagnetic effect based on excitation of 'localised surface plasmons' on the surface of the metal substrate. Whereas Albrecht and Creighton's group proposed that enhancement was caused by a charge transfer effect between adsorbed molecule and metal, thereby a chemical enhancement. (McNay, Eustace, Smith, Faulds, & Graham, 2011), both of which have been determined as imperative for increasing Raman scattering. This provides the ability to detect molecules with cross-sections of at least 10^{-16} cm^2/molecule, reaching enhancement factors up to 14 orders of magnitude compared to normal 'non-resonant' Raman (Kneipp et al., 2002).

2.1.5. SERS: Electromagnetic Enhancement

Electromagnetic enhancement is viewed as the dominant mechanism that causes enhanced signal by SERS, usually in the range of 10^6-10^8 (Bantz et al., 2011). The enhancement comes about due to the characteristics exhibited by metals, which possess free conduction electrons around ions within the structure. These generally remain in a neutral oscillating state, where the plasmons exist by themselves in a neutral zero charge (Le Ru & Etchegoin, 2009). Metals also possess a negative real and small positive imaginary dielectric constant upon the surface, such as in thin films. Therefore, when an incident wavelength interacts with these free conduction electrons and there is coherence between the oscillation of the conduction electrons and the electromagnetic wavelength, surface plasmon polaritions of the electrons will occur, causing the electrons to have additional energy and oscillate between the metal and the dielectric interface, also known as surface plasmon resonance (SPR), (Fig. 2.7a)(Stiles, Dieringer, Shah, & Van Duyne, 2008). With regards to localised surface plasmon resonance (LSPR) it typically occurs in metal nanostructures, whereby the incident electromagnetic wave interacts with a particle which is much smaller than the wavelength and this causes plasmons to oscillate locally around the nanostructure at a frequency known as LSPR (Fig. 2.7b) (Willets & Van Duyne, 2007).
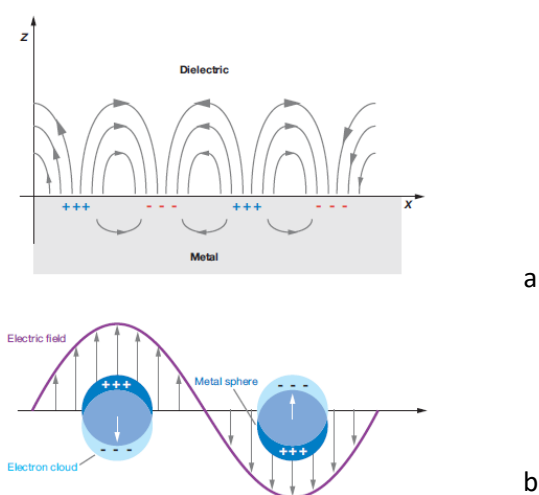
Figure 2.7: Diagrams to show a) relationship between dielectric and metal, causing surface plasmon polaritions when an incident electromagnetic wave of relative frequency to the electrons is used, b) relationship of plasmons within metal structures smaller than the incident electromagnetic wavelength that induce local surface plasmon resonance of the electrons. (Stiles et al., 2008)

The wavelength-dependent effect of surface plasmon resonance causes an enhancement of the incident electric field within the range of 10^2-10^4 in the vicinity of the metal surface (Bantz et al., 2011). The magnitude of the electromagnetic field outside of the particle depends quite significantly on the type of metal, the wavelength used and the dielectric material or environment the metal is in.

$$E_{out}(x, y, z) = E_0 \hat{z} - \left[\frac{\varepsilon_{in} - \varepsilon_{out}}{(\varepsilon_{in} + 2\varepsilon_{out})} \right] a^3 E_0 \left[\frac{\hat{z}}{r^3} - \frac{3z}{r^5}(x\hat{x} + y\hat{y} + z\hat{z}) \right]$$

Equation 2.5: Equation to show the magnitude of the electromagnetic field outside the particle, Eout, εin is the dielectric constant of the metal and εout is the dielectric constant of the external environment, α is the metal polarizability , r=radial distance and x, y and z are the Cartesian coordinate axes from the metal surface.

The electromagnetic field outside of the metal can be calculated using Equation 2.5, however one must note that surface plasmon resonance is not infinite and with time and distance from the electromagnetic radiation incident point, the SPR field will decay. The electromagnetic field outside of the metal surface is typically within the range of 0-50nm, however different groups have shown different field enhancement distances, Van Duyne and co-workers showed with silver film on nanospheres (AgFON) at a separation of 2.8nm between the analyte and the surface, the SERS activity decreased tenfold (Bantz et al., 2011). Therefore, SERS can be determined as a surface technique for analyte detection.
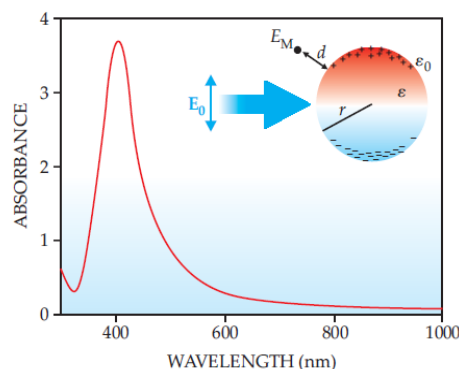
Figure 2.8: Shows the electromagnetic enhancement field from a silver nanoparticle, in relation to respective distance it can exert from outside the metal surface when an electromagnetic wavelength of 400nm which resonates with silver electrons is exerted on the nanoparticle. (Kneipp et al, 2007)

$$E_M = E_0 + E_{sp}$$ a

E : field of a point dipole
in the center of the
sphere

$$E_{sp} = r^3 \frac{\varepsilon - \varepsilon_0}{\varepsilon + 2\varepsilon_0} E_0 \frac{1}{(r+d)^3}$$ b

Equation 2.6: Equation shows firstly a) that the overall electromagnetic enhancement, EM, is comprised of the incoming field electromagnetic enhancement, E_0 and electromagnetic enhancement from the field of a dipole, E_{SP}, b) shows a simple equation to understand the effects of electromagnetic enhancement, where; ε is the dielectric permittivity of the metal and ε_0 is the dielectric permittivity of the surrounding media, r is the radius of the particle and d is the distance. (Kneipp et al., 2002)

Electromagnetic enhancement to obtain SERS spectra for an analyte of interest occurs through generally three steps (McNay et al., 2011);

1. The analyte is adsorbed or in adequate vicinity from a roughened, patterned or nanoparticle metal surface.

2. The energy from the plasmon when excited by an incident wavelength is transferred to the adsorbed molecule, whereby the Raman process will occur (dipole moment, scattering of a different wavelength to incident wavelength).

3. After the process, less energy is transferred back to the plasmon.

To optimise the electromagnetic enhancement, two significant characteristics need to be taken into consideration. Firstly, the use of an adequate metal that resonates with an electromagnetic wavelength commonly used (Fig. 2.9). Gold (Au) and silver (Ag) noble metals are typically used for SERS substrates as their plasmon resonance frequencies are at a high quality factor within the visible and NIR range (Sur et al., 2008). Whereby Au and Ag at these wavelengths have adequate permittivity for electrons within their structure to become polarized. These noble metals are also quite inert and so are easy to handle. Both gold and silver however have different chemistries and therefore bind to analytes of interest at different affinities. Gold typically is present in an Au^0 state and many analytes can physisorb to the surface, inorganic and organic from a media; however,

there is a high affinity for analytes containing a 'soft-binding' group such as thiols. Silver on the

other hand typically resides as Ag+ ions and binds to a 'wider range of donor groups; carboxylates,

thiols' (McNay et al., 2011) and typically oxygen, chloride or other 'organic complexing agents' are

physisorbed onto the silver wire surface, as a layer. The binding of an analyte of interest within the

distance where electromagnetic enhancement can take place is critical for SERS and therefore

different surface modifications for assay development are used (discussed further in sections 2.2.6

and 2.3.5).
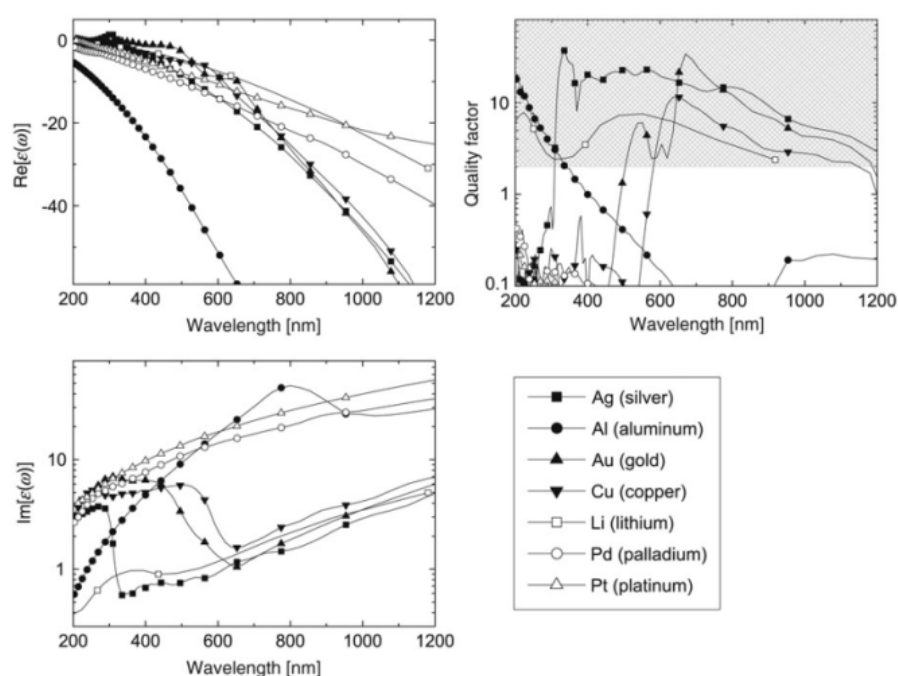
Figure 2.9: To show the relationship of metal with wavelengths over an extended visible range, a) show the metals in relation to the real dielectric permittivity, b) shows the metals in relation to the imaginary dielectric permittivity's and c) shows the quality factor (Q) of the localised surface plasmon resonances for metals nanoparticles in a metal/air configuration. (Le Ru & Etchegoin, 2009)

The second criterion that needs to be taken into account is that the metal surface needs to be

rough, as a plasmon within a smooth surface is more closely bound. When a perpendicular

component to the plasmon occurs, the electromagnetic field outside of the metal surface increases

as there are a larger amount of plasmons that can travel between the surface and the dielectric

interface (Fig. 2.10) (McNay et al., 2011). Larger EM intensity can also be observed when metal

nanoparticles come within a desired distance from one another (Fig. 2.10d).

a

d
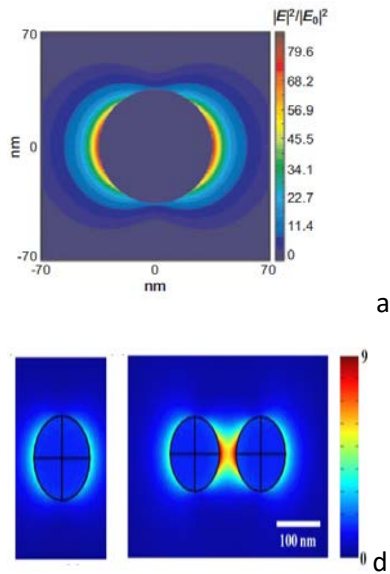
Figure 2.10: Computational models to show the LSPR and EM intensity that can be exhibited by a) spherical metal nanoparticles, b,c) metal nanoparticles with sharper features and d) when nanoparticles come into close vicinity to one another. (Prof.Xies group, 2015; Stiles et al., 2008; X. Zhang, Chen, Liu, & Tsai, 2013)

For each SERS substrate, optimised roughness needs to take into account the incident wavelength frequency, the metal/dielectric environment (Fig. 2.11), and the use of the SERS substrate with the specific analyte to prepare an optimised SERS substrate design.

a

b
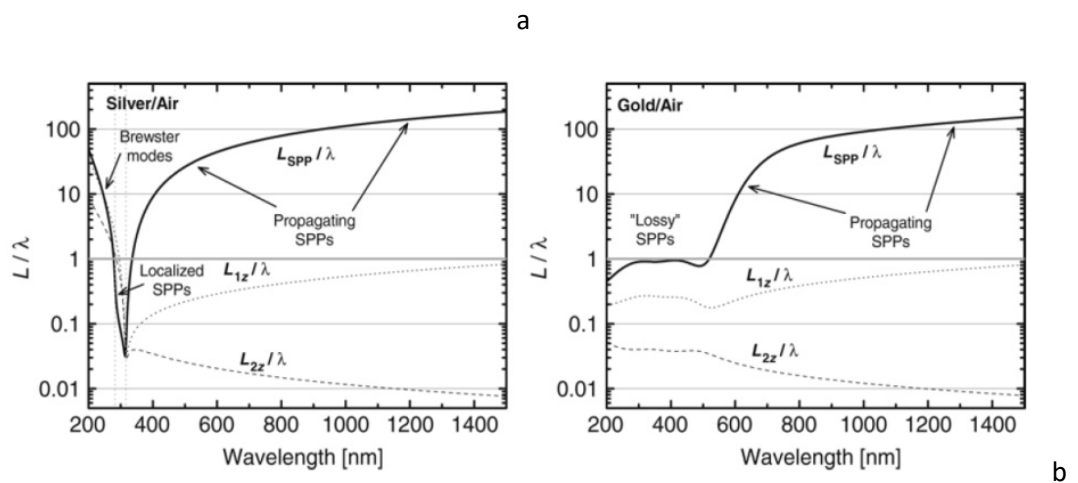
Figure 2.11: Highlights the importance of choosing the right wavelength with regards to the where the SERS enhancement will take place, metal/dielectric interface a) Silver/Air and b) Gold/Air. Propagation decay lengths (L/λ) of surface plasmon polaritions (SPP) of the surface wave in relation to incident wavelength. 'L1 and L2 are decay lengths along 2 axes away from the interface.' (Le Ru & Etchegoin, 2009)

The roughness however is required to be repeatable for reliable SERS substrate fabrication. With SERS substrate having an ideal uniform roughness. If an area on the surface has increased roughness compared to other areas; when hit by the incident EM wavelength it will cause an increased EM intensity, high-field gradient, to be exerted, known as a 'hot-spot'. If an analyte is attached to that region, an increase in SERS signal intensity is obtained (McNay et al., 2011). With

22

further scans taken on other areas of the SERS substrate with different roughness morphologies, the Raman spectral intensity differs, this is detrimental to the use of SERS as a quantitative technique as the analyte concentration is less accurately determined, with a requirement of increased scans taken for reliable results. Therefore, SERS substrate design is an imperative step for improving SERS and implementing it commercially for disease diagnosis and monitoring.

2.1.6. SERS: Chemical Enhancement

Chemical enhancement is also noted as one of the two mechanisms that contribute to the SERS effect, providing an enhancement factor of 10^2 (Stiles et al., 2008) for the overall SERS intensity. It has been defined as 'corresponding to any modification of the Raman polarizability tensor upon adsorption of the molecule onto the surface' (Le Ru & Etchegoin, 2009).

The general method by which chemical enhancement occurs is through a charge-transfer mechanism and there are three different types of charge-transfer chemical enhancement for SERS that can occur (Le Ru & Etchegoin, 2009).

- Type I: the molecule does not bind covalently to the metal; however the metal when in close proximity to the molecule causes a mild change to the molecule's electronic structure, which causes a change in polarizability.

- Type II: The molecule binds to the metal through direct binding (covalent bonds) or indirect binding, which causes a new surface complex to be created. This new structure has an altered intrinsic polarizability of the molecule.

- Type III: this is a photon-driven charge transfer, whereby the molecule is bound to the metal surface as with type II, but additional charge-transfer is caused through the incident electromagnetic wavelength matching the metal's Fermi level, for the highest occupied molecular orbital (HOMO) or lowest unoccupied molecular orbital (LUMO). This causes a charge transfer between the HOMO and unoccupied states above the

Fermi level or between the LUMO and occupied states slightly below the Fermi level. This alteration causes an electron-hole pair to be formed which transfers energy to the bound molecule within the new bond, causing the molecules structure and polarizability to be altered within the complex.

All three types can contribute to the chemical enhancement exhibited by SERS however type III is the one that can be altered using SERS, through choice of wavelength used on metal.

2.2.   SERS: Substrates

The typical components that comprise a Raman spectrometer are (Vandenabeele, 2013); a monochromatic light source (laser, laser emitting diode), sample (solid, liquid or gas), dispersive spectrometer and detector. For SERS an additional component is added to the system, in the form of an optimised substrate onto which the molecule of interest is bound to for increased enhancement. SERS substrates can be generally classified into three sub-sections (Le Ru & Etchegoin, 2009):

1.   Metallic Electrodes

2.   Metallic nanoparticles

3.   Planar metallic structures

The metallic substrate as mentioned in section 2.2.5, are commonly silver, gold or copper, as these three metals have localised surface plasmon resonance that occur within the 'visible and near infrared wavelength range' (Sharma et al., 2013).

There have been a large number of methods employed for SERS substrate design from the original method, where SERS was first discovered using electrochemical oxidation-reduction cycles (EC-ORC) on silver electrodes, to provide a roughened surface. To methods involving the incorporation of nanotechnology, from the fabrication of nanoparticles to highly ordered nanoscale SERS structures.   Multiple SERS substrate design methods have been used, most commonly

nanolithography, bottom-up methods using chemical reduction and recently there is a growing presence of inkjet and screen printing (Le Ru & Etchegoin, 2009; Wu et al., 2015; Q. Yang et al., 2015).

2.2.1. Commercial SERS Substrates

An ideal SERS substrate which most researchers desire fits 5 criterion (Lin, Cui, Xu, Ren, & Tian, 2009; Wu et al., 2015);

1) Capable of high SERS enhancement and therefore high sensitivity

2) Uniform SERS, with a deviation in enhancement of less than 20%

3) Good stability and reproducibility, with a deviation of SERS enhancement between batches of less than 20%.

4) A clean substrate that can detect both large molecules as well as small molecules that have weaker signal.

5) Ability to fabricate on the large-scale at low-cost

As of yet the fulfilment of all 5 criteria for a SERS substrate is a challenge. Commercial SERS substrates are available in multiple designs; from solid SERS substrates to nanoparticles within a solution. However the scope of the SERS substrates available have not been fully looked into and standardisations between groups has not occurred.
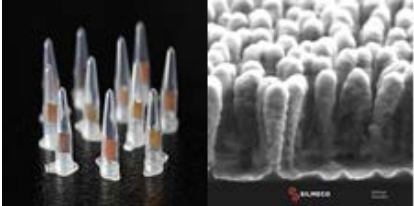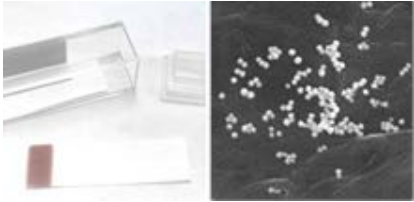
The types of designs that have been successful for commercialisation are shown in Table 2.1. It shows that with the use of lithographical and etching methods, the price of the SERS substrate is higher within £30-50 range for SERStrate and Randa individual pieces. This increased price is mainly due to the time-consuming and costly methods used, from lithographical patterning to maskless-etching. The price also highlights the deterrent many research groups face for using commercial SERS substrates for experimentation and standardisation as well as the short half-life of the commercial SERS substrate, highlighted by the SERS substrate 'Randa' which has a shelf-life
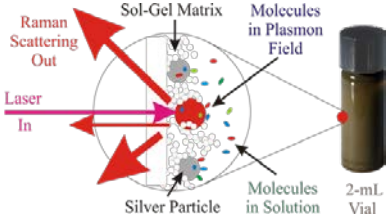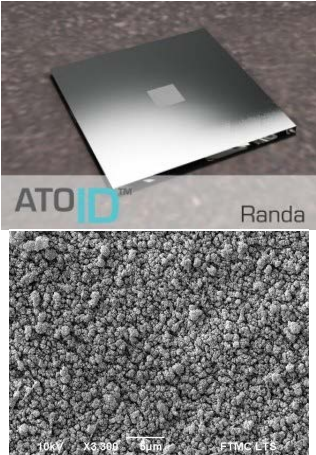
of 2 months once fabricated. However these SERS substrates are claimed to have high sensitivity, parts per billion (ppb), with a range of wavelengths such as for SERStrate. (AtoID, 2015; Silmeco, 2015)

Another interesting commercial SERS substrate that has been highlighted is PSERS, which is quite an affordable substrate at individual strips being less than £4, and claims for versatility in use. The method uses the increasingly popular idea of ink-jet printing, which is most cost-efficient for mass production. However when observing the uniformity of the gold nanoclusters on the cellulose paper shown in Table 2.1, one would need to question how uniform the SERS substrate is, as hot-spots would be present by looking at the design (Diagnostic anSERS, 2015).

The use of NPs has opened up multiple new possibilities for SERS substrate design. Typically the NPs for commercial use have not been shown to be by themselves within solution for SERS testing. Instead they appear to be within a structural matrix such as the SERS vials produced by Real Time Analysers, that show the silver nanoparticles entrapped within a sol-gel matrix (Real Time Analyzers, 2015). There are research groups that use nanoparticles by themselves for SERS testing. However one would assume that the additional structure encapsulating the nanoparticles in commercial SERS substrates enables improved reproducible results for a more reliable system.

Table 2.1: Shows the different SERS substrate designs that have been successful for commercialisation, with focus placed on material, methods, claims and cost of the SERS substrates (AtoID, 2015; Diagnostic anSERS, 2015; Real Time Analyzers, 2015; Sers, 2015; Silmeco, 2015).

SERS substrate	Company	Image of SERS substrate	Material used	Method used for fabrication	Claims & Specifications	Cost
SERStrate	Slimleco, Denmark		Silicon nanopillars coated with either gold or silver.	Two step process; 1) Maskless dry etching to create the silicon nanopillars. 2) Electron beam evaporation of gold or silver to coat the silicon.	• 16mm2 SERS active area • 4x4mm dimension • Sensitivity: ppm to ppb • Laser power density: <10 W/cm2 • Excitation wavelengths: 514nm, 532nm, 633nm, 780-785nm.	10 SERStrates: $525 which is equivalent to £336.17 Individual SERStrate: ~£33.62
PSers	Diagnsotic anSERS inc, USA		Typically cellulose paper with gold nanoclusters on the surface	Uses inkjet printing to deposit gold nanoclusters onto cellulose paper.	• Flexible, quick sample application. Can be down via pipetting sample, dipping or swabbing. • Sensitivity: ppb • Shown to detect drugs, narcotics, bacteria, proteins, pesticides, insecticide residue and explosives.	10 pieces: $60 (~£38.42), 1 Pice: ~£3.84

SERS Vials	Real-Time Analyzers, Inc, USA		Sol-gel matrix with silver particles embedded within structure.	Patented SERS active sol-gel method used.	• Long shelf-life • Reproducible (vial to vial) • Fast response time: <1 second • Sensitivity: ppb, nM, mg/L • Used to test drugs, bacterial endospores, pesticides and food adulterants.	Depends on order
Randa	Integrated Optics, Lithuania		Silver deposited on soda-lime glass	Nanopatterning used via ultra-short pulse laser method. After which silver is deposited.	• SERS active area can be varies from 4x4mm to 10x10mm. • Feature on surface from 70nm to almost micron size. Therefore recommended focusing of 20 microns or more to create adequate laser spots. • Shelf life: 2 months	One piece: $75 (~£48.02)

2.2.2. SERS Substrate: Metal Wire

Metal wire or metal electrodes comprise one of the three main categories used as a SERS substrate (Le Ru & Etchegoin, 2009). Metal electrode roughening is traditionally accomplished through; electrochemical oxidation and reduction cycles (EC-ORC) or vacuum deposition methods. These methods fabricate random, non-uniform substrates, typically with surface features within the range of 25-500nm (Lin et al., 2009). They were used in the early stages of SERS, with roughened silver electrodes being the first SERS substrate. The use of metal wire and electrodes is still an area of interest, due to the robustness and availability of the material. Through simple roughening of the metal surface, the substrate can be used straight away for binding to an analyte for SERS testing and therefore substrates fabricated within this field would be cost-effective (Vo-Dinh, 2014).

Methods to produce more uniform and controlled roughness have come about, through the advancement of etching techniques with 100nm surface features on the metal surface being obtained, necessary for LSPR for SERS (Vo-Dinh, 2014). One such technique that can be applied to SERS substrates is the use of chemical etching (Rajesh, Mahendar, & Sunandana, 2013).

There are three types of chemical etching methods: wet, dry and electrolytic, each has its advantages and disadvantages for creating a controlled rough surface. The simplest etching has to be the traditional wet chemical etching, whereby a metal is immersed in a dilute solution of strong acid which causes the silver metal surface to react; corroding the surface through a redox reaction. This occurs at a certain rate depending on the acid and the metal used, creating a rough surface. Etching chemistry is typically an electrochemical process, caused by the oxidation of a metal surface. An oxidising agent, an acid or base to dissolve the oxidising agent and a diluent media for removing the reactants and products are desirably present (MicroChemicals, 2013; Walker & Tarn, 1991).

$$\text{Metal} + \text{H}+ \rightarrow \text{metal}+ + \text{H}$$
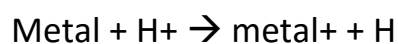
Equation 2.7: General equation for how chemical etching of a metal occurs. (MicroChemicals, 2013)

The process can occur in less than a minute depending on the size of the metal required to be etched. Strong acids which act as oxidizing agents are typically used in dilute form such as nitric acid, sulphuric acid or hydrochloric acid. Deionised water is commonly used as the diluent and an extra step through the use of an alkali, such as ammonia can serve as the base to help with dissolving the oxidised surface, it also has the extra property of acting as a cleaning agent (Walker & Tarn, 1991). Therefore the chemically etched metal should also have less contaminants' present on the surface.

2.2.3. SERS Substrate: Silver and Gold Nanoparticles

Nanotechnology is the 'study, manipulation, creation and use of materials, devices and systems typically with dimensions smaller than 100nm' (Jianrong, Yuqing, Nongyue, Xiaohua, & Sijiao, 2004). This size reduction causes nanoparticles to possess differing physical and chemical properties compared to the bulk material due to an (Domènech et al., 2012);

- Increased surface to volume ratio

- Changes in the electronic structure

- Changes in inter-atomic distances and the presence of defects

- Different structural confinement causing quantum characteristics.

Nanoparticles can thus have enhanced surface plasmon resonance, super paramagnetism or increased strength through the quantum confinement of the electron movement (García-Barrasa, López-de-Luzuriaga, & Monge, 2011). These advantageous properties have 'revolutionised' the way in which we approach problems from current techniques and enabled the production of new methods to benefit multiple fields, one of which being biosensors within lab on a chip devices.

There are various methods used for nanoparticle synthesis but depending on the application of the nanoparticles, different approaches are undertaken. In general, there are two routes nanoparticle synthesis can go through: physical and chemical.

This is further subdivided into either the top-down or the bottom-up approach, whereby material is either broken down from the bulk material into smaller parts, or the nanoparticles are assembled from corresponding precursors (Fig. 2.12) (Domènech et al., 2012).
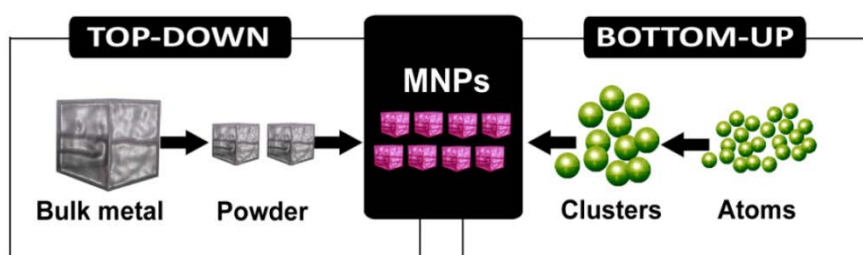
Figure 2.12: Diagram to show the two general approaches nanoparticle synthesis can follow. Top-down or bottom-up. (Domènech et al., 2012)

Generally top-down approaches, follow the physical route for nanoparticle synthesis by the breaking down of particles; such as through milling, grinding or alloying, which occurs under solid phase. Whereas bottom-up approaches usually follow the chemical route for nanoparticle synthesis by building up nanoparticles from atoms; this process takes place either in the liquid or the gas phase (R. Nagarajan, 2008).

The chemical route is typically considered as the cheaper route for nanoparticle production and is typically based on the reduction of metal salts in solution, following a 2 stage process; nucleation and growth. The nucleation stage requires high activation energy to form, whereas the growth stage requires low activation energy. This is due to the entropy within the system, which requires a higher amount of energy to form bonds within nucleation, compared to within the growth stage, where additional by products and metal ions add onto the metal surfaces. The relative rates of these two stages implements size and shape of the nanoparticles within the solution, therefore careful control of parameters affecting these two rates is imperative (Fig. 2.13) (García-Barrasa et al., 2011). An additional stage can also be noted, known as the termination stage, as nanoparticles

31

within solution have a tendency to aggregate, growing beyond the desired size with increased time, implementation of a stabilising agent is added typically to prevent the loss of integrity (Domènech et al., 2012).
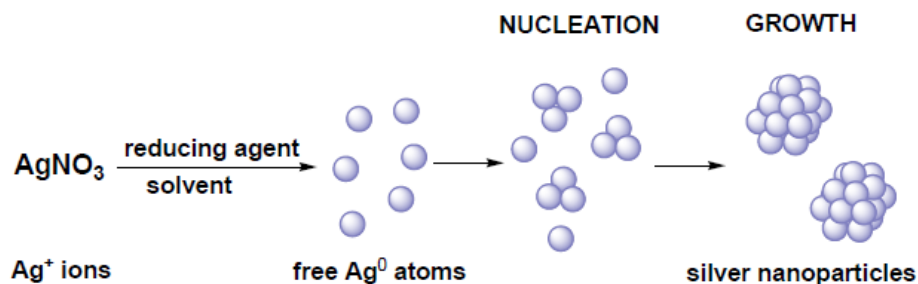
Figure 2.13: Diagram to show the commonly attributed stages associated with nanoparticle synthesis following the bottom-up chemical approach (García-Barrasa et al., 2011).

There are multiple methods that employ the chemical route of NP synthesis, however for SERS NP substrates, typically a Tukevich method or a Lee-Meisel method to prepare gold and silver nanoparticles respectively is used. These methods give a broad distribution of NP size (García-Barrasa et al., 2011; Le Ru & Etchegoin, 2009) and if manipulated desired shape, can be altered through the use of different reducing agents and stabilising agents.
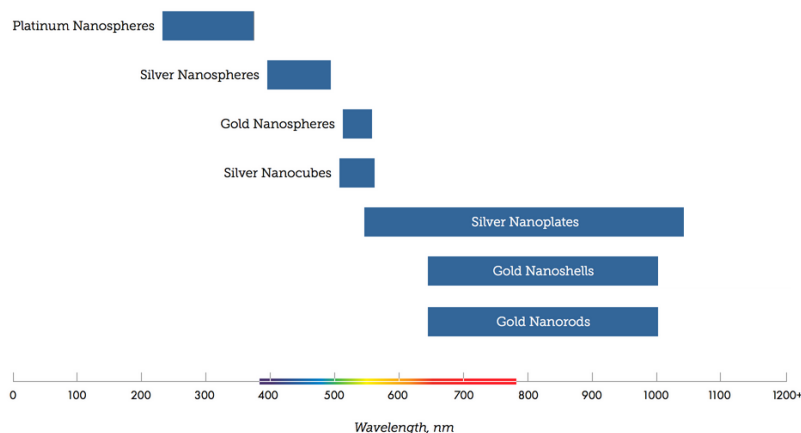
Figure 2.14: Diagram to provide a rough idea of the different shapes can be synthesised for metal nanoparticles, in particular silver and gold, for plasmon resonances that correlate with specific wavelength ranges (nanoComposix, 2015).

Figure 2.14 highlights that nanomaterials can have different structures, and that not all the dimensions for a material need to be smaller than 100nm for it to be deemed part of nanotechnology (Cash & Clark, 2010). There are 3 general groups that nanomaterials can fall into

32

regarding dimensions where nanometer size is accomplished; 1D nanometer size objects typically

are thin films; 2D nanometer size depict objects such as nanowires or nanotubes and 3D nanometer

size objects would be nanoparticles for example (Domènech et al., 2012).
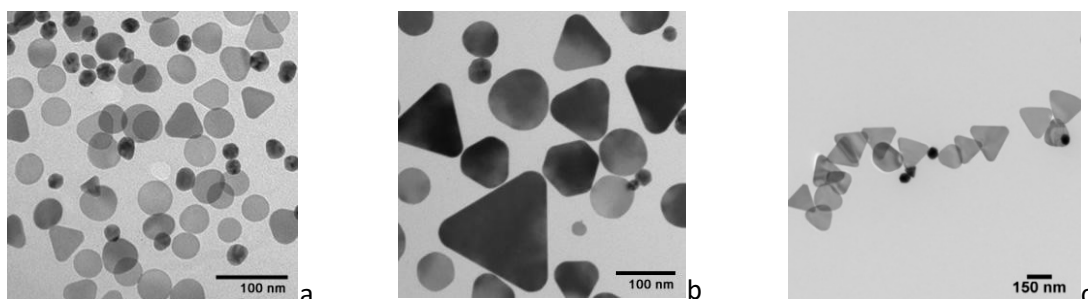
Figure 2.15: TEM images for commercially available silver nanoplates with specific size and shape for different plasmon resonance wavelengths, a) 550nm, b) 750nm and c) 1050nm (nanoComposix, 2015).

The TEM images for commercial silver nanoplates (Fig. 2.15) highlight that specific size and

shape ranges are needed for optimisation of wavelength with regards to SERS as well as that the

nanoparticle size range increases with increasing wavelength, as at 550nm the nanoplate size was

optimised to 40-60nm, at 750nm the size range was 80-100nm and at 1050nm the size range was

100nm±10nm (nanoComposix, 2015). This is due the optical characteristics of the nanoparticles

being altered with increased size and as such the optimised propagation of free electrons upon the

surface requires higher wavelengths.

The commercial substrates although readily available for sizes suitable to wavelengths typically

used for SERS, these nanoparticles are expensive for use within research, as for 25ml of silver

nanoplate solution it would cost $50 USD, whereas for other shapes such as silver nanocubes which

are noted for high SERS activity the price for 1ml would be $295 USD (nanoComposix, 2015). Also

as of yet an ideal SERS substrate has not been produced, so for potential to alter the size and shape

for better SERS signal, in-lab nanoparticle synthesis is desired.

2.2.4. Microemulsions: Nanoparticle Synthesis

Due to the ease of preparing one's own NPs within solutions through the use of chemical

methods, many research groups generally prepare their own NPs. The Lee-Meisel and Tukevich

methods although able to produce nanoparticles, require an additional surfactant or polymer to alter the shape of the nanoparticles, such as with the addition of Cetyl Trimethyl Ammonium Bromide, (CTAB) or poly(vinylpyrrolidone), PVP (García-Barrasa et al., 2011; nanoComposix, 2015). Microemulsions are one of the most popular surfactant-based techniques for nanoparticle synthesis due to multiple advantages (Sanchez-Dominguez, Aubery, & Solans, 2011; Uskoković & Drofenik, 2005);

- Versatility in materials that can be prepared

- High degree of control for particle size and composition

- High specific surface area (nanocatalysts prepared in this way are shown to have better performance than other methods)

- Synthesis can take place at/or near ambient temperature and pressure and simple equipment used

- Reproducible

- Low aging time

- Low energy consumption

These advantages have made nanoparticle synthesis within microemulsions a desirable method for use within research, for developing better nanostructures for improving techniques and introducing new instrumentation, such as in the use of nanoparticles with different shapes and sizes and their optimisation as a SERS substrate.

2.2.4.1. Principles

Microemulsions were first proposed in 1943 by Schulman & Hoar and defined in 1954 by Winsor. They described a system comprising of three to four main components, a hydrophobic region (oil/solvent) a hydrophilic region (water) and a component that has both hydrophilic and hydrophobic regions (surfactant, co-surfactant), Figure 2.16. Depending on the solution

composition of these three to four components, different characteristic phases are present (Najjar, 1970).
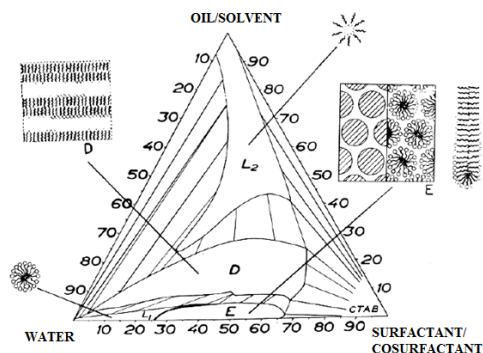
Figure 2.16: Pseudoternary phase diagram to show the different phase equilibriums water, oil and surfactant/cosurfactant can exist in (modification of Uskoković & Drofenik, 2005 diagram).

The Pseudoternary phase diagram shown in Figure 2.16 shows that depending on the ratio of these 3 to 4 components the composition of the solution changes. For nanoparticle synthesis the water-in-oil inverse micelle structure is typically used, as shown in the L2 region. The water core behaves as a 'nanoreactor' where polar and water soluble reactants are dissolved (Shchukin & Sukhorukov, 2004). Through the dynamic characteristics of the microemulsion system, random Brownian motion is consistently taking place, whereby the inverse micelles collide and then coalesce, causing an exchange of contents before breaking apart to resume their inverse micelle structure. This exchange process varies depending on the microemulsion system used and it has been noted that there is an effective exchange of reactants for every 1 in 10^2-10^4 collisions (Ganguli, Ganguly, & Vaidya, 2010). Intermicellar exchange is the rate-limiting step for nanoparticle synthesis, with significant influence on the size and shape of the nanoparticles produced, the exchange time between two inverse micelles depends on the characteristics of the microemulsion system but is generally shown to vary between 10μseconds to 1 millisecond (Eastoe, Hollamby, & Hudson, 2006).

The most commonly used method for nanoparticle synthesis within inverse micelles requires the preparation of two separate microemulsion systems for the addition of different reactants, typically a metal salt precursor and a reducing agent for the formation of inorganic

nanoparticles (Fig. 2.17). The reactants due to polar and hydrophilic qualities dissolve into the water

cores of the systems and once mixed, as discussed above, cause exchange of reactants, which

reduces the metal precursor within a confined chamber, and thus forms nanoparticles (Eastoe et

al., 2006).
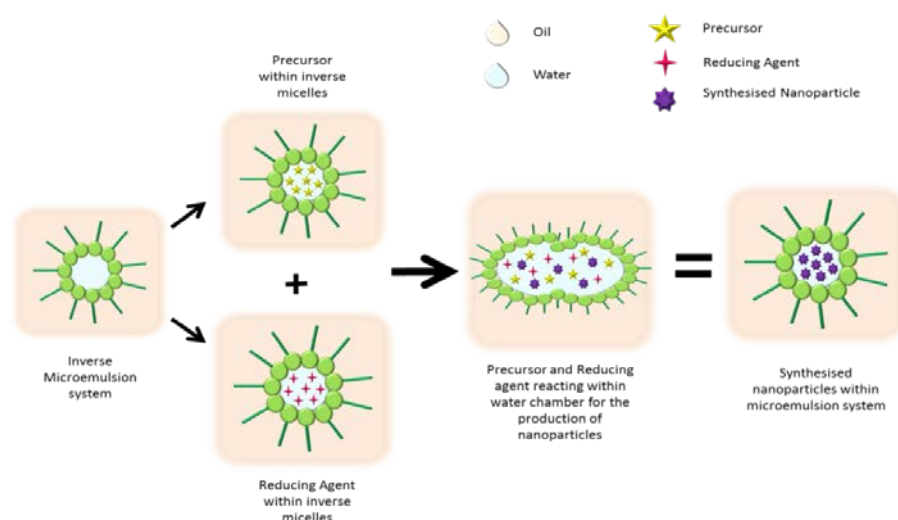
Figure 2.17: Diagram to show the most commonly used method for nanoparticle synthesis using microemulsions.

As discussed previously, NP synthesis following the bottom-up approach consists of two main

stages; nucleation and growth, by varying the rates of these two stages, nanoparticle size can be

controlled.

2.2.4.2. Size & Shape control theory

Microemulsions for NP synthesis have been used by multiple research groups with various

organic and inorganic precursors, producing different shapes and sizes. As of yet the design

procedure is not cemented and relies on a trial and error approach for the fabrication of ideal

nanoparticles for individual research needs (Uskoković & Drofenik, 2005).

There is more research that considered the manipulation of NP size within microemulsion

systems, than the control of NP shape (M.-P. Pileni, 2003). NPs within micelles have generally been

shown to form spherical structures (Li, Xu, Zhou, Yang, & Liu, 2012). However there is a growing

interest in creating anisotropic nanoparticles as they would be more effective in multiple fields, one such being SERS (M.-P. Pileni, 2003).

The underlying process, by which NPs of different size and shape are produced within the microemulsions, is predominantly determined by intermicellar exchange of reactant contents. Nucleation is observed to occur instantaneously once an efficient transfer of reagents takes place within a fused dimer state, supported by nucleation sites starting on the edges of the micelle. Growth of the nanoparticles then takes place at the nucleation site, with the 'selective adsorption of molecules or ions to the facets of the nanocrystal' (Eastoe et al., 2006) moving towards the core of the micelle (Fig. 2.18). For the creation of anisotropic nanomaterial within the micelles, selective adsorption of molecules during crystal growth on certain facets of the crystalline structure is key for controlling nanocrystal shape (M.-P. Pileni, 2003). A defect engineering theory is proposed for anisotropic shape, hypothesised due to the presence of a forbidden reflection 1/3{422} being observed using electron diffraction of silver nanodisks, this was hypothesised to occur due to a stacking fault in the [III] plane of the metals crystalline structure (Fig. 2.18b). This fault caused growth of the nanomaterial within the area parallel, due to the favourability of nucleation and growth, thus causing an anisotropic structure to appear and thus the presence of the nanodisks within the study by Pileni's group (Eastoe et al., 2006; Germain, Li, Ingert, Wang, & Pileni, 2003).
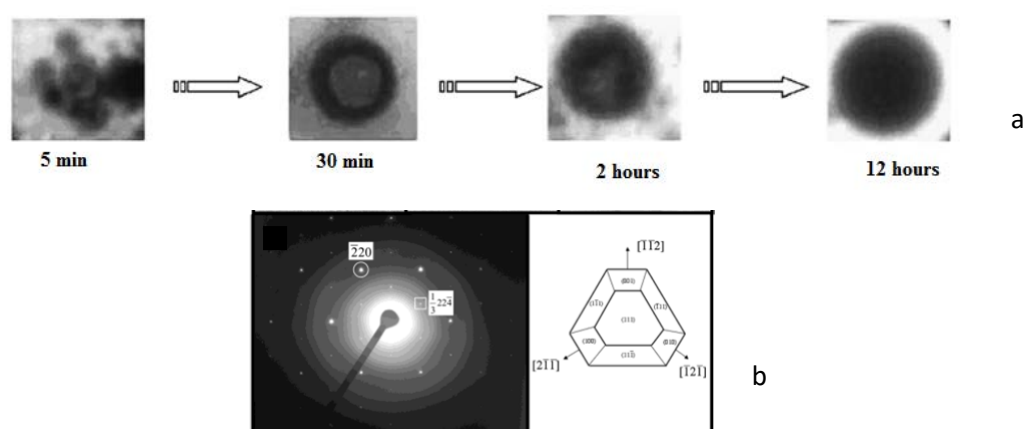
Figure 2.18: Diagrams a) shows TEM images of ZnS and the formation of nanoparticles with aging of the solution, with nucleation being shown to occur at the micelle edges and then moving towards the centre of the micelle (Modification of diagram from Eastoe et al, 2007) and b) left image shows the

crystallographic orientation of the typical [111] pattern of silver nanodisks{220} Bragg reflection and 1/3
224, the right image shows the selected area diffraction (SAED) of the [111] plane of the typical nanodisks
structure (Germain et al., 2003).

There are 5 main parameters that have been highlighted for affecting the size and

polydispersity of nanocrystals within the microemulsion system and it has been noted within

literature that 3 of these main parameters also affect the shape of the particle, through the

influence of the micellar template, anions and molecular adsorption (Eastoe et al., 2006; Ganguli et

al., 2010; M. P. Pileni, 2006; M.-P. Pileni, 2003; Zielinska-Jurek, Reszczynska, Grabowska, & Zaleska,

2012) the 5 main parameters are:

1. Surfactant/Co-surfactant

2. Solvent

3. Addition of electrolyte

4. Concentration of reagents

5. W number

2.2.4.3. Parameter: Surfactant

There are three characteristics of surfactants that cause the controlled size and shape of

nanoparticles. Firstly the surfactant is a molecule that has both hydrophilic and lipophilic qualities,

typically having a structure with a polar head and a hydrophobic tail, different surfactants have

different ratios of lipophilic to hydrophilic quantity within the molecule and this is known as the

hydrophilic-lipophilic balance (HLB) (Griffinn, 1949). When the surfactant is added to a solution

containing two immiscible phases, typically oil and water, it becomes a surface active agent,

reducing the interfacial tension within the solution. Secondly one should note, only if a certain

concentration of surfactant is added to the solution, known as the critical micelle concentration, it

is able to form micelles. This leads thirdly to the dependency of the size of the surfactant that is

used for forming the micelles, if a surfactant has a larger polar head and short hydrocarbon tails, it

leads to cone shape micelles forming and spherical nanoparticles, however if the micelle has small

polar heads and multiple hydrocarbon chains, the surfactant may exhibit a different micelle

morphology, this is defined under the surfactant packing parameter (Ganguli et al., 2010; M.-P. Pileni, 2003).

It has been shown that the micelle template can influence the resultant nanomaterial shape, through the micelle constricting the growth of the nanomaterial by Pileni et al. Micelles can be altered through the chemistry of the surfactant or through external parameters, as shown by Zhang's group through the use of ultrasonification on AOT/Isooctane microemulsions. The ultrasonication caused the micelle structure to go from spherical to ellipsoidal and the silver nanoparticles were then converted from spherical to nanorod morphology (Li et al., 2012).
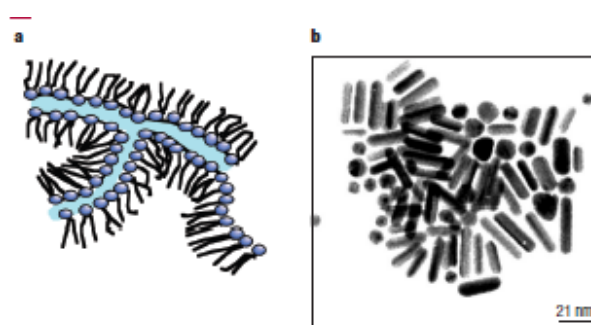
Figure 2.19: Diagrams to show a) pictorial image of altered shape of inverse micelles and b) copper nanoparticles produced within these micelles using AOT/Isooctane (image modified from Pileni et al, 2003).

Surfactants can be anionic, cationic or neutral and the most commonly used surfactants from each group are AOT, CTAB and Triton X-100 respectively (Fig. 2.20) (Eastoe et al., 2006). The affinity the surfactant has with the nanomaterial has been hypothesised to affect the growth of the nanomaterial, with low affinity of surfactant to metal centre causing an increase in final size (Ganguli et al., 2010).

These surfactants as well as having different charge characteristics, have an affinity to form different micelle structures, with AOT micelles commonly having a higher packing density than CTAB, thus forming more rigid micelle structures. The rigidity of the micelle is important due to the successful collision and coalescence of micelles with one another within the solution. As AOT has a more rigid structure, smaller nanoparticles that are typically spherical are commonly fabricated,

compared to CTAB which has a lower packing density, thus a higher fluidity within the solution. This allows higher exchange of reactants, forming larger nanomaterials (Ganguli et al., 2010; Zielinska-Jurek et al., 2012). Experimental evidence that surfactant packing density and therefore rigidity plays a role, disregarding charge effect, is through the swapping of TritonX-100 for Tergitol within a microemulsion solution, it caused the conversion of spherical nanoparticles 5nm in size to larger cubes 50nm in size respectively, as tergitol has a lower packing density compared to Triton X-100 and therefore the fluidic structure allows a higher intermicellar exchange rate and freedom of therefore growth of the nanoparticle (Ganguli et al., 2010).
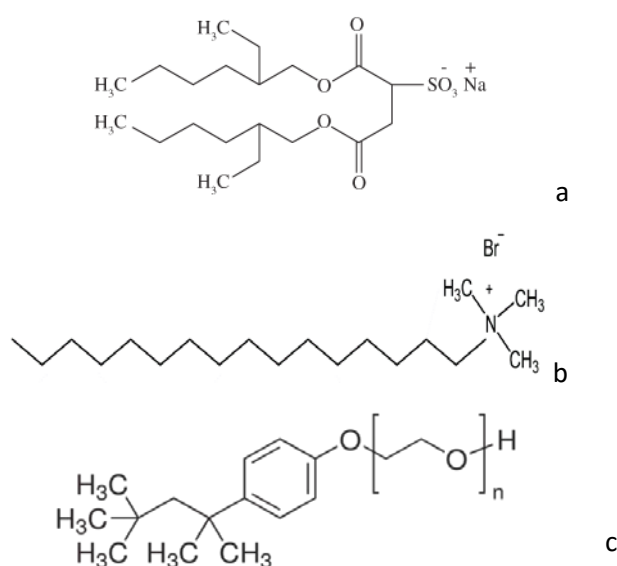
Figure 2.20: Shows the chemical structure of a) AOT, b) CTAB and c) Triton X-100.

The role of the co-surfactant is to implement a 'higher fluidity of the interfacial film' (Ganguli et al., 2010) which increases interfacial exchange rate, they also increase the curvature of the micelle structure. Co-surfactants are typically intermediate chain length alcohol such as butanol (Eastoe et al., 2006) and are required to aid in the micelle formation for some surfactants such a CTAB.

2.2.4.4. Parameter: Solvent/Oil

The implementation of a solvent is critical for microemulsion systems as it one of the three main components. Solvents can have varying chain lengths and their interaction with the surfactant

is significant for the formation of nanomaterials. This is through the control of the bending rigidity of the interfacial film of the micelle (Ganguli et al., 2010).

Bagwe & Khilar, 1999, investigated this parameter with effect to silver nanoparticle size produced. They used three solvents; cyclohexane, n-heptane and decane, which have increasing chain lengths, they found that the rate of micellar exchange increased with increasing chain length. As the interaction with the surfactant and solvent caused different surfactant packing densities and in this case looser structures with increased chain length. Thus increased successful coalescence of micelles. The size of the nanoparticles was shown to increase from cyclohexane at 5.4nm to n-heptane 22nm and thereafter decreased in particle size for decane with average size of 6nm (Zielinska-Jurek et al., 2012). One can say that there is not a straightforward rule for the use of solvents on nanoparticle size obtained. However the small size shown with cyclohexane can be due to the ability of these solvent molecules to penetrate between the surfactant molecules and thus increase the curvature and rigidity of the film, shown by the lowest micellar exchange rate. (Eastoe et al., 2006) The use of larger solvents, such as in the case of decane compared with heptane is as the solvent chain increases the interaction with the surfactant may be less, which causes the increase in micellar exchange. However, if the micellar structure is too loose, the control of the nanoparticles synthesised and directed growth to the centre may be deterred, causing smaller nanoparticles. Heptane perhaps created an optimised balance between fluidity and control of the micelles.

Particle size was also shown to increase in another study with cyclohexane and isooctane with copper nanoparticles. With increased chain length it was also shown to increase particle size. However, they noted that with increased time the copper nanoparticles within the cyclohexane microemulsion became larger. Therefore, even with increased rigidity, one may hypothesise that the nanoparticles, if space is present, may grow to the final size within the microemulsion despite lower intermicellar exchange rates (Eastoe et al., 2006).

2.2.4.5. Parameter: Electrolyte

The addition of salt when dissolved within the microemulsion system, produce electrolytes, which are ionised molecules. These molecules have been shown, in some microemulsion systems, to increase the particle growth rates through the destabilisation of the micellar system (Eastoe et al., 2006). This instability is caused through the 'dissociation of emulsifier, solubility of emulsifier and aggregation of micelles' (Zielinska-Jurek et al., 2012).

It was shown by Chiang et al that upon addition of 2.5M NaCl, Au nanoparticles in water-AOT-Isooctane microemulsion systems caused a shape change from spherical to cylindrical, trigonal and cubic shapes (Jurek et al). This characteristic of salt addition was also highlighted by Pileni et al, through the alteration in Cu nanomaterial shape in Cu(AOT)2-isooctane-water systems with addition of different types of salt at a $2x10^{-3}$M concentration (Fig. 2.21) (M. P. Pileni, 2006).
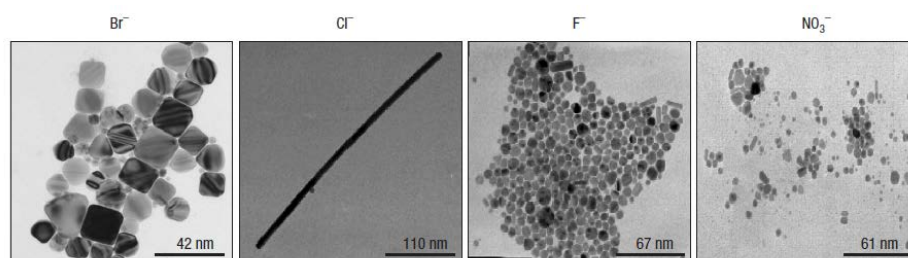
Figure 2.21: TEM images of copper nanomaterial with altered shape with the addition of different electrolytes to the Cu(AOT)2-isooctane-water systems (M.-P. Pileni, 2003).

The addition of different electrolytes to the solution, as shown in Figure 2.21 highlights the variation in shape. Bromide ions cause the copper nanomaterial to form cubic structures. Chloride ions cause formation of rod like structure for copper. Further addition of fluoride ions appear to cause the aggregation of the nanoparticles but the integrity of the shape and polydispersity for the individual copper nanoparticles is maintained. In contrast, addition of NO_3^- ions causes increased particle size distribution for copper nanoparticles, which is postulated to take place through the selective adsorption of ions to the facets of the nanocrystal, affecting the direction of growth (Eastoe et al., 2006). Pileni et al noted that the template structure for all the microemulsion systems remained the same and therefore one would note that the micellar template was not imperative

for shape control. They did however highlight that they could not claim that the addition of these specific salts with different nanomaterial would have the same effects on nanoparticle shape (M.-P. Pileni, 2003).

2.2.4.6.   Parameter: Reagent concentration

The addition of metal precursor salt and reducing agent is imperative for the synthesis of metal nanoparticles within microemulsions. With the increased addition of precursor concentration, polydispersity decreased (Eastoe et al., 2006), which could be due to fact that the ratio in concentration between the metal precursor and the reducing agent used for the initial synthesis depicts the number of nuclei that would be present and through this the particle size and shape of the nanoparticles (Destrée & B.Nagy, 2006). With increased precursor concentration, more of the micelles would have the possibility of nuclei formation once mixed at the same time, thus the nanoparticles would grow at the same rate, providing improved monodispersity.

The shape of the NPs was shown to be altered with variation of the metal precursor to reducing agent ratio. This was experimentally supported through work by Chiang et al, whereby the formation of Au nanoparticles when there was a decrease in reducing agent to precursor or the direct injection of precursor to mixed micelles containing the reducing agent, anisotropic Au nanomaterials such as cylinders and trigons were formed (Zielinska-Jurek et al., 2012).

The nanoparticle size is also influenced by this ratio, shown by Pileni et al,2003 where silver nanodisks were formed at an initial hydrazine concentration shown in Figure 2.22a, with increased hydrazine concentration to silver nanodisks within the microemulsion system, there was an increased size shown by TEM images (Fig. 2.22). This is theorised as being caused by the adsorption of hydrazine, hydrogen or hydroxyl ions on to the faces of the copper crystal and causing increased growth in those areas (M.-P. Pileni, 2003).
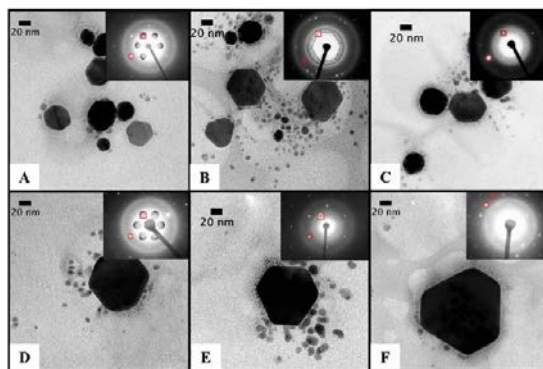
Figure 2.22: TEM images and correlated diffraction patterns showing forbidden reflections of silver nanodisks. With the progression from a) to f) there is an increasing size of the silver nanodisks with increasing concentration of hydrazine (M. P. Pileni, 2006).

The type of reducing agent and precursor salt used also has the influence of electrolyte formation, which, depending on the affinity of adsorption discussed in section 2.3.4.5., would influence the size and shape of the nanoparticles produced.

2.2.4.7.   Parameter: W number

The W number is the water to surfactant molar ratio, Equation 2.8 and is a critical value for determining the amount of water present within the system. The water chamber within inverse micelles, as discussed previously is where the polar reactants go into and when enough reactant is present when exchanged through coalescence, nucleation can take place. The particle size and monodispersity depends on the number of nuclei present at the beginning of reduction, as discussed previously. Therefore the number of water chambers present has a determinative role in particle size for initial synthesis (Destrée & B.Nagy, 2006; Eastoe et al., 2006).

$$W_0= [Water]/[Surfactant]$$

Equation 2.8: Equation to show how to calculate the W number for specific microemulsion systems.

There are three kinds of water that can exist within a microemulsion system; bulk, bound and trapped within the inverse micelles polar surfactant heads to water interface. These three have different characteristics and the ratio between them determines the nanoparticle growth rate and final size. Bulk water is the water present within the centre, known as the water core of the inverse

micelle, bound water is the water that interacts with the surfactants polar heads and trapped water is the water that is trapped within the interface (Destrée & B.Nagy, 2006).

If there is a high amount of bound water to bulk water, nanoparticle size is typically smaller due to the constrictions to growth of the particle, which typically goes from the micellar edge to the water core. The bound water also increases the rigidity of the micelle so there is a slower rate of intermicellar exchange taking place. With increased amounts of bulk water compared to bound water, the micellar film is more fluidic and therefore there is a higher rate of intermicellar exchange as well as larger nanoparticle sizes due to the availability of a larger area for the nanoparticles to grow. This is determined up to a point, whereby further increase in bulk water causes the dilution of the reagents within the water chamber and therefore a lower rate of reaction, causing a decrease in particle size (Eastoe et al., 2006).

These characteristics can be correlated to a microemulsion system's W number. For each microemulsion system, the amount of water added correlates to a specific number. For inverse micelles, when the W number is above 10-15, there is too much bulk water causing a reduction in particle size. (Eastoe et al., 2006) Optimisation of size based on W number depends on the microemulsion system and the desired size of the end product. Solanki et al, reported the influence of W number on silver nanoparticle size using water-AOT-Cyclohexane microemulsions. They compared the size of silver nanoparticles at W number of 5 and 8 and saw and increase in size from 4-9mm to 50-58nm (Solanki & Murthy, 2010; Zielinska-Jurek et al., 2012).

2.2.4.8. Nanoparticle Separation

Following synthesis, the NPs of desired shape and size within the microemulsions are usually required to be separated for obtaining pure NPs as a powder or in solution. There has been significant research into multiple techniques and methods for nanoparticle synthesis, but little research into the separation of nanoparticles from the original reaction mixture (Nazar,

Myakonkaya, Shah, & Eastoe, 2011). This is especially imperative for nanoparticles synthesised within microemulsions, since the surface of the nanoparticles is contaminated with surfactant(s), salts and oil. Also, for application as SERS substrates, consideration should be given for maintaining the integrity of the size and shape of the separated nanoparticles.

There are typically 6 methods that are commonly used of nanoparticle separation (Kowalczyk et al, 2011; Nazar et al., 2011) : electrophoretic, chromatographic, membrane filtration, thermal, centrifugation and extraction.

Within the thesis, extraction methods were mainly used. This method encompasses the separation of compounds based on differences in their solubility in different solvents. Separation is typically achieved through phase disruption with the use of an anti-solvent or water (Kowalczyk et al., 2011). This type of extraction is environmentally friendly and requires minimal energy, especially when it involves water phase disruption for nanoparticle separation (Myakonkaya & Eastoe, 2009). For example, gold nanoparticles within the CTAB microemulsion system can be separated from solution through the addition of excess water, which breaks the microemulsion system and causes nanoparticles to separate from the surfactant, Figure 2.23 (Hollamby et al., 2010).

The different types of nanoparticle separation, although provide separation with the maintenance of nanoparticles size and shape, more research is required into this area for nanoparticle separation, especially for microemulsion systems, as the surfactant layer around the nanoparticle may be of a hindrance for a SERS substrate. Currently extraction techniques and centrifugation techniques appear the most advantageous for use within these systems.
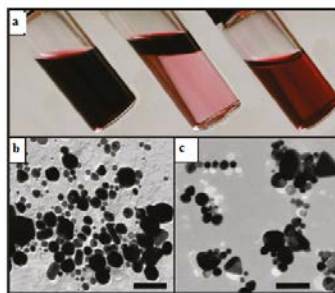
Figure 2.23: Nanoparticle separation through water phase disruption a) left image: shows Au NPs within CTAB/Butanol/Octane microemulsions, middle image: lower phase, water-rich solution after excess water is added to the microemulsion system, right image: upper phase, oil rich solution after excess water added to the microemulsion system b) TEM image of upper phase and c) TEM image of bottom phase (Hollamby et al., 2010).

2.2.5. SERS substrate: NPs on electrospun membranes

The third design type used for SERS substrates is planar metallic structures. These structures assemble metallic nanomaterial onto a commonly 2 or 3 dimensional plane, through methods typically which are labour intensive, expensive and hard to scale-up for mass production (He, Hu, Yao, Wang, & Yu, 2009). As discussed in section 2.3.1, this substrate design is most commercially used, as the substrate surface has the ability to provide controlled uniform features with varying shapes, within a manipulated distance from one another, they also are an advantageous platform for analyte adsorption and detection, through ease of use, shown with commercial substrates having versatility, such as P-SERS (Diagnostic anSERS, 2015) or SERStrate, (Silmeco, 2015) There is a need for low-cost SERS substrates and so a different methodology for providing planer metallic structures for SERS has been proposed through the use of nanomaterial incorporated onto electrospun membranes (Polavarapu & Liz-Marzán, 2013).

Electrospinning uses high electrostatic forces to produce polymer fibres within the nano-meter to sub micro-meter range. The process and fibres produced have multiple advantages (Huang, Zhang, Kotaki, & Ramakrishna, 2003; C.-L. Zhang & Yu, 2014);

- Low-cost

- Flexible

- Simple

- Large surface to volume ratio

- Superior mechanical performance

- Large range of material can be used

This has allowed electrospinning to be used within mass production, within multiple fields such as from the first commercial use as filters to the use in tissue engineering and within the biosensor field. Additional advantages noted for the nanoparticles on electrospun membrane design for a SERS substrate are high sensitivity, reproducibility, stable, portable ability and low-cost (He et al., 2009).

2.2.5.1. Background Principles of Electrospinning

Electrospinning was first discovered in the 1600's (Gilbert, W. (2013). However it was only in the 1980s that there was increased attention for the technique through the 'boom' of nanotechnology (Lukáš et al., 2009; C.-L. Zhang & Yu, 2014). There are three main components that comprise a typical electrospinning set-up; high voltage supply, capillary tube with a metallic blunt tipped needle and grounded conductive collector (Huang et al., 2003).

In the electrospinning process, a polymer with a sufficient molecular weight and thus ability for chain entanglement is dissolved within an appropriate solvent, to obtain an optimised viscosity. The polymer solution is then traditionally placed within a syringe and pumped at a certain flow rate to move through a capillary to a metal blunt tipped needle. A high voltage is exerted at the needle tip and causes the polymer solution to become charged. If the repulsion of the 'charges within the solution is sufficient, it is able to overcome the surface tension' (C.-L. Zhang & Yu, 2014) typically shown by the formation of a Taylor cone. The particles that are able to overcome the surface tension then form a jet that is stretched and elongated within an electric field, and directed to the grounded collector through electrostatic potential.
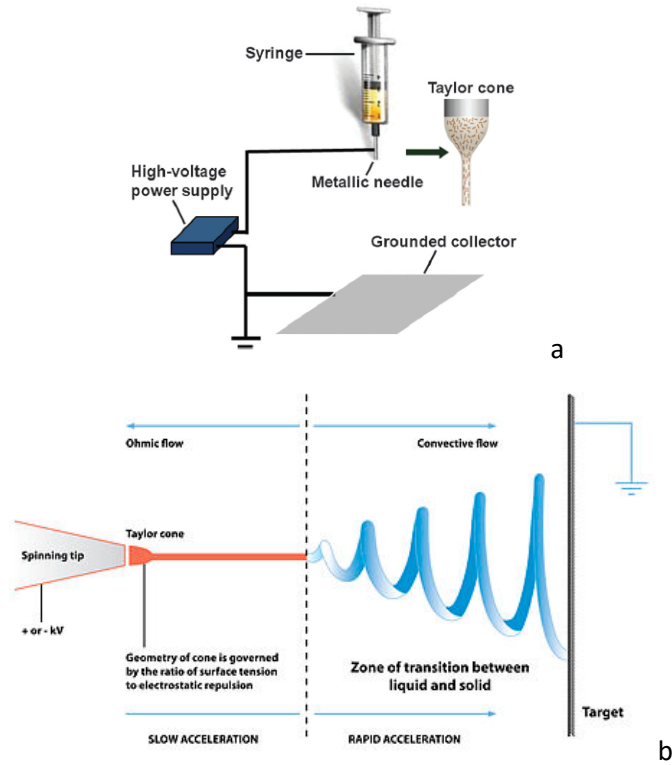
Figure 2.24: Diagram to show a) the typical requirements for electrospinning and b) the electrospinning characteristics of a polymer jet from needle tip to grounded collector (C.-L. Zhang & Yu, 2014).

The fundamental physical principles for electrospinning rely on electrostatic and capillary forces. The capillary forces enforce the polymer particles to 'flock' together to minimise surface area and energy, causing inter-molecular interactions of the particles on the quantum level. When the particles are exerted from the Taylor cone, high viscosity is required of the solution for a jet to form, through electrostatic forces, if the viscosity is to low electrospraying will occur instead. The liquid jet, through the internal pressure of the electric field cause the particles to become aligned and concentrate, stretching them longitudinally. The elongation causes a decrease in the jet radius and an increased curvature of the jet, which pushes out the solvent through evaporation causing the polymer jet to solidify (Fig. 2.24). The fibres are then of sub-micron to nanometer size and settle onto a grounded collector in a disorganised matrix pattern (Lukáš et al., 2009).

For the basic electrospinning of the polymer, three main parameters must be optimised; solution, process and ambient (Ramakrishna, Fujihara, Teo, Teik-Cheng, & Ma, 2005).

49

For the solution parameters, the solution viscosity, conductivity and molecular weight has to be taken into account. In general, most polymers can be electrospun if able to be dissolved within appropriate solvent. Additional components such as cross-linker, or higher molecular weight polymers can be added to obtain the appropriate solution parameters for electrospinning.

For the process parameter, surface tension, applied electric field, distance from needle to collector and feeding rate (flow rate) of the polymer solution to the needle tip are required to be optimised. Furthermore, the ambient parameter consisting of temperature and humidity of the environment wherein the polymer is electrospinning must be within the right range. The different electrospinning parameters are typically required to be optimised individually for electrospinning each polymer (Ramakrishna et al., 2005).

2.2.5.2.   Methods for nanoparticle incorporation on membrane

'Incorporating functional nanoparticles on electrospun fibres has emerged as one of the most exciting research topics in the field of electrospinning' (Zhang & Yu, 2014). There are two main strategies for producing nanoparticles on electrospun fibres:

- Electrospinning both the polymer and nanoparticles in-situ
- Coating nanoparticles on electrospun fibres after the electrospinning process

Metal nanoparticles can be mixed with the polymer and then electrospun or incorporated within the solution (Fig. 2.25).
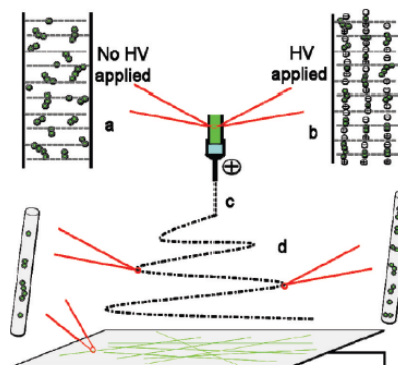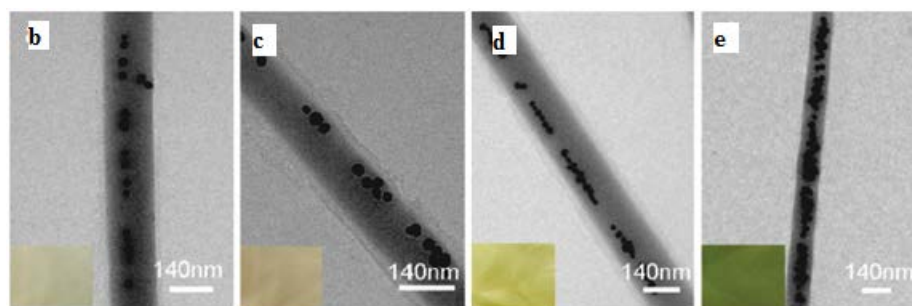
Figure 2.25: Images to show a)schematic for the polarisation of nanoparticles when the high voltage is applied during electrospinning and the corresponding alignment of nanoparticles, b-e) TEM images to show the increasing concentration of Ag NP's within the PVA : Ag NP solution and corresponding increased concentration and alignment of Ag NP's within the fibre (He et al., 2009).

A problem with in situ electrospinning of the metal NPs mixed with the polymer is that the polymer fibre may encapsulate the nanoparticle, thus preventing access for analytes of interest to the surface of the nanoparticles for SERS detection.

An additional step to overcome this issue is through the use of calcination, used by Wang et al, for the preparation of copper oxide nanofibers. Cupric acetate was added to PVA solution and electrospun, and then the electrospun membrane was calcinated, at 500°C for 5 hours to decompose the functional groups on the PVA fibre. This left just the carbon backbone and copper oxide, to produce a copper oxide nanofiber (Fig. 2.26) (W. Wang, Zhang, Tong, Li, & Song, 2009). Therefore the nanoparticles if used for similar strategies for SERS substrates would provide that the nanoparticles are free for contact with analytes of interest.
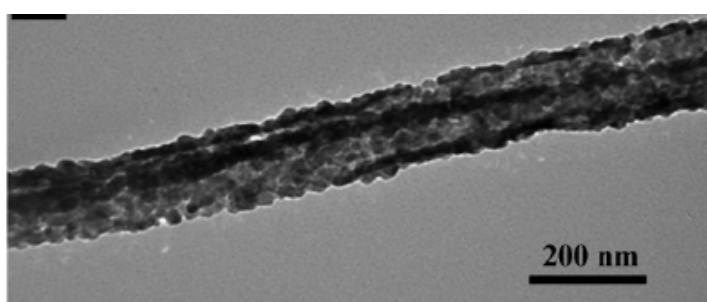
Figure 2.26: TEM image to show the morphology of calcinated copper oxide nanofibers (W. Wang et al., 2009).

Surface treatment of electrospun membranes after electrospinning for the addition of nanoparticles, is noted to be the simplest methodology to achieve np's on nanofibers. It has been shown to be more popular for use to produce SERS substrates with two different strategies being undertaken.

Most groups appear to add the metal precursor salt to the polymer solution for electrospinning. Once electrospun, the polymer precursor mesh is immersed into a reducing agent solution and the nanoparticle synthesis then takes place. Both Cao et al, and Guo et al, showed the efficiency of this method for producing a SERS substrate. Both morphologies shown in Figure 2.26, gave high, reproducible SERS enhancement with thiol compounds. They however showed different morphologies as Guo et al, added additional acid and seeding methods to obtain a more random, fractal thorny structure, which appears more advantageous for SERS (Cao et al., 2012; Guo, Han, Li, & Zhao, 2010).
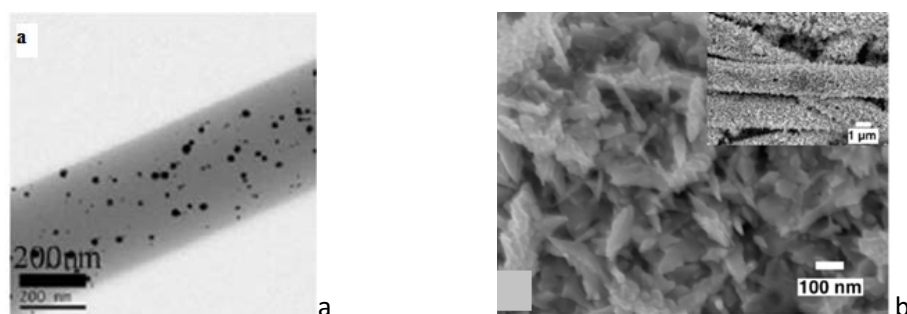
Figure 2.27: TEM images to show a) Gold nanoparticles on PVA fibres (Cao et al., 2012) and b) Gold nanoparticles on PMMA fibres (Guo et al., 2010).

NPs can also be bound to the electrospun fibre through covalent binding, shown by Xu et al's group where copper sulphate nanoparticles bound to PVA through the –OH functional groups on PVA to form a uniformly distributed nanoparticle structure on the PVA surface, Figure 2.28b (Xu, Sun, Liu, Wang, & Yan, 2011).

NPs can also be bound indirectly shown by Wang et al, whereby gold nanoparticles were bound to cross-linked PVA fibres through the use of MPTES. MPTES was able to bind to the hydroxyl groups on the PVA fibre and as there was a thiol group present within its structure had a strong affinity to bind with gold nanoparticles (Fig. 2.28c) (J. Wang, Yao, He, Zhang, & Yu, 2012).
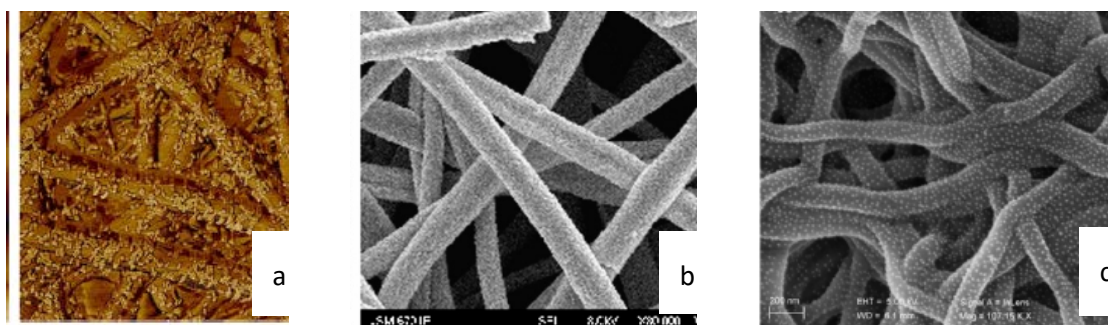
Figure 2.28: SEM images to show a) Gold nanorods on PV2P fibers (Lee et al., 2011), b) CuS nanoparticles on PVA fibres (Xu et al., 2011) and c) Gold nanoparticles PVA/GA fibres (J. Wang et al., 2012).

The configuration of PVA with glutaraldehyde (GA) used by Wang et al, also highlights an imperative point for the use of electrospun fibres. Depending on the use of the electrospun membranes, once electrospun if placed in the presence of solvents it is able to dissolve in, the integrity of the fibre membrane will be lost, as the polymer dissolves back into the solvent.

This is beneficial if the electrospun membranes were to be of use within tissue engineering for example, however for use as SERS substrate; where the integrity of the polymer structure must be maintained, an additional step needs to be undertaken. This step is the use of cross-linking the electrospun membrane to make it insoluble.

2.2.5.3. Insoluble electrospun membranes: Cross-linking

Cross-linking is the formation of chemical (covalent or ionic) bonds between polymer chains. The chemical bonding of polymers typically relies on the bonding to different functional groups present within the polymer structure. The variety of chemical functional groups that can be present for a polymer causes the cross-linking process to use different reaction methodologies and cross-linking agents. Cross-linking has been shown with electrospinning to occur either during the electrospinning process or afterwards. During the electrospinning process the cross-linking agent is typically added with the solution for a one-step process with no post-treatment required.

After electrospinning, cross-linking can occur by immersing the electrospun membrane in the cross-linking agent solution or vapour, or through initialising the cross-linking reaction with the addition of heat, pressure or pH change (Tang, Saquing, Harding, & Khan, 2010).

53

Meng et al, 2015 used this methodology for cross-linking PAA. PAA is an anionic, water soluble polymer and ethylene glycol (EG) was added to the solution for electrospinning with a small amount of sulphuric acid to work as catalyst. Once an electrospun membrane was obtained, PAA-EG membranes were placed into an oven at 130°C to activate the cross-linking reaction. They successfully produced insoluble PAA-EG membranes in this fashion as shown in the SEM images in Figure 2.29b&c (Meng et al., 2015).
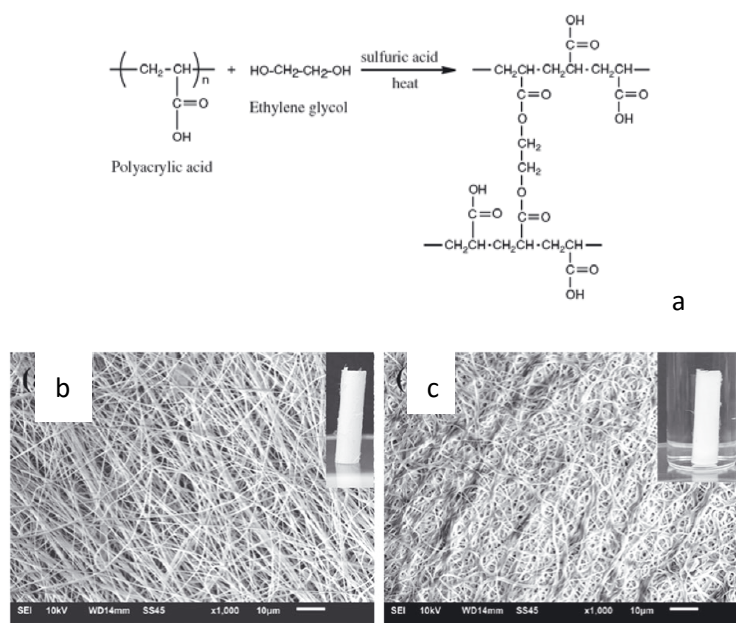
Figure 2.29: Images to show a) the chemical reaction between PAA and EG to produce cross-linked PAA-EG membranes, b) SEM image of PAA-EG electrospun fibres before addition of water and c)SEM image of PAA-EG electrospun fibres after addition of water (Meng et al., 2015).

Once the electrospun membrane is made insoluble through cross-linking an array of new applications are available as the integrity of the membrane will be maintained and additional advantages such as increased mechanical strength are obtained. Therefore, electrospun membranes are applicable for use as SERS substrates as they are stable, cost-effective, versatile in production and controls fibres within the nanofiber range for increased functions.

2.2.6. SERS: Assay development methods for Biological analytes

The design of optimised SERS substrates is one of the main steps for implementation of SERS within a LOC setting. One aspect of SERS substrate design concentrates on fabrication of the SERS

substrate structure, while the other aspect requires assay development, with respect of bringing the analyte of interest to the surface, within the plasmonic field on the surface of SERS substrate.

2.2.6.1. General methods

SERS assays can either be intrinsic or extrinsic. In the intrinsic pathway, the analyte of interest is selectively brought within the surface plasmonic field on the SERS substrate for a label-free and direct detection of the analyte. This approach is convenient and cost effective compared to extrinsic pathway. However, it is prone to poor selectivity and poor sensitivity in complex mixtures, especially in the detection of higher molecular weight biomolecules (Han, Ozaki, & Zhao, 2012).

The extrinsic pathway is an indirect method wherein, one or more Raman active molecules are bound on the surface of the SERS substrate, and protected by a transparent silica coating. These assemblies, known as SERS probes, are then coated with an affinity molecule, e.g., an antibody, and used as a probe for analyte detection, instead of the traditional fluorescence probes. Unlike fluorescence probes, the SERS probes do not suffer from loss of signal intensity. The Raman probes having affinity to specific analytes can then be designed and used for sandwich, competitive or similar other assay methods (e.g., ELISA) for analyte detection. (Reyes-Goddard, Barr, & Stone, 2005) (Han et al., 2012; Reyes-Goddard et al., 2005) The extrinsic method is a more sensitive detection technique, but expensive.

Both the intrinsic and extrinsic pathways can undergo different surface modifications to increase the affinity of the analyte to the metal surface. These surface modifications can be either non-covalent or covalent. The former method typically involves physisorption, while the later involves the covalent binding of specific ligand on the SERS substrate's surface (Ferretti, Paynter, Russell, Sapsford, & Richardson, 2000).

The most simplistic assay that can be developed is based on an analyte's physical adsorption to the metal surface. This can be done typically through hydrophobic-hydrophobic, van der Waals or

electrostatic interactions. This method, however, can provide unstable bonds with random orientation of the molecule onto the surface, causing irreproducible results (Ferretti et al., 2000). Also, for molecules that have a weak affinity with the surface, weak or no SERS signal would be produced. The orientation of the molecule on the surface is highly significant for use with SERS. Typically, SERS intensities of the functional groups bound or close to the surface of the SERS substrate are amplified while those away from the surface are weak or absent. It was highlighted by McNay et. al. that pyridine molecules at low concentrations on silver wire lay on the ring plane of the structure parallel to the surface. However as their concentration increases, the rings became stacks, thus the ring plane orients perpendicular to the surface. The displaced carbon atoms, thus have increased intensity at high concentrations, therefore, the spectra had altered for the same molecule (McNay et al., 2011).

Improvements to the method for physisorption and thus increasing affinity of weak analytes as well as improving control of orientation can be improved through additional mechanical or chemical influence. Mechanical force can be through the use of centrifugation of the SERS substrate with the analyte of interest of with silver electrodes, an additional voltage can be applied to increase the electrostatic charge on the surface. They can also additional chemical influence to induce aggregation of SERS nanoparticles within solution through addition of salt or acid, which can aggregate around the molecule of interest to obtain higher SERS detection (Fig.2.30)(Ramon a. Alvarez-Puebla & Liz-Marzán, 2012; Bell & Sirimuthu, 2008; Han et al., 2012).
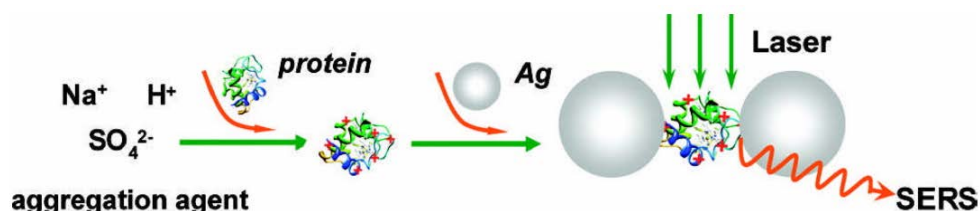
Figure 2.30: Diagram shows silver nanoparticles in a solution with proteins and acid and the corresponding aggregation of these nanoparticles for increased SERS signal (Bantz et al., 2011).

Covalent binding for modification of SERS surface, on the other hand, involves binding of specific molecules or ligands to the metal surface, forming irreversible and stable bonds (Sperling & Parak, 2010). This method can be used to increase the specificity of analyte binding (Fig. 2.31).

A less energy intensive approach following this methodology is through the spontaneous binding of thiol molecules to a metal surface to form self-assembled monolayers (SAMS), thiol compounds have a high affinity for binding of their sulphur groups to the metal surface. SAMS are noted to be a versatile technique with controlled packing density; therefore the orientation of the molecules on the surface can be controlled (Ferretti et al., 2000). Yonzon et al used this approach to bind two different thiol groups; mercaptohexanol (MH) and Decanethiol (DT) on a SERS AgFON substrate. The altering chain length of the thiols was used for entrapment of glucose and lactate for SERS detection. This approach/method was shown to have high sensitivity and selectivity of the sugar molecules. The SERS substrate with this morphology was even implanted within a rat model to show real-time monitoring of glucose and lactate using a flow cell (Lyandres et al., 2007; Yonzon, Haynes, Zhang, Walsh, & Van Duyne, 2004).
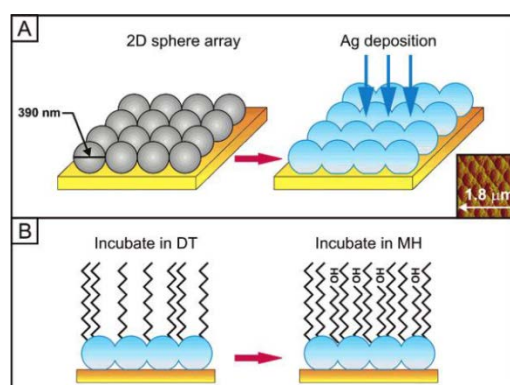
Figure 2.31: Diagram to show AgFON SERS substrate with the addition of DT and MH for glucose and lactate binding (Lyandres et al., 2007).

A more intensive and costly covalent binding procedure is through the use of antibody immobilisation. Antibodies increase sensitivity through the selective binding of target analytes. This method is commonly used within an extrinsic pathway for SERS as typically it binds higher molecular weight biomolecules, therefore an additional SERS probe is present to increase the SERS intensity

of the biomolecules. The antibodies are attached to the SERS substrate through covalent bonds, to control the stability of the surface and antibodies are also bound to a Raman probe. When an analyte of interest is present, the analyte binds to both antibodies on the SERS substrate as well as antibody on the Raman probe. This is the typical set-up antibody immobilised SERS substrates use (Fig. 2.32). It has been shown using this methodology to provide multiplexing capabilities as SERS spectra of different analytes of interest were able to be detected simultaneously using gold nanoparticle substrates. The disadvantage to the technique however is the cost, irreversibility and specificity, therefore for a more cost-effective, universal SERS platform; this method may not be as advantageous (Reyes-Goddard et al., 2005).
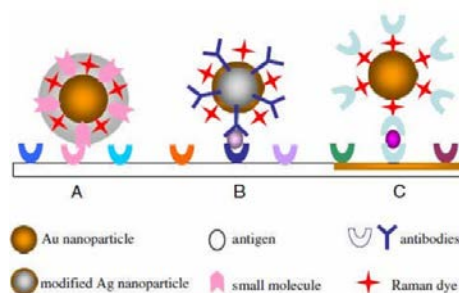
Figure 2.32: Diagram to show the methodology of antibody immobilisation for SERS testing (Bantz et al., 2011).

2.2.6.2.   Biomolecules of interest for SERS testing

Within the scope of this thesis, two groups of biomolecules: carbohydrates and proteins are of interest for detection and monitoring of diabetes biomarkers, discussed in further detail in section 2.5. Other biomolecules have been shown to bind to SERS substrates following the designs discussed above and therefore at a later date can be optimised with the SERS substrates to provide increased number of analytes that can be detected.

Carbohydrates are a large group of organic compounds that comprise of carbon, oxygen and hydrogen. Carbohydrate analysis has been challenging using direct methods due to the molecules having 'no endogenous chromophores' therefore SERS intensity may be weak (Vangala et al., 2010). However as noted in the previous section, this has been overcome by alternative methods, such as

through entrapping selectively different carbohydrates such as glucose and lactate by Yonzon et al. With the glucose SERS spectra typically giving peaks at 1342cm^{-1} for the C-C-H bend, 1270, 1164 and 1116cm^{-1} for the C-C and C-O stretch and 840cm^{-1} for the C-C stretch (Yonzon et al., 2004). Typically for quantitative measurements, as some peaks have higher intensity and affinity for SERS scattering than others, either an individual peak or a ratio between two peaks is taken to determine concentration.

The other class of biomolecules of interest for diabetes testing is proteins. For SERS testing of proteins, one needs to understand the basics of the protein structure. A complex protein is comprised of amino acids, there are 20 naturally occurring amino acid each with individual side chains (Table 2.2). These amino acids bind to one another through peptide bonds to form differing polypeptide chains in a primary structure. These chains can then interact with one another to for a secondary structure comprised of alpha helixes, beta sheets or random coils. These complexes can then interact further to enclose the structure through non-covalent interactions to form a tertiary and then quaternary structure, which is how a typical complex protein appears.

Table 2.2: The functional groups present for the 20 naturally occurring amino acids (wiki, 2015).

SERS spectra for proteins can depict individual amino acid peaks that comprise the protein, therefore an understanding of the primary structure of a protein may be necessary to decipher the protein SERS spectra given and the orientation of the protein on the SERS surface (Fig. 2.33). Amino acids are larger than 10-100nm and so only sections of the substrate would in theory be scattered via SERS. However, it was shown by Suh et al, that the amino acid can bind to the surface via both the functional groups present, such as for glycine and alanine. Thus it can be hypothesised that the amino acids are aligned onto the metal surface, which has been supported by other research groups (Reyes-Goddard et al., 2005). This is of interest as it can then be reliably hypothesised that the peaks given within a spectrum is for individual amino acids that have bound to the surface. Therefore, depending on the affinity of alignment of the protein under the same conditions, the same amino acids should in theory bind to the surface to give spectra.
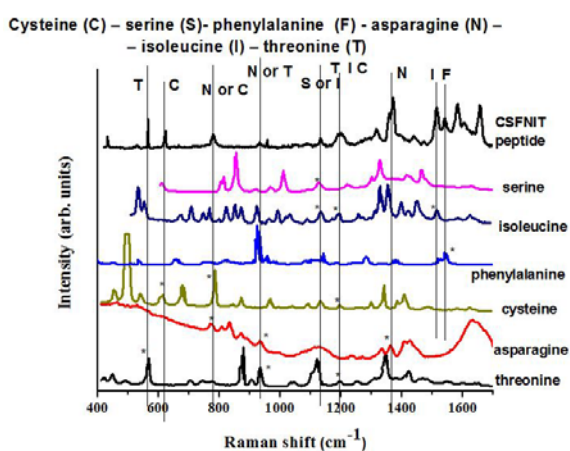
Figure 2.33: SERS spectra of different amino acids and the corresponding peptide that comprises these peaks (ChiLab, 2015).

The SERS spectra for a protein also depicts different ranges where the amide bonds within proteins can such as amide I, II and III bands which are near 1650cm^{-1}, 1550cm^{-1} and 1300cm^{-1} Raman shifts (cm^{-1}) respectively. The amide Raman bands depict different proportions of the protein structure, at the amide I band 80% of the band is due to C=O stretching, at amide II, 60% is N-H bending and 40% C-N stretching and at Amide III, 40% C-N stretching and 30% N-H bending (Scientific, 2012). Thus SERS spectra can be shown for efficient protein identification.

As of yet to my knowledge, there have been no clinical, routine tests that are used that use SERS, within a label-free fashion, as the gold standard for analytical testing within aqueous solutions (Ramón a. Alvarez-Puebla & Liz-Marzán, 2010; Han et al., 2012). This problem may come about due to label-free SERS being a first-layer surface technique, with multiple biomolecules within a biological fluid, SERS substrates may get saturated with interference molecules that may prevent the binding to the surface of the analyte of interest. An additional step would need to be taken to produce a SERS test within an analytical setting, significantly for LOC designs which deal with sample preparation.

2.3.   Diabetes Screening & Monitoring using SERS

Diabetes Mellitus is a metabolic disorder that is caused through the breakdown of the insulin pathway, either through lack of insulin being produced (type 1) or through desensitisation of the cells to bind with insulin (type 2). The disease as of yet is incurable. When the pathway is disrupted this leads to disturbances in protein, fat and carbohydrate metabolism (WHO, 2015). The progression of diabetes can be detected and monitored through diabetes biomarkers. These are analytes which deviate in concentration when not controlled by the insulin pathway. If the diabetes biomarkers, predominantly glucose, is not controlled within a specific range; acute and chronic complications occur. Acute complications are episodes of hyper- or hypoglycaemia, which if untreated can lead to coma and even death, whereas chronic complications are typical multi-system organ failures with regards to; retinopathy, nephropathy, neuropathy, cardiovascular disease and vascular system alterations (Diabetes UK, 2014; WHO, 2015).

It has been highlighted by the World Health Organisation (WHO) that 382 million people have diabetes, which is predicted to double by 2030, with costs in relation to diabetes within the NHS accounting for 10% of the budget, £10 billion spent (Diabetes UK, 2014; WHO, 2015).

It has been found through multiple studies, most significantly the 'Diabetes Control and Complications trial' (DCCT) for type 1 diabetes and UK prospective diabetes study for type 2 diabetes, that early detection and monitoring of glucose with adequate action taken to maintain glucose within a specific range, reduced and reverted, in some instances, diabetes from occurring and the chronic complications associated (Baynes & Dominczak, 2005).

Therefore, better screening and monitoring for diabetes would be a significant area to look into for improving and reducing the continuing growth of diabetes and chronic complications associated with it. Multiple innovations have been looked into by research groups from the design and implementation of implantable glucose sensors (N. Wang et al., 2013) to the use of different diabetes biomarkers.

Glucose is the gold standard biomarker that is used for diabetes screening and monitoring. However problems associated with the use of the biomarker is firstly within the bloodstream glucose fluctuates within a 24 hour period, wherein a 3-4 times per day point testing could miss episodes of hypo- or hyperglycaemia. Secondly the SMBG devices on the market have a ±20% error margin and so testing of glucose may not even be accurate for administration of a response. Finally glucose for use for the general population may be inadequate for certain individuals, such as those going through pregnancy, as illustrated in Table 2.3 (Clarke & Foster, 2012).

Another gold standard that is now used as a diabetes biomarker for monitoring purposes is the use of glycated haemoglobin in the HbA_{1c} format. Glycosylation of proteins within the blood, occurs non-enzymatically, wherein glucose binds to amino acids on proteins that have free amine ($-NH_2$) residues on their side-chains. HbA_{1c} is the glycated from of haemoglobin, wherein glucose binds to the lysine residue on the N-terminus of the beta-chains in the haemoglobin molecule. The rate of glycosylation of the protein correlates with the level of glucose within the blood (Heuck, Home, Reinauer, & Kanagasabapathy, 2002; Plus, 2007). HbA_{1c}, due to the red blood life cycle of 120 days gives an average glycaemic measurement for 3-6 months (Zaidi, Ali, Bernet, & Comstock, 2008).

HbA$_{1c}$ is usually measured as a percentage ratio between HbA and HbA$_{1c}$ and is typically measured using one of two characteristics exhibited by HbA$_{1c}$, in relation to structural alteration or charge alteration of the protein (Hoelzel, Hoshino, & Miedema, 2002). High performance liquid chromatography (HPLC) is the gold standard for testing HbA$_{1c}$, which uses the charge difference between the two formats for measurement. This analytical test is done in a lab setting due to the large equipment required. Limitations to the use of HbA$_{1c}$ is through firstly the average glycaemic reading is for a time period quite distant from that detected and monitored using glucose. Therefore, action taken to correct the glycaemic levels may occur too late in some instances. However, the corrective measures taken based on HbA$_{1c}$ readings have been reported to achieve a 40% reduction in chronic complications (World Health Organization, 2011). The second limitation is the cost of the current gold standard testing of HbA$_{1c}$ in the laboratory. Hence, HbA$_{1c}$ is not a routine test administrated to the general population of diabetic patients. The final limitation for HbA$_{1c}$ detection is that it will not be adequate for monitoring purposes in certain individual groups such as those with anaemia, shown in Table 2.4.

Table 2.3: Standard score and concentration of HbA$_{1c}$ (shown as a %) and Glucose within the blood and related action require for diabetes care (Bahari, 2015).

Due to the limitations of both the biomarkers described above, other diabetes biomarkers have been looked into by researched for use in diabetes screening and monitoring. One such biomarker which has gained significant popularity is glycated albumin.

Albumin is on the largest components that comprise the proteins present within the plasma, making up '60% of the total plasma protein concentration' and '80% of the total molecules' present within the plasma, with a concentration range between 3.5-5.5g/dL. Glycosylation of albumin can serve as an adequate intermediate diabetes biomarker, due to the half-life of albumin being 2-4 weeks and is measured as with HbA_{1c} as a percentage between glycated and normal protein. Studies have shown that there was significance in using glycated albumin for short-term changes in glycaemic control when compared with HbA_{1c}. It was shown that glycated albumin decreased more rapidly as glycaemic control improved and the ratio of this biomarker was higher in hyperglycaemic episodes than HbA_{1C}, it was also shown to correlate in relation to increased concentration with coronary artery disease (MedScape, 2015; Roohk & Zaidi, 2008). Limitations for the use of glycated albumin comes through despite the multiple methods available for detection from HPLC to colorimetric methods. There is a variance in percentage results for glycated albumin that is obtained using HPLC method is between a 0.6-3% range, whereas, that determined by an enzymatic methods is between 11-16% (Medicine, 2015). Another limitation for use as with the other biomarkers is that certain individuals within the population cannot use the biomarker for diabetes control, shown in table 2.4.
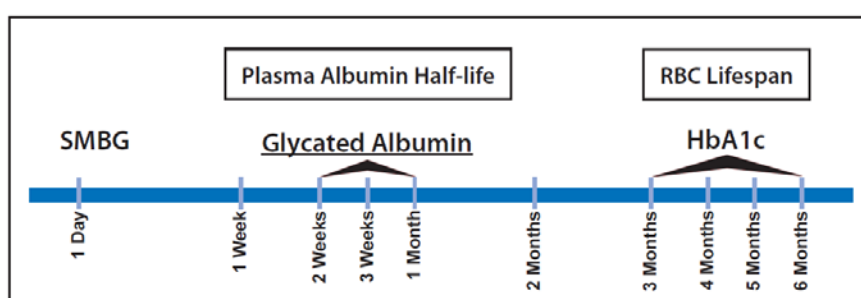
Figure 2.34: Diagram to show the biomarkers and the relationship in regards with time for glycaemic indicators (Zaidi et al., 2008).

Glucose was tested using SERS by Van Duyne's group, who demonstrated real-time testing of glucose using mixed SAMs of DT and MH (Lyandres et al., 2007). For glycated haemoglobin and glycated albumin, the use of surface enhanced resonance Raman spectroscopy (SERRS) by Kiran et. al. and drop-coated deposition Raman (DCDR) by Barman et. al. was reported, wherein, it was

shown that HbA$_{1c}$ and haemoglobin can be differentiated by Raman spectra. Similarly, Dingari et al, 2012 also used DCDR to show that glycated albumin can be differentiated from albumin (Barman et al., 2012; Dingari et al., 2012; Kiran et al., 2010).

The application of SERS in the detection of diabetes biomarkers is still limited and there are no SERS based technologies currently available for diabetes diagnosis and monitoring. However, due to the better understanding and improved fabrication techniques available for SERS substrate design as well as the promising results obtained through Raman spectra for the glycated and non-glycated proteins, there is scope for the use of SERS for diabetes screening and monitoring.

Table 2.4: Table to show limitations of glucose, HbA$_{1c}$ and glycated albumin testing for certain individual groups within a population (Aguiree et al., 2013; Burge, 2001; Clarke & Foster, 2012; Little et al., 2008; Medicine, 2015).

Limitation	Glucose	HbA$_{1c}$	Glycated Albumin
Pregnancy	✓		
Ketosis	✓		
Sugar interferences (galactose and xylose)	✓		
High Altitude	✓		
Critically ill	✓		
Neonates	✓		
Vitamin C supplements	✓		
Nephropathy	✓	✓	✓
Paracetomol (high concentrations)	✓		
Cirrhosis	✓		✓
Hepatitis	✓		
Anaemia	✓	✓	
Dehydration	✓		
Lung diseases	✓		
Bone marrow disorders		✓	
Varients of Hb		✓	
Red blood cell transfusion		✓	
Hypertiglycerdaemia		✓	✓
Alcohol abuse		✓	
Aspirin			✓
Hyperthyroidism			✓
Glucocorticoid administration			✓
Smokers			✓
Hyperuricemic patients			✓

2.4.   Lab on a Chip devices for Point of Care testing

Lab-on-a-chip device technology, also known as Micrototal Analysis Systems (µTAS), is a subset of microfluidics that deals with the 'integration of multiple laboratory functions onto a single chip which is a few mm^2 to cm^2 in size'(Fig. 2.35)(Gene Quantification, 2015). The scaling down process provides multiple advantages such as; low sample volumes required, which is beneficial for improved well-being of patients as well as providing safer platforms for analysis. With miniaturisation, there is an increased compactness of the device which enables portability and ability to access a wider population. It also increases turnover time of results and due to small size, can be cost-effective (Gene Quantification, 2015; MacPherson & Ravichandrian, 2011).
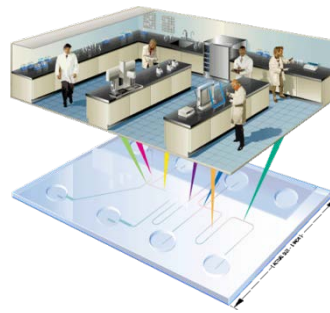
Figure 2.35: Diagram to show the concept behind lab-on-a-chip design (Gene Quantification, 2015).

For screening and monitoring of diabetes, as with most diseases, clinical determination of the disease is undertaken through laboratory testing. One of the significant problems with the state of laboratory testing for clinical use is the turnaround time taken for tests results to be available and the resulting repeat visits patients need for disease determination and accurate monitoring, as in the case of diabetes (Hawkins, 2007). Point-of-care testing (POCT) enables a reduction in time needed for clinical decisions to be made. POCT can be done at close proximity to the patient and provides advantages of quantitative or semi-quantitative single measurements, short turnaround time, no sample preparation, user friendly and results available for clinicians to make on the spot therapeutic decisions (Luppa et al., 2011).

The improvement in LOC designs would enable more POCT for a wider range of applications to be undertaken. As of yet LOC devices have not reached their goal of automated system for point of care, with rapid detection and assays for most analytes.

Chapter 3: Materials & Methods

3.1.   Introduction

This chapter presents the materials and the methods used for the fabrication of SERS substrates, and the characterisation of their properties (morphology, physical, and chemical), as well as their SERS enhancement efficacy using a model Raman active molecule, namely 4-methylbenezenthiol (MBT) and 514nm and 1064nm Raman spectrometers. Furthermore, some of the optimised SERS substrates were tested for their efficacy in the selective detection of the diabetes biomarkers: glucose, haemoglobin, glycated haemoglobin (HbA_{1c}), albumin and glycated albumin. In addition, a versatile electrospinning set-up that has humidity and temperature control was designed and manufactured for the fabrication of one of the SERS substrate variants designed in this study

3.2.   Materials

Chemical Roughening of Silver Wire: Silver wire, 99.99% (Ag10T) 0.25mm diameter with a Teflon coating purchased from MedWire, Sigmund Cohn. Ammonia hydroxide solution (35% analytical grade) and nitric acid (≥69%) were purchased from Sigma-Aldrich, UK.

Nanoparticle Synthesis and Separation using Microemulsions: Silver nitrate ($AgNO_3$), gold (III) chloride ($HAuCl_4$), hydrazine hydrate (50-60%), sodium borohydride ($NaBH_4$), ascorbic acid, sodium chloride (NaCl), dioctyl sulfosuccinate sodium salt (AOT), hexadecyltrimethylammonium bromide (CTAB), cyclohexane, butanol, isopropyl myristate (IPM) were all purchased from Sigma-Aldrich, UK.

Electrospun Membranes with incorporated nanoparticles: Polyacrylic acid (M_w 450,000), ethylene glycol (EG), ethanol, sulphuric acid, cysteamine hydrochloride, N-hydroxysuccinimide (NHS), N-(3-dimethylaminopropyl)-N'-ethylcarbodiimide hydrochloride (EDC), 2-(N-morpholino-ethane sulfonic acid hydrate (MES) buffer controlled at pH 5.3 using 1N NaOH and/or 1N HCl were all purchased from Sigma-Aldrich, UK.

Electrospinning components: Polytetrafluoroethylene (PTFE) tubing 1/16', 10ml luer-lock plastic BD syringes, and flangeless ferrule ethylene tetrafluoroethylene (ETFE) 1/16' were

purchased from Cole-Parmer, UK. Union LP ETFE ¼-28', female luer to male ¼-28 ETFE and male to luer lock ¼-28 adaptors were purchased from IDEX-HS, Germany.

Additional Commercial and Synthesised SERS substrates: P-SERS – gold nanoparticles that were inkjet printed on cellulose acetate filter paper were purchased from StellarNet Inc, USA. Ag and Au coated on silica nanopillars (SERStrates) were purchased from Silmeco, Denmark. $HAuCl_4$, 2-[4-(2-hydroxyethyl)piperazin-1-yl]ethanesulfonic acid (HEPES) buffer pH 7.4 (pH adjusted with 1N NaOH), were purchased from Sigma-Aldrich, UK. Advantec cotton cellulose filter paper, 55mm were purchased from Fisher Scientific.

Enhancement Testing: 4-Methylbenzenethiol (98%) (4-MBT) as a control Raman probe molecule and ethanol were purchased from Sigma-Aldrich, UK.

Diabetes Biomarkers: Bovine lyophilised haemoglobin, bovine serum albumin, D-(+)-glucose, phosphate buffered saline tablets (PBS), human glycated haemoglobin (HbA1c), human glycated albumin, human haemoglobin, human albumin were all purchased from Sigma-Aldrich, UK.

Microfluidic Chips: Microfluidic moulds were fabricated by 3D printing techniques with an Objet 30 Pro (Stata-sys, US) using jetted photopolymer deposition of Accura 60 resin purchased from 3D Systems Inc, USA. Isoproponal purchased from Sigma-Aldrich was used for removing excess resin from the mould. QSil 218 PDMS purchased from ACC Silicones, UK was used for fabricating the microfluidic chips.

Deionised (DI) water purified at 18MΩ using a Barnstead water purification system was used for all experiments.

3.3. Preparation of SERS substrates

There are three main design categories used for SERS substrate design; metallic electrodes, nanoparticles and metallic nanostructures on planar arrays (Le Ru& Etchegoin, 2009). For the fabrication of SERS substrates within each design category, with optimised 'hot-spot' uniformity

and desirable broadband characteristics, cost-effective methods with simple equipment requirements and fast turnaround time for SERS substrates were used.

3.4. Chemically Roughened Silver Wire

For uniform roughness with control to peak heights, chemical treatments were used. Ammonia hydroxide (NH_4OH) and Nitric Acid (HNO_3) have different degrees of etching noted within literature. Ammonia hydroxide typically is used for cleaning and polishing metals such as Silver however at higher concentrations, in this case 30%, small protrusions can be indented upon the surface. With HNO_3, diluted to 6M, it is a strong acid, which etches the surface quite violently to produce protrusions. With varying immersion times of the Ag wire and different combinations of chemical treatment it was presumed that surface roughness could be altered within a μm to nm range. Additional heat was used to implicate increased uniformity of the protrusions as well as for removal of residue from the treatments.

Silver wire segments, ~1.5cm in length, were cut and Teflon removed. These wires were flattened using a mechanical press. To remove any contaminants on their surface, the flattened wires were first cleaned in deionised water for 30 minutes in an ultrasonication water bath using a Branson 1510 sonicator. After which chemical etching treatments for roughening the surface of silver wires took place through immersing the silver wire in alkali, ammonia and/or acid, nitric acid solutions for a specific time and then cleaning the surface with deionised water (Table 3.1). Additional heat treatment, 130°C for 1 hour was used on a set of Ag wires with the different treatments as extra variable. Modifications of protocols by Wang et al and Miller et al, were used for preparing silver wire(Miller et al, 1984; Wang et al., 2013).

Chemical Treatment	Flattened Ag Wire	
	Non-heated	**Heated**
30 seconds NH_4OH	✓	✓
10 seconds HNO_3	✓	✓
2 minutes HNO_3	✓	✓
30s NH_4OH + 10s HNO_3	✓	✓
30s NH_4OH + 2 minutes HNO_3	✓	✓

3.5. Metal Nanoparticles synthesised in Microemulsions

Microemulsions are a bottom-up, chemical method, that are simple, can be done within ambient conditions with little equipment requirements and the synthesis of NPs can occur instantaneously. The NPs have long shelf-lives due to the stability of the microemulsion system and maintain their integrity to the presence of surfactant that surrounds the NPs produced. For controlling the size and shape of silver (Ag) and gold (Au) NPs 7 main parameters for addressed, noted within literature as affecting the size and shape of NPs (Eastoe, Hollamby, & Hudson, 2006); surfactant, co-surfactant, solvent, precursor concentration, reducing agent and thereafter concentration, W number and electrolyte addition.

3.5.1. Microemulsion System

The microemulsion systems prepared and tested extensively for effectiveness of fabricating Au and Ag NPs SERS substrates were:

- AOT/IPM

- AOT/Butanol/IPM

- AOT/Butanol/Cyclohexane

- CTAB/Butanol/Cyclohexane

The surfactant concentration within the microemulsion system was 0.1M and the co-surfactant, butanol, added to the microemulsion systems was added at a 1:1 molar concentration ratio with surfactant. Surfactant characteristics for nanoparticle synthesis were identified by the use of an

anionic surfactant, AOT and a cationic surfactant CTAB, with different chemical structures to alter packing density of the inverse micelles. The solvent characteristics and its effect on size and shape of the nanoparticles was identified by using two different solvents, one with a long carbon chain structure, IPM and one with a small molecule structure, cyclohexane.

3.5.2. Precursor Concentration

Gold chloride (HAuCl$_4$) or Silver nitrate (AgNO$_3$) was prepared as stock solutions in deionised water at concentrations of; 0.29, 0.59, 1.18, 1.77 and 4.22M to evaluate the effect of precursor concentration on size of nanoparticles produced. These were tested within AOT/IPM microemulsion systems. Thereafter concentration stock solutions for HAuCl$_4$ and AgNO$_3$ at; 1 and 1.77M were tested within AOT/Butanol/IPM and AOT/Butanol/Cyclohexane microemulsions, 1M stock for precursor concentrations was then optimised for use for additional tests.

3.5.3. Reducing Agent

Ascorbic acid (AA), sodium borohydride (NaBH$_4$) and hydrazine hydrate were used as reducing agents for gold and silver salt precursor. Reducing agent stock solutions were also made by dissolving in deionised water. The final concentration optimised for all the reducing agents added to Au or Ag precursor in microemulsions was set to 0.1M.

Au and Ag NPs synthesis solutions behaved differently with addition of reducing agent added and post-synthesis steps; AA was shown to only reduce AgNO$_3$ for Ag NPs, Ag NPs microemulsion systems also required post centrifugation once initially synthesised, 14.5 krpm (Eppendorf, Minispin plus, Cole-Parmer, diameter 8.9cm) for 15 minutes to remove by-product sediment that would disturb the balance within the microemulsion system.

3.5.4. Electrolyte Addition

Addition of electrolyte was highlighted in literature to have an influence on nanoparticle size and shape. (Pileni, 2003) 1M NaCl stock solutions were dissolved in deionised water and added to shortlisted Ag NP and Au NP microemulsion systems.

3.5.5. Shortlisted Microemulsion systems for Ag and Au NPs SERS substrates

After extensive testing of the 7 parameters; 3 microemulsion systems for Ag NPs and 4 microemulsion systems for Au NPs were shortlisted, as they provided size ranges and shapes that could have potential benefits as SERS substrates, (Table 3.2 and Fig. 3.1).

Table 3.2: Shortlisted microemulsion systems for Au and Ag NPs SERS substrates

Microemulsion System	Precursor	Reducing Agent	W number
AOT/Butanol/Cyclohexane	$AgNO_3$	Ascorbic acid	6-7
AOT/Butanol/Isopropyl myristate	$AgNO_3$	$NaBH_4$	6-7
CTAB/Butanol/Cyclohexane	$AgNO_3$	$NaBH_4$	6-7
AOT/Butanol/Cyclohexane	$HAuCl_4$	Hydrazine	5-6
AOT/Butanol/Cyclohexane	$HAuCl_4$	$NaBH_4$	5-6
AOT/Butanol/Isopropyl myristate	$HAuCl_4$	$NaBH_4$	5-6
CTAB/Butanol/Cyclohexane	$HAuCl_4$	$NaBH_4$	5-6
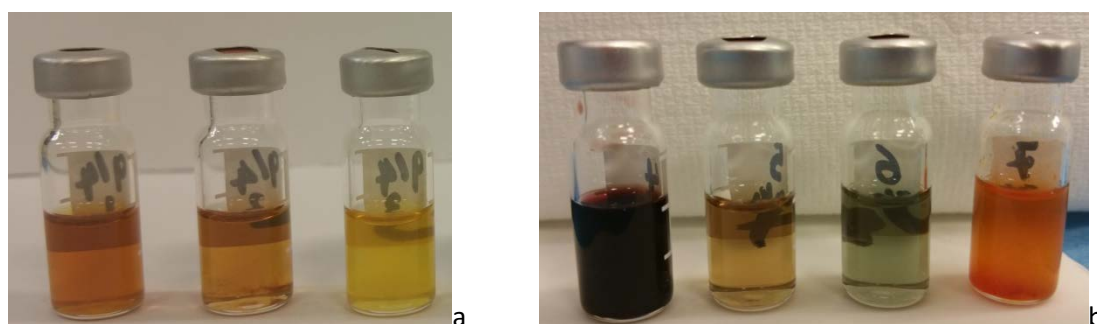
Figure 3.1: Images of a) Ag nanoparticles and b) Au nanoparticles in shortlisted microemulsion systems.

Once fabricated, the NPs produced were tested within the solution or incorporated within a different format; filter paper or on electrospun membranes (detailed in section 3.7), for testing with 514nm and 1064nm Raman.

3.6. Nanoparticle Separation

Within this study, water phase disruption was used for NP separation of the NPs from the microemulsion systems. Ag NP microemulsion systems required additional centrifugation to break-down the microemulsion components further surrounding the metal. Water phase disruption was used as it was simple, green and cost-effective, as well as producing NPs within a medium with no strong peaks within the 1064nm spectra that would mask the signal of the NP SERS substrates (Kowalczyk, Lagzi, & Grzybowski, 2011).

3.6.1. Water phase disruption

Following modification to protocols by Nazar et al and Hollamby et al, water phase disruption of NPs in microemulsions was used. Deionised water was added at a 1:1 ratio with the microemulsion volume and then the solution was left to equilibrate for a minimum of 1 hour. Two to three phases appeared, solvent rich upper phase, surfactant rich middle phase and water rich bottom phase (Fig. 3.2). The top phase was removed for the NP separation systems and excess water was added to it again to break down further the microemulsion systems. This process was repeated 3 times, with Ag NP solvent rich systems having an additional centrifugation step, 15 minutes, 12000 rpm (Hollamby et al., 2010; Nazar, Myakonkaya, Shah, & Eastoe, 2011).
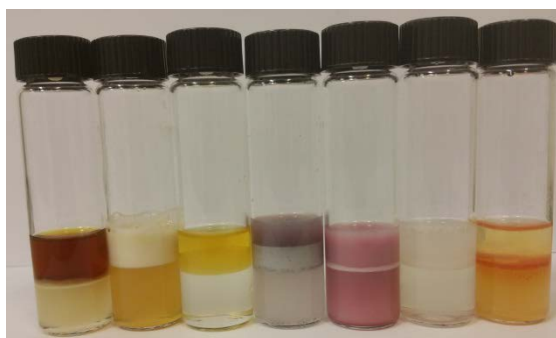
Figure 3.2: Water phase separation of Au and Ag NPs from microemulsion systems and resultant phases produced.

3.7. Metal Nanoparticles incorporated onto Electrospun membranes

Electrospinning is versatile, cost-effective technique, which produces controlled, uniform nanofibers of a polymer of interest through subjection of the polymer solution to a high voltage, within an electric field. The electrospun membranes have high porosity, surface to volume ratio and ability for miniaturisation, essential for a future lab on a chip SERS substrate and beneficial for optimising SERS. For the fabrication of SERS substrates within the 3rd category, NPs on electrospun membranes was used, due to these characteristics.

The polymer used for these SERS substrates was Polyacrylic acid (PAA), which was cross-linked with ethylene glycol (EG) for fabrication of insoluble electrospun membranes.

3.7.1. General Set-Up

The electrospinning set-up was manufactured with the help of AC solutions, UK. The machine consisted of two chambers; an outer chamber of 480x490x830mm in width, depth and height respectively and an inner chamber 400x410x750mm. The outer material was composed of aluminium and the inner material was Perspex with an insulating layer of polyurethane between the two chambers. This was necessary for more control over humidity and temperature during electrospinning. An additional controller for temperature and humidity input into the electrospinning design was present; for temperature a 'cool master' control box purchased from Maxkold, UK and for humidity WH8040 control box was purchased from Willhi, China with the temperature and humidity sensors placed at the bottom left wall of the inner chamber. All controllers were annually calibrated by AC solutions and the machine was PAT tested and certified. An additional shelf was present above the temperature and humidity controller and next to the electrospinning box, where the syringe pump 'Fusion 100' purchased from Chemyx, USA, sat.

The inner chamber contained a vertical set-up for electrospinning, with a ground wire attached to a 16x16cm^2 steel plate with aluminium foil coated on top of it for a collector. The spinneret needle was secured and the distance from the collector could be varied using a manual vertical stand. A high voltage power supply (EL30R1.5, Glassman High Voltage Inc., UK) was attached to the spinneret stand to induce electric potential between the spinneret and the collector. When the voltage was switched on a safety lock purchased from RS Supplies, UK, was in place for protection from high voltage and would cut the circuit if the door of the box was not closed (Fig. 3.3).

Figure 3.3: In-house electrospinning box produced with the help of AC solutions.

3.7.2. Electrospinning insoluble PAA-EG fibres

PAA-EG electrospun fibres were produced following modification of a protocol by Meng et al. Solution parameters were; PAA, 4% (w/v) dissolved in ethanol using an external magnetic stirrer purchased from Fisher Scientific, to aid in dissolving. Once dissolved under ambient temperatures, which typically took 1-2 hours, EG was added to the solution at a 12% w/w ratio relative to PAA. This was then left to mix and age under ambient temperatures for 72 hours. Before electrospinning the solution, 1M Sulphuric acid stock solution dissolved in deionised water was prepared and 25µl for every ml of polymer solution was added as a catalyst for post-electrospinning cross-linking.

For electrospinning PAA-EG the process parameters were; 20cm distance, 0.8ml/hr flow rate, 15-21kV voltage, humidity <10% and temperature of the solution had to be maintained at 4oC or less within the syringe pump, a light air flow was required inside the electrospinning box and temperature within the inner chamber varied but did not affect PAA electrospun fibres significantly (Meng et al., 2015).

Deposition times for electrospinning were varied at 5, 10, 20, 40, 60 and 120 minutes and a deposition time of 40 minutes was optimised for electrospinning PAA-EG. Once electrospun, the

membrane was placed in the oven for 30 minutes at 130°C to complete the cross-linking process (Fig. 3.4).
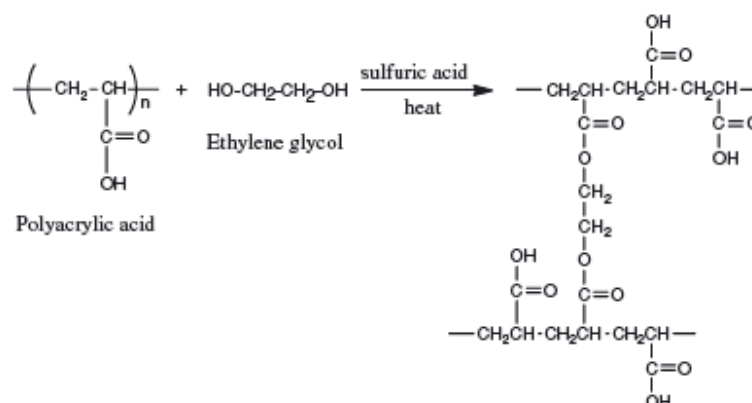
Figure 3.4: Chemical reaction depicting the cross-linking of Polyacrylic acid with ethylene glycol (Meng et al., 2015).

3.7.3. Surface modification of PAA-EG

PAA-EG was surface modified with cysteamine to increase the affinity and binding of Au and Ag NPs to the surface of the PAA-EG fibres for fabrication of a SERS substrate.

3.7.3.1. Nanoparticles on PAA-EG membranes

The –NH2 groups of Cysteamine were bonded to the –COOH groups of PAA in PAA-EG electrospun fibres using carbodiimide cross-linking. This was to enable a higher affinity of gold and silver nanomaterial to bind to the surface of the PAA-EG fibres through the –SH group on Cysteamine.

MES buffer was firstly prepared at 0.05M with a set pH of 5.3 using 1N NaOH and/or 1N HCl and tested using a pH probe (Ultrabasic by Denver Instruments). PAA-EG membranes were then cut into 8mm circular discs using a disposable biopsy punch with a 8mm diameter, and then a maximum of 40 of these discs were placed in 10ml of MES solution. EDC and NHS at a 0.1M concentration were added to the MES solution with the PAA-EG discs. This all took place under ice-conditions due to EDC degrading exponentially at ambient temperatures. Cysteamine hydrochloride was then added at 0.1M the solution for the reaction to take place. After 1 hour the solution was taken out of ice-conditions and left on a mechanical stirrer (New Brunswick Scientific, Classic series) at 150

rpm for a minimum of 12 hours. The resultant PAA-EG-Cysteamine discs were then washed 3 times with deionised water using a vortex at 3000rpm for a minimum of 10 seconds each wash.

The PAA-EG-Cysteamine discs were then added to nanoparticle solutions within microemulsion systems and nanoparticle separated solutions, left for a minimum of 12 hours on a shaker at 150 rpm for the Ag and Au NPs to bind to the fibre surface. The membranes were then removed from the solutions and washed three times with deionised water using a vortex at 3000 rpm until the solution became clear.

3.8. SERS enhancement

The SERS substrates fabricated within the 3 different design concepts; chemically etched silver wire, synthesised Au and Ag NPs and NPs on electrospun membrane were tested for SERS enhancement characteristics through the immersion with a SERS enhancer molecule 4-methylbenzenthiol (4-MBT) and then resultant SERS testing using 514nm and 1064nm Raman lasers.

All the substrates fabricated within the 3 different designs were tested initially with 4-MBT at 1mM MBT, with stock concentration dissolved in ethanol. The substrates were immersed in these two solutions under a fume hood and left for direct adsorption for 24 hours. The substrates were then cleaned using DW with a vortex at 3000rpm, 3 times. After which they were tested with 514nm and 1064nm Raman. Commercial SERS substrates, P-SERS and Au and Ag SERStrate were also characterised with 1mM MBT for comparison to fabricated SERS substrates. Control Raman spectra of MBT solid was also tested using the two wavelengths so enhancement factor (EF) could be calculated, using Equation 3.1.

$$\mathrm{AEF} = \frac{I_{\mathrm{SERS}}/c_{\mathrm{SERS}}}{I_{\mathrm{RS}}/c_{\mathrm{RS}}}.$$

Equation 3.1: Equation to calculate the enhancement factor of the SERS substrate in relation to Raman scattering (*RS*), *I* is the intensity of the signal and *C* is the concentration of the molecule (Le Ru & Etchegoin, 2009).

The substrates which showed the highest reliable SERS from each category and commercial PSERS, were further tested with 4-MBT at concentration; 1M, 0.1M, 0.01M, 0.1mM, 0.01mM, 1μm, 0.1μM, 0.01μm, 1nM, 1pM, 1fM and 1aM. To evaluate the limit of sensitivity of the SERS substrate as well as if the concentration of 4-MBT could be quantitatively calculated.

3.9. Diabetes Biomolecules & SERS

Optimised chemically etched Ag Wire, 30s NH_4OH+ 10s HNO_3, was used for proof-of-concept work regarding selective detection and SERS enhancement of diabetes biomarkers; glucose, bovine haemoglobin and bovine serum albumin with 514nm and 1064nm Raman. Due to the high power of 1064nm Raman, protein biomarkers were being burnt at rate where the heat within the fluidic chips made could not dissipate. Therefore, 1064nm Raman was used for glucose testing whereas 514nm Raman was used for all the diabetes biomarkers.

Diabetes biomarker concentrations were calculated for the high values shown within the physiological range. For glucose testing 30mM concentration within PBS, Deionised water and synthetic saliva was additional tested, to observe the effect increased complexity of the medium has on SERS signal of glucose.

For protein biomarkers, bovine Haemoglobin (Hb) and bovine serum albumin (BSA) were initially used for SERS testing, with concentrations made within the physiological range as well as diluted concentration, for the study 2.77mM and 0.5g/dL is shown for Hb and BSA respectively. Thereafter testing of human protein forms for Hb, Albumin and glycated proteins, HbA_{1c} and glycated Albumin were undertaken at concentrations of 1M for Hb and 0.05g/dL for albumin configurations. Concentrations made up due to preliminary experiments where the most signal was observed within these ranges for the bovine samples, as well as ease in making up the concentration regarding Hb.

Glucose, bovine Hb and BSA were further tested for their quantitative characteristics with chemically etched Ag wire SERS substrates as well as to provide calibration curves with limit of

detection of the substrate with the biomarker. The maximum concentration observed within the physiological range was taken for each biomarker and diluted 10-fold into multiple lower concentrations. Such as for glucose 30mM glucose solution was prepared and diluted to 3mM, 0.3mM and 0.03mM. Chemically etched Ag wire was then immersed within the solution for 24 hours and then removed for testing. This protocol was repeated for the other two biomarkers.

3.10. Raman Instrumentation

Two Raman instrument designs with differing laser wavelengths of 514nm and 1064nm were used for SERS testing (Fig.3.5).

For the 514nm laser wavelength; a benchtop InVia Raman microscope from Renishaw was used. It had a maximum power output of 50mW and power to the sample could be altered using a percentage bar in correlating WiRE 3.3 software, this was optimised to 10%. The exposure time of the laser to the sample was set to 1.00 second and the instrument was set to high confocality, so a 20μm range was depicted as a 2 pixel CCD area with 1500 counts. The Raman laser was correlated with a light microscope which had three magnifications of 5x, 20x and 50x which could be used, 20x magnification was optimised for use and enabled a sample spot size of 0.15μm. For the experiments 3 acquisition accumulations was set to reduce signal to noise ratio. Due to the platform design of the Raman machine, it was optimised for solid samples that could be set on glass slides, liquids were measured with dipped glass slides made by Brunel University. Calibration before Raman testing of samples occurred at the beginning and after every 27 samples with a reference silicon wafer.

For the 1064nm laser, a Raman probe from Stellarnet was used. The portable design was more adapted to liquid sampling and therefore a platform was made to test solid samples. The working distance of the laser to the sample was set between 5-10mm, typically at 7.5mm to obtain a Raman spectra, between a spectral range of 250-3900cm-1. The laser power was a 4ns pulsed jet of 2x consecutive 25mJ, with power to sample being 6 MW. The laser pulse could be delayed using a photo trigger delay with 8 settings; 1 = Disable trigger line, 2 = 2μs delay, 3 = 24μs, 4 = 28μs, 5 =

32μs, 6 = 38μs, 7 = 55μs and 8 = 105μs, this was beneficial to obtain more scattered photons however with samples that burnt quickly the delay meant that the spectra depicted a burnt portfolio and missed the spectra present for the sample (PORTA LIBS User Manual, 2015). The data acquisition time was optimised to 3000 milliseconds and spectra was taken after 3 averaged scans, shown using SpectraWiz software. Calibration of the laser before sample testing occurred using the reference sample mannitol.

Figure 3.5: Image a) shows the 514nm InVia Raman set-up from Renishaw, b) shows the 1064nm portable Raman probe set-up by Stellarnet in modified 3D printed platform.

For the two Raman set-ups, alterations in sample testing was require, for the 514 nm laser, it was found that the microemulsion solutions and any solution within a solvent was unable to be tested by the machine efficiently as the solvent would evaporate and it was difficult to focus the laser to obtain a Raman spectra, therefore an additional design of nanoparticles on filter paper occurred, the filter paper was immersed in the different nanoparticle solutions and the inorganic nanomaterial was adsorbed onto the surface of the filter paper, no additional surface modifications occurred so as not to tamper too much with the nanomaterial integrity. This design enabled better Raman spectra b overcoming the two problems that were listed.

The second design alteration was due to the 1064nm laser having such a high power output, it was shown to burn any sample that was unable to dissipate the heat quick enough, therefore Hb and albumin due to the lower melting points of 80°C and 60°C and despite no delayed photo trigger

time, was unable to provide reliable spectra with 3 acquisitions. Glucose was the only assay that was pursued with this spectrum for the SERS substrates and LOD as its melting point was the highest at 146°C and so Raman spectra was able to be obtained. A closed chip design was used to try and increase dissipation of heat with the nanoparticles on filter paper and nanoparticles in the electrospun membrane design. Silver wire was able to dissipate heat efficiently to be used as it was.

An open chamber microfluidic chip mold was designed by a post-doctoral researcher within the group using SolidWorks CAD software and saved as an STL file. The dimensions of the open chamber design was; 3mm long sample inlets, 250μm high with a 1mm diameter, 10mm entrance port at the bottom of the chamber, 500μm wide which led to a 8mm diameter collection outlet chamber of 2mm depth and collected a total volume of 250μl, the total chip size was 50x75mm with 12 identical wells. This design was 3D printed using Accura 60 resin with an Objet 30 Pro 3D printer. Once printed, the mold was cleaned using isoproponal and cured in an ultraviolet oven for 30 minutes. The mold was then placed within a stainless steel frame and PDMS solution was prepared using QSil 218 PDMS. The PDMS was mixed in a ratio of 1:10 for PDMS A and B respectively and then centrifuged or degassed. The PDMS was then applied onto the mould and placed within an oven at 45°C for 4 hours. Once mold had set a 75x50mm glass slide was corona treated using a handheld corona treater, BD20-AC (Electro-Technic Products Inc, US) and the glass slide was pressed against the PDMS base. This was then cured at 54°C for 8 hours to produce the open chamber microfluidic chip used 1064nm Raman testing, enabling hydration of the sample with deionised water, dissipating heat of the SERS substrates (Fig. 3.6).

Figure 3.6: Fabricated open chamber PDMS cartridge for 1064nm Raman testing

3.11. Characterisation of Materials

The surface morphology and chemical characteristics of the SERS substrates is pinnacle to the SERS enhancement characteristics. Step-by-step characterisation using adequate techniques detailed below for each SERS design as well as for the assays was undertaken.

3.11.1. Morphological

For morphological characterisation of chemically etched silver wire SERS substrates, scanning electron microscopy (SEM) was used in a Benchtop JCM-6000 NeoScope SEM by JEOL; the silver wire substrates were placed on carbon tape and scanned using a 15kV accelerating voltage. The roughness of the silver wires was also quantitatively assessed using an interferometer, Zygo New View 5000 with MetroPro software.

For morphological characterisation of silver and gold nanoparticles synthesised within microemulsions, the microemulsion systems were firstly analysed using UV-visible spectroscopy, from Perkin Elmer and Shimadzu, the presence of gold and silver nanoparticles was shown within the spectra and also the characteristics of the curve, and the shift in wavelength depicts different sizes and shapes of the nanoparticles and gives a rough guide to nanoparticle morphological characteristics. Transmission electron microscopy (TEM) in a JEOL 2100 machine was used, to give an accurate image of the size and shape of the nanoparticles present, the nanoparticles within the solutions were drop coated on carbon coated copper grids for testing.

For morphological characterisation of PAA-EG electrospun membranes, for firstly optimising the electrospinning parameters, fibres were checked under a light microscope, (Brunel SP500) and photos taken using a Nikon camera. The optimised PAA-EG fibres once electrospun and grafted with different surface modification coatings, were then analysed in more detail using SEM. The electrospun fibres were firstly sputter coated for 30 seconds using an AGAR high resolution sputter-coater and then scanned using SEM (JCM-6000, JEOL). Thickness of the electrospun membranes was also analysed using a thickness gauge by Mitutoyo and measuring mass of the membranes with an analytical balance from Denver Instruments.

For analysis of nanoparticles on the electrospun membranes, SEM (JCM-6000) was firstly used but as he nanoparticles for most of the compositions could not be seen effectively, TEM was used for characterisation. The nanoparticles on the electrospun membranes for characterisation with TEM had to go through some initial samples preparation, the membranes were immersed in concentrated sucrose solution and after which they were cryogenically frozen and cut into thin slices before loading onto a carbon coated copper grid.

3.11.2. Spectroscopy

For chemical characterisation of silver wire, energy dispersive spectrometry (EDS) was used in correlation with SEM images, to obtain the elemental analysis of the surface of the silver wires.

For chemical characterisation of silver and gold nanoparticles, ATR-FTIR spectra using a Perkin Elmer Spectrum One Fourier Transform Infrared (FTIR) spectrometer equipped with a Specac Golden Gate ATR accessory was used, spectrum was acquired in transmittance mode, was an average of 128 scans at a resolution of 4 cm^{-1} for PAA-EG electrospun membranes and surface modified counterpart, it was used again to test the efficiency of cross-linking of the electrospun membranes as well as the alteration in surface chemistry of the membrane with the additional chemical grafting, spectra as with before was obtained in transmission mode from an average of 128 scans. Before electrospinning the PAA-EG solution, the conductivity using a Primo 2 by Hanna Instruments and alterations were made to the amount of sulphuric acid catalyst added through this process.

Additional characterisation of the assays also took place, with the use of ATR-FTIR following the same protocol as with before, bovine and human counterparts were taken in solid and liquid form to obtain spectra to be compared with Raman. The assay solutions made were also tested with a conductivity meter. However the sensitivity of the meter was in microsiemens and with complicated solutions, typically in buffer or saliva solutions, conductivity could not be measured. Typically the biomarkers within DW, pH on the other hand was obtained for all assay solutions, to be correlated with binding affinity to the different SERS substrate surfaces.

3.11.3. Statistical

Image-J was used to measure the diameters of the electrospun fibres given with SEM, as well as nanoparticles size given with TEM, an average of 20 fibres was taken for SEM image and for nanoparticles, depending on the amount of nanoparticles present, a minimum of 10 if possible was taken from each TEM image.

SPSS was used for statistical analysis and corresponding significance of data accumulated within excel was analysed, with a standard deviation, standard error and average typically calculated and quantitative result.

Chapter 4: SERS Substrate Design: Chemically Roughened Silver Wire

4.1 Introduction

SERS was accidentally discovered with the use of Ag electrodes, wherein the electrochemical process introduced a roughened Ag surface required for SERS enhancement (Fleischmann et. al., 1974). Traditionally, roughened surfaces on a solid metal substrate are accomplished through electrochemical oxidation and reduction cycles or vacuum methods (Lin et. al., 2009). However, these methods are typically time consuming and expensive due to equipment (e.g. potentiostat, vacuum pump) required. The use of chemical roughening provides a simple, fast and cost-effective method to generate simple SERS substrates. To the best of my knowledge, chemically etched SERS substrate designs have been sparsely noted within the literature, typically on a preliminary level (Mattel et. Al., 1990; Rajesh & Sunandana., 2015). I am not aware of any such substrates that are commercially available. The objective for this chapter was to evaluate simple chemical etching methods to generate roughened solid Ag surfaces for SERS, and identify one such method that provides a reproducible surface roughening (hotspots) and better SERS sensitivity on a solid Ag wire. Specifically, I evaluated the effects of chemical etching using nitric acid (HNO_3) and/or ammonia hydroxide (NH_4OH), and/or heat treatment on the roughening of flattened Ag wires. The resulting wires were characterized for their roughness using SEM and interferometry, surface composition using EDX and Raman spectroscopy (514nm), and SERS efficacy using 1mM 4-methyl benzene thiol (MBT) as a model Raman active molecule and Raman spectrometers equipped with 514nm and 1064nm lasers for recording SERS spectra.

4.2. Chemical Etching and/or Heat Treatment of Ag Wires and their Effect on Surface Roughness

Ag wires were flattened using a mechanical press to provide a flat surface for ease of use and maximizing surface area for Raman instrumentation. To generate roughened Ag wire surfaces for SERS substrate we used the following chemical etching treatments:

- Ammonia hydroxide (NH_4OH)

    o 30 seconds (30s) NH_4OH

- Nitric acid (HNO_3)

    o 10 seconds (10s) HNO_3

    o 2 minutes (2m) HNO_3

- NH_4OH and HNO_3

    o 30s NH_4OH followed by 10s HNO_3

    o 30s NH_4OH followed by 2m HNO_3

4.2.1 Etching with 30% Aqueous Ammonia (NH_4OH)

NH_4OH is a weak base that is commonly used for household cleaning and polishing of jewellery, wherein, it is typically used at concentrations of 5 to 10%. This generally lifts off any dirt and grime from the surface. However, when used at higher concentrations and longer immersion durations for cleaning silver metal, aqueous NH_4OH is known to cause surface etching. In this study, we need microscale etching to generate SERS transduction signal. Therefore, the use of the weak base NH_4OH at a higher concentration (30%), was envisioned to produce a roughened surface on the flattened Ag wire.

The morphology and topography of the native and NH_4OH treated Ag wire is shown in Figure 4.1. The flattening process using a mechanical press introduced some debris (dark spots) on

the Ag wire surface (Fig. 4.1a). However, when this wire was treated with 30% NH$_4$OH for 30s, its surface changed into a bright, shiny and reflective silver colour to the naked eye. Further, when observed under SEM, the NH$_4$OH treated wire appeared clean and had a smoother surface (Fig. 4.1b) compared to the original flattened Ag wire (Fig. 4.1a). In addition, the topography of the Ag wires were mapped and their roughness quantified using interferometry (Fig 4.1c&d).
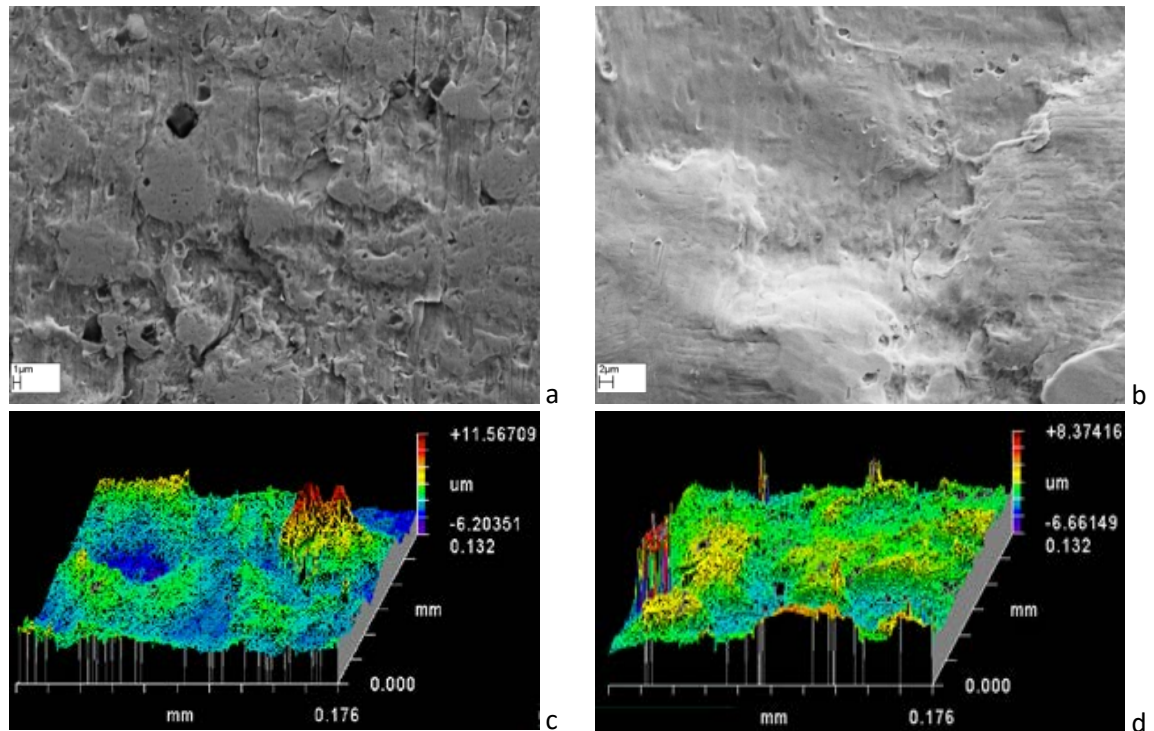
Figure 4.1: Surface morphology as visualised by SEM (a & b) and topography as mapped by interferometry (c & d) of flattened Ag wires - native (a & c) and those that were etched with 30% ammonia for 30 seconds (b & d).

The topography data presented here is the 3D surface maps recorded using Zygo New View 5000 interferometer equipped with MetroPro software. The quantitative data, namely, roughness parameters, associated with these 3D surface maps represent the non-periodic finer irregularities in the surface texture that provide a measure of the vertical characteristics of the surface (Zygo, 2013). The different roughness parameters used for analysing the effect of chemical etching on the surface roughness, in this study, are summarised in Table 4.1. Roughness parameters are generally abbreviated with R followed by letters in subscript, and are calculated on a profile (line) or on a surface (area). R_t is the sum of the maximum peak height (R_p) and the maximum valley depth (R_v)

as measured from the mean linear surface on the Ag wire surface. R_a is the arithmetic mean roughness, while R_q is root mean square roughness (Table 4.1). The difference between R_a and R_q indicates the uniformity in roughness, since R_q is more weighted by large values of peak height and valley depth (Lowe and Spindloe, 2006-2007). The RMS value is typically 10%-25% larger than the mean value of roughness depending on the nature of the surface (Whitehouse, 2002).

Table 4.1: The surface roughness parameters (associated with the 3D surface maps) used to analyse the effects of chemical etching treatments on the surface roughness of Ag wires (Zygo, 2013).

Parameter	Description	Schematic representation
R_a	Arithmetical mean deviation. The arithmetic average of the absolute values of the roughness profile. $$R_a = \frac{1}{L}\int_0^L |z(x)|\,dx$$	
R_q (rms)	Root-mean-square (rms) roughness. The average of the measured height deviations taken within the evaluation length or area and measured from the mean linear surface. R_q is the rms parameter corresponding to R_a. $$R_q = \sqrt{\frac{1}{L}\int_0^L z^2(x)\,dx}$$	
R_t (PV)	Maximum peak-to-valley height. The absolute value between the highest and lowest peaks. $$R_t = R_p + R_v$$	
R_p	Highest peak. The maximum distance between the mean line and the highest point within the sample. It is the maximum data point height above the mean line through the entire data set.	
R_v	Lowest valley. The maximum distance between the mean line and the lowest point within the sample. It is the maximum data point height below the mean line through the entire data set.	

The SEM image (Fig 4.1a) and the surface map (Fig 4.1c) show that the flattened native Ag wires have an inherently rough topography with plateaus (green and yellow colours), troughs (blue colour indicating valleys) and irregular features (red colour indicating peaks/summits). The measured roughness parameters for the Ag wires with and without chemical etching treatments

are listed in Table 4.2. The roughness of flattened native Ag wires was in the microscale with an R_t

value of 11.15±0.89µm and an R_a of 0.95±0.10µm. The R_a lesser than 1 and the greener colour

compared to yellow in the surface topography maps could indicate that the mean linear surface of

the Ag wires is skewed towards the valleys (more average valleys compared to the average peaks

across the surface profile) (Fig 4.1c and Table 4.2). However, a 32.20% higher R_q value compared to

its corresponding R_a indicates that there are more number of high peaks and deep valleys deviating

from mean linear surface of the Ag wires (Table 4.2) leading to an overall rougher surface.

NH₄OH has a caustic effect on Ag surface, wherein, it lifts off any dirt, loose particles as well

as Ag metal from the surface. In this process, NH₄OH treatment not only removed any debris, but

also etched a layer of Ag metal on the inherently rough flattened Ag wire surface. This etching is

reflected by the decrease in roughness parameters R_q (1.02±0.19µm vs 1.27±0.17µm) and R_a

(0.77±0.15µm vs 0.95±0.10µm), without significant difference in the percentage increase in R_q vs

R_a (31.90% vs 32.20%)) for NH₄OH treated Ag wires compared to that for the native Ag wires (Table

3.2 and Fig 3.1d). However, R_a was significantly lower than 1 for the NH₄OH treated Ag wires which

could indicate that the mean linear surface is acutely skewed towards the valleys. Thus, the NH₄OH

treatments appear to wear the surface peaks faster than the valleys.

Table 4.2: Surface (area) roughness data for the native flattened Ag wire and the different flattened Ag wires
after chemical etching treatments. (n=6, mean ± standard error of mean)

	R_t (PV) (µm)	R_p (µm)	R_v (µm)	R_q (RMS) (µm)	R_a (µm)	$(R_q-R_a)/R_a$ (%)
Native	11.15±0.89	5.83±0.64	5.31±0.53	1.27±0.17	0.95±0.10	32.20
30s NH₄OH	12.04±1.15	5.99±0.84	6.06±0.67	1.02±0.19	0.77±0.15	31.90
10s HNO₃	14.63±2.09	6.48±1.01	8.15±1.10	1.33±0.27	1.03±0.21	28.96
2m HNO₃	10.04±0.59	4.97±0.39	5.06±0.23	1.23±0.10	0.96±0.09	27.51
30s NH₄OH + 10s HNO₃	13.09±0.98	6.05±0.58	7.03±0.52	1.40±0.30	1.05±0.21	33.52
30s NH₄OH + 2m HNO₃	14.08±1.92	5.98±0.98	8.10±1.10	1.95±0.41	1.39±0.30	40.08

4.2.2 Etching with 6M Nitric Acid (HNO₃)

Unlike NH₄OH, HNO₃ is a strong acid that rapidly dissolves Ag metal. In this study, I used 6M aqueous HNO₃ for etching the surface of the flattened Ag wires, and the etching durations were either 10s or 2m. Their respective morphology and topography are shown in Figure 4.3. The surface of the 10s HNO₃ treated Ag wire appeared flaky, with narrow gaps in between the flaky structures that are numerous compared to the rough features observed on the native as well as the NH₄OH treated Ag wires (Fig 4.2a). On the 2m HNO₃ treated surface, the flakes were worn out into smaller separated protrusions that appear like elevated peaks (Fig 4.2b).
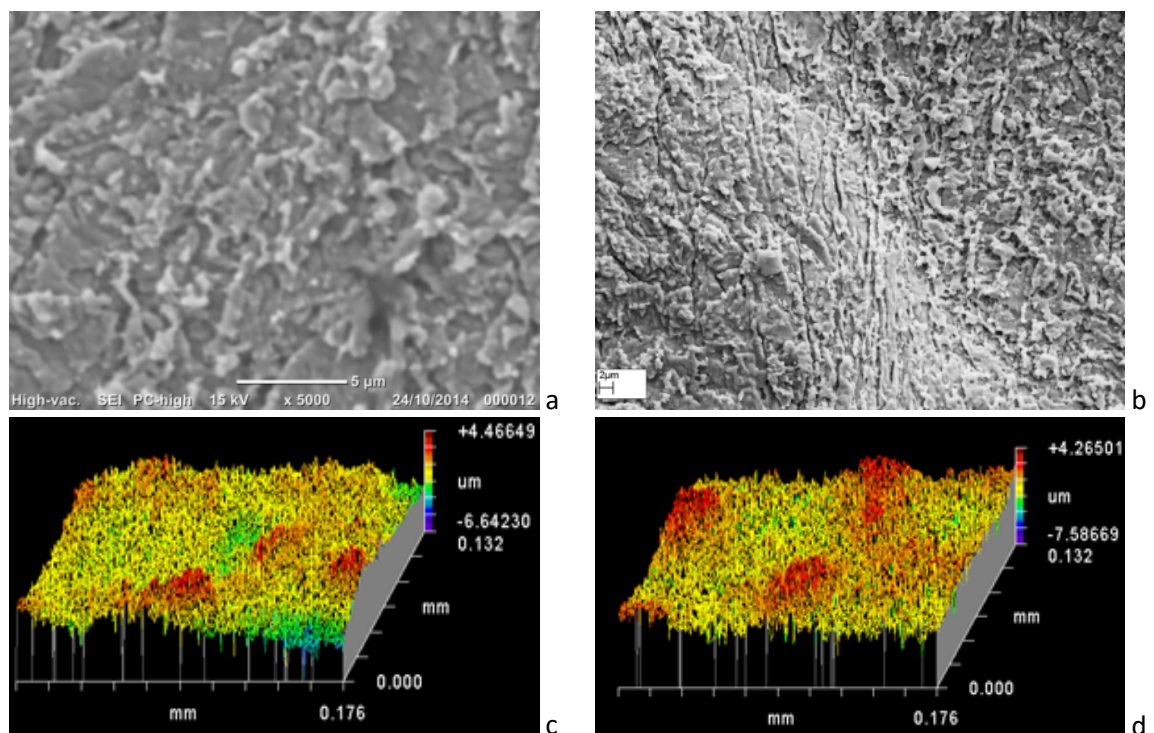
Figure 4.2: Surface morphology as visualised by SEM (a & b) and topography as mapped by interferometry (c & d) of flattened Ag wires – etched with HNO₃ for 10 seconds (a & c) and 2 minutes (b & d).

The quantitative topography data further reflected the differences in the surface roughness on the Ag wires induced by HNO₃ treatments, when compared to that observed on the native and NH₄OH treated Ag wire surfaces (Table 4.2 and Fig 4.2c&d). For both 10s and 2m HNO₃ treatments, the R_q and R_a values were not significantly different with that observed on the native Ag wires. However, a lower percent increase in R_q vs R_a for both 10s and 2m HNO₃ treated surfaces compared

to native Ag wire surface indicate that there are now lesser number of high peaks and deep valleys deviating from mean linear surface on the HNO_3 surfaces making their roughness relatively uniform. The R_a values close to 1 further indicate that there is a balance between the number of peaks and the number of valleys on the HNO_3 treated Ag wire surfaces. Thus, the stronger HNO_3 solutions appear to cause uniform etching, when compared to NH_4OH treatment that caused faster etching of peaks vs valleys. In addition, there appear to be more surface features that are uniformly distributed on the surface, which is a desired surface for SERS signal enhancements. Between the 10s and 2m HNO_3 treatments, there is significant difference in the features on the surface as discussed above. It is the anisotropic shapes and separation of these surface feature, that determine the degree of SERS enhancement, and hence we have two interesting surfaces with different surface features, but similar roughness between the 10s and 2m HNO_3 treated Ag wires.

4.2.3 Etching with 30% NH_4OH followed by 6M HNO_3

Thereafter, we studied the synergistic effect of surface cleansing and smoothening caused by NH_4OH treatment and the uniform etching caused by HNO_3 treatment on the surface features and roughness on Ag wires. The morphology and topography of the 30s NH_4OH + 10s HNO_3, and 30s NH_4OH + 2m HNO_3 treated Ag wires is shown in Fig 4.3. As seen in the SEM images (Fig 4.3a&b), the combination of NH_4OH followed by 10s or 2m HNO_3, resulted in similar morphology to that observed with the respective 10s and 2m HNO_3 treatments, except that the valleys between the flaky or discrete features respectively appeared wider and deeper. This adds variety to the surface features on the Ag wires, which could potentially provide varying degrees of SERS enhancements.

The 30s NH_4OH + 10s HNO_3 treated Ag wires showed an R_a value of 1.05±0.21µm and percent increase in R_q vs R_a of 33.52%, slightly higher than that observed with the native Ag wires (0.95±0.10µm), skewing the mean linear surface towards the peaks (Table 4.2 and Fig 4.3c). But, the higher R_q (1.40±0.30µm) indicates that there are more high peaks and low valleys away from

the mean linear surface, which in turn is suggestive of more surface features per unit area on the 30s NH_4OH + 10s HNO_3 treated Ag wires compared to the native Ag wires (Table 4.2 and Fig 4.3c).

On the other hand, 30s NH_4OH + 2m HNO_3 treated Ag wires had significantly higher R_a, R_q, and percent increase in R_q vs R_a, suggesting the roughest surface among all the chemical etching treatments in this study (Table 4.2 and Fig 4.3d). The reference mean linear surface is significantly skewed towards peaks (R_a of 1.39±0.30µm). There are more number of high peaks and deep valleys away from the mean linear surface (R_q of 1.95±0.41µm). It also has the significantly rougher surface (40.08% higher R_q vs R_a) among all the chemical treatments tested in this study (Table 4.2 and Fig 4.3d).
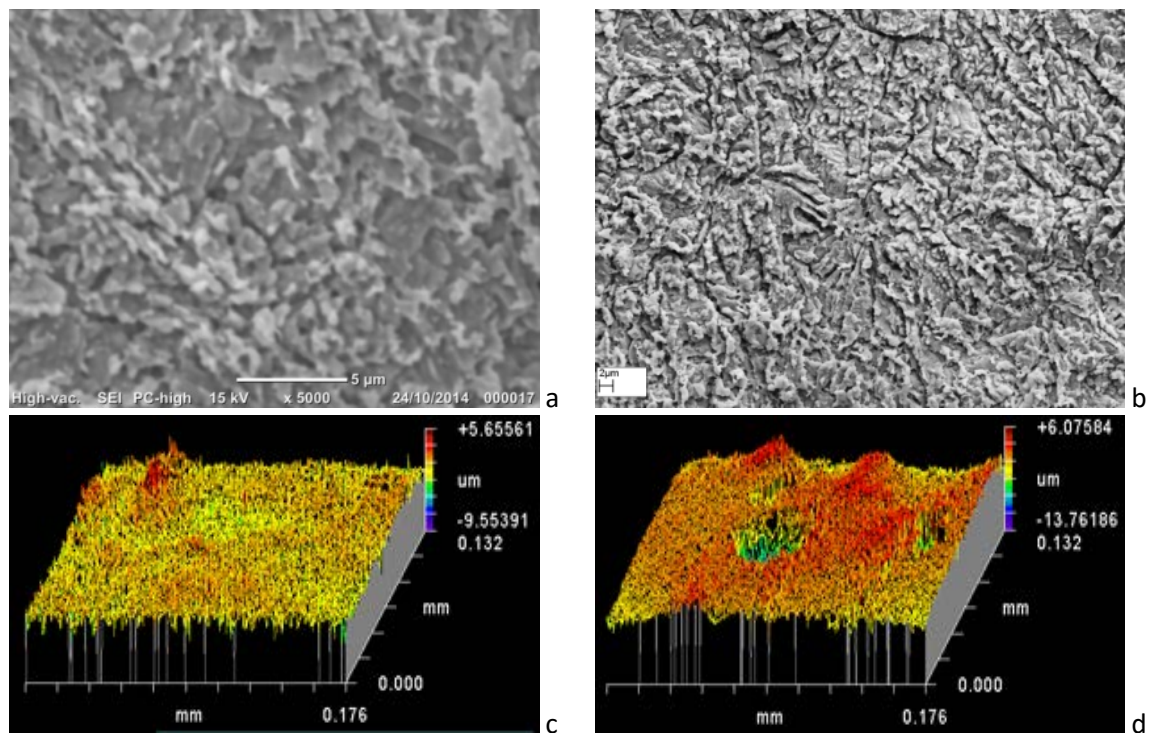
Figure 4.3: Surface morphology as visualised by SEM (a & b) and topography as mapped by interferometry (c & d) of flattened Ag wires – etched first for 30 seconds with ammonia followed by HNO_3 for 10 seconds (a & c) and 2 minutes (b & d).

4.2.4 Effect of heat treatment on the surface roughness of native and etched Ag wires

The etching agents, NH_4OH and HNO_3, can potentially leave some chemical residues as well as fragile surface features on the Ag wire surface. Hence, we utilized heat treatment at $130^{\circ}C$ for 1 hour to evaluate its physical and chemical influence on the surface properties of the native and the chemically etched Ag wires. Their morphology and topography was studied using SEM and interferometry.

The SEM images of the heat treated native (Fig 4.4a), 30s NH_4OH (Fig 4.4b), 10s HNO_3 (Fig 4.5a), 2m HNO_3 (Fig 4.5b), 30s NH_4OH + 10s HNO_3 (Fig 4.6a), and 30s NH_4OH + 2m HNO_3 (Fig 4.6b) all showed similar morphology as their non-heated counter parts (Figures 4.1 to 4.3). NH_4OH still caused the smoothing of the silver wire, HNO_3 an increased surface etching, and the longer the duration of HNO_3 treatment the increased roughness on the Ag wire surface. However, the quantitative topography results showed differences in surface roughness parameters between the heated (Table 4.3) and their non-heated Ag wire counterparts (Table 4.2).
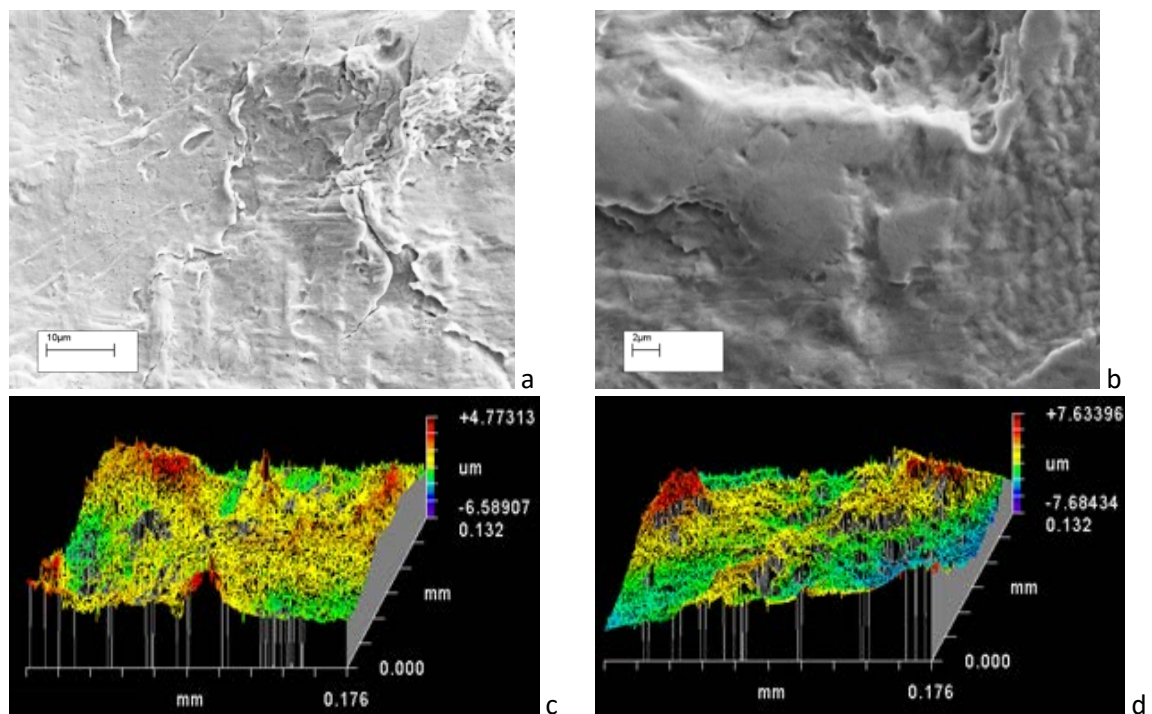
Figure 4.4: Surface morphology as visualised by SEM (a & b) and topography as mapped by interferometry (c & d) of flattened Ag wires - native (a & c) and those that were etched with 30% ammonia for 30 seconds (b & d) that were heated at $130^{\circ}C$ for 1 hour after the chemical etching treatments.

Table 4.3: Surface (area) roughness data for heat treated (130°C for 1 hour) native flattened Ag wire and chemical etched flattened Ag wires. (n=6, mean ± standard error of mean)

	R_t (PV) (µm)	R_p (µm)	R_v (µm)	R_q (RMS) (µm)	R_a (µm)	$(R_q-R_a)/R_a$ (%)
Native	9.59±0.75	4.39±0.25	5.20±0.59	1.20±0.11	0.93±0.08	29.18
30s NH$_4$OH	12.99±1.33	7.12±0.59	5.87±0.93	1.53±0.15	1.19±0.12	28.62
10s HNO$_3$	14.79±1.17	6.88±0.97	7.90±0.35	1.29±0.04	1.00±0.03	29.75
2m HNO$_3$	11.69±1.94	6.02±1.33	5.67±0.80	1.35±0.23	1.07±0.18	26.30
30s NH$_4$OH + 10s HNO$_3$	15.18±1.55	7.23±0.86	7.95±0.89	1.58±0.19	1.19±0.14	32.66
30s NH$_4$OH + 2m HNO$_3$	12.69±0.48	5.67±0.40	7.02±0.25	1.40±0.11	1.09±0.08	29.11
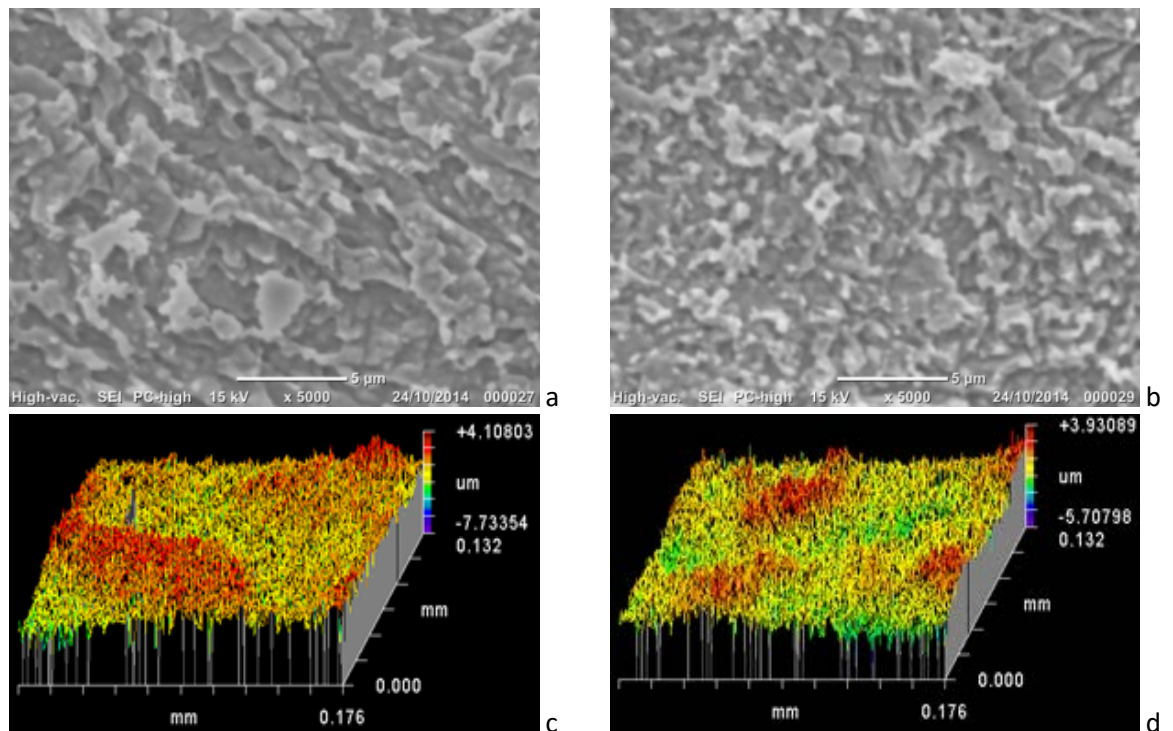
Figure 4.5: Surface morphology as visualised by SEM (a & b) and topography as mapped by interferometry (c & d) of flattened Ag wires – etched with HNO$_3$ for 10 seconds (a & c) and 2 minutes (b & d) that were heated at 130°C for 1 hour after the chemical etching treatments.
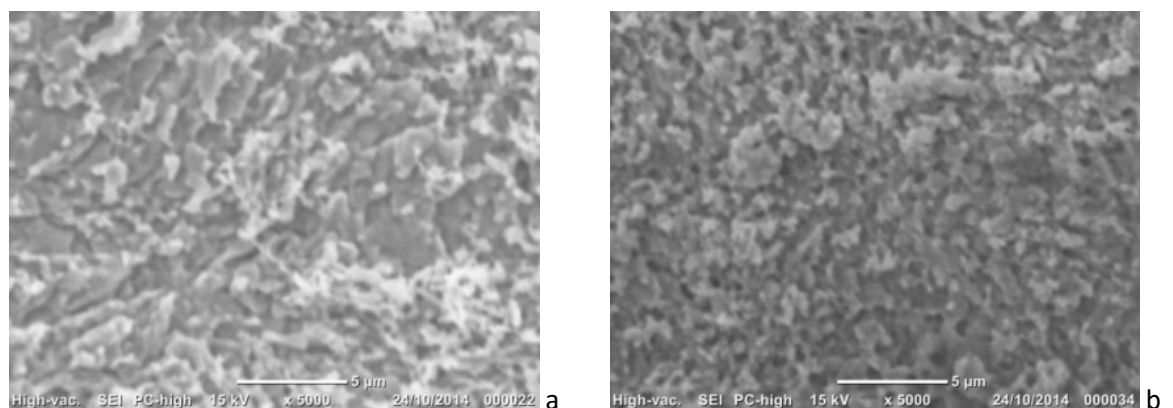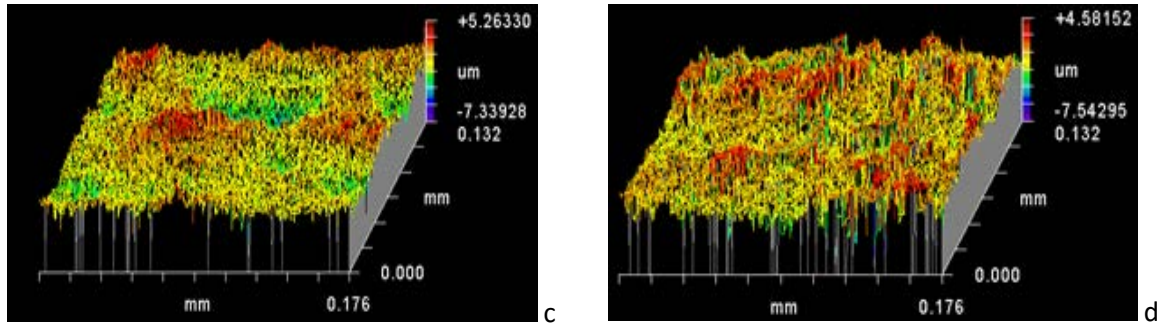
Figure 4.6: Surface morphology as visualised by SEM (a & b) and topography as mapped by interferometry (c & d) of flattened Ag wires – etched first for 30 seconds with ammonia followed by HNO$_3$ for 10 seconds (a & c) and 2 minutes (b & d) that were heated at 130°C for 1 hour after the chemical etching treatments.

Ag is a soft and malleable metal, and the changes in the roughness parameter R$_a$, R$_q$ and percent increase in R$_q$ vs R$_a$ for all Ag surface variables, in this study, were suggestive that heating at 130°C for 1 hour induced restructuring of surface features on the Ag wires into less rougher surfaces compared to their respective non-heated counterparts. The percent increase in R$_q$ vs R$_a$ for the different heated Ag wires ranged between 26 and 33%, which was lower compared to their non-heated counterparts (27 to 40%). This indicates that the number of peaks higher and valleys deeper than the mean linear surface reduced. This was also visually evident upon closer inspection with the higher magnification SEM images, as illustrated for the 30s NH$_4$OH + 2m HNO$_3$ treated Ag wires in Fig 4.7. However, for 30s NH$_4$OH treatment, heat treatment resulted in an increased R$_a$ and R$_q$ values compared to its non-heated counterpart. This was in contrast to all the other chemical etching treatments, where heating reduced the R$_a$ and R$_q$ values. One explanation for this could be that, the NH$_4$OH treatment could leave amine residues on the Ag surface from the NH$_4$OH by products, since Ag metal is known to passively react with amines. NH$_4$OH residues on a metal, when heated, are known to cause the nitriding effect, wherein the NH$_4$OH dissociates into N$_2$ and H$_2$. N$_2$ diffuses onto the metal surface creating a nitride layer that is known to increase the mechanical properties and roughness of the surface (Rolinski et. al., 2007).

a

b
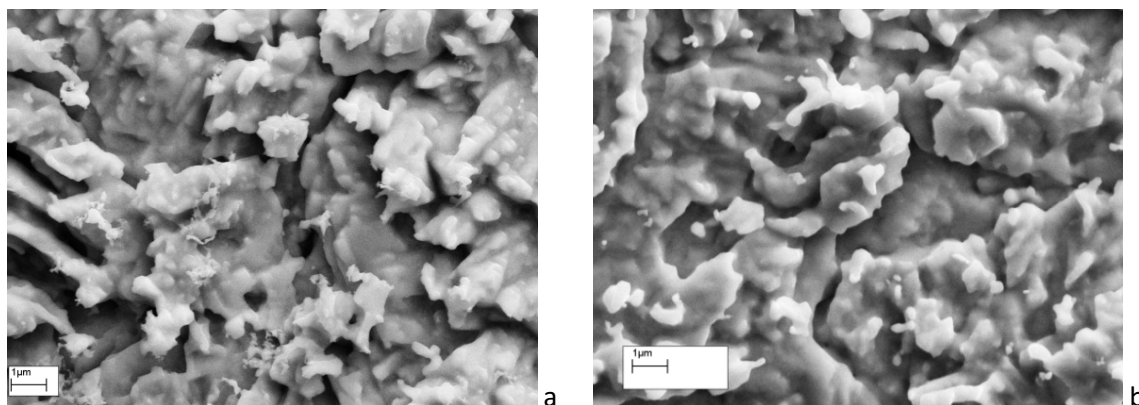
Figure 4.7: SEM images at x25000 magnification to show surface morphology of silver wire etched with 30s NH₄OH and 2m HNO₃ treatment: a) non-heated and b) heated post chemical etching treatment.

4.3. Surface chemical composition as a function of etching treatments

SERS, being a sensitive transduction mechanism, requires a clean metal surface before it is treated with an analyte of interest for detection or assay. Any contaminant on the SERS substrate surface could give unwanted SERS spectral peaks. Hence, it was important to evaluate the chemical composition, which was accomplished by recording energy-dispersive X-ray (EDX) and Raman spectra. EDX spectra provide information about the changes in the elemental composition, while Raman spectra pick up organic and inorganic residues on the silver wire surfaces.

As shown in the SEM image (Fig 4.1a), the native flattened Ag wire surface was contaminated with debris picked up during the flattening process using a mechanical press. EDX spectra for the dark dots of debris and the clear Ag surface on the native Ag wires are shown in Fig 3.8a&b respectively. The debris suppressed the Ag peaks, and showed prominent peaks for carbon, oxygen, sulphur, silicon, sodium, potassium, chloride, calcium and other metals including iron, aluminium, and titanium (Fig 4.8a). This indicates the presence of contaminants including hydrocarbons, sand, salts and metals in the debris. However, on the native flattened silver wire surface clear of the debris, the primary peaks observed were that of Ag (indicating high purity, >99%). A very small peak for carbon and occasional peaks for oxygen, magnesium and aluminium were also observed (Fig 4.8b), indicating the presence of residual hydrocarbons and trace amounts

of metals (Mg, Al). Interestingly, irrespective of the chemical treatment performed in this study to etch the Ag wires, all the silver wires showed EDX spectra similar to that observed on the clean areas on the native flattened Ag wires (Fig 4.8), all surfaces containing traces of hydrocarbons and metals..
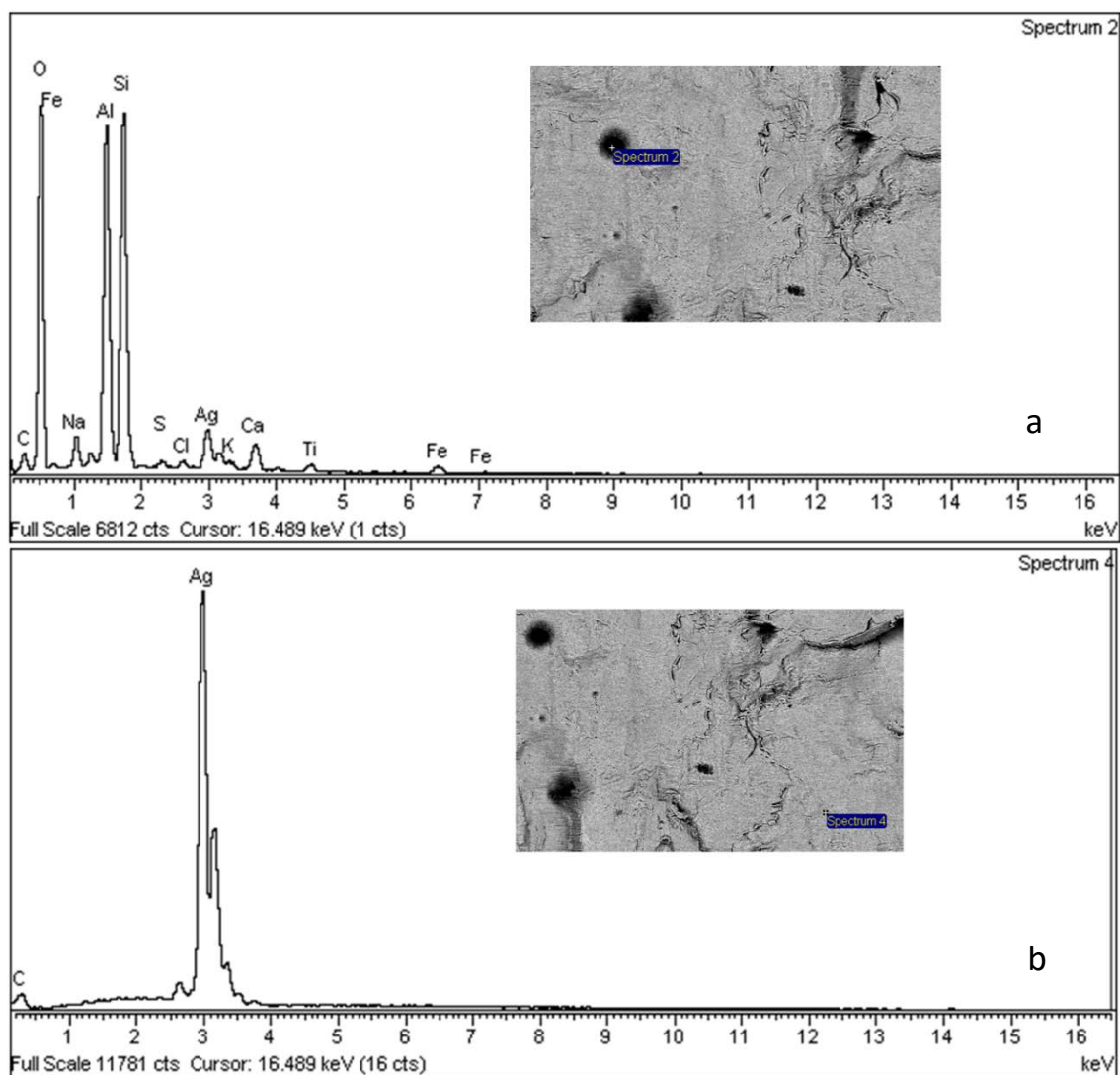
Figure 4.8: Energy-dispersive X-ray (EDX) spectra for the surface of the native flattened Ag wires, a) on the debris adsorbed on the Ag wire surface, and b) an area clear of debris. The latter spectrum is similar to that of a typical high purity Ag wire, and the chemically etched Ag wire surfaces prepared in this study all had a similar spectrum.

Raman spectral signals are inherently weak due to <0.01% inelastic scattering and inability to pick up molecules with smaller spectral cross-sections. Hence, any peaks that we see on the different Ag wires should be the SERS enhancements of contaminants on the Ag wire surface. The 514nm Raman spectra for the non-heated and heated Ag wire surfaces are presented in Figures

3.9a&b respectively. In fact, we saw Raman peaks on the native as well as all the chemically etched

Ag wires. The observed Raman peaks are listed in Table 4.4.
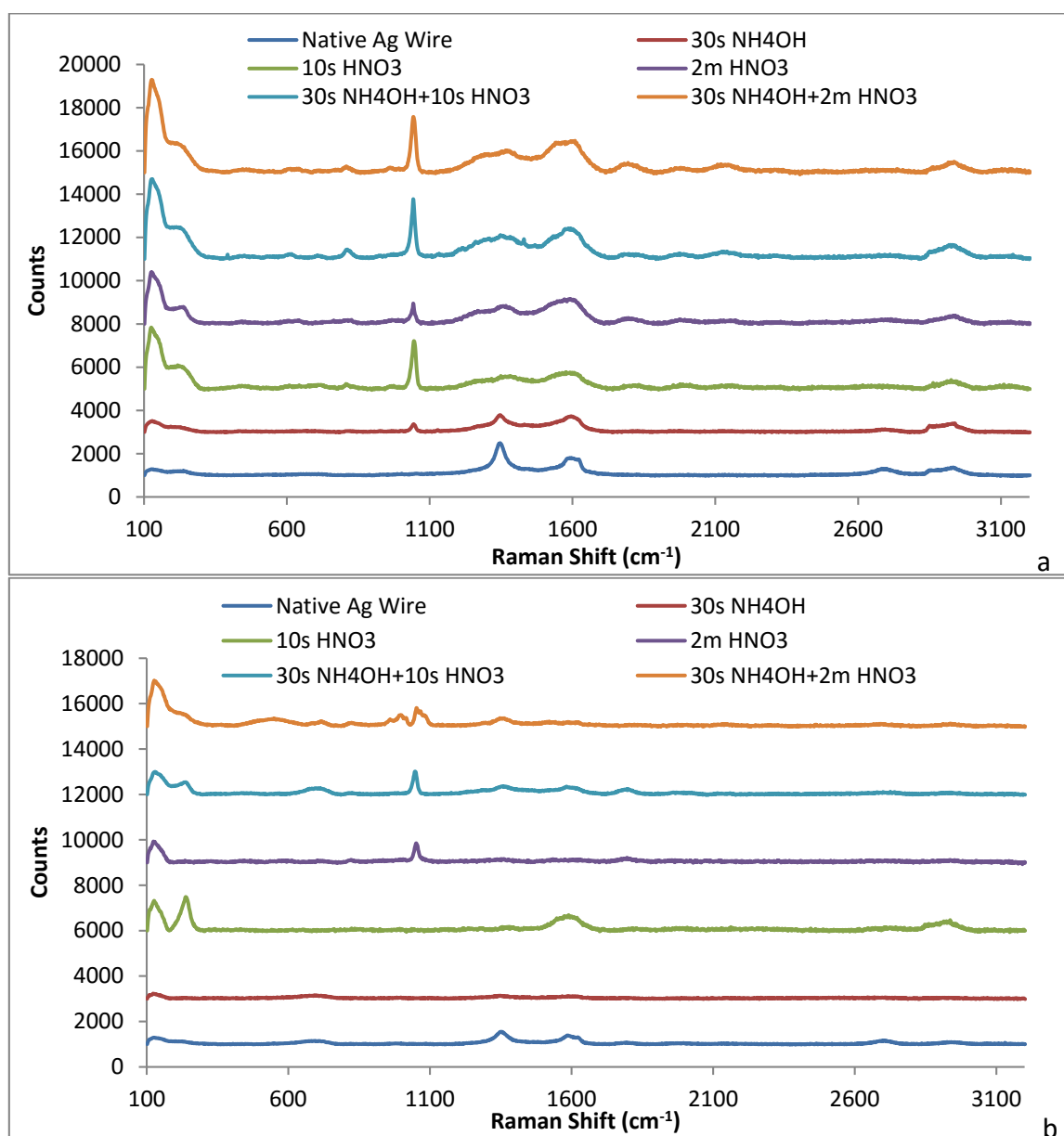
Figure 4.9: 514nm Raman spectra for the native and chemically treated Ag wires: a) non-heated, and b) heated. The spectra are offset sequentially by 1500 to 2000 counts for clarity.

Table 4.4: Raman peaks (cm^{-1}) and their corresponding peak assignments on the 514nm Raman spectra for the different Ag wires.

Non-heated						Heated						Peak Assignment
Native	30s NH$_4$OH	10s HNO$_3$	2m HNO$_3$	30s NH$_4$OH + 10s HNO$_3$	30s NH$_4$OH + 10s HNO$_3$	Native	30s NH$_4$OH	10s HNO$_3$	2m HNO$_3$	30s NH$_4$OH + 10s HNO$_3$	30s NH$_4$OH + 10s HNO$_3$	
133	129	125	125	134	135	124	123	129	124	128	126	Lattice vibrations
		132	134								137	
228			237					238		238	540	Metal-O stretch
				393								Metal-O stretch or CC bend
						696						O-C=O bend
		807		811	808		700		823	702	718	CH out-of-plane deformation
											823	
											958	
	1043	1045	1043	1043	1044				1052	1048	999	C-O stretch
											1053	
1346	1348	1364	1357	1346		1355	1348			1358	1347	CH$_3$ deformations
					1382							CH$_3$ deformations or COO- symmetric stretch
				1430								In-plane OH bending
1599		1591	1595	1588	1609	1588	1594	1590		1583		NH$_2$ deformation or COO- antisymmetric stretch
2693	2674	2926	2923	2929	2936	2706		2937				CH$_3$, CH$_2$, antisymmetric and symmetric stretching respectively or O-H stretch.
2933	2926					2933						

The native Ag wire showed the Raman peaks: 133, 228, 1346, 1598, 2692 and 2933cm⁻¹, representing lattice vibrations, metal oxide stretch, C-H deformations, COO- asymmetric stretch, C-H asymmetric and C-H symmetric stretches respectively. Essentially, these peaks are indicative of hydrocarbons and Ag oxide, in agreement with the EDX data. These peaks did not change when the native Ag wires were heat treated. However, the intensity of the peaks decreased significantly, indicating that heat either removed the contaminants to a great extent or the altered surface roughness influenced the SER enhancement (Fig.4.9).

An additional sharp peak around 1043cm⁻¹ appeared in all the chemically etched Ag wires indicating a C-O stretch (Fig 4.9 & Table 4.4). On the HNO₃ treated surface there was a peak at 807cm⁻¹ indicating C-H out-of-plane deformation. SERS spectra of organic molecules, often, do not show all the peaks seen with its bulk molecule. Potentially, the chemical etching treatments are causing a conformational change in the contaminant molecules binding onto the Ag wire surface to produce the additional C-H out-of-plane deformation peaks. Similar to that observed with native Ag wires, heat treatment caused the absence or the decrease in the intensity of the interferents' Raman peaks as seen in Fig 4.9b.

4.4. Efficacy of the Roughened Ag Wires in Enhancing SERS Signal

Raman spectra for solid MBT using 514nm and 1064nm wavelengths showed similar spectral peaks and correlating bonds for CC bend, CH out-of-plane deformation, C-S stretch, CC stretch, CH₃ symmetric deformation, carbon ring stretch, S-H stretch, =C-H stretch, C-H antisymmetric and C-H symmetric stretches respectively. Additional peaks were observed for both wavelengths, with 514nm showing bonds for out-of-ring bending and CH₂ out-of-plane wag, whereas 1064nm showed an additional peak for C-S stretch (Table 4.5). When compared with peaks present on the control Ag wire, the presence of multiple thiol and carbon ring peaks, is beneficial for reliably determining the presence of MBT upon the Ag surface. The intensities of the MBT

Raman spectra showed increased intensity for peaks with 1064nm whereas with 514nm the peaks are sharper, with increased intensity for thiol and carbon ring bonds (Figure 4.10).
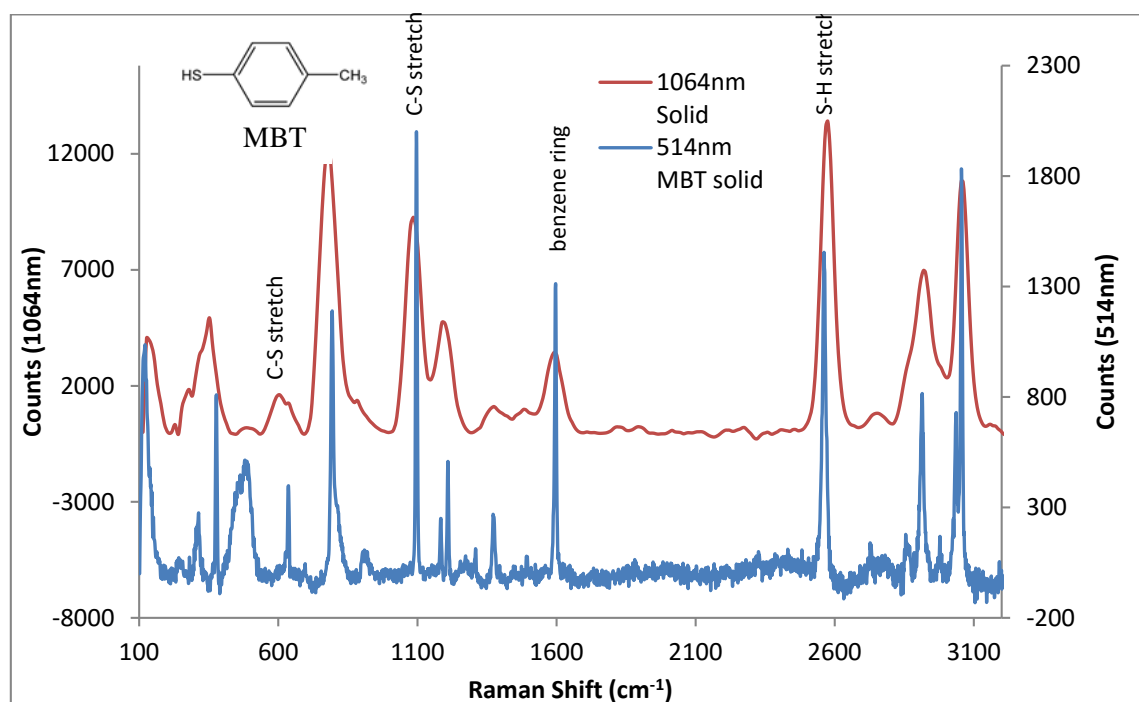
Figure 4.10: 514nm and 1064nm Raman spectra to show Raman peaks of the bulk MBT (98%). 1064nm Raman spectra offset for clarity.

Table 4.5: 514nm and 1064nm Raman Spectra corresponding peaks (cm^{-1}) for control solid MBT.

514nm MBT solid	1064nm MBT solid	Peak Assignment
119		Lattice vibrations in Crystal
377	347	CC bending
483		Out-of-ring bending
	599	C-S stretch
637 794	779	CH out-of-plane deformation
904		CH2 out-of-plane wag
1184 1097	1086	C-S stretch
1210 1309	1197	CC stretch
1373	1371	CH$_3$ symmetric deformations
1597	1592	Carbon ring stretch
2562	2568	SH stretch
2869 2914 2978	2918	CH$_3$, CH$_2$, antisymmetric or symmetric stretching respectively or OH stretch
3036 3056	3059	=C-H stretch

The native and chemically etched variants of silver wire were immersed in 1mM MBT and left for a minimum 12-hour period. They were then washed with deionised water 3 times, to remove any MBT that had not bound with the Ag wire surface and dried under ambient conditions before testing with both 514nm and 1064nm Raman.

The 514nm spectra for both non-heated and heated chemical silver wire variants show spectra resembling that observed by the MBT control with two distinct sharp peaks that correlate with C-S stretch and ring stretch (Fig. 4.10). An additional C-S stretch is also present in all the spectra except heated 30s $NH_4OH+10s$ HNO_3 Ag wire, shown by a small peak around $622cm^{-1}$ (Table 4.6). Therefore, one could successfully determine SERS enhancement of the Ag wire for MBT.

The Ag wire variants with 1mM MBT spectra show non-heated variants of the Ag wire have higher intensity than that of the heated alternative (Fig. 4.11). In the non-heated Ag wire series, 30s $NH_4OH+10s$ HNO_3 chemical treatment showed the highest enhancement of MBT with untreated wire showing lowest (Fig.4.11a). Whereas in the heated alternative, 30s $NH_4OH+10s$ HNO_3 Ag wire again had the highest SERS enhancement and 30s NH_4OH+ 2m HNO_3 showed the lowest SERS enhancement (Fig.4.11b).

The low enhancement shown by the 30s NH_4OH+ 2m HNO_3 Ag wire for both heated and non-heated versions with 1mM MBT was interesting when observing its morphology and interferometer results (Figs 4.2; 4.7 & Table 4.2; 4.3). As the chemical treatment on Ag wire was shown to have a high roughness values and uniformity. When comparing with the 30s NH_4OH+ 10s HNO_3 Ag wire for both treatments that showed the highest SERS enhancement, this too showed high uniformity of roughness upon its surface however the roughness values were lower than the aforementioned wire. It can be hypothesised that there is a limit to roughness upon the surface and that 30s NH_4OH+ 2min HNO_3 is out of that range.

The increased roughness also shown by 30s NH$_4$OH (Fig.4.5 & Table 4.3) with heat treatment does not correspond with increased SERS enhancement, which would be assumed with increased roughness features on the surface, therefore the characteristic protrusions developed with the use of HNO$_3$ appear imperative for causing increased SERS activity upon the surface (Fig. 4.11b).

For Raman spectroscopy, particular wavelengths have specific resonance with particular molecular bonds. The use of 514nm wavelength shows resonance within the visible range whereas 1064nm wavelength shows resonance in the near infrared region (Horiba Scientific, 2015). The alternate regions of resonance provide the ability to scatter different molecular bonds to produce Raman peaks. SERS substrates currently are optimised for use with certain wavelength ranges and the provision of a broadband SERS substrate would be beneficial for a universal lab-on-a-chip device (Zhang et al, 2015). Therefore, the fabrication of a SERS substrate that provides enhancement for both 514nm and 1064nm would be highly desirable for further research purposes and commercial use.

When the chemically etched silver wires with 1mM MBT were tested with 1064nm Raman, the results showed promise for a broadband SERS substrate. Ag wire variants for both the non-heated and heated series showed MBT Raman shift signature peaks, for C-S stretch and Ring stretch within the same ranges shown with 514nm Raman as well as an additional S-H stretch around 2570cm^{-1} (Table 4.6).
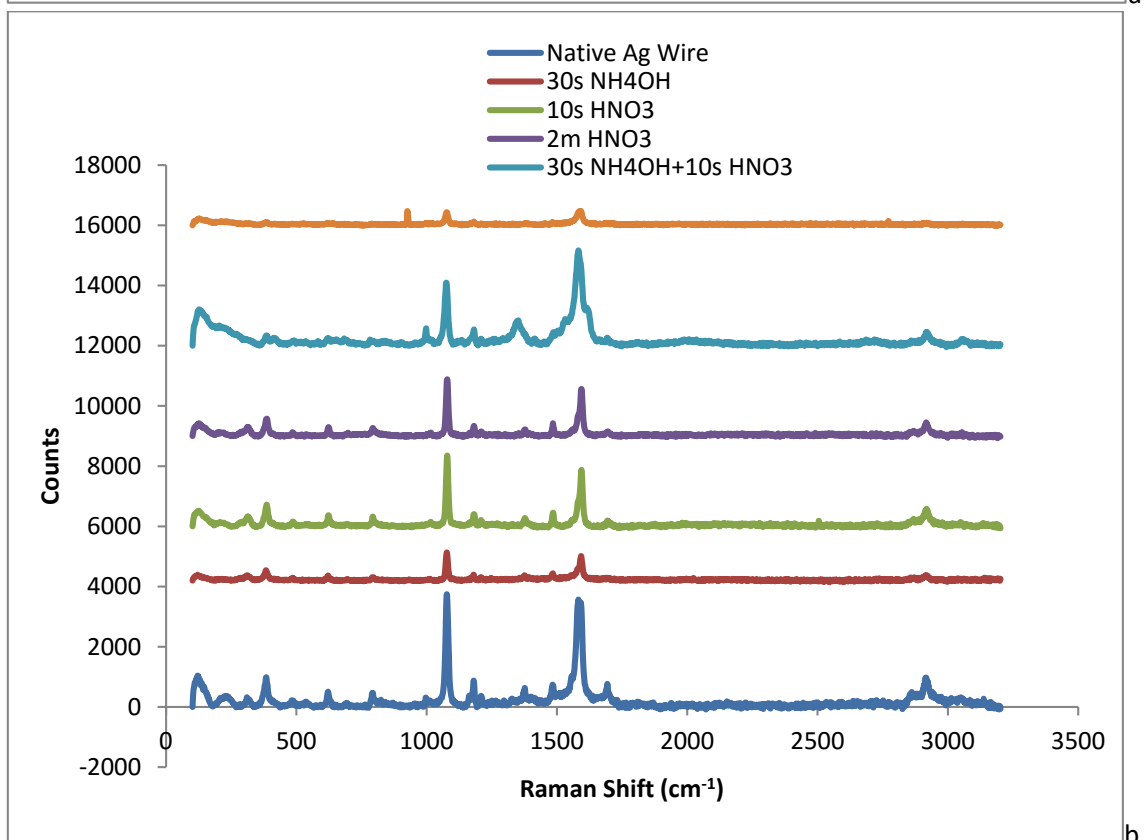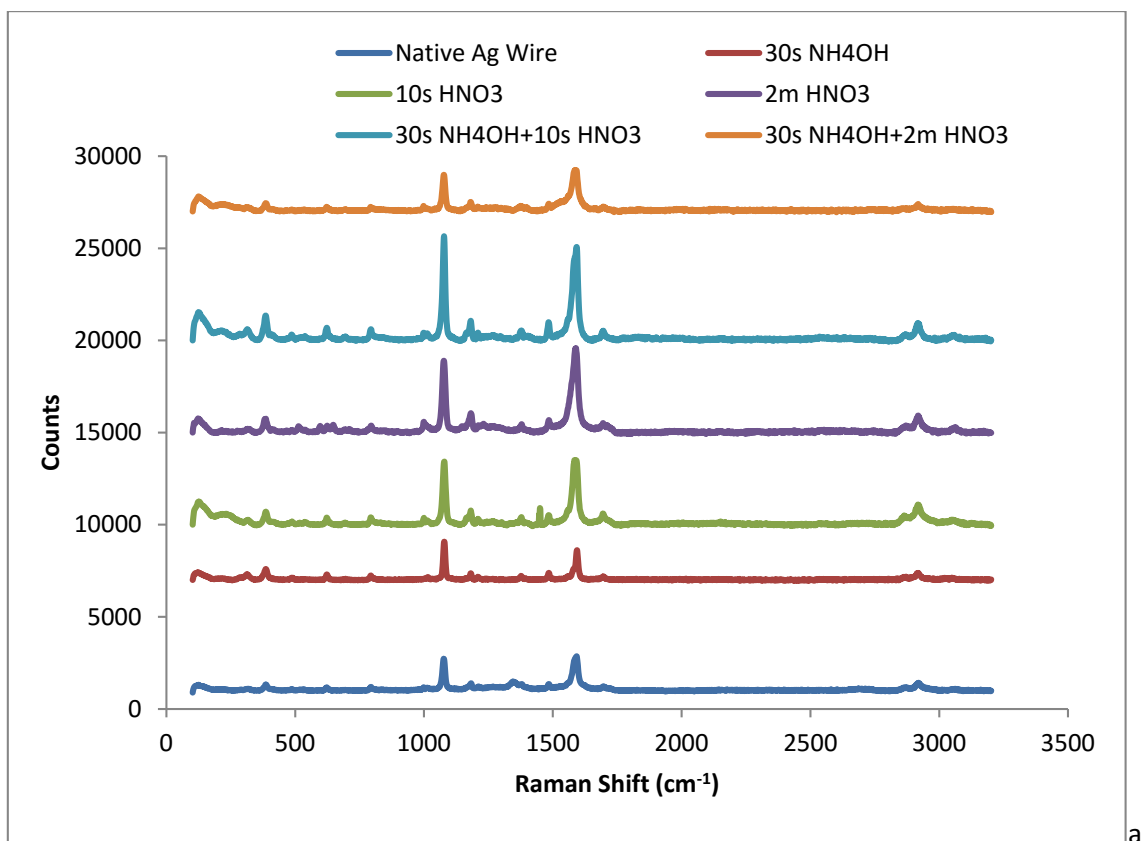
Figure 4.11: 514nm Raman spectra for the native and chemically treated Ag wires with 1mM MBT: a) non-heated, and b) heated. Spectra offset for clarity.

The non-heated chemically etched wire which used HNO_3 at 10s, 2min or 30s NH_4OH+10s HNO_3 showed peaks for MBT. With all three variants showing similar MBT peak intensities and Ag wires chemically treated with 10s or 2m HNO_3 showing the additional S-H peak within the spectrum (Fig. 4.12a & Table 4.6). Non-heated, native Ag wire showed no peaks for MBT, whereas 30s NH_4OH and 30s NH_4OH+2m HNO_3 showed peaks for MBT however at very low intensity.

The addition of heat with chemical treatment caused an alteration in the SERS activity for the Ag wire variants. All the wires did show a peak for MBT, however when observing the graph, native, 10s HNO_3 and 2m HNO_3 Ag wires showed the characteristic MBT spectrum, with 10s HNO_3 showing the highest intensity (Fig. 4.12b & Table 4.6).

When comparing the MBT peaks exhibited within the 1064nm spectrum for wires compared to solid MBT at 1064nm (Table 4.5) the results show that non-heated 30s NH_4OH+ 10s HNO_3 has the closest Raman shift (cm^{-1}) values for C-S and ring stretch peaks to the control.

The results indicate that there is a threshold peak roughness range required to produce an effective broadband SERS substrate. Non-heated Ag wire with 30s NH_4OH+ 10s HNO_3 treatment, concurred the most positive results with both 514nm and 1064nm wavelengths, whereas 30s NH_4OH+2m HNO_3 Ag wires showed a decrease in SERS activity at odds with its increased roughness and uniform surface morphology.
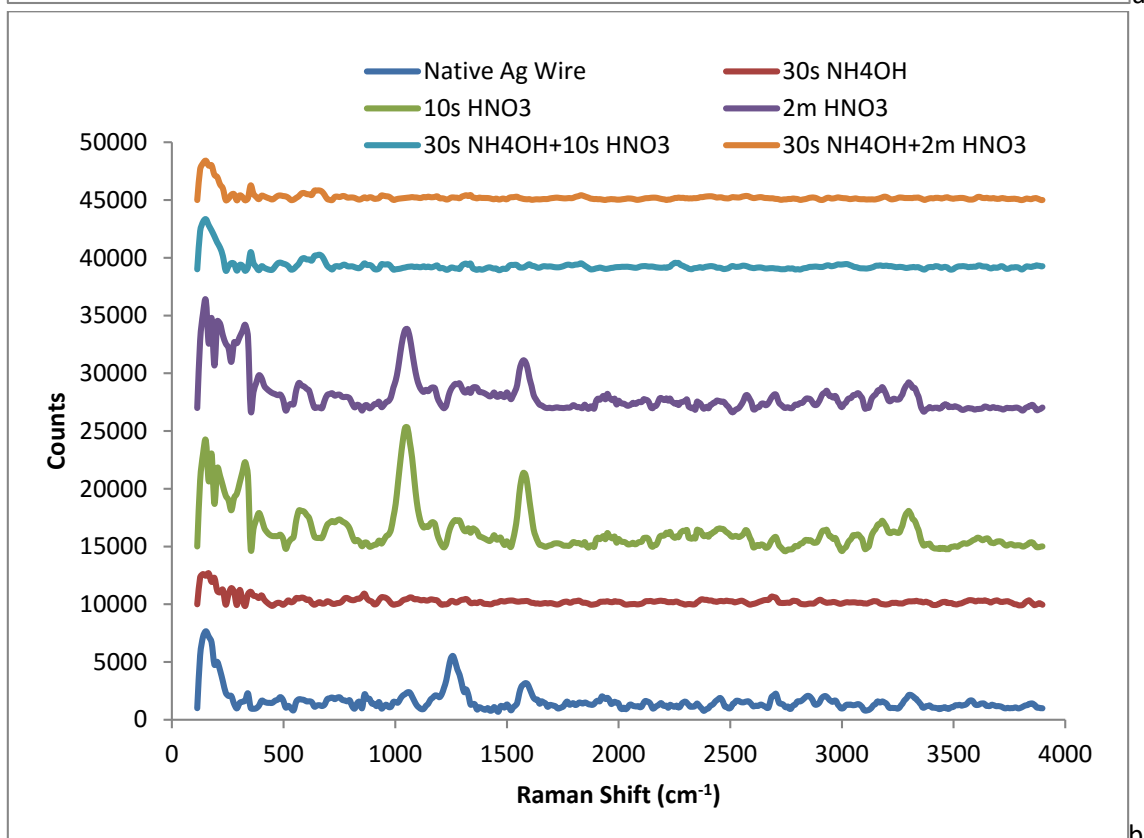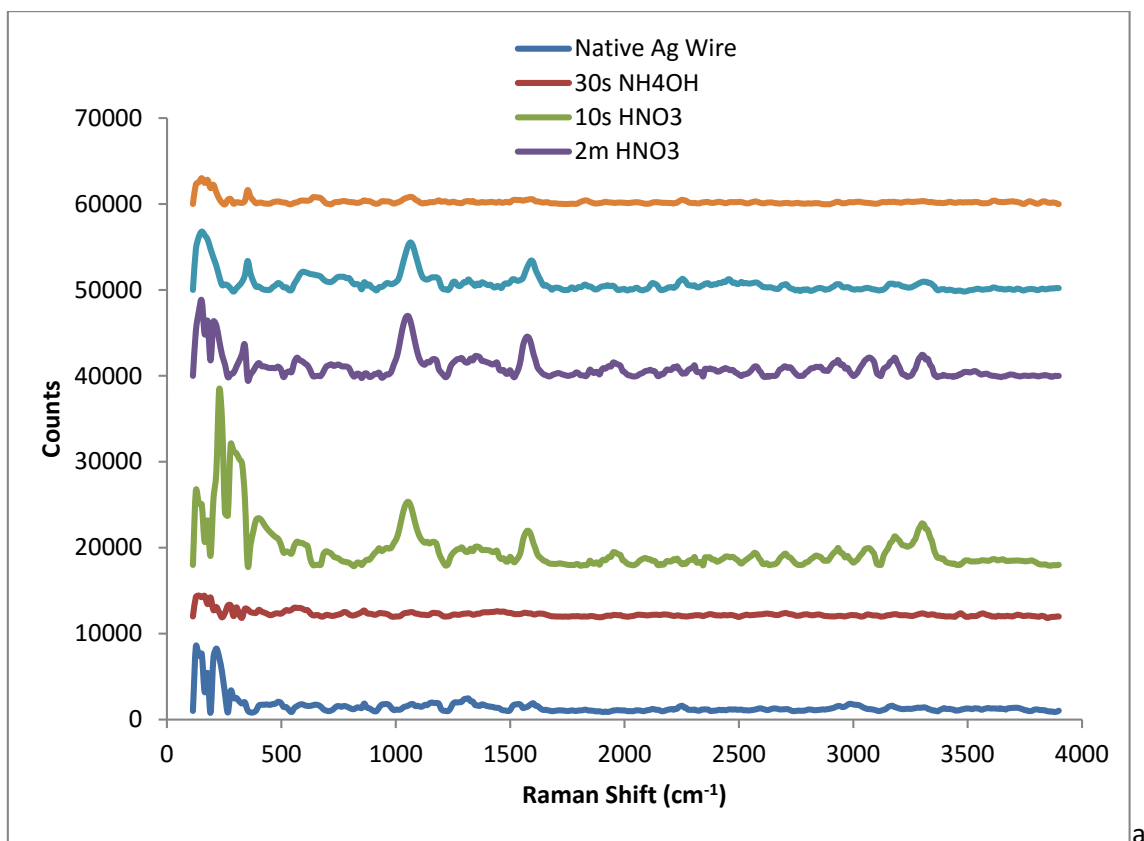
Figure 4.12: 1064nm Raman spectra for the native and chemically treated Ag wires with 1mM MBT: a) non-heated, and b) heated. Spectra offset for clarity.

Table 4.6: Raman peaks (cm^{-1}) and their corresponding bond assignments with regards to MBT definitive peaks on the 514nm Raman spectra for the different Ag wires.

Non-heated						Heated						Peak Assignment
Native	30s NH$_4$OH	10s HNO$_3$	2m HNO$_3$	30s NH$_4$OH + 10s HNO$_3$	30s NH$_4$OH + 10s HNO$_3$	Native	30s NH$_4$OH	10s HNO$_3$	2m HNO$_3$	30s NH$_4$OH + 10s HNO$_3$	30s NH$_4$OH + 10s HNO$_3$	
622	623	623	598 624 647	622 696	621	621	623	623	624	684		C-S stretch
1077	1078	1078	1077	1077	1077	1078	1077	1079	1079	1076	1078	C-S stretch
1484 1588 1592	1485 1594	1485 1587	1484 1588	1484 1587	1484 1586	1485 1586	1483 1593	1485 1594	1485 1594	1584	1592	Ring stretch or COO- antisymmetric stretch

Table 4.7: Raman peaks (cm^{-1}) and their corresponding peak assignments on the 1064nm Raman spectra for the different Ag wires with 1mM MBT

Non-heated						Heated						Peak Assignment
Native	30s NH$_4$OH	10s HNO$_3$	2m HNO$_3$	30s NH$_4$OH + 10s HNO$_3$	30s NH$_4$OH + 2m HNO$_3$	Native	30s NH$_4$OH	10s HNO$_3$	2m HNO$_3$	30s NH$_4$OH + 10s HNO$_3$	30s NH$_4$OH + 2m HNO$_3$	
	576.871		568.214	595.881 626.132 757.093	652.387 773.046			581.391	568.742	655.92	657.345	*C-S stretch*
		1052.77	1050.15	1062.49	1066.31	1058.73		1049.56	1049.15			*C-S stretch*
1595.63		1573.5	1575.28	1591.5	1521.23 1594.1	1582.5		1576.97	1576.36	1599.58		*Ring stretch*
		2570.33	2571.07									*S-H stretch*

4.5. Chapter Summary

Ag wires were roughened with chemical treatments, were characterised for their surface features, and efficacy as SERS substrates was evaluated. The material proved to be quite robust and quick to roughen, through the use of chemical treatments with NH_4OH and/or HNO_3. Specifically, flattened 0.125mm diameter Ag wires were treated for 30s in NH_4OH, 10s or 2m in HNO_3 and combinations of 30s NH_4OH followed by 10s or 2m HNO_3. All the resulting chemically etched Ag wires were also tested with and without heat treatment, $130^{\circ}C$ for 1 hour.

SEM and Interferometry were utilized to visualize and quantify the roughness on the different test Ag wires. The base Ag wires had inherent roughness, but with uneven surface features. NH_4OH predominantly smoothened the surface, while HNO_3 treatments produced flake-like structures on the surface. The interferometer results, gave quantitative results for the surface morphologies, with the roughness parameters; R_t (PV), R_p, R_v, R_q(RMS) and R_a. The roughness obtained by the different chemical etching treatments were in the microscale, consisting of valleys and peaks (maximum peak to valley distance ranging between 10 and 16µm). The highest values for Ag wire within the chemical etching treatment variables showed that the use of 10s HNO_3 on Ag wire had the highest R_t of 14.63±2.09µm but 30s NH_4OH+2m HNO_3 was shown to have the highest R_q value of 1.95±0.41µm as well as the R_a value 1.39±0.30µm. These results indicated that 10s HNO_3 provided the most roughened surface, with the highest peaks and valleys, however with the use of NH_4OH and increased immersion time with HNO_3 of 2 minutes, the Ag wire became more uniform in roughness, with increased peaks present upon the surface at closer proximity to one another, thus higher R_a and R_q values. The addition of heat was

110

shown in SEM and interferometer results to cause a slight decrease in protrusions present upon the surface and rounding of sharp features at the tips of the metal protrusions, essentially, smoothening the Ag wire surface. Moreover, there were no obvious differences in chemical composition between the different chemical treatments as well as their heat treated counterparts, as evident from the EDX spectra. In agreement with elemental peaks observed on EDX spectra, SERS peaks observed with the different test Ag wire on their baseline SERS spectra were that of hydrocarbon contaminants on the Ag wire surface.

The SERS efficacy of the different test Ag wire variants, was then tested for their SERS spectra after treatment with 1mM MBT (model Raman active molecule). The covalent grafting of MBT on the Ag SERS substrates, through the spontaneous reaction of the thiol group on MBT with Ag metal, was confirmed by the presence of C-S stretch ($598cm^{-1}$, $1085cm^{-1}$) and C-C ring stretch ($1592cm^{-1}$) peaks and the absence of the free S-H stretch ($2561cm^{-1}$) peaks on the SERS spectra, recorded using 514nm and 1064nm laser Raman spectrometers. The SERS spectra for MBT were observed for all test Ag wire variants with 514nm Raman, while that with 1064nm was typically only observed with HNO_3 treated Ag wires. Heat treated test Ag wires, typically gave lower peak intensities for the different MBT peaks, when compared to their non-heated counterparts. The highest intensity for the SERS peaks for MBT were observed with non-heated 30s NH_4OH + 10s HNO_3. Despite their higher roughness as indicated by the R_q (RMS) roughness of 1.95±0.41µm, 30s NH_4OH + 2m HNO_3 treated Ag wires gave lower SERS intensity with both 514nm and 1064nm Raman compared to the 30s NH_4OH + 10s HNO_3 treated Ag wire that has similar flake-like surface morphology. This result indicated that it was not the roughest surface, but a threshold inter-surface feature distance that is important for providing best SERS enhancement.

To conclude, sharp protrusions on the surface, with specific distance from one another, appear to control hot-spot formation as well as demonstrate 'broadband' SERS characteristics of the substrate by working at two different wavelengths. 30s NH_4OH + 10s HNO_3 treatment provided an optimum surface morphology for SERS enhancement. This study has shown that a less energy intensive and time consuming methodology through the use of chemical etching can be used for fabrication of planar metallic (Ag) SERS substrates.

Chapter 5: SERS Substrate Design: Ag and Au Nanoparticles prepared within microemulsions

5.1. Introduction

Owing to their anisotropic shapes and sizes, metal nanoparticles (NPs) offer versatility to SERS substrate design and use within compact, minimised equipment, such as within lab on chip devices. Bantz et al. (2011) reported that the SERS activity of spherical Ag NPs decreased by 10-fold when analytes were 2.8nm away from the Ag NP surface. Methods for SERS substrate design to enable increased enhancement of analytes at larger distances and for larger molecules was obtained through either spacing the spherical Ag NPs close to one another; the SERS activity was enhanced for a distance up to 50nm from the Ag NP surface (McNay et al, 2011; Stiles et al, 2008). Also through the addition of perpendicular components on the metal NP by way of anisotropic shapes and increased size, as well as their proximity to one another, these changes were predicted to cause enhanced electromagnetic intensity over longer distances away from the NP surface. This is beneficial for testing larger sized and a wider library of analytes with significantly better SERS sensitivity and enhancement. Hence, a key objective for our research was to prepare Au and Ag NPs of anisotropic shapes (non-spherical) and larger sizes (≥30nm), and test their efficacy as SERS substrates.

Metal NPs are commonly synthesized by bottom-up chemical methods, wherein, aqueous metal salts are boiled and a reducing agent is slowly added to the mixture. Often, these mixtures are refluxed for several hours to weeks to obtain metal NPs. However, the yield is usually low, and the method is lab and energy intensive. Moreover, for long term storage, these metal NPs require stabilization with surfactants, e.g., sodium citrate, to maintain their size and integrity.

Another bottom-up approach for metal NP synthesis uses microemulsion systems. This method is rapid (seconds to minutes), achieved at room temperature, requires little equipment, low reactant volumes and cost-effective. In addition, the microemulsion compositions provide

versatility in controlling size and shape of the NPs, stability of dispersion of NPs and aid in their long-term storage (Sanchez-Domiguez et. al.).

Although microemulsions have been used for NP synthesis since the 1970's (Eastoe et al, 2006) as of yet the fabrication of ideal nanoparticles for individual research aims relies heavily on a trial and error methodology, with literature defining how to produce larger nanoparticles with altered shapes found to be not fully repeatable (Uskokovic & Drofenik, 2005). There have been 7 parameters that are highlighted for controlling size and shape of nanoparticles within the microemulsion methodology; surfactant, co-surfactant, solvent, W number, precursor concentration, reducing agent and electrolyte (Eastoe et al, 2007). The specific aim of this chapter was to evaluate the effect of these 7 parameters in tailoring the anisotropic shapes and sizes greater than 30nm of Au and Ag NPs within microemulsions for SERS substrates. The prepared Au and Ag NPs were characterised using TEM and UV-Vis spectroscopy. The different compositions for the microemulsions evaluated in this study are listed in Table 5.1.

Table 5.1. Components tested of different microemulsion system parameters for the synthesis of Au or Ag NPs of different shapes and sizes.

	Parameter	Components
1	Surfactant	AOT, CTAB
2	Cosurfactant	Butanol
3	Solvent	IPM, Cyclohexane
4	Precursor Concentration	0.1-4.1M
5	Reducing agent	Hydrazine, Ascorbic acid, NaBH$_4$
6	Electrolyte	1mM NaCl
7	W number	0-12

5.2. Gold and Silver nanoparticles in the AOT/IPM microemulsion system

A typical microemulsion system is composed of a surfactant, a solvent (oil) and water. I utilised a simple microemulsion system consisting of the surfactant AOT and the solvent IPM, for the synthesis of Au or Ag NPs. AOT was first dissolved in IPM at a concentration of 0.1M, using an ultrasonic bath. The clear solution was then used to prepare two separate microemulsion systems.

The first system had the metal salt precursor and the second system had the reducing agent. The salt precursors were either HAuCl$_4$ (0.56M) or AgNO$_3$ (1.77M), and the reducing agent was hydrazine hydrate (40mM). Both the salt precursors and reducing agents were prepared in deionised water. The metal salt containing microemulsion was mixed with that containing the reducing agent to prepare the nanoparticles. As soon as the two microemulsions were mixed, the colour changed instantaneously. For the Au NPs the colour was wine red and for Ag NPs it was dark yellow. Colour change is indicative of nanoparticle presence in the microemulsions, which was evident from their typical absorption peaks - Au (500-600nm) or Ag NPs (400-500nm) - in their respective UV-Vis spectra (Fig 5.1).
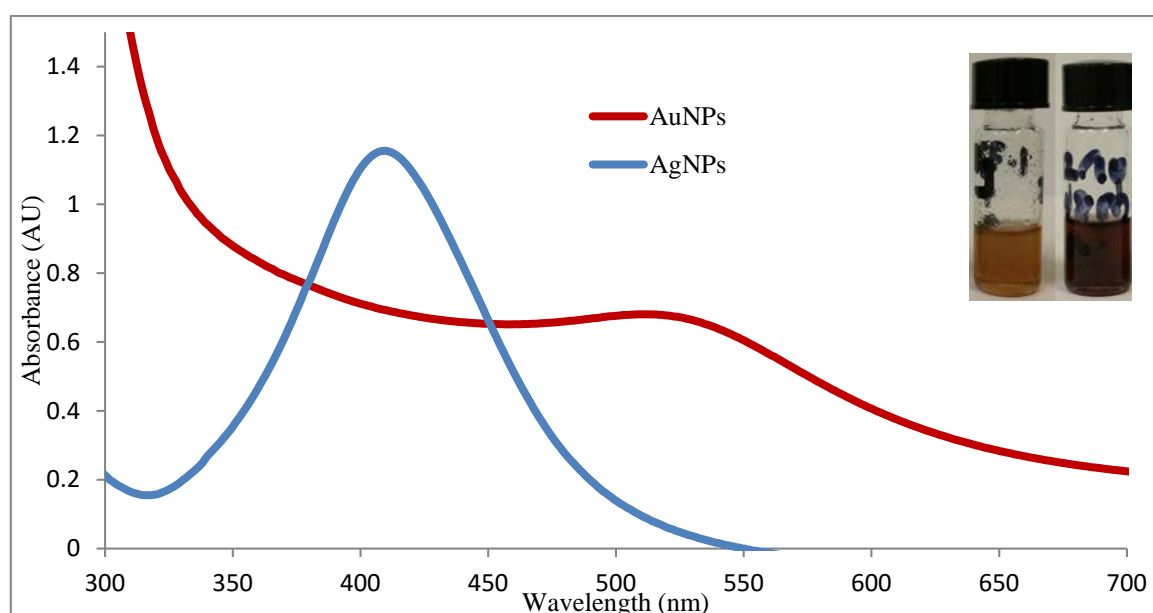
Figure 5.1: UV-Vis spectra for the Au and Ag NPs prepared using AOT/IPM microemulsion with precursor concentrations of 0.56M for HAuCl$_4$ and 1.77M for AgNO$_3$, 40mM hydrazine and a W number of 1.

The nanoparticles were visualized under TEM, and their size measured on the TEM images using Image J software. Figure 5.2 shows the TEM images and their corresponding NP size distribution histograms. Both Au and Ag NPs were spherical and had average diameters of 5.1nm and 10.1nm respectively. The NP sizes ranged from 2.4-8nm for Au NPs and 3.7-27.6nm for Ag NPs. The sizes for both Au NPs and Ag NPs were less than the desired >30nm, and had spherical shape. However, the higher precursor concentration for AgNP preparation gave larger sized NPs. So, potentially,

increasing the precursor concentrations could yield larger NPs. Hence we looked at increasing precursor concentration to investigate its effect on NP size.
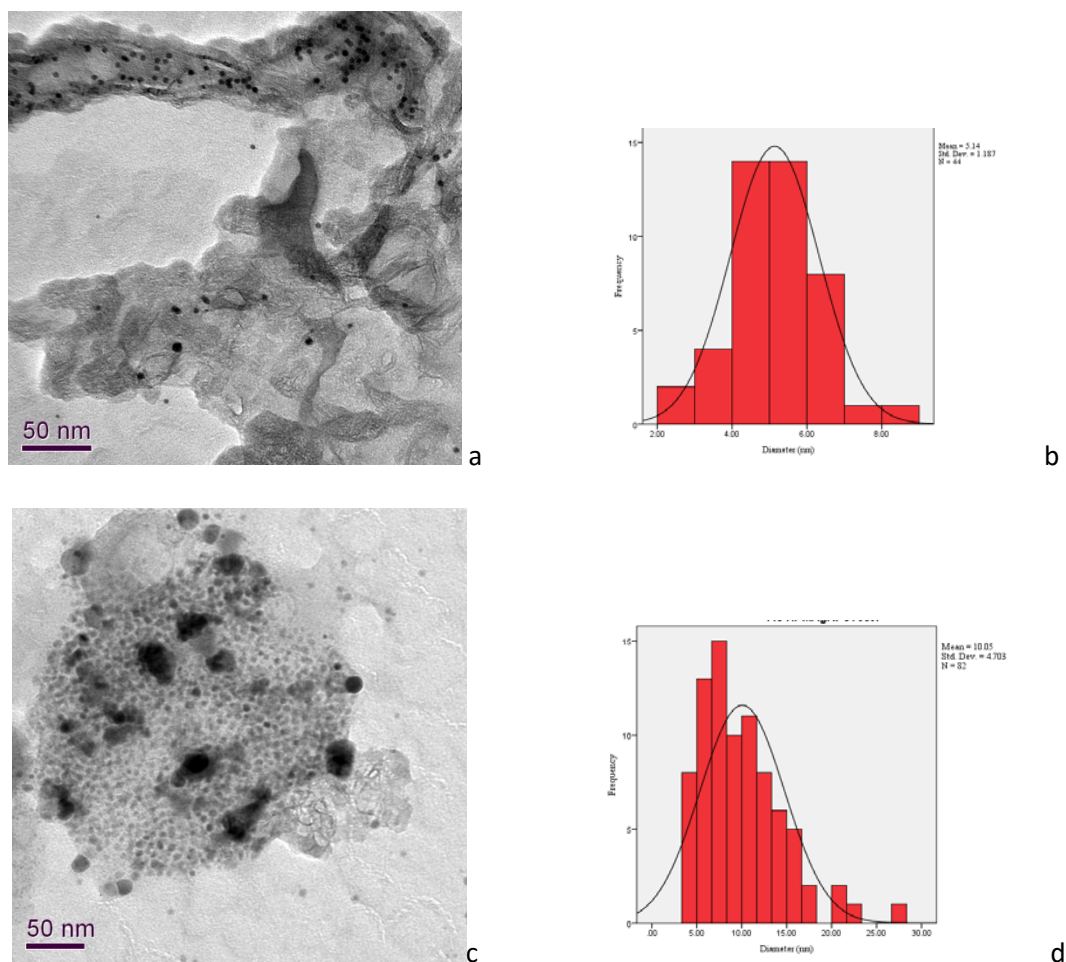
Figure 5.2: TEM images (a&c) and the corresponding NP size distribution histograms (b&d) for the Au (a&b) and Ag NPs (c&d) prepared using AOT/IPM microemulsion with precursor concentrations of 0.56M for HAuCl$_4$ and 1.77M for AgNO$_3$, 40mM hydrazine and a W number of 1.

5.3. Precursor Concentration

Precursor concentration on NP size was analysed using 0.1M AOT in IPM, a W number of 1 (0.1M water), and 40mM hydrazine, the precursor concentration for HAuCl$_4$ and AgNO$_3$ was varied at 0.29M, 0.59M, 1.18M, 1.77M and 4.12M solutions in water. The intensity of the yellow and red colour of the resulting Ag and Au NPs respectively in microemulsions increased with increase in

precursor concentration. This increase was reiterated with the increase in the absorption peak for the Ag and Au NPs in the UV-Vis spectra (Fig 5.3a&b).

Typically, the absorption peak for the NPs would shift to longer wavelengths with increased size. However, with increased precursor concentration, we did not see an increasing trend. The absorption peaks for Ag NPs were in the range of 404-412nm, with 0.29M showing 412nm, while 1.18M showed 404nm. This indicated that increasing precursor concentration did not have the desired effect of increase in Ag NP size. This was further confirmed with the UV-Vis results for Au NPs where the absorption peaks were in the range of 507-526nm, with 0.59M showing 526nm, while 1.77M showed 507nm. TEM images and NP size distribution histograms for the Ag NPs prepared using the precursor concentrations of 0.29M, 1.77M, and 4.12M are shown in Fig. 5.2c&d and 5.4, support that the precursor concentration did not significantly influence NP size.

Irrespective of the precursor concentration the Ag NPs were spherical with sizes close to 10nm. Specifically, the size ranges were 7.2-11.6nm (average of 9.1nm), 3.7-27.6nm (average of 10nm) and 3.9-14.2nm (average of 7.2nm) for 0.29M, 1.77M and 4.12M respectively. Essentially, the concentration of hydrazine was used in excess compared to the precursor concentrations. This potentially was causing an increase in the number of nucleation sites for Ag NPs. To confirm this hypothesis, we next looked at varying the reducing agent (hydrazine hydrate) concentration, while keeping other parameters constant.

5.4. Reducing agent Volume

Reducing agent concentration was varied to study its effect on the size of Au and Ag NPs, while having 1.77M $HAuCl_4$ or $AgNO_3$, 0.1M water and 0.1M AOT in IPM in the AOT/IPM microemulsion system constant. The reducing agent (hydrazine hydrate) concentrations tested were 8mM, 40mM and 80mM.
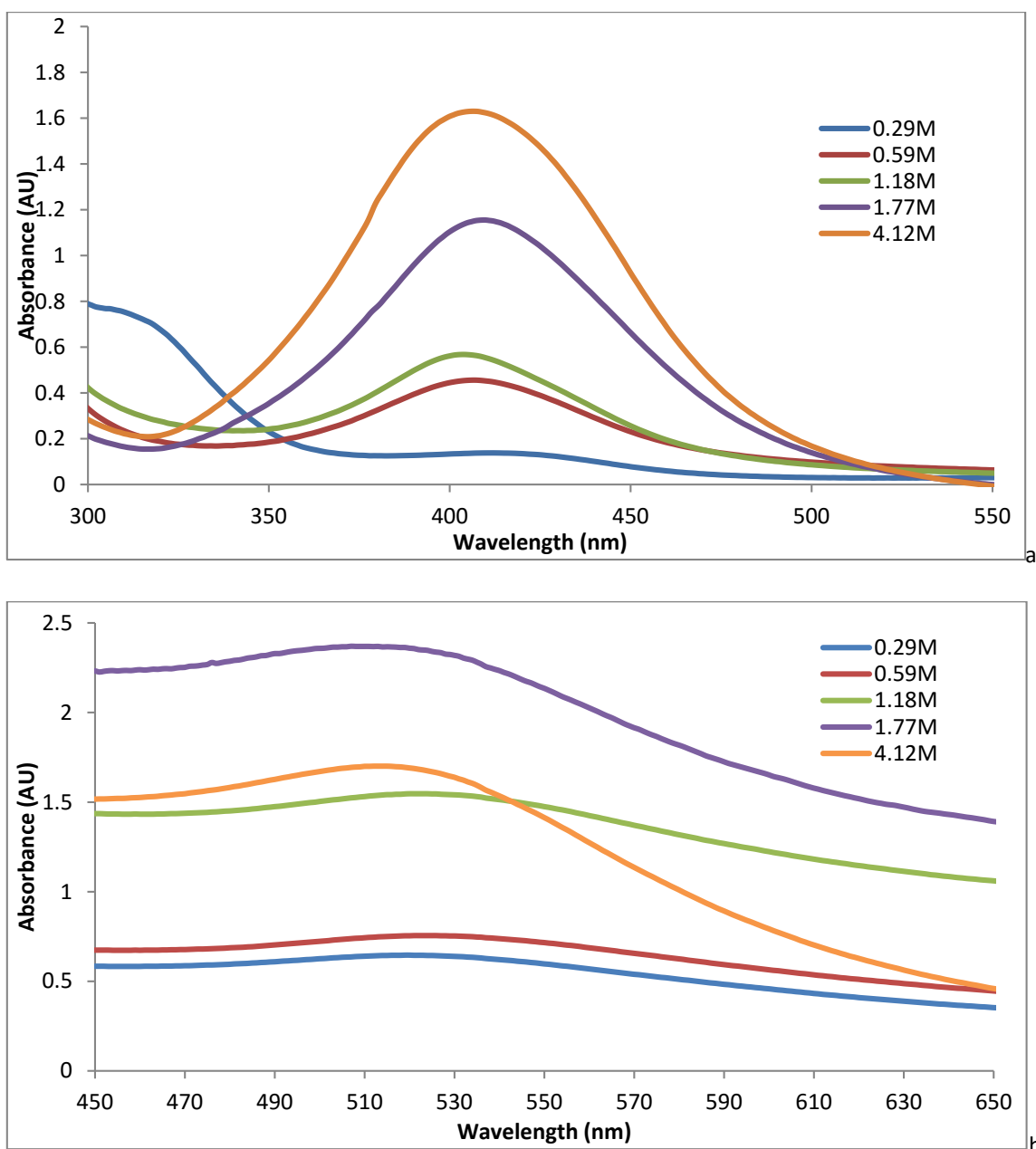
Figure 5.3: UV-Vis spectra for a)Ag and b)Au NPs prepared using AOT/IPM microemulsion having 0.1M AOT

in IPM, W number of 1 (0.1M water), and 40mM hydrazine, while varying the precursor (AgNO$_3$ or HAuCl$_4$)

concentrations at 0.29M, 0.59M, 1.18M, 1.77M and 4.12M.

The formation of the Au and Ag NPs was evident from the visible colour change and the

intensity of the colour increased with increasing hydrazine concentration. But, there was no

significant difference in colour to naked eye indicating NPs of similar sizes despite difference in

hydrazine hydrate concentrations. The UV-Vis absorption peaks ranged between 507nm to 543nm

for Au NPs and 400nm to 409nm for Ag NPs (Fig. 5.5). However, there was no clear trend in NP size

change with increasing hydrazine concentration. The TEM images and their corresponding NP size distribution histograms for Au and Ag NPs with varied hydrazine hydrate concentration further support that size is not significantly influenced by varying hydrazine hydrate (reducing agent) concentration (Fig. 5.6 & 5.7). The NPs were still predominantly spherical in shape and sizes close to 10nm (smaller than the desired ≥30nm) (Table 5.2).
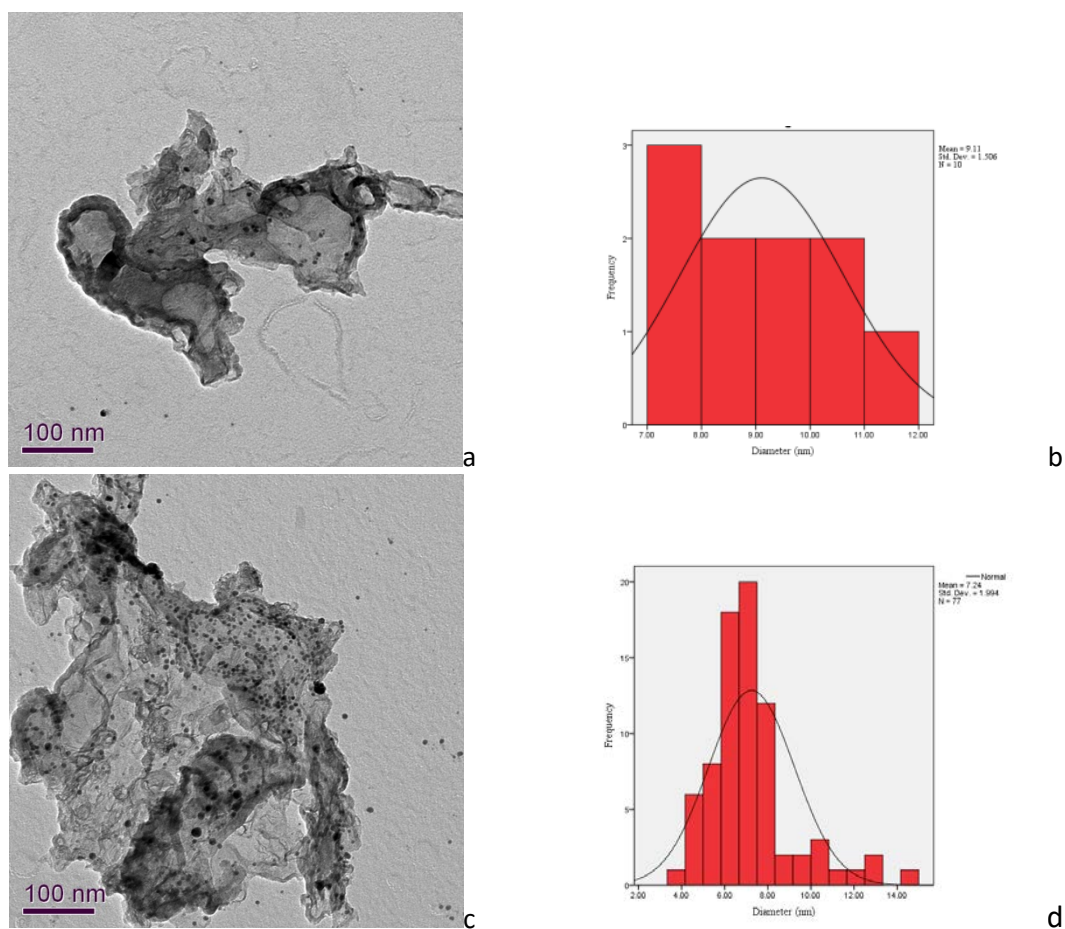
Figure 5.4: TEM images (a&c) and the corresponding NP size distribution histograms (b&d) for Ag NPs prepared using AOT/IPM microemulsion having 0.1M AOT in IPM, W number of 1 (0.1M water), and 40mM hydrazine, while varying the precursor (AgNO$_3$) concentrations at 0.29M (a&b) and 4.12M (c&d).
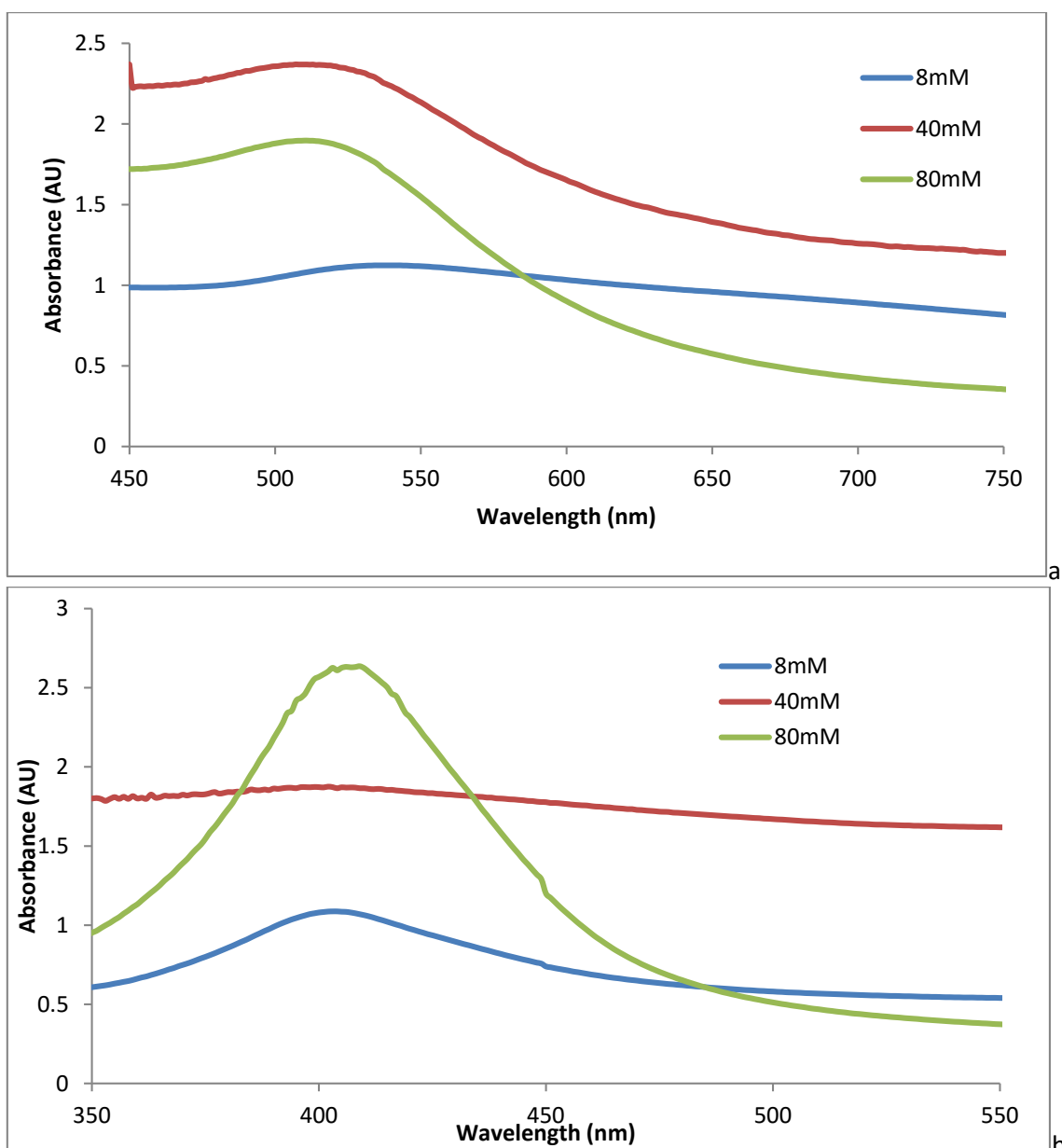
Figure 5.5: UV-Vis spectra for a) Au NPs and b) Ag NPs prepared using AOT/IPM microemulsion having

0.1M AOT in IPM, W number of 1 (0.1M water), and 1.77M HAuCl$_4$ or AgNO$_3$, while varying the reducing

agent (hydrazine) concentrations at 8mM, 40mM and 80mM.

Table 5.2: Nanoparticle sizes as a function of increasing reducing agent (hydrazine) concentration.

Hydrazine Concentration (mM)	Au NPs		Ag NPs	
	Average NP Size (nm)	Size Range (nm)	Average NP Size (nm)	Size Range (nm)
8	7.9	4.9 to 10.6	8.1	2.8 to 18.2
40	5.3	2.4 to 8	10.1	3.7 to 27.6
80	14.4	4.5 to 37.2	9.3	4.5 to 37.2
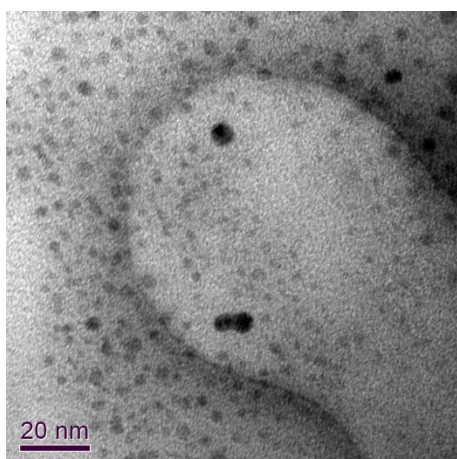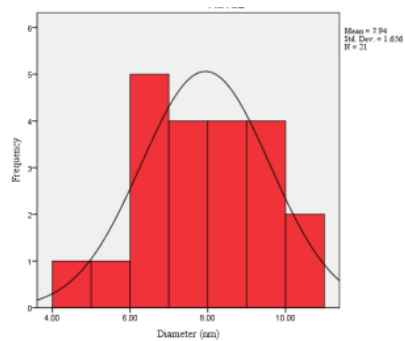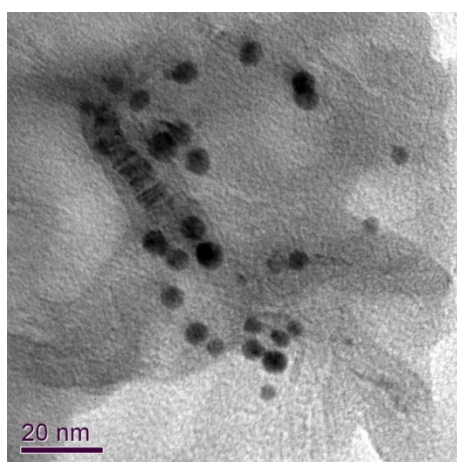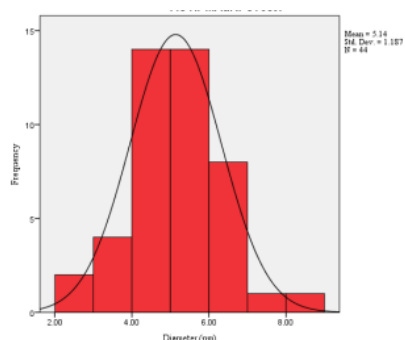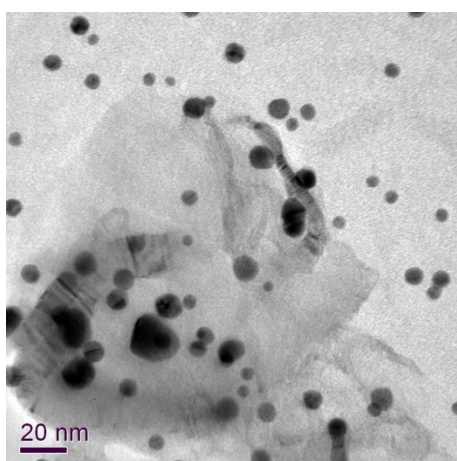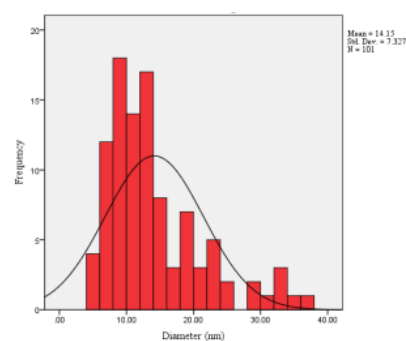
Figure 5.6: TEM images (a,c&e) and corresponding NP size distribution histograms (b,d&f) for AuNPs prepared using AOT/IPM microemulsion having 0.1M AOT in IPM, W number of 1 (0.1M water), and 0.56M HAuCl₄, while varying the reducing agent (hydrazine) concentrations at 8mM (a&b), 40mM (c&d) and 80mM (e&f).
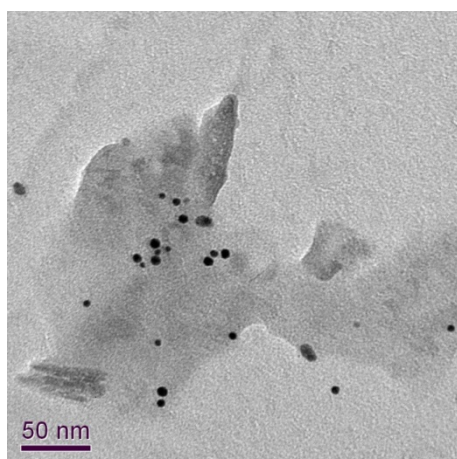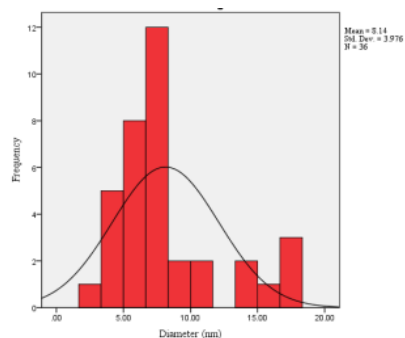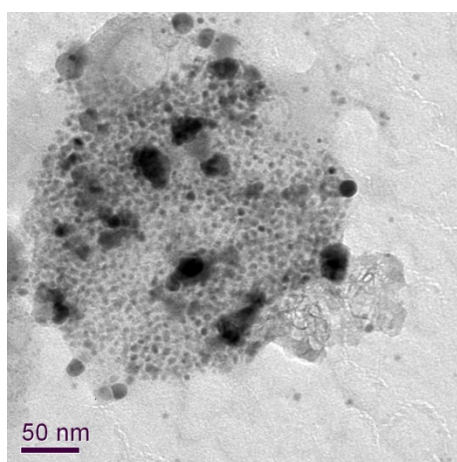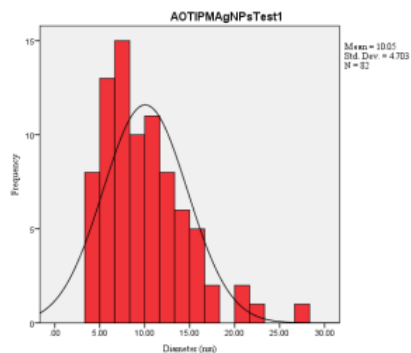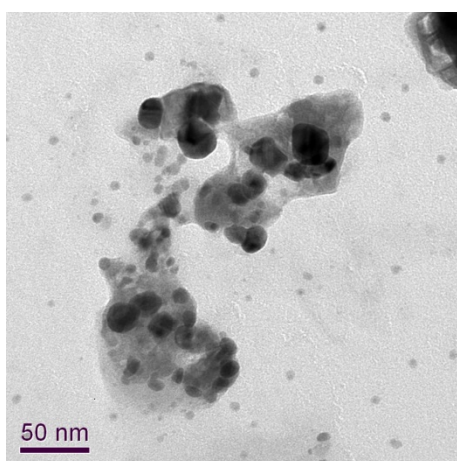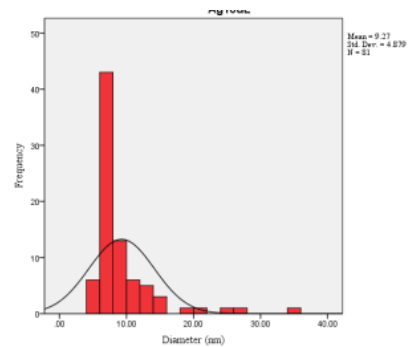
Figure 5.7: TEM images (a,c&e) and corresponding NP size distribution histograms (b,d&f) for AgNPs prepared using AOT/IPM microemulsion having 0.1M AOT in IPM, W number of 1 (0.1M water), and 1.77M AgNO₃, while varying the reducing agent (hydrazine) concentrations at 8mM (a&b), 40mM (c&d) and 80mM (e&f).

5.5. Addition of Co-surfactant

The co-surfactant is an additional amphiphilic molecule, typically with a short-chain structure that is added to a microemulsion system. This addition enables increased rigidity of the inverse micelle structure, through increased curvature and interaction with the water chamber. Butanol (But) was added at a 0.1:1 mass ratio with AOT respectively to produce AOT/But/IPM microemulsions. Au and Ag NPs were synthesised from 1M and 1.77M precursor stock solutions respectively with 40mM hydrazine as the reducing agent. The volume of precursor and reducing agent concentration was then increased from 1µl per ml, which has been used in all previous experiments detailed, to 10µl per ml with 80mM hydrazine hydrate concentration added, to improve the density of NPs for the effect of increasing proximity of NPs to one another, as well as producing increased anisotropy of the NPs within the system, both beneficial characteristics for a SERS substrate. The Ag NP and Au NP microemulsions altered in colour instantly when the reaction began in AOT/But/IPM to form characteristic Red solutions for Au NPs and yellow solutions for Ag NPs.

The UV-Vis results in Figure 5.8 show that NPs are present for both metals; Au NPs (Fig. 5.8a) is shown to have a wavelength of 513mm for 1.77M $HAuCl_4$ concentration which increased in wavelength to 524nm at 1M $HAuCl_4$, therefore for the co-surfactant system as well increased precursor concentration does not cause a linear increase in NP size. When comparing the results of 1.77M $HAuCl_4$ from the AOT/But/IPM system with the AOT/IPM system there is an increase in peak given with the AOT/But/IPM system from 507nm to 513nm respectively. Therefore the addition of the co-surfactant can be predicted as causing an increase in the size of the nanoparticles. With the increased curvature and rigidity of the microemulsion system, being significant for causing an increase in size. For Ag NPs (Fig.5.8b) the peak wavelength is 418nm for 1.77M concentration and 406nm for 1M concentration. When comparing the AOT/But/IPM results for 1.77M with AOT/IPM

at the same concentration there also is a peak shift with an increase in the AOT/But/IPM system from 409nm respectively. Therefore, the use of butanol has enabled an increase in NP size.
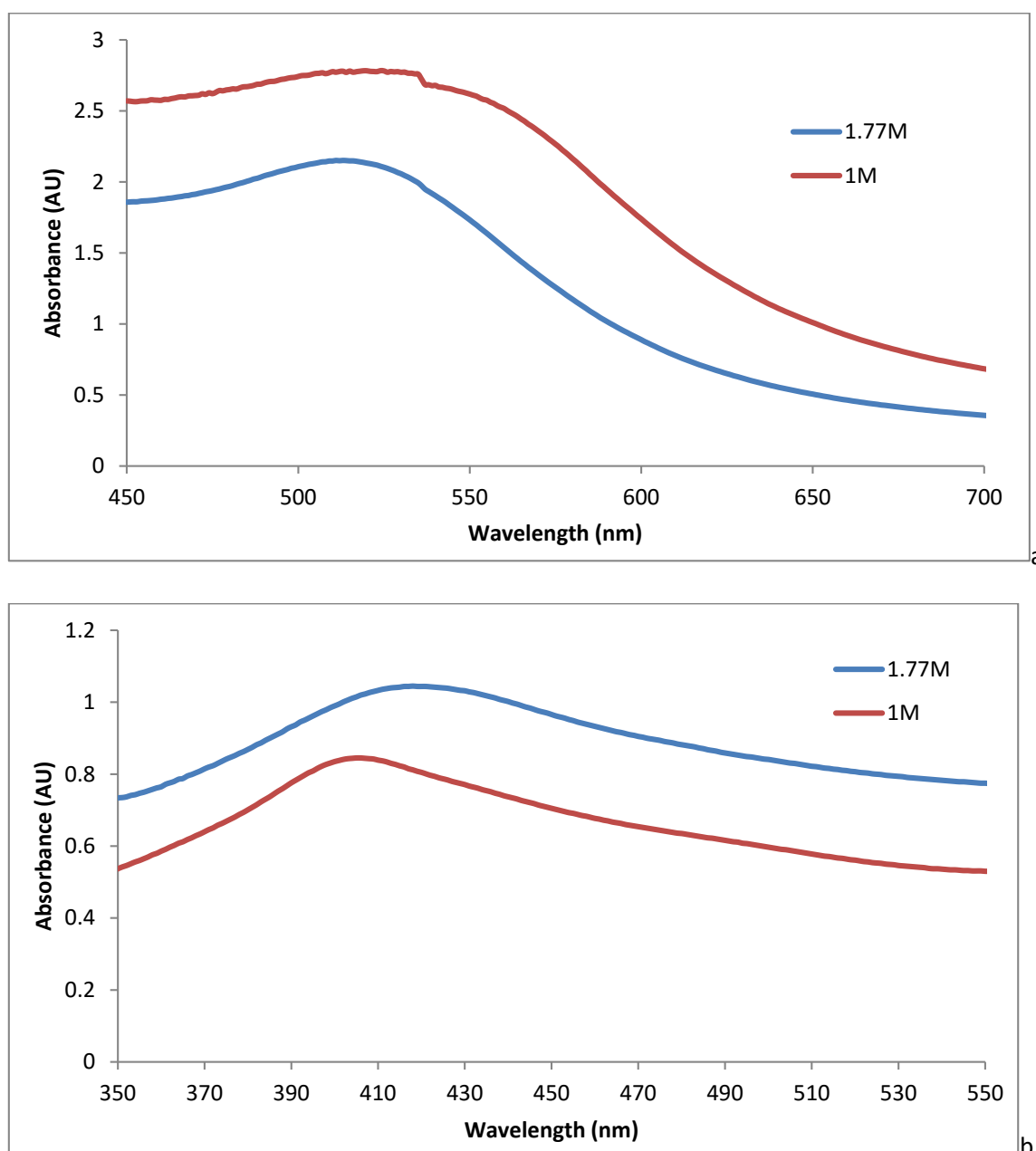
Figure 5.8: UV-Vis spectra for Au(a) and Ag(b) NPs prepared using AOT/But/IPM microemulsion having a W number of 1 (0.1M water), and 1.77M and 1M HAuCl$_4$ or AgNO$_3$ stock solutions with 1µl per ml of Precursor concentration added and 40mM hydrazine.

When the volumes of precursor were increased from 1µl per ml to 10µl per ml of microemulsion solution, the UV-Vis results, Figure 5.9 shows that the absorbance of the NP solutions increases logically due to increased moles of precursors and reducing agent present. However the NP size

does not appear to be affected significantly with increasing volumes of precursor and reducing agents. The UV-Vis spectra for each volume variation for both Au and Ag NPs did not significantly shift to larger values, an indicative marker for larger sized nanoparticle. With 10µl per ml added of 1M $HAuCl_4$ with 80mM hydrazine, Au NPs peak wavelength is now 514nm whereas Ag NPs peak wavelength is 404nm. The W number for the 10µl systems shows an increase in water within the system with a W number between 1-2. The TEM image and correlating NP size histogram in Figure 5.10 supports the increase in NP size and closer proximity of NPs induced with the addition of 10µl per ml of 1M $HAuCl_4$.
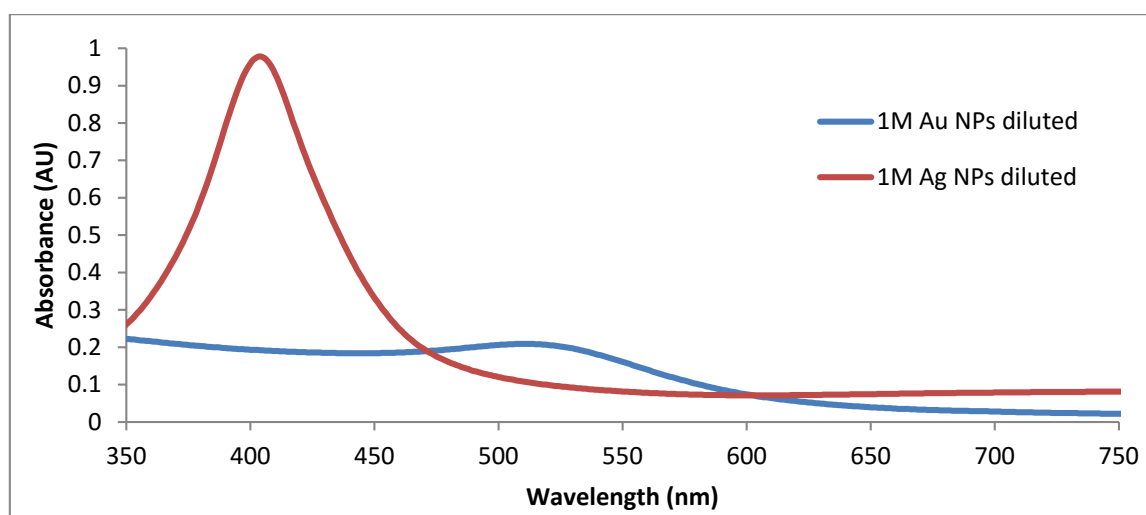
Figure 5.9: UV-Vis spectra for diluted Au and Ag NPs prepared using AOT/But/IPM microemulsion having a W number between 1-2 and 1M $HAuCl_4$ or $AgNO_3$ stock solutions with 10µl per ml of Precursor concentration added and 80mM hydrazine.

The Au NPs show increased proximity to one another, with spherical as well as ansitropically shaped NPs present, with an average NP size of 34.9nm and a range between 5.2-127nm. As co surfactant is shown to alter the size and shape of the NPs within the microemulsions system, to obtain varied NP sizes and shapes that would be beneficial as SERS substrates for testing, alteration in the fluidity of the microemulsion system and thus intermicellar exchange rate for influence of nucleation and growth stages would be of interest for altering size and shape.

<div style="text-align:center">a   b</div>
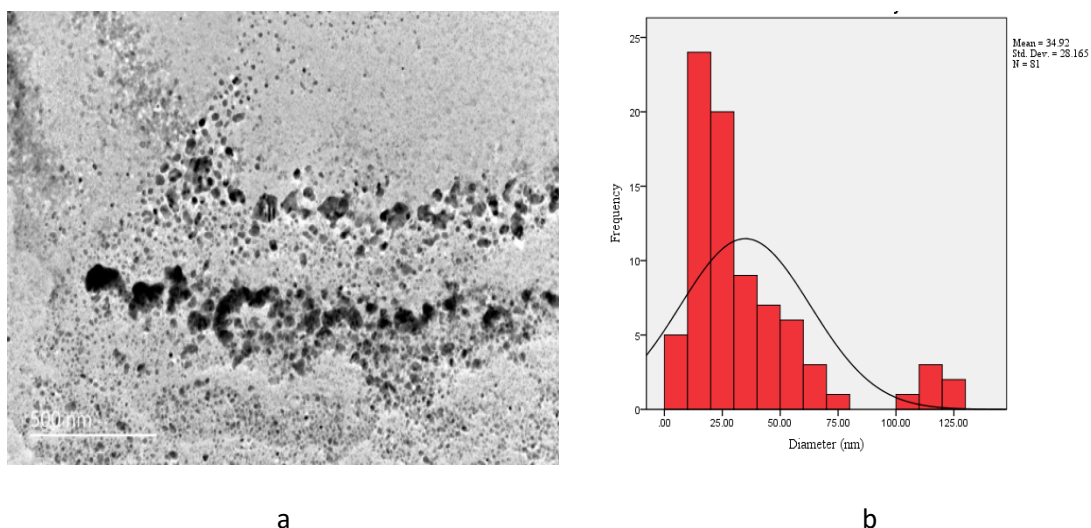
Figure 5.10: TEM image (a) and corresponding NP size distribution histogram (b) for Au NPs from AOT/But/IPM, with a W number between 1-2, 1M HAuCl$_4$ at 10µl per ml and 80mM hydrazine.

5.6. Solvent effect

Different solvents have different chemical structures which interact with the surfactant and co-surfactant in different ways, IPM is a 17 carbon single chain molecule which due to size and structure cause a rigidity to the inverse micelle structure and thus a less dynamic microemulsion system. This causes a particular rate of nucleation and growth and thus could affect the overall maximum size, uniformity and shape of the NPs within the system. With the use of a small aromatic solvent such as cyclohexane (cyclo), there should be increased fluidity within the microemulsion system and a different nucleation and growth rate, for alteration in NP size and shape.

To support this theory, 0.1M AOT with butanol at a 0.1:1 ratio were dissolved in cyclohexane, Au and Ag NPs were prepared from 1M stock, 10µl per ml added with 80mM Hydrazine concentration, the W number was within the 1-2 range. When the solutions were mixed instant colour change occurred, with Au NPs within the AOT/But/Cyclo system turning a dark red colour and for Ag NPs yellow. The UV-Vis results in Figure 5.11 for the effect of solvent on the microemulsion system shows high absorbance for both Au and Ag NPs, with Au NPs having a peak wavelength at 514nm whereas Ag NPs had a peak wavelength at 407nm. Au NPs unlike in the

AOT/But/IPM system had a higher absorbance than Ag NPs. When comparing the results with the same system in AOT/But/IPM the absorbance peaks appear quite similar with Au NPs at 511nm and Ag NPs at 404nm in AOT/BUT/IPM. The TEM image and corresponding NP size distribution histogram, Figure 5.12, support the increase in size and more anisotropic shape when compared with AOT/IPM Au NP systems (Figure 5.6).
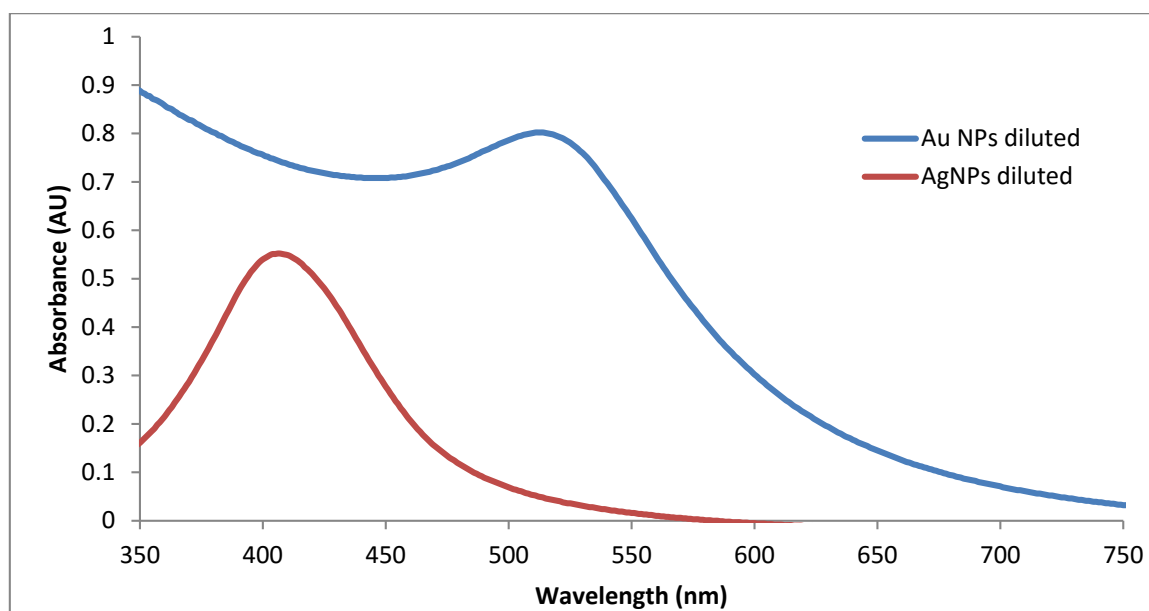
Figure 5.11: UV-Vis spectra for diluted Au and Ag NPs prepared using AOT/But/Cyclo microemulsion having a W number between 1-2 and 1M HAuCl4 or AgNO3 stock solutions with 10μl per ml of Precursor concentration added and 80mM hydrazine.

Anisotropic octagonal and square-like shapes of Au NPs are shown, with an average size of 21.1nm and range between 18.1-23.8nm, one could hypothesise that the presence of these more anisotropic shapes could be due to either the surfactant or the reducing agent. Hydrazine hydrate is a strong reducing agent, with neutral chemical characteristics; therefore, the synthesis of more uniform, typically spherical shapes of small size could be caused by the reducing agent. As of yet, although anisotropic characteristics are developed, the sharp features present on the structure are minimal, therefore the use of a milder reducing agent or one with a charge could alter the growth of the NPs into more anisotropic shapes. Through favouring of further growth on certain facets of the nanoparticle structure.
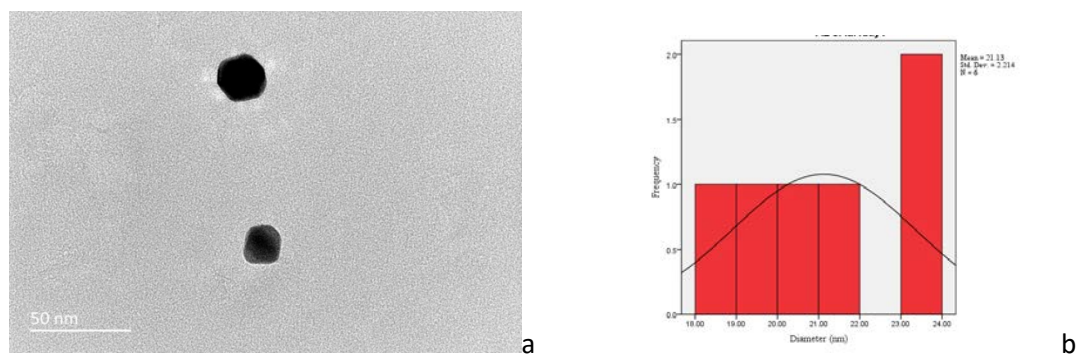
Figure 5.12: TEM image and correlating histogram for Au NPs in AOT/Butanol/Cyclohexane microemulsion with 1M HAuCl4, 10μl per ml stock solution used with 80mM Hydrazine, W number 1-2.

5.7. Reducing Agent: Ascorbic acid

Ascorbic acid is noted as having milder reducing agent qualities when compared with hydrazine, causing a slower reaction rate for the synthesis of nanoparticles within the microemulsion system. This could be of benefit for increasing the growth stage within the microemulsion system. To investigate this theory, 0.1M AOT/But/IPM or AOT/But/Cyclo microemulsions were prepared with stock solutions of 1M $AgNO_3$ or $HAuCl_4$ and 0.1M Ascorbic acid (AA) dissolved in deionised water, 10μl per ml were taken for both precursor and reducing agent for NP synthesis, causing the W number to increase to 5 for Ag NPs and 6 for Au NP systems. The use of ascorbic acid was unsuccessful for the synthesis of Au NPs as when the solutions were mixed no colour change was observed. With Ag NPs on the other hand, the microemulsion solutions for both AOT/But/Cyclo and AOT/But/IPM gradually turned a dark yellow colour.

When tested with UV-Vis, Figure 5.13, the Ag NPs were shown to have similar absorbance curves and intensities, for both microemulsion systems and similar peak wavelengths of 418nm and 413nm for AOT/But/IPM and AOT/But/Cyclo respectively. When compared with Ag NPs reduced by hydrazine in the same microemulsion systems the peak wavelengths are shown for both to have increased, from 404nm and 407nm for AOT/But/IPM and AOT/But/Cyclo respectively. Therefore, the UV-Vis results support that the Ag NPs increased in size slightly with the use of AA when

compared with hydrazine. The shapes of the Ag NPs when reduced with AA were also shown to have more anisotropic features beneficial to a SERS substrate shown in Figure 5.14.
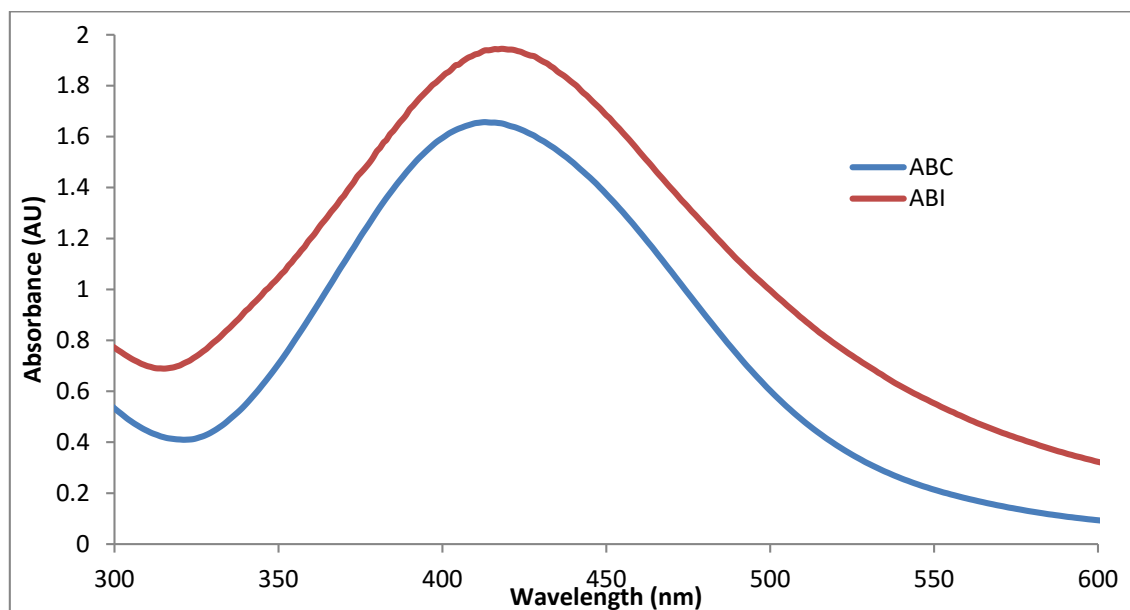
Figure 5.13: UV-Vis graphs to show Ag NPs in AOT/Butanol/IPM (ABI) and AOT/Butanol/Cyclohexane (ABC) microemulsions when 10µl of both 1M AgNO3 and 0.1M Ascorbic acid is added, W number 5.

The TEM results for Ag NPs within the AOT/But/Cyclo system reduced with AA, were shown to have a uniform anisotropic shape of larger spherical NPs with smaller spherical NPs attached onto the surface, the NPs had an average size of 37.9nm with a size range between 12-59nm. The size, shape, uniformity and close proximity of the Ag NPs to one another within the microemulsion system is predicted as beneficial as a SERS substrate device. Alteration of reducing agent is shown as with co-surfactant addition to have the most significant impact of NP size and shape within the microemulsion system. Use of different reducing agents could therefore cause desired alterations in NP shape and size for Au NPs as well which was not able to be synthesised with AA.
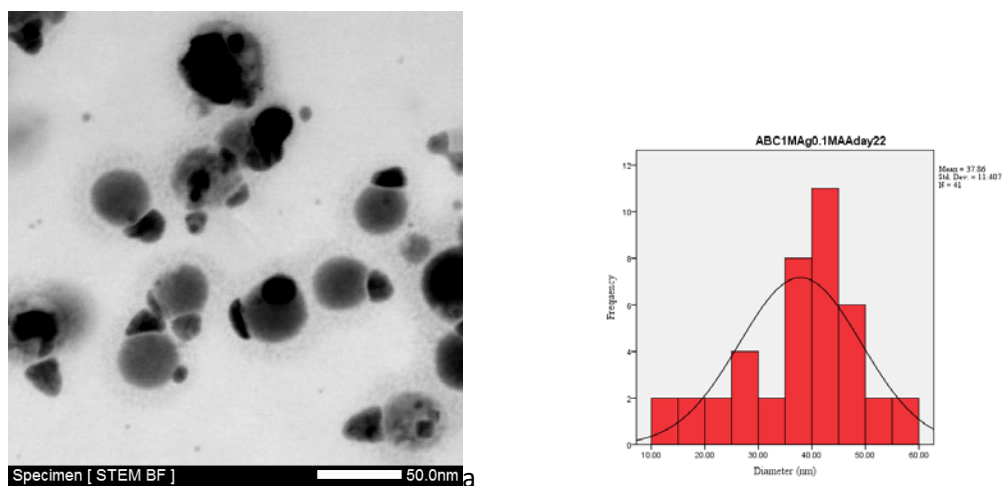
Figure 5.14: The TEM image (a) and corresponding NP size distribution histogram (b) shown for Ag NPs within AOT/But/Cyclo microemulsions with 1M AgNO₃ and 0.1M AA stock solutions where 10µl per ml was taken, with a W number of 5.

5.8. Reducing Agent: NaBH₄

Due to the success of altering the reducing agent for preparing Ag NPs beneficial for a SERS substrate design, sodium borohydride (NaBH₄) was used within the same manner for preparation of both Ag and Au NPs. 0.1M ABI and ABC microemulsions were prepared, with 1M AgNO₃ or HAuCl₄ precursor and 0.1M NaBH₄ stock solutions prepared, 10µl per ml of stock solution was taken for NP synthesis reactions. Both Au and Ag NPs were successfully prepared within the microemulsion systems with the use of NaBH₄, shown visibly through solution colour change. Ag NPs turned to a typical yellow colour, whereas Au NPs altered in colour twice, firstly to dark green within the ABI system and a light red which turned green after an hour within the ABC system, to a yellow colour after 12 hours. UV-Vis result was taken, Figure 5.15, to evaluate the size associated with the colour changes for both Ag and Au NPs. Au NPs (Fig. 5.15a) for both microemulsion systems show a very flat peak with low absorbance at peak wavelengths of 559nm and 558nm for ABI and ABC respectively. These peaks when compared with Au NPs reduced with hydrazine within ABI and ABC systems show an increase in peak, as in the hydrazine system, Au NPs have peak wavelengths of

511nm and 514nm for ABI and ABC respectively. Therefore, one would presume that the Au NP size within these systems is larger when $NaBH_4$ is used.

For Ag NPs (Fig. 5.15b), differing absorbance curves are shown for the two microemulsion systems. For ABC a wavelength peak is present at 380nm which is not within the Ag NP range, therefore the Ag NPs may either be a larger size or an anisotropic shape has been produced which is causing alterations in absorbance. For Ag NPs within the ABI system there is a peak wavelength at 428nm, which is the largest peak shift shown when compared with the other two reducing agents under the same conditions; Ag NPs in the hydrazine ABI system had a peak wavelength of 404nm and Ag NPs in the AA ABI system had a peak wavelength of 413nm. Therefore, the NPs within this system are predicted as being larger.

The TEM results (Fig. 5.16) for Ag NPs show different size and shape ranges within the microemulsion being formed, whereas for Au NPs (Fig. 5.17) more definitive anisotropic shapes are being fabricated with increased size, supported by the UV-Vis results. The TEM images for Ag NPs (Fig. 5.16) show a large aggregated mass of Ag NPs, which presumably causes the lack of an absorbance peak within UV-Vis results in Figure 5.15b. The smaller Ag NPS within the images showed an average nanoparticles size of 14.7nm and a range between 3.1-45.5nm. For the Ag NPs within the ABI system, there are clearer separated NPs of three different sizes and shapes with the larger Ag NPs showing a more anisotropic shape, with sharper edges, the range is between 1.8-34.5nm with an average nanoparticle size was 8nm. The aggregation of Ag NPs within ABC highlights that the intermicellar exchange rate and fluidity of the system may be too high and therefore the inverse micelle template is not rigid enough to prevent aggregation of the Ag NPs with a charged reducing agent. Whereas within the ABI system the Ag NP shape and size integrity is maintained, perhaps due to the lower intermicellar exchange rate and less fluidic microemulsion system.
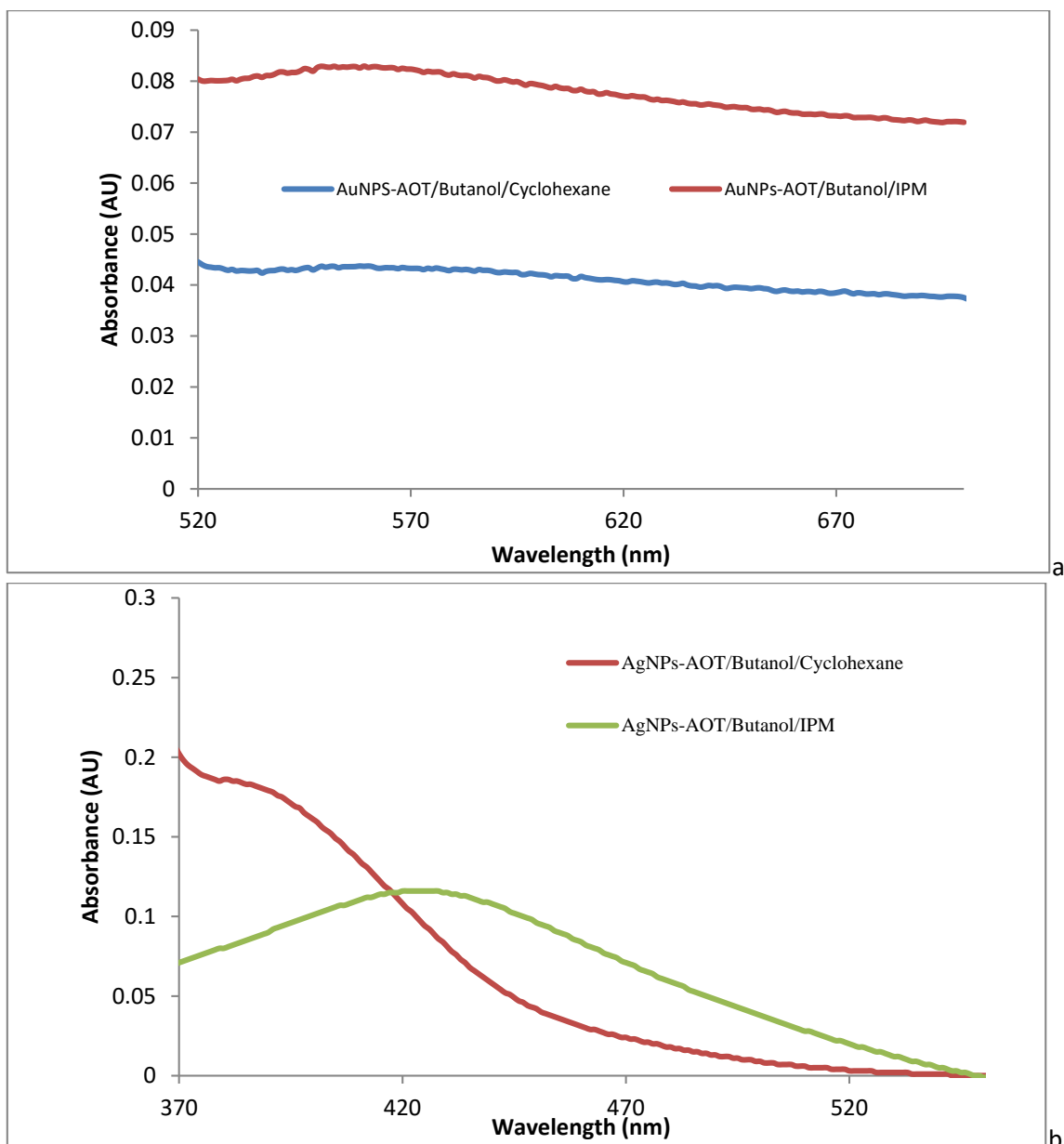
Figure 5.15: UV-Vis graphs to show Ag NPs in AOT/Butanol/IPM and AOT/Butanol/Cyclohexane microemulsions when 10µl of both 1M $AgNO_3$ and 0.1M $NaBH_4$ is added, W number 6 for Au NPs and 5 for Ag NPs.
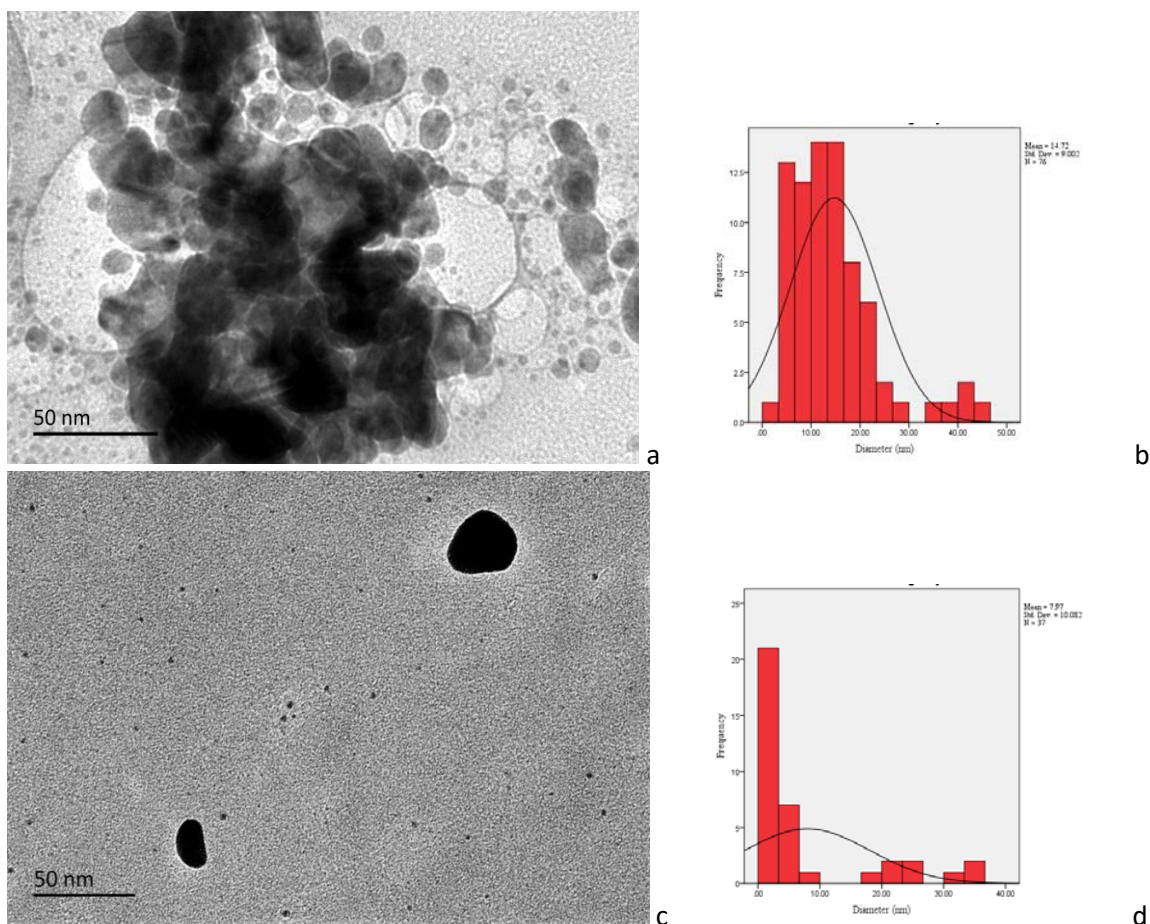
Figure 5.16: TEM images and corresponding histograms for Ag NPs in a&b) ABC and c&d) ABI microemulsions, when 1M AgNO$_3$ and 0.1M NaBH$_4$, 10µl per ml, W5.

For Au NPs (Fig. 5.17) the effect of using NaBH$_4$ as reducing agent has a significant impact on anisotropic shape formation and size. Au NPs show controlled aggregation to form square structures within the ABC microemulsion system, with an average size of 113.6nm and large range between 29.7-505.7nm. For Au NPs within the ABI microemulsion system anisotropic shapes were also produced however the shapes were less defined compared with the ABC system. The average NP size was 16.28nm with a size range between 5.4-49.7nm. The difference in anisotropic shape and size as discussed previously for the Ag NP system could be caused due to the rigidity of the microemulsion system and the inverse micelle template. Also mentioned previously, NaBH$_4$ unlike hydrazine has an induced charge when used for nanoparticle synthesis, as Au NPs have a neutral charge, the addition of charge from NaBH$_4$, could result in the directed growth on crystal facets of the Au NP structure, and due to the neutral charge an even growth rate is instated and thus uniformity of square shapes within the system. With the use of a different surfactant, the

microemulsion templates role on the resultant size and shape of the Au and Ag NPs can be more defined.
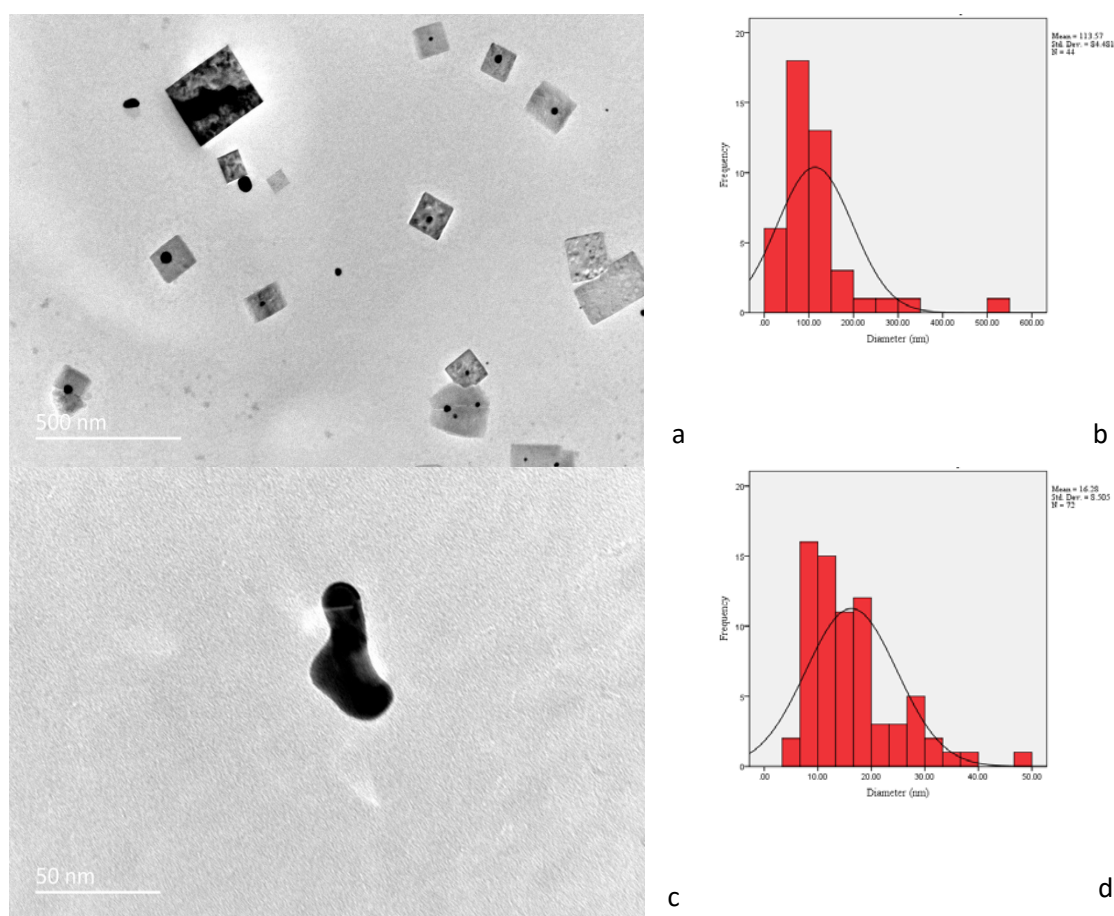
Figure 5.17: TEM images and corresponding size distribution histograms for Au NPs in a&b) AOT/But/Cyclo and c&d) AOT/But/IPM, with 1M HAuCl$_4$ and 0.1M NaBH$_4$ stocks, 10µl per ml taken, W6.

5.9.   Surfactant: CTAB

CTAB was used as an alternative surfactant to AOT, to understand in more detail the influence the microemulsion template has on the resultant Au and Ag NPs and thus produce a range of NPs that are beneficial as SERS substrates. This is of importance as different wavelengths have differing resonance with particular metals and it was shown in chapter 4, that if the size of the roughness can be controlled, broadband SERS substrates can be produced. The use of CTAB to AOT induces a change in charge of the microemulsion system from anionic to cationic as well as the fluidity of the system. CTAB has a longer chemical structure, with a single hydrophobic tail of 17 carbons attached to a cationic polar head compared with AOT which has a more compact chemical structure with

two hydrophobic side chains, 10 carbons in length, attached to an anionic polar head. Au and Ag NPs were synthesised in 0.1M CTAB/Butanol/Cyclohexane (CBC) microemulsions with 10µl per ml of stock 1M precursor, HAuCl$_4$ or AgNO$_3$ and 10µl per ml of 0.1M NaBH$_4$ stock reducing agent, W number 5 or 6 respectively.

There was a visible colour change for both Au and Ag systems, with Ag NPs which turned light yellow, and Au NPs which became a dark orange colour. The UV-Vis results, Figure 5.18 show a peak for Ag NPs within the CBC system at 415nm, whereas with Au NPs despite the colour change, no visible peak within the Au NP range is seen. The TEM images for both Ag and Au system showed the presence of NPs (Fig. 5.19).

The TEM image for Ag NPs, Figure 5.19a, within the CBC system show two different sized nanoparticles, one larger sized and more anisotropic shape NP which is shown to be clumped together and the other smaller spherical NP, that predominated the image. The average NP size within this system was 32.68nm with a large range between 1.7-443.4nm. For Au NPs within the CBC system, figure 5.19b, there was a close proximity of Au NPs, spaced roughly around 1-2nm from one another with more anisotropic shapes with sharper edges and in some cases definitive diamond and triangle structures present. The average nanoparticle size within this system was shown to be 43.92nm with a larger range between 3.5-188nm. The increased closeness of the NPs is highly desirable for a substrate design as it produces an increased electromagnetic intensity which should give better SERS enhancement properties.

The alteration in size and shape as well as proximity of the NPs to one another highlights the effect of the microemulsion system with the reducing agent, CTAB due to its cationic charge and larger molecular structure firstly causes an increased attraction of the NPs to one another as well looser micelle structures shown through the larger NPs produced for both Ag and Au NPs within the system.

With alteration to the microemulsion components within the system, size and shape has been effectively altered to differing degrees to provide structures that show promise as SERS substrates. An additional characteristic for NPs within solution to provide SERS efficacy is through the close proximity they have to one another. This would provide a reliable and repeatable substrate that controls and increased the presence of hot-spots within the solution. Therefore, an additional parameter, mentioned for SERS substrate design within microemulsion was tested, this was the use of electrolyte to the system.
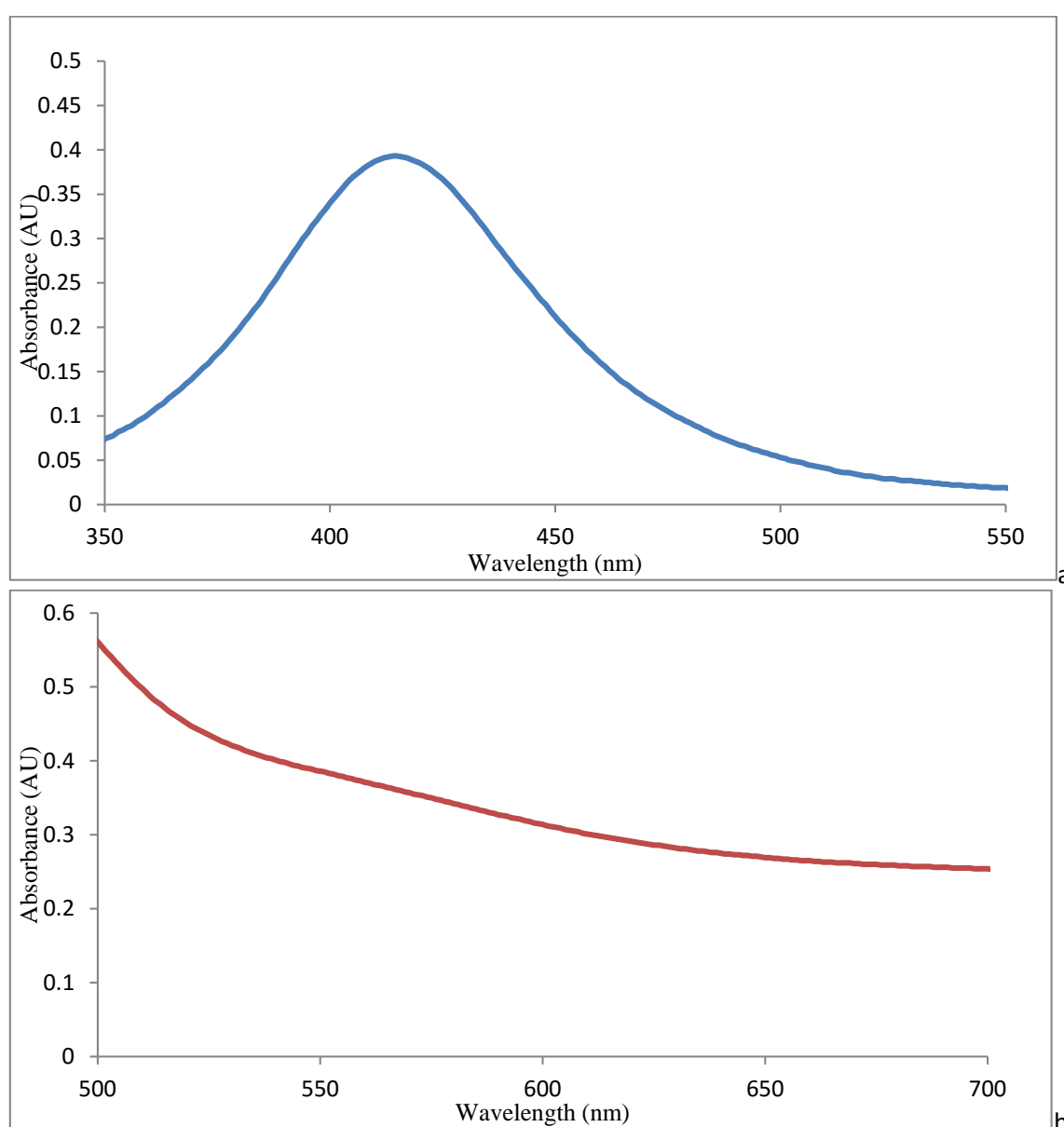
Figure 5.18: UV-Vis graphs to show Ag NPs (a) and Au NPs (b) in CTAB/But/Cyclo microemulsions when 10µl of 1M $AgNO_3$ or $HAuCl_4$ and 0.1M $NaBH_4$ is added, W number 6 for Au NPs and 5 for Ag NPs.
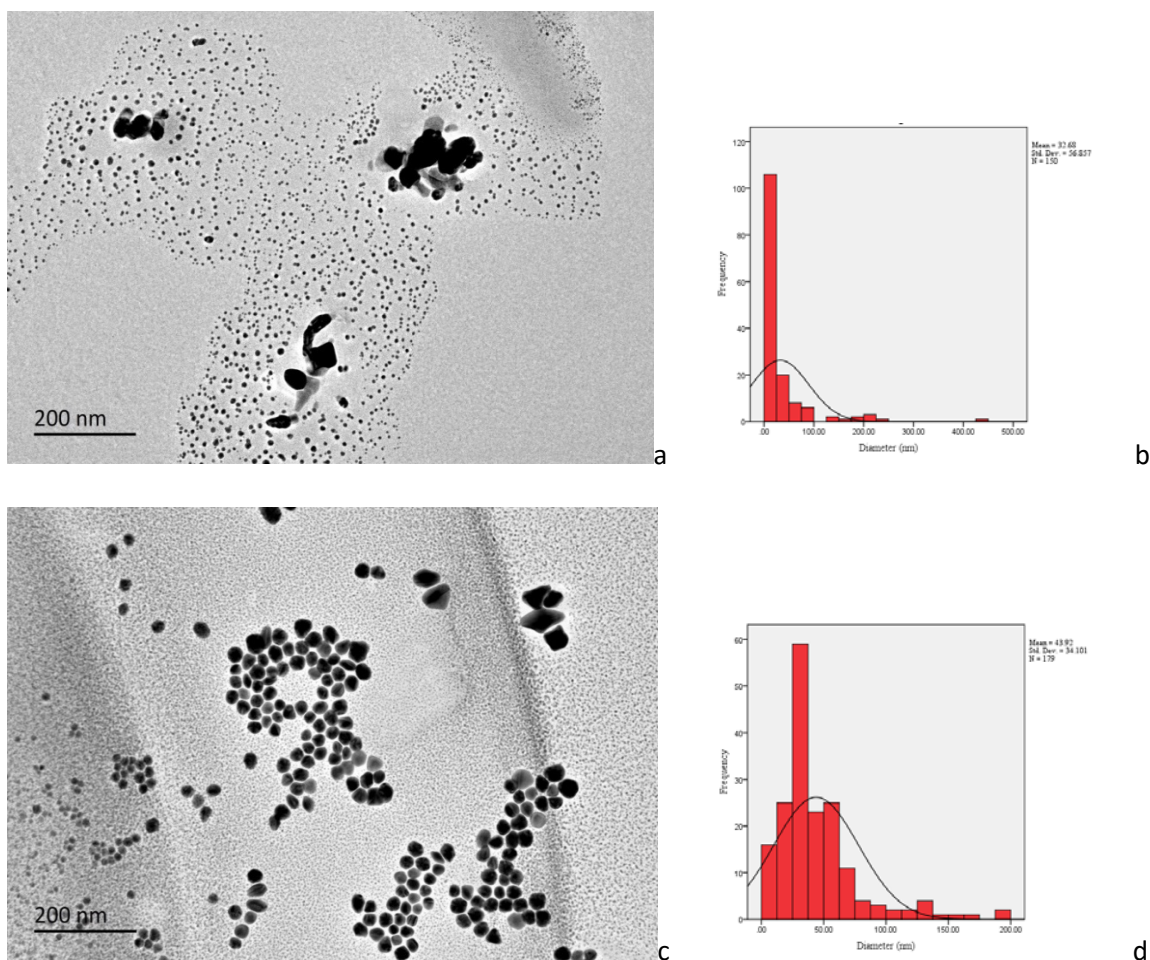
Figure 5.19: TEM images and corresponding size distribution histograms for a&b) Ag NPs and c&d) Au NPs in CTAB/Butanol/Cyclohexane microemulsions with 1M AgNO₃ or HAuCl₄ and 0.1M NaBH₄, 10µl per ml is taken from both stocks, W number 6 for Ag NPs and 5 for Au NP systems.

5.10. Electrolyte

To achieve closer proximity of the NPs within the microemulsion system for a more effective SERS substrate, the addition of an electrolyte was used. Electrolyte has been shown within NP systems to cause the aggregation of NPs (Eastoe et al, 2007). With the presence of the microemulsion template, it was the expectation that the integrity of the NP size and shape would not be compromised by the addition of the electrolyte instead it would cause the movement of the NPs to a closer distance from one another. Sodium chloride (NaCl) was added to 7 different microemulsion systems that showed varied sizes and morphologies, of interest for further SERS substrate design. For all the systems 10µl per ml was taken of precursor and reducing agent stock solutions.

For Ag NPs, 3 different microemulsion systems were used:

1. ABC, 1M $AgNO_3$ + 0.1M Ascorbic acid (ABC Ag AA)

2. ABI, 1M $AgNO_3$ + 0.1M $NaBH_4$ (ABI Ag N)

3. CBC, 1M $AgNO_3$ + 0.1M $NaBH_4$ (CBC Ag N)

For Au NPs, 4 different microemulsion systems were chosen;

1. ABC, 1M $HAuCl_4$ + Hydrazine (ABC Au H)

2. ABC, 1M $HAuCl_4$ + $NaBH_4$ (ABC Au N)

3. ABI, 1M $HAuCl_4$ + $NaBH_4$ (ABI Au N)

4. CBC, 1M $HAuCl_4$ + $NaBH_4$ (CBC Au N)

NaCl at a 1M concentration was prepared and 20µl per ml, was added to all the microemulsion systems. The microemulsion solution did not alter in colour with the addition of NaCl, however with increased time the Au NP ABC system which used hydrazine as the reducing agent began to agglomerate and form Au particles instead and the colour diminished. The UV-Vis results shown in Figure 5.20, for the 7 microemulsion systems, show that when NaCl was added to the systems, no peaks were present for Au and Ag NPs in the ABI microemulsion systems as well as for Ag NPs in ABC reduced with AA or NaBH4. Only Ag NPs in the CBC microemulsion system reduced with $NaBH_4$ gave a peak within the NP range at 416nm which is the same peak wavelength as that observed in the normal microemulsion system. Au NPs after a 100-fold dilution showed a peak at 510nm which was similar to the control system which had a peak wavelength of 514nm. The results implicate that the effect of the electrolyte on the system is minimal for increasing NP size and detrimental to maintaining the integrity of the NPs within the system. One should note however that the addition of the electrolyte is one of the two parameters affecting the systems as with NaCl addition, additional water is added, causing the microemulsion systems to increase to W12 for Ag NPs and W10 for Au NPs. As the NPs are formed within inverse micelles, one could presume the additional

water would affect the inverse micelle structure and alter the dynamics of the system to some

extent.
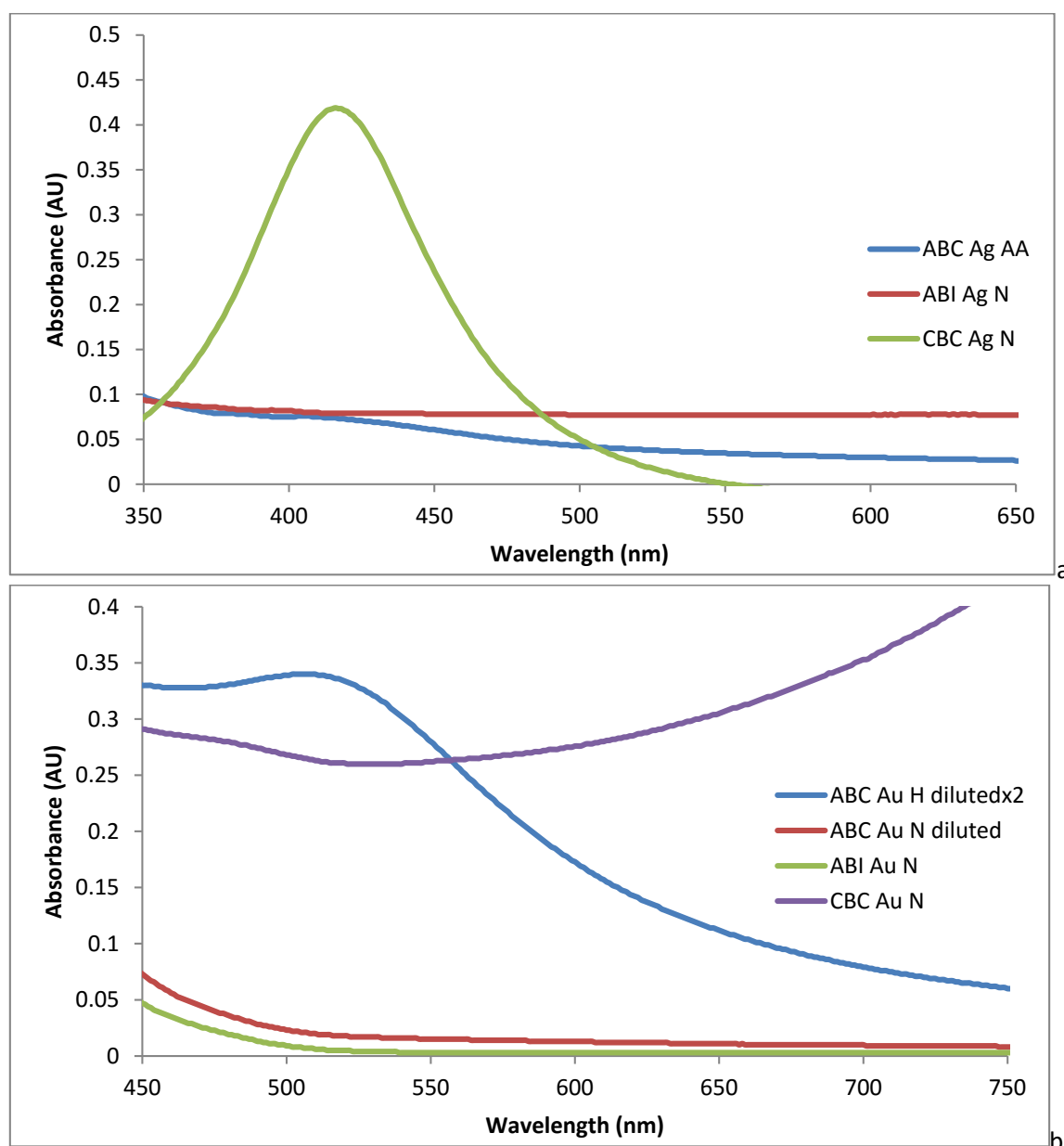
Figure 5.20: UV-Vis graphs to show Ag NPs (a) and Au NPs (b) from the shortlisted microemulsion systems with 1M NaCl added 1M $AgNO_3$ or $HAuCl_4$, 0.1M AA or $NaBH_4$ or 80mM Hydrazine, 10µl take from each stock. W number 12 for Ag NPs and 10 for Au NPs.

The TEM images show for some systems that the addition of NaCl does still have an effect on

reducing the distance between the NPs despite increased W number. However, it also shows a

reduction in NP size with the addition of NaCl in other systems, which could be due to the increased

W number (Fig. 5.21).

Ag NPs in the ABC microemulsion with the reducing agent AA (Fig. 5.21a), shows the aggregation of Ag NPs into a larger size, however NPs remained predominately spherical with an average size of 4.8nm with a size range between 1.5-44.6nm. The lack of peak within the UV-Vis may indicate that NPs are widely distributed within the microemulsion system. For Ag NPs in ABI with $NaBH_4$ as the reducing agent, when 1M NaCl is added to the system, a positive effect is concurred, whereby Ag NPs are within a closer proximity to one another. The average NP size is 9.67nm and the range is between 2.7-22.9nm. For Ag NPs in CBC reduced with NaBH4, and with the addition of 1M NaCl, the Ag NPs have a more uniform nanoparticle range between 2.5-8.2nm with a smaller average size of 5.1nm. The nanoparticles have moved into closer proximity to one another.

Overall the addition of NaCl to the system was not beneficial for most of the shortlisted microemulsion systems, with only Ag and Au NPs within AOT/But/IPM showing closer proximity to one another. The addition of increased water within the system can be hypothesised as causing the reduction in NP size within the system as the water chambers have now become larger as well and the integrity of the inverse micelle system could be destabilised. This is more apparent with cyclohexane microemulsion systems whereby the already fluidic nature of the microemulsion system causes reduced integrity with increased water chambers. Whereas due to the rigidity of the IPM system, one could hypothesise the inverse micelle structure maintains its integrity and thus with increased water addition the micelles are just brought closer to one another as they try to reject any excess water that would destabilise the system.
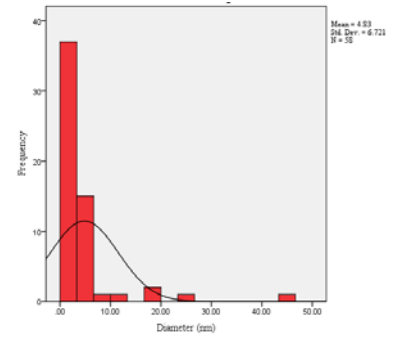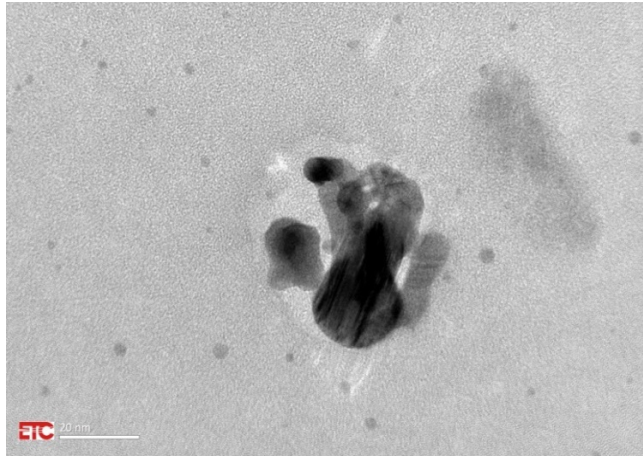
a

b
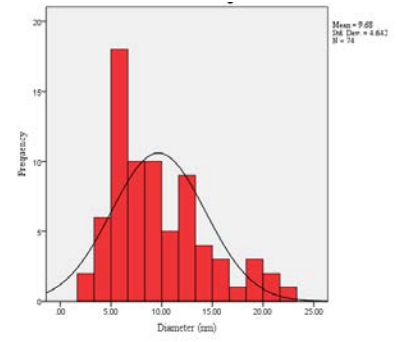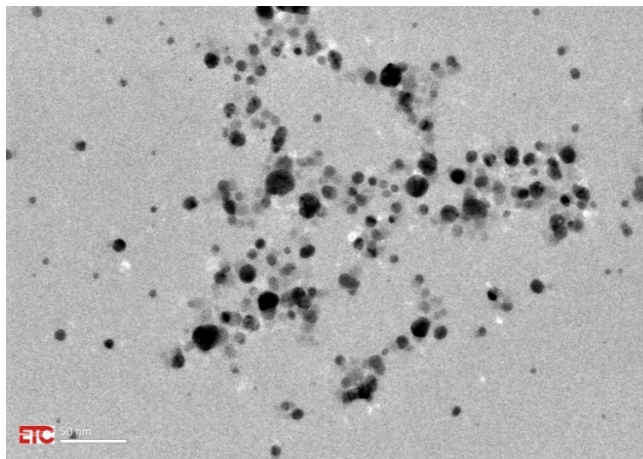
c

d
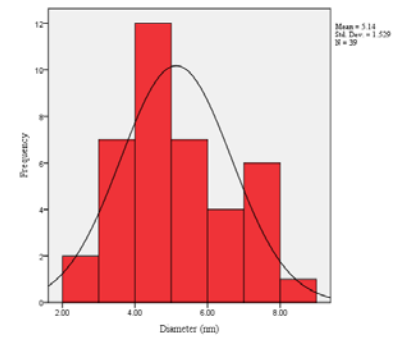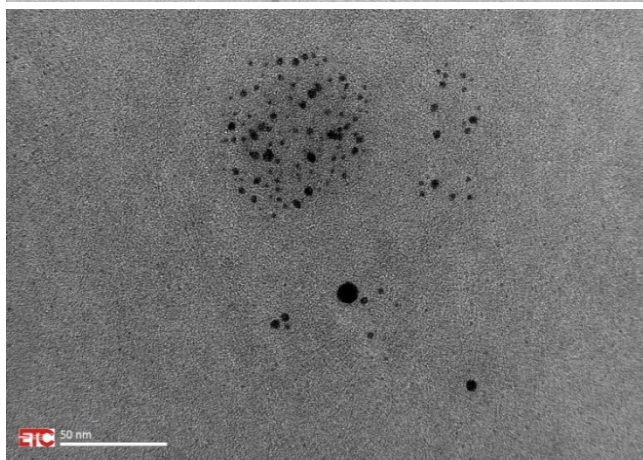
e

f
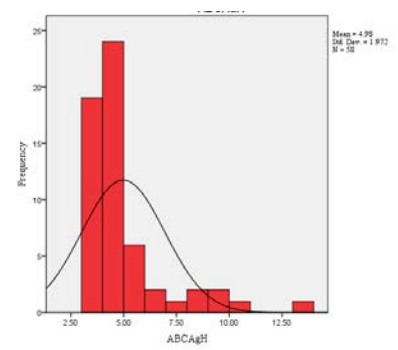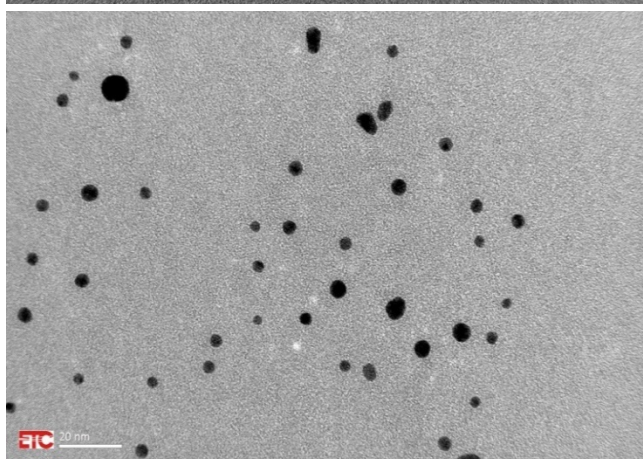
g

h
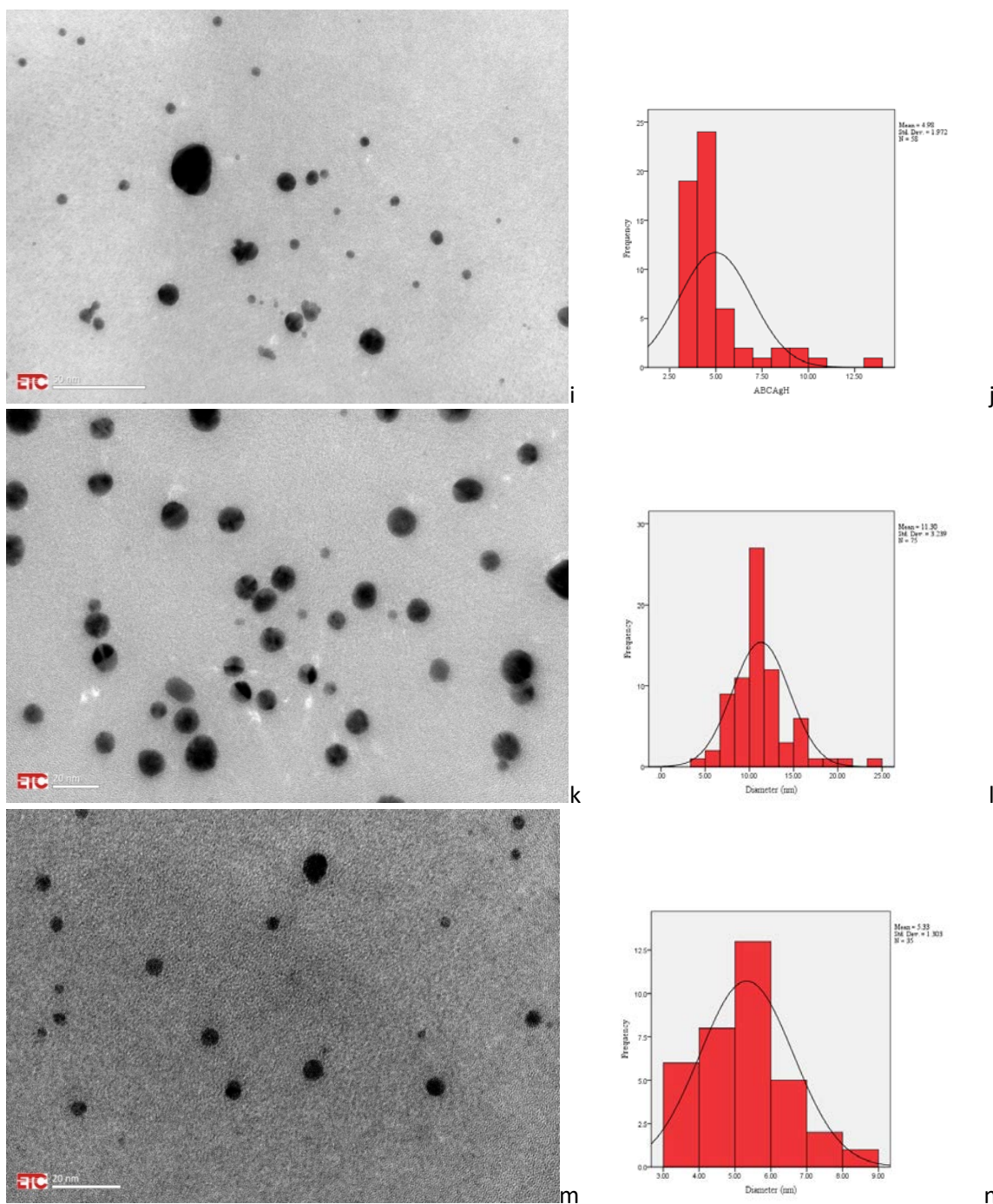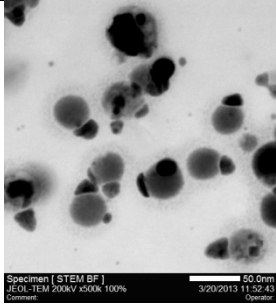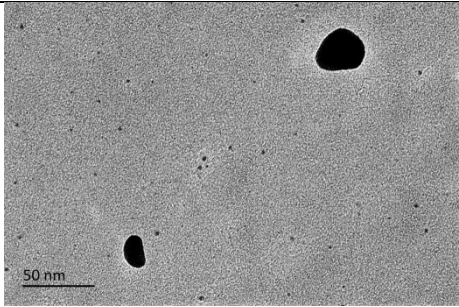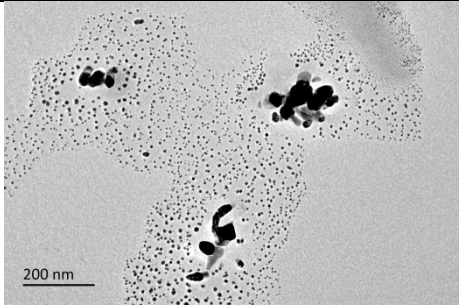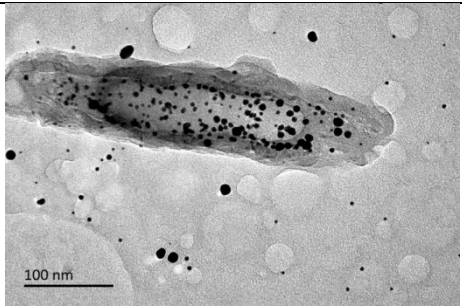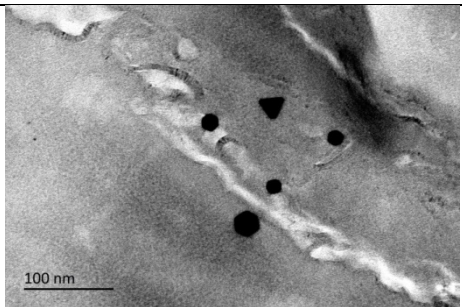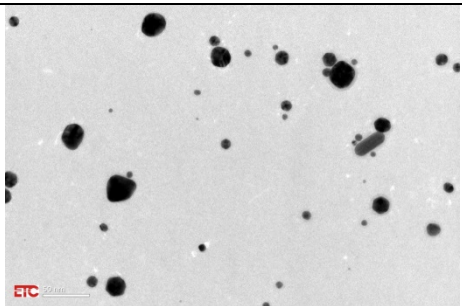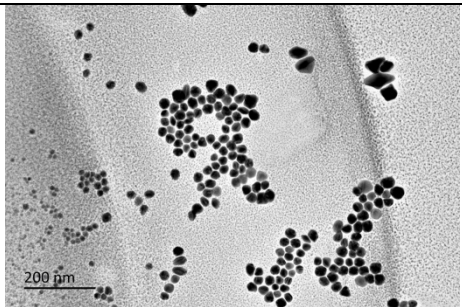
Figure 5.21: TEM images and corresponding size distribution histograms for a&b) ABC Ag AA, c&d) ABI Ag N, e&f) CBC Ag N, g&h) ABC Au H, i&j) ABC Au N, k&l) ABI Au N and m&n) CBC Au N all with 1M NaCl addition, 20µl per ml.

For the AuNP systems (Fig 5.21g), Au NPs in ABC reduced by hydrazine with the addition of NaCl, a slight increase in aggregation of nanoparticles. The average nanoparticle size was 5nm with a range between 3.1-13.1nm which was similar to the control microemulsion, thus the UV-Vis results, (Fig. 5.20a), is supported for peak wavelength exhibited. Au NPs in ABC reduced by NaBH4 with the addition of 1M NaCl (Fig. 5.21i) shows an average nanoparticle size of 5nm and a size range

of 3.9-26.3. For Au NPs in AOT/Butanol/IPM microemulsions reduced by NaBH₄ with the addition of NaCl, figure 5.21k, the Au NPs have moved within a closer proximity to one another, beneficial for a SERS substrate. The average NP size is 11.3nm with a range between 4.5-24.1nm, therefore the NPs are quite uniform in size and shown to be similar shapes. Au NPs in CBC reduced with NaBH₄ (Fig. 5.21m), show a negative response to the addition of NaCl to the system, as the NPs are no longer within close proximity to one another and have a smaller average size of 5.33nm with a range between 3.-8.7nm, the nanoparticle morphology has also become more rounded.

Table 5.3: Short-listed Ag and Au NP systems shortlisted for SERS testing.

Microemulsion System (volume per ml)	Image	Average Nanoparticle Size and (Range) nm	Nanoparticle Morphology
AOT/Butanol/Cyclohexane, 1M AgNO₃ (10µl) + 0.1M AA (10µl)		37.7nm (12-59nm)	
AOT/Butanol/IPM, 1M AgNO₃ (10µl) + 0.1M NaBH₄ (10µl)		8nm (1.8-34.5nm)	
CTAB/Butanol/Cyclohexane, 1M AgNO₃ (10µl) + 0.1M NaBH₄ (10µl)		39.6nm (4.2-43.4nm)	

AOT/Butanol/Cyclohexane, 1M HAuCl$_4$ (10µl) + Hydrazine (10µl)		9.7nm (3.1-33.8nm)	
AOT/Butanol/Cyclohexane, 1M HAuCl$_4$ (10µl) + 0.1M NaBH$_4$ (10µl)		29.5nm (17.6-49nm)	
AOT/Butanol/IPM, 1M HAuCl4 (10µl) + 0.1M NaBH$_4$ (10µl)		16.3nm (5.4-49.7nm)	
CTAB/Butanol/Cyclohexane, 1M HAuCl$_4$ (10µl) + 0.1M NaBH$_4$ (10µl)		40nm (13.8-171nm)	

5.11.   Shortlisted Nanoparticle Systems for further SERS testing

As detailed in section 5.10, 7 different microemulsion systems were identified for SERS substrates; they showed varied nanoparticle size, morphology and in some instances increased

proximity through altering of the parameters. These microemulsion systems were short-listed for further SERS testing as summarised in Table 5.3.

5.12. Chapter Summary

In this study, the requirement for size and shape control for SERS substrates was focused upon with the fabrication of Ag and gold (Au) NPs within microemulsions. Microemulsions provided a simple methodology, that required little equipment requirements, could be undertaken in ambient conditions, with fast reaction time (seconds to minutes) and long-term stability within the solution (>3 months). The NPs were desired to be within narrow size ranges, preferably ≥30nm with anisotropic shape, for increased roughness and thus SERS enhancement. Density of NPs within the solution and proximity of the NPs to one another was also looked into for the fabrication of the SERS substrates.

Within the study 7 parameters; surfactant, co-surfactant, solvent, precursor concentration, reducing agent, W number and electrolyte were looked into for the preparation of Ag and Au NPs, which were characterized with UV-Vis and TEM. The results highlighted the significance of 4 parameters in particular; co-surfactant, solvent, reducing agent and surfactant. The use of co-surfactant, butanol, caused the size of the NPs to increase, such as for Au NPs reduced with hydrazine, the average size increased from 5.1nm in AOT/IPM microemulsions to 34.9nm in AOT/But/IPM microemulsions.

The use of solvent, from long chained isopropyl myristate (IPM) to short-chained cyclohexane (Cyclo), altered the fluidity of the system and caused an increase in size as well as a slight increase in shape under the same reducing agents; with Ag NPs showing octagonal features within the AOT/But/Cyclo system compared with the IPM alternative which was typically spherical, with average size increasing to 21.1nm for AOT/But/Cyclo compared to 10.1 in AOT/IPM reduced with hydrazine.

The effect of the reducing agent appeared the most significant, with concentration as well as type having an effect on the NP morphology. The use of milder reducing agent AA compared to hydrazine in AOT/But/Cyclo caused the average NP size to increase to 37.9nm with a conjoined morphology of the NPs observed within TEM. The results highlighted that with a milder reducing agent, there would be a predicted alteration in the nucleation and growth stages within the microemulsions, with a larger growth stage, thus the morphology and increase size. With the use of $NaBH_4$, which became charged within the reduction process, compared with the other two reducing agents, increased anisotropic shapes were observed, desirable for SERS; with Au NPs within AOT/But/Cyclo presenting uniform square-like morphologies within solution of aggregated Au NPs with an average size of 16.3nm shown.

The effect of charge on the growth of anisotropic NP shapes was further looked into with the alteration of the surfactant used, from anionic AOT to cationic CTAB. The results supported that charge did affect the resulting shape of the NPs present within the solution, with CTAB/But/Cyclo microemulsions producing more anisotropic Au and Ag NPs, with an additional desired characteristic of being within a closer proximity to one another, with Au NPs showing a diamond-like and irregular morphology with an average size of 43.9nm and Ag NPs showing an average size of 32.7nm.

As observed throughout the process visibly, the NPs showed difference in colours of the solution which indicated the size and shape of the nanoparticles within, more significantly shown for gold whereby solutions of a dark red colour showed NPs less than 10nm in size and spherical, whereas solutions that were dark green showed increased anisotropic shapes; squares, triangles and hexagons with increased NP size. UV-Vis as with TEM was effective in characterising all the solution, with peak shift for NPs showing increased NP size as well as the shape of the UV-Vis peak, indicating in some ways the presence of anisotropic shapes, as with the CTAB and $NaBH_4$

microemulsion systems where the most anisotropic shapes were present the UV-Vis peak became flatter compared to the systems where spherical NPs of small size were shown.

The use of microemulsions was thus shown with the alteration of chemical parameters to produce NPs with controlled size ranges and anisotropic shapes that were desirable as SERS substrates; as such 7 microemulsion systems were shortlisted, 3 for Ag NPs and 4 for Au NPs. These shortlisted systems were taken further for SERS testing with both 514nm and 1064nm Raman with 1mM MBT.

Chapter 6: SERS Substrate Design: application of Ag and Au nanoparticles prepared within microemulsions as SERS substrates.

6.1. Introduction

Gold (Au) and silver (Ag) nanoparticles (NPs) were successfully prepared within microemulsions (Chapter 5) and a set of seven shortlisted NP variants were carried forward for further testing for their use in the second category of the SERS substrate design as presented in this chapter. NPs, as long as were in the microemulsions, were stable. However, the presence of the microemulsion constituents, especially the surfactants could potentially interfere with SERS detection. Hence, for the SERS efficacy studies, we tested the shortlisted NPs, of different size ranges and shapes, both within the microemulsions and separated from the microemulsions. NPs were separated from the microemulsions using water phase disruption method. The separation process was monitored using UV-Vis, 1064nm Raman and TEM. The Au and Ag NPs shortlisted for further testing, as described in this chapter, were as follows:

1. AOT/Butanol(But)/Cyclohexane(Cyclo) with 1M $AgNO_3$ and 0.1M Ascorbic acid (AA) [ABC Ag AA]

2. AOT/But/Isopropyl myristate (IPM) with 1M $AgNO_3$ and 0.1M $NaBH_4$ [ABI Ag N]

3. CTAB/But/Cyclo with 1M $AgNO_3$ and 0.1M $NaBH_4$ [CBC Ag N]

4. AOT/But/Cyclo with 1M $HAuCl_4$ and 80mM Hydrazine [ABC Au H]

5. AOT/But/Cyclo with 1M $HAuCl_4$ and 0.1M $NaBH_4$ [ABC Au N]

6. AOT/But/IPM with 1M $HAuCl_4$ and 0.1M $NaBH_4$ [ABI Au N]

7. CTAB/But/Cyclo with 1M $HAuCl_4$ and 0.1M $NaBH_4$ [CBC Au N]

For testing SERS efficacy, 1mM 4-methylbenzenethiol (MBT) was added to the microemulsion systems, as well as to NPs removed from the microemulsion systems. Both SERS substrate designs

were tested using 514nm and 1064nm Raman lasers, however due to the different Raman set-ups, modifications to the SERS substrate design were implemented. With the 514nm Raman instrumentation, solid substrates were more effective for testing compared with solutions. Therefore, the NPs from both the microemulsion and separated systems were coated on cellulose filter paper and tested with 514nm Raman using dry samples. For the 1064nm Raman instrumentation, both liquids and solids could be tested, and obtained SERS spectra for NPs both in microemulsions and separated from the microemulsions. However, in the dry form, the filter papers coated with the NPs were susceptible to burning due to the high power output of the laser. To overcome the burning issue, the NP coated filter papers were incorporated in microfluidic chips to keep them hydrated for the 1064nm Raman scans.

6.2.   Nanoparticles Separation from Microemulsions

The common methods used are; centrifugation and phase disruption. All these methods were tested for the separation of the different shortlisted NP microemulsions systems. The NP reduction process produces a black precipitate which is the waste by-product salt from the reaction. When the NP microemulsion systems were centrifuged, with Ag NPs it was seen that the black precipitate was deposited at the bottom with the Ag NPs remaining in the microemulsions, which was good for purifying the NPs. For Au NPs, centrifugation was detrimental, because the Au NPs were also deposited along with the salt precipitate at the bottom of the centrifugation tubes. When the precipitate was re-suspended the Au NPs no longer were present. Hence we looked at using phase disruption methods. A variety of anti-solvents: ethanol, octane, THF, acetone, cyclohexane and butanol, in combination with water were added to the NP microemulsions systems to disrupt the microemulsions. This typically produced two or three (water, oil, and precipitate of surfactant) phases. In most of these phase disruptions, the NPs were distributed in both the oil and the water phases. Often their morphology was altered, as observed under TEM. Thus, the phase disruption methods using anti-solvents were not only time consuming, but also inefficient. Finally, the use of

water alone for phase disruption was sufficient for separating the NPs. The method involved repeated washes (three in total) in water, with NPs gradually moving into the water phase. The NPs dispersed in water (water phase) were used for further testing.

The method for water phase disruption of NPs containing microemulsions was that modified from that reported by Hollamby et al, 2007. The addition of water produced two phases within the solution, a solvent rich phase and a water rich phase, with NPs present in both phases as evident from the colour of both the phases (Fig. 6.1). However, on allowing the solutions to stand undisturbed, more NPs, especially Au NPs, diffused passively into the water phase (bottom layer). In the case of Ag NPs, an additional step of centrifugation was necessary for the faster/efficient transfer of the NPs from the oil (top) phase into the water (bottom) phase. After a minimum of one hour, the top (oil) phase was carefully removed and collected in a fresh vial. To this oil phase, fresh water was added, mixed and allowed to stand again for Au NPs and centrifugation for Ag NPs to move into the water phase. This, washing step was repeated again, and by third wash, there was hardly any colour left in the upper oil phase to indicate the presence of residual NPs. The water phases containing the NPs were pooled together and the NPs typically remained suspended in the solution.

The NPs separated from the microemulsions, dispersed in the water phase, it could be presumed the NPs present within the water cores of the inverse micelles in the microemulsion solution, favoured a more polar environment. The separations were characterized using UV-Vis and TEM. The colour of the separated NP solutions (Fig. 6.1) were different from that in their corresponding original microemulsion system (Table 5.3) and therefore the NP size and shape may also have been altered by the NP separation process. As illustrated in Figure 6.2a, the Ag NPs separated from ABC AA, ABI N and CBC N, all showed broad visible absorption peaks at 418nm, 397nm and 393nm respectively. The broad peaks are indicative of wide NP size distributions. For Au NPs (Fig. 6.2b) separated from ABC H, ABC N, ABI N and CBC N, also showed broad UV-Vis

absorption peaks at 518nm, 544nm and 488nm for ABC H, ABC N and CBC N systems respectively, indicating a wide NP size distribution ranges.
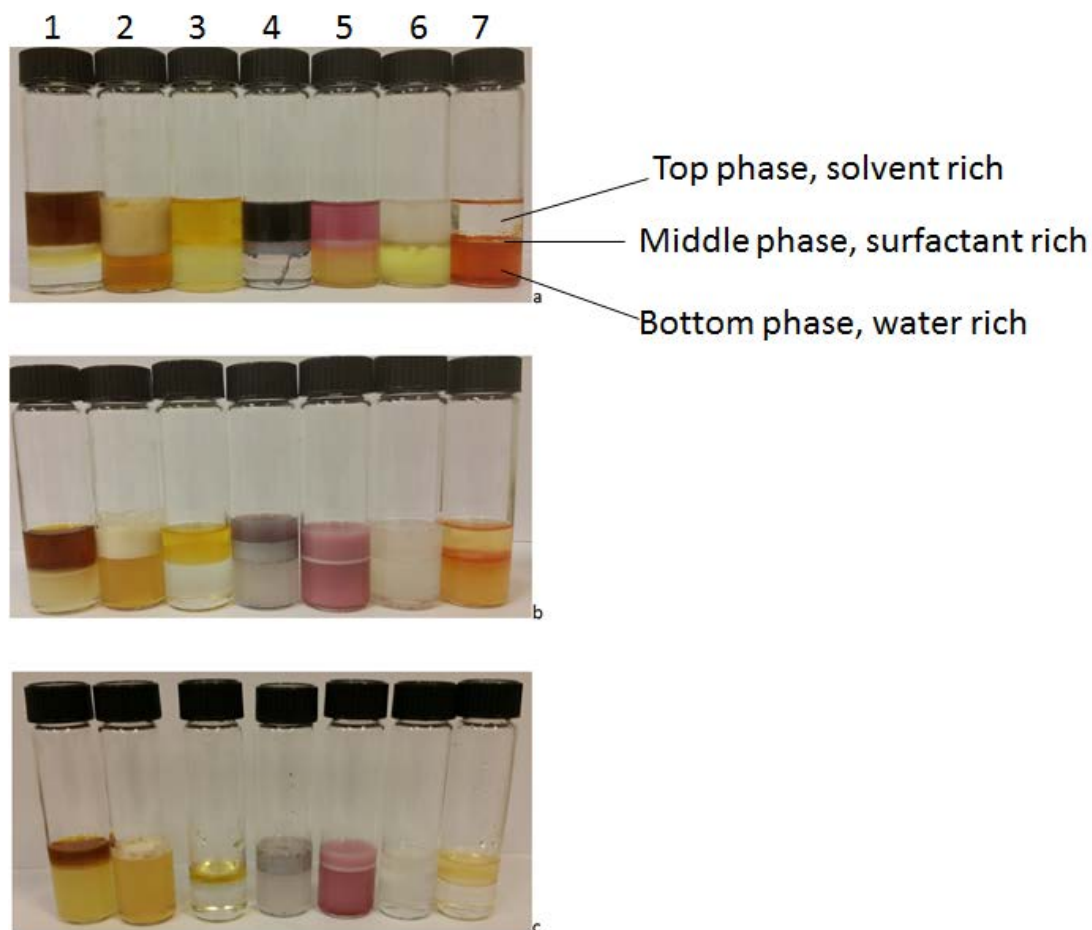
Figure 6.1. Images to show NP separations from the microemulsion system for the shortlisted NP systems 1-7, 1) Ag NPs in ABC reduced by AA, 2) Ag NPs in ABI reduced by NaBH$_4$, 3) Ag NPs in CBC reduced by NaBH$_4$, 4) Au NPs in ABC reduced by hydrazine, 5) Au NPs in ABC reduced by NaBH$_4$, 6) Au NPs in ABI reduced by NaBH$_4$ and 7) Au NPs in CBC reduced by NaBH$_4$. Figure a) 1st water addition, b) 2nd water addition and c) 3rd water addition.
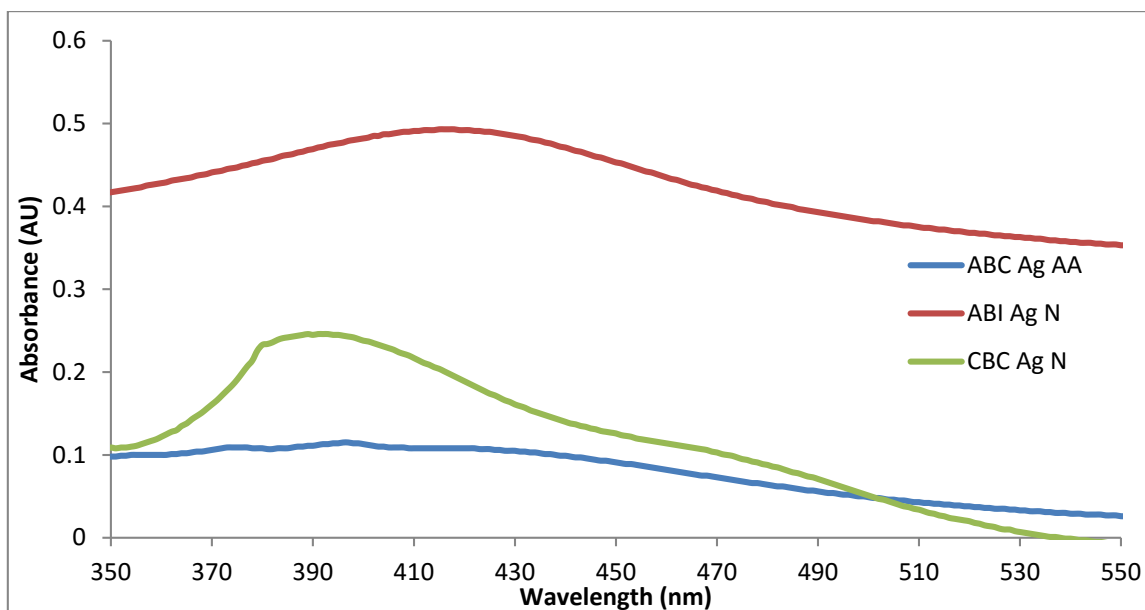
a
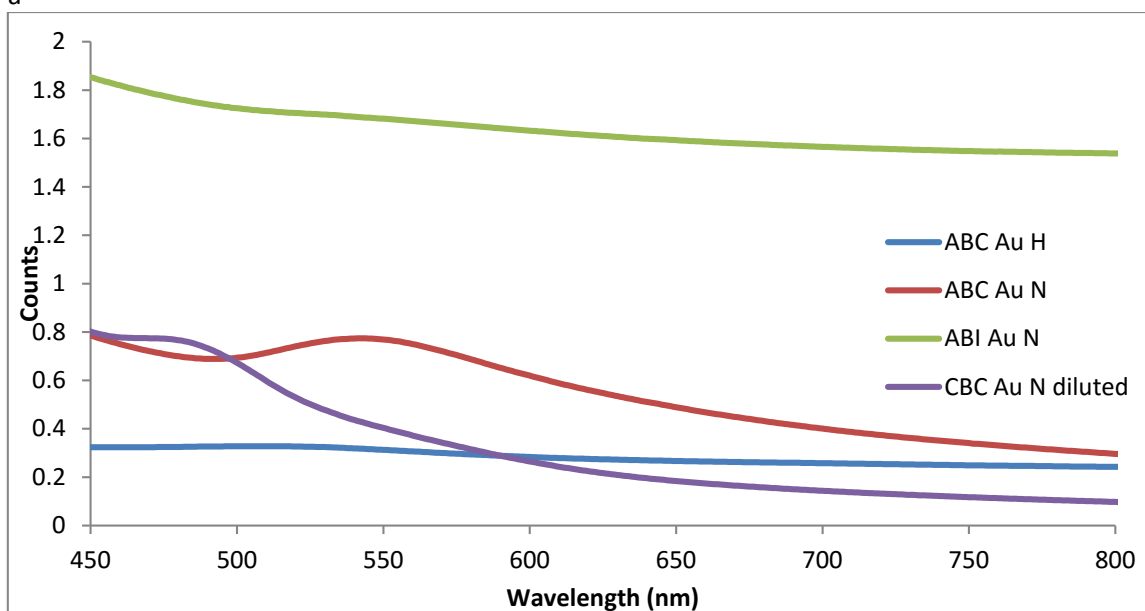
b

Figure 6.2: UV-Vis graphs to show NPs separated a) Ag NPs and b) Au NPs from shortlisted systems.

For the different NPs separated from the microemulsions, TEM was used for characterisation and the resulting NP diameters (size) were measured and summarised in Table 6.1. For separated Ag NPs (Fig. 6.3), the NPs maintained their sizes and shape when compared with their microemulsion counterparts in chapter 5. In the case of Au NPs the shapes were similar (Fig 6.4), but differences in sizes for those separated from ABC N and CBC N were shown, which could be due to incomplete recovery of the Au NPs during the separation process. The NP separations could be roughly supported as successful in maintaining the size and shape of the NPs depending on the microemulsion system used.

Table 6.1: Average NP sizes, size ranges and shapes for the shortlisted NPs systems within microemulsions and those separated from the microemulsions.

Microemulsion System	NPs in Microemulsion		Separated NPs	
	Avg NP Size (Size Range), nm	Shape	Avg NP Size (Size Range), nm	Shape
Ag NPs in ABC AA	37.9 (12-59)	Conjoined	31.9 (7.3-75.4)	Conjoined
Ag NPs in ABI N	8 (1.8-34.5)	Elliptical	8.7 (2.8-22.1)	Irregular
Ag NP in CBC N	39.6 (4.2-443.4)	Irregular		
Au NPs in ABC H	9.7 (3.1-43.8)	Irregular	7.7 (2.7-110.1)	Irregular
Au NPs in ABC N	29.5 (17.6-49)	Cuboids, Triangles, Hexagons, Rods	25.7 (11.2-56.1)	Cuboids and spherical
Au NPs in ABI N	16.3 (5.4-49.7)	Octogons, Irregular and Rods	83.3 (12.6-469.8)	Octogons, pentagons, hexagons
Au NPs in CBC N	39.9 (13.8-170.6)	Diamond, Irregular	13.9 (2.5-53.7)	Irregular
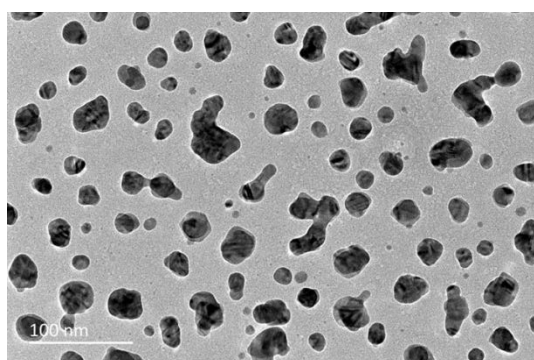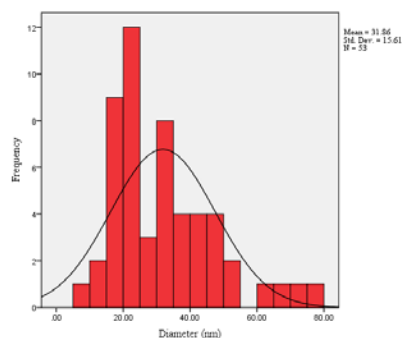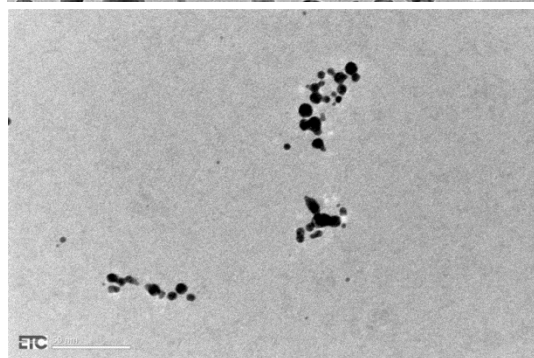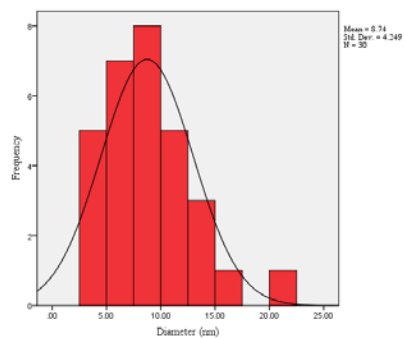
Figure 6.3: TEM images and corresponding size distribution histograms for NP separated Ag NPs within the bottom layer of the solution from a&b) ABC Ag AA and c&d) ABI Ag N.
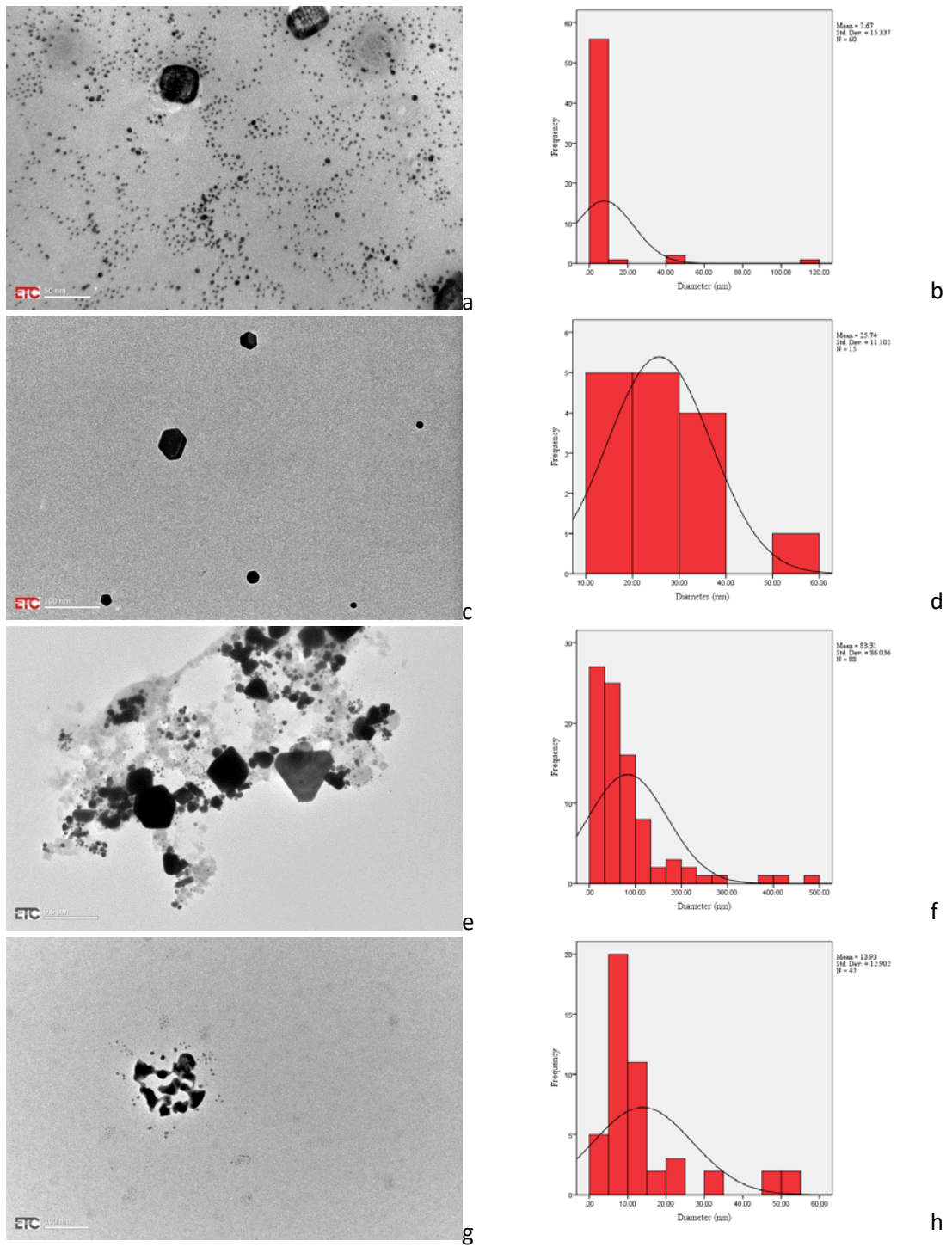
Figure 6.4: TEM images and corresponding size distribution histograms for NP separated Au NPs bottom layer from a&b) ABC Au H, c&d) ABC Au N, e&f) ABI Au N and g&h) CBC Au N.

Thereafter, the different shortlisted NPs both within microemulsions and those separated and dispersed in water, were tested for their SERS efficacy using both 514nm and 1064nm Raman spectrometers.

6.3.   Controls at 514nm and 1064nm Laser Wavelengths

The hindrance of scanning the microemulsion solutions with the 514nm laser was that the Renishaw set-up was not customised for liquid testing and within the microemulsion systems which had more volatile solvents, such as cyclohexane the microemulsions were shown to evaporate at an increased rate during the ongoing experiment. Therefore an alternative set-up was prepared; alpha cotton cellulose filter paper cut into 8mm circular discs and were immersed in the nanoparticle solutions for 24 hours, after which they were removed and the filter paper was shown to be coated with the NPs, through physisorption, taking the colour exhibited by the NPs within the microemulsion solution, which ranged from dark red, green and yellow for Au NPs and different shades of yellow for Ag NPs (Fig.6.5a), therefore it was presumed that the size and shape of the NPs shown within the solution were maintained on the filter paper.

The filter paper was then focused on using a light microscope component at 20x magnification (Fig.6.5b) within the 514nm Renishaw Raman bench-top system and tested. Control spectra for filter paper and NPs on filter paper were taken before addition of 1mM MBT for reliable results (Fig.6.5c). Few peaks were shown for the control systems (Table 6.2), with all the controls exhibiting a peak for lattice vibrations around 130 cm^{-1}. NPs on filter paper controls, except for Au NPs in the ABC systems, showed peaks for C-O stretch around 1094cm^{-1} and CH$_3$, CH$_2$ antisymmetric and symmetric stretching or O-H stretch around 2900cm^{-1}, which are all bonds that are associated with the cellulose chemical composition, supported by CH$_3$, CH$_2$ antisymmetric and symmetric stretching or O-H stretch also present within the cellulose filter paper control, albeit at a lower intensity compared to when NPs were added to the surface. The intensity of these peaks with the addition of NPs when compared to the filter paper control by itself shows that SERS is taking place as those particular bonds and additional ones not observed with the control filter paper can now be observed. The sharpness of the peaks for Ag NPs and Au NPs from the ABI systems, especially with

155

regards to the Au NP system, would indicate that these NP sizes and morphologies show the most

promise as SERS substrates with 514nm Raman.
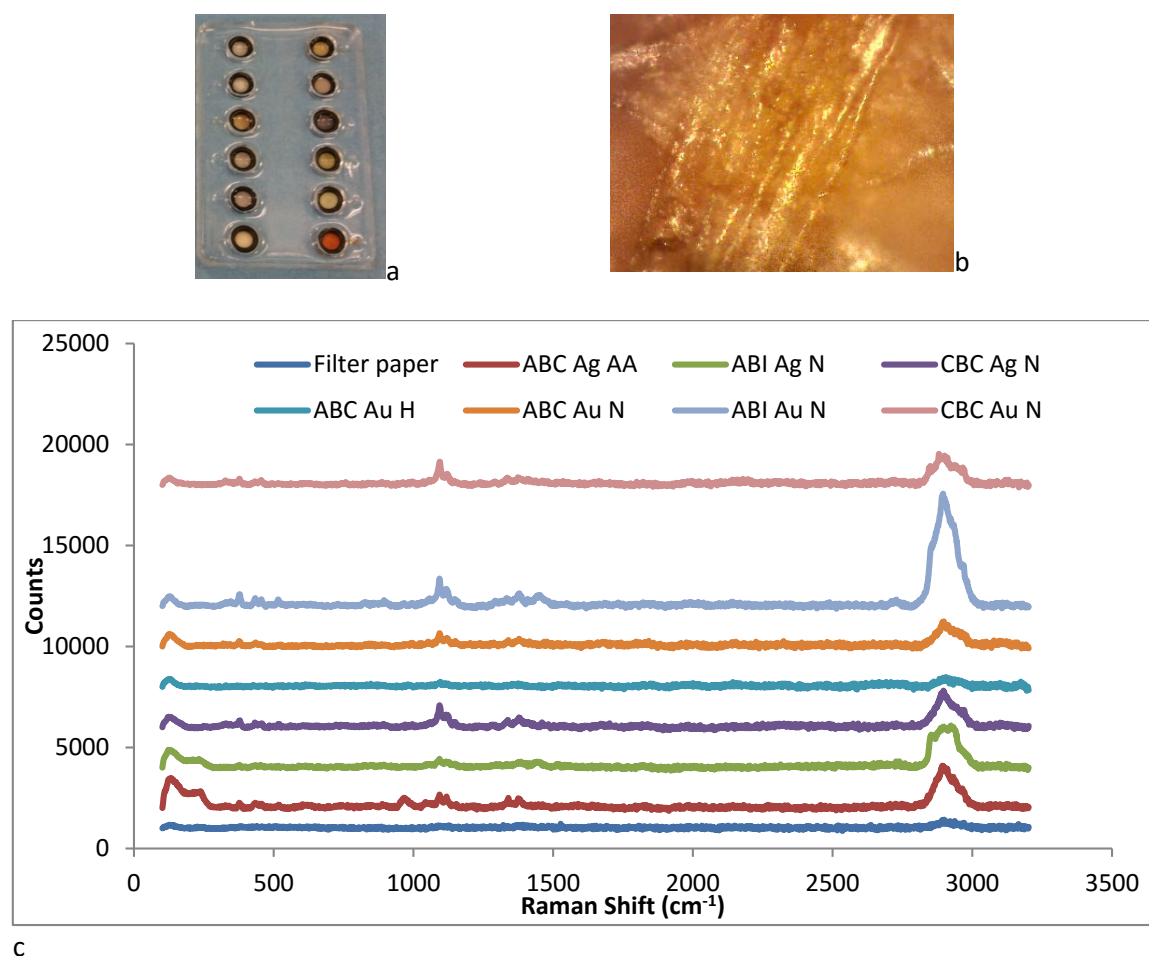
Figure 6.5: NPs from microemulsion on Filter paper, a) NPs on filter paper within an open-chip design, b) light microscope 20x magnification on filter paper fibres coated with NPs and c) 514nm Raman Spectra. Spectra offset for clarity.

For 1064nm Raman, NPs, both in solution and on filter paper could be tested using the portable

set-up. When NPs in microemulsion systems were tested (Fig.6.6a), there were strong peaks for the

microemulsion constituent's (Table 6.3). NP separated solutions (NPs in water) were also scanned

for their baseline Raman activity (Fig 6.6b). There were no notable peaks above noise to suggest

the presence of SERS peaks shown by NPs in water. This is indicative of the successful washing off

of any adsorbed microemulsions constituents on the NPs.
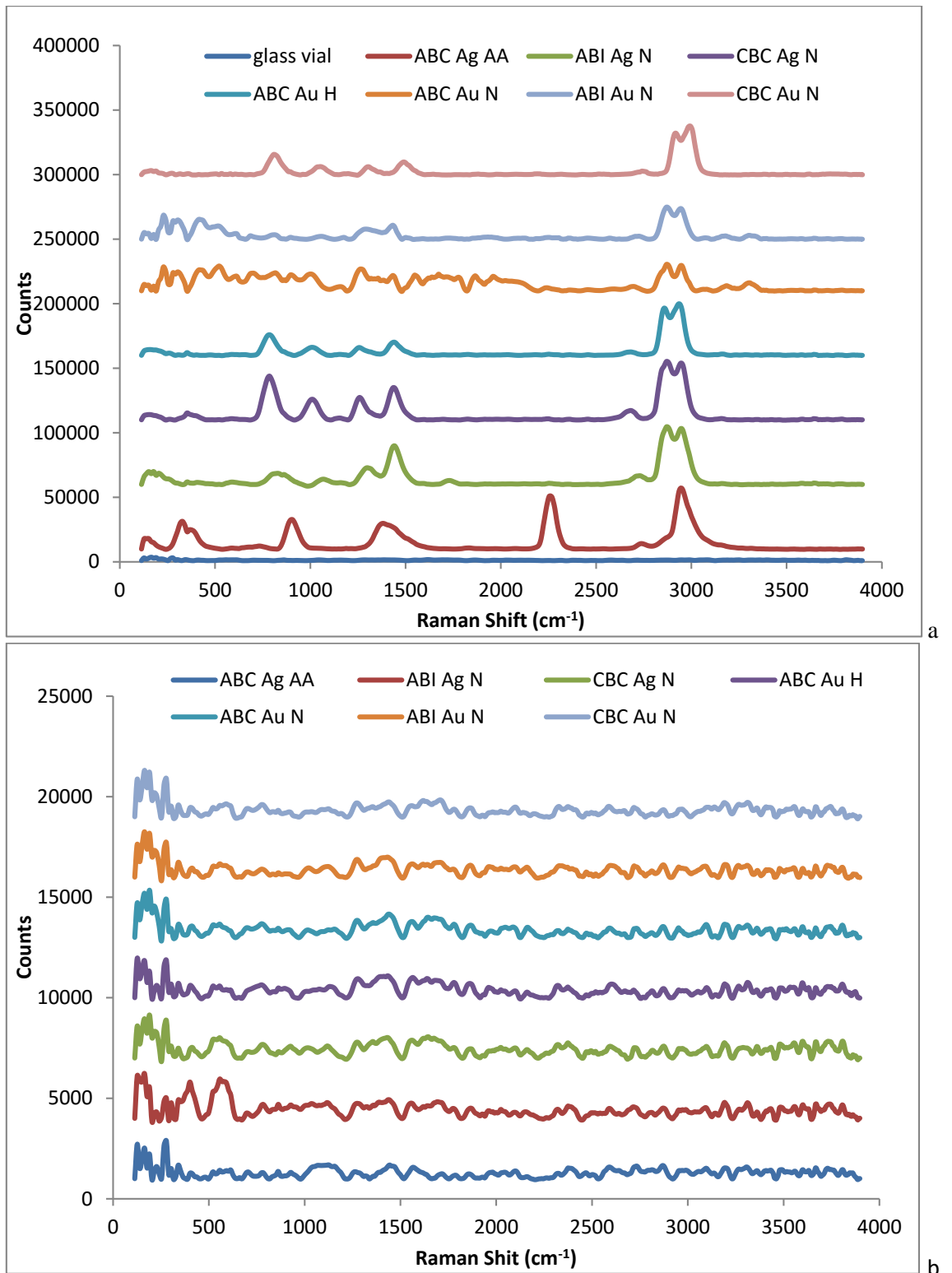
Figure 6.6: 1064nm Raman Spectra for a) NPs in microemulsions and b) Separated NPs in water. Spectra offset for clarity.

Table 6.2: 514nm Raman Peaks (cm^{-1}) and correlating bonds for filter paper and NPs on filter paper controls

Filter paper	ABC Ag AA	ABI Ag N	CBC Ag N	ABC Au H	ABC Au N	ABI Au N	CBC Au N	Peak Assignment
126	132.3	130.092	130.1	127.532	131.1	128.9	125.7	*Lattice vibrations in crystals*
	238.2 378.7		377.6		377.7	377.6	327.9 377.6	*CC symmetric bending or Metal-O stretch*
	434		408.5 457.6		435.9	433.7	455.3	*Metal-O stretch*
						516.8		*C-O-C bend*
	966.8							*=CH out-of-plane deformation or ring breathing mode*
	1094.1	1092.92	1093.9		1094.2 1285.7	1093.4 117.3	1093.5	*C-O stretch*
						1148.2		*C-O-C antisymmetric stretch*
	1339.8		1337.6		1378.7		1335.5	*COO- symmetric stretch*
	1375.2	1383.5	1377.6			1377.7	1379.2	*CH3 symmetric deformation*
		1451.34				1450.6		*CH3 antisymmetric deformation*
2899.4	2900.3	2851.78 2886.3 2934.01	2985.8		2389.8	2900.2	2881.1 2965.4	*CH3, CH2 antisymmetric, symmetric stretching respectively or OH stretch*
			3099.3			3085		*=C-H stretch*

Table 6.3: 1064nm Raman Peaks (cm⁻¹) and correlating bonds for glass vial and NPs in microemulsion solution controls

Glass Vial	ABC Ag AA	ABI Ag N	CBC Ag N	ABC Au H	ABC Au N	ABI Au N	CBC Au N	Peak Assignment
164.3								Lattice vibrations
					230.1	231.9 419.0		Metal-O stretch
	328.1		360.7	354.8		399.0		Metal-O stretch or CC bend
					520.7		516.7	C-O-C bend
		593.4						C-CO-C bend
612.8								C=O out-of-plane bend
					694.5			C-C-CHO bend
	731.5							CH$_2$ rocking
855.8		835.6	786.0	786.2			783.8	CH out-of-plane deformation
	902.9							CH$_2$ out-of-plane wag
			1010.6	1009.4	1005.4		1012.9	Ring breathing mode or CC stretch
1043.9		1065.4				1053.9		C-O stretch
			1259.5	1258.5	1265.7		1260.6	C-O-C antisymmetric stretch or CC stretch
	1402.2		1439.2	1438.9		1427.8		In-plane OH bending
		1442.3					1442.5	CH$_3$ antisymmetric deformation
					1551.8			CC stretch
1617.6								C=C stretch
		1728.2			1732.1	1731.0		C=O stretch
1864.3	1828.1							C=O antisymmetric stretch
	2260.3	2258.9		2249.6	2098.7	2120.3 2247.2	2134.1	C≡C stretch
						2461.6		OH stretch
		2720.9	2677.1	2677.0	2694.2		2688.3	Overtone of CH bend
	2736.9					2719.0		CH stretching modes
	2949.8	2908.5 2875.4 2946.3	2902.6 2946.9 2875.4	2925.8	2868.7 2946.0	2877.8 2946.3	2929.0	CH$_3$, CH$_2$ antisymmetric, symmetric stretching respectively or OH stretch
		3648.5	3064.9 3159.0	3162.5	3182.5	3175.9 3313.0		OH stretch
			3647.5	3647.2			3700.8	O-H stretch

When NPs from microemulsions or separated solutions were incorporated on filter paper were tested with 1064nm Raman, the SERS substrates were shown to burn. Therefore an open chamber microfluidic chip was prepared for testing the NPs on filter paper in a wet state with deionised water. The results for the control NPs on filter paper baseline with 1064nm Raman, showed no significant peaks (apart from lattice peaks below 150cm^{-1}) above the noise within the spectra (Fig. 6.7).
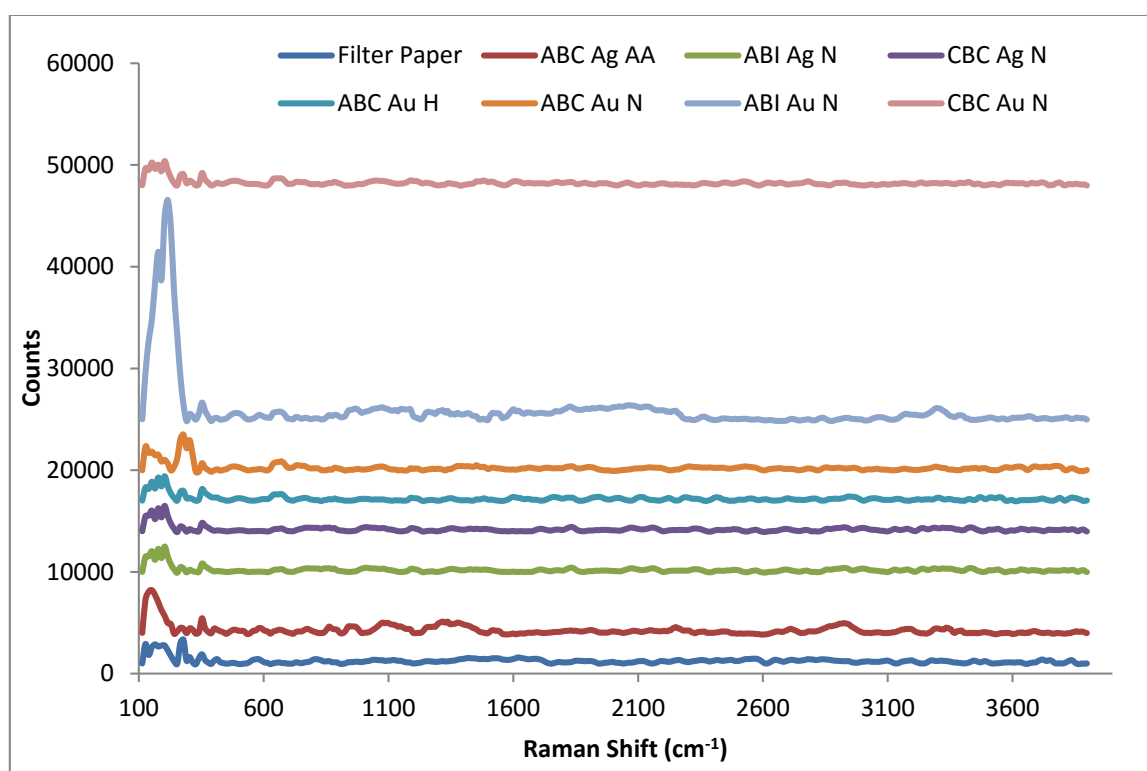
Figure 6.7: 1064nm Raman Spectra for NPs from microemulsion solutions incorporated on filter paper. Spectra offset for clarity.

The separated NPs in water were also incorporated on filter paper and tested for their baseline SERS spectra with 514nm and 1064nm Raman (Fig. 6.8). Again there was no significant peaks present within the spectra above the noise.
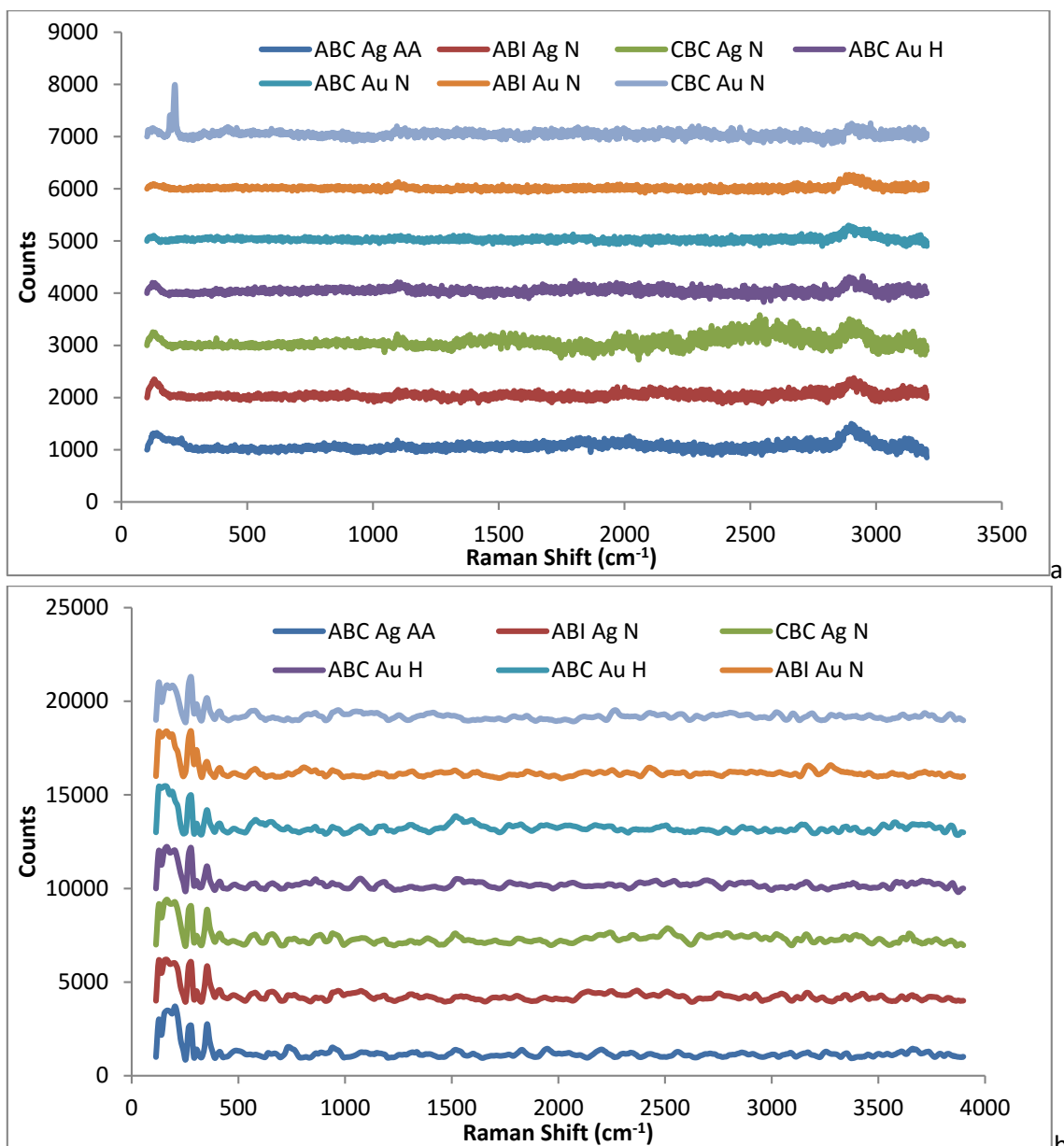
Figure 6.8: Separated NPs from shortlisted microemulsion systems on filter paper and control spectra obtained for a) 514nm Raman and b) 1064nm Raman. Spectra offset for clarity.

6.4. MBT enhancement of NP SERS substrates from microemulsions and NP separated solutions

The base spectra and corresponding peaks for solid MBT acquired using 514nm and 1064nm Raman are presented in Figure 4.10 and Table 4.5 in chapter 4. Not all peaks are usually seen in the SERS spectra of MBT. When the MBT is attached on the SERS substrates, enhancement of particular peaks, namely C-S stretch (~10946m^{-1}) and carbon ring stretch (~1594cm^{-1}), was prominent.

For testing the SERS substrates, as with Ag wire substrates in Chapter 4, 1mM MBT dissolved in ethanol was prepared and NPs on filter paper were immersed within the solution for a minimum of 12 hours and then dried before testing. For testing NPs in microemulsion and in separated forms in solution, 20µl of 1mM MBT was added to 1ml solutions for a minimum of 12 hours before testing as well.
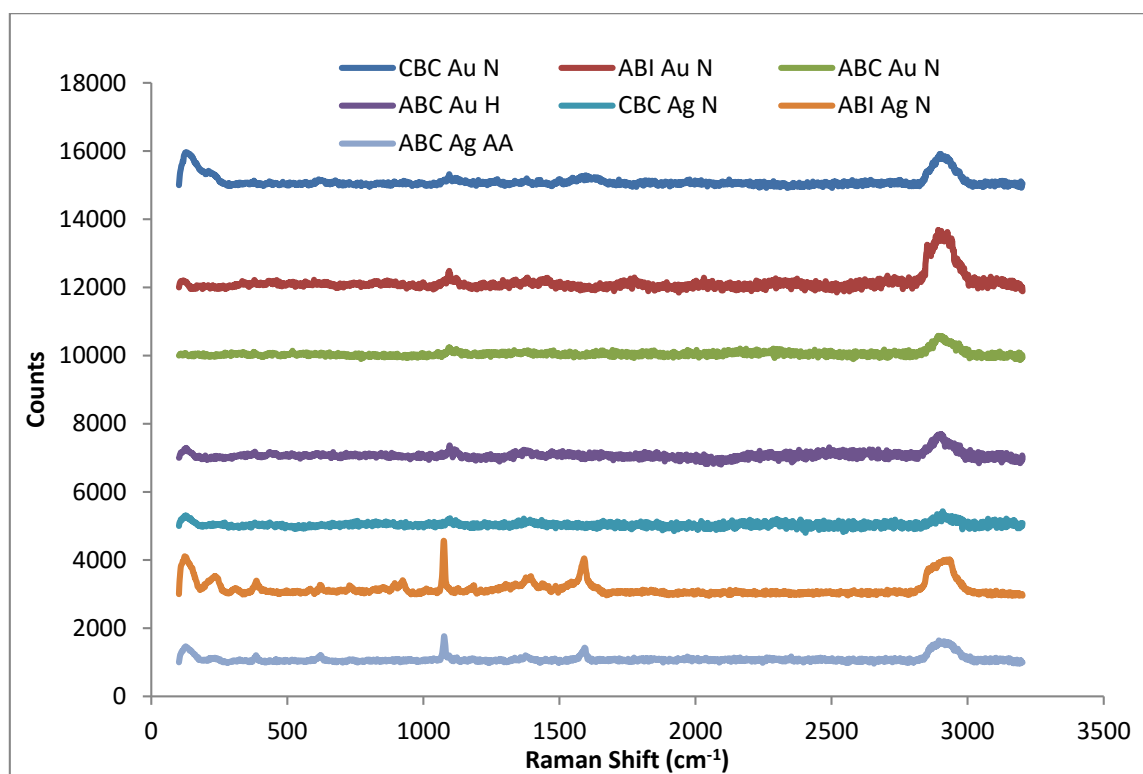
Figure 6.9: 514nm SERS Spectra for shortlisted NP from microemulsions with 1mM MBT on filter paper. Spectra offset for clarity.

514nm Raman spectra shown in Figure 6.9 for 1mM MBT with NPs on filter paper, SERS enhancement was observed for Ag NPs from ABC AA and ABI N microemulsion systems. Ag NPs from the ABI microemulsion system showed the highest enhancement. Despite the preference of 514nm Raman for resonance with Ag SERS substrates, Ag NPs from CBC N microemulsion system did not show SERS enhancement of MBT. Au NPs from all microemulsion systems on filter paper provided a C-S stretch (~1096cm^{-1}) and Au NPs from CBC N also provided an additional peak for ring stretch (1596cm^{-1}) (Table 6.4).

Table 6.4: 514nm Raman peaks (cm^{-1}) associated with MBT bonds shown on NP systems on filter paper.

ABC Ag AA	ABI Ag N	CBC Ag N	ABC Au H	ABC Au N	ABI Au N	CBC Au N	Peak assignments
	584.5						C-S stretch
	1186.0		1094.4	1099.7	1094.6	1095.3	C-S stretch
	1588.9					1588.4	Ring stretch doublet
1593.5							Ring stretch

When NPs on filter paper with 1mM MBT were tested with 1064nm Raman shown in Figure 6.10, the results in general did not show definitive MBT peaks within the spectra. With only Ag NPs from the CBC N microemulsion showing a C-S stretch related to MBT.
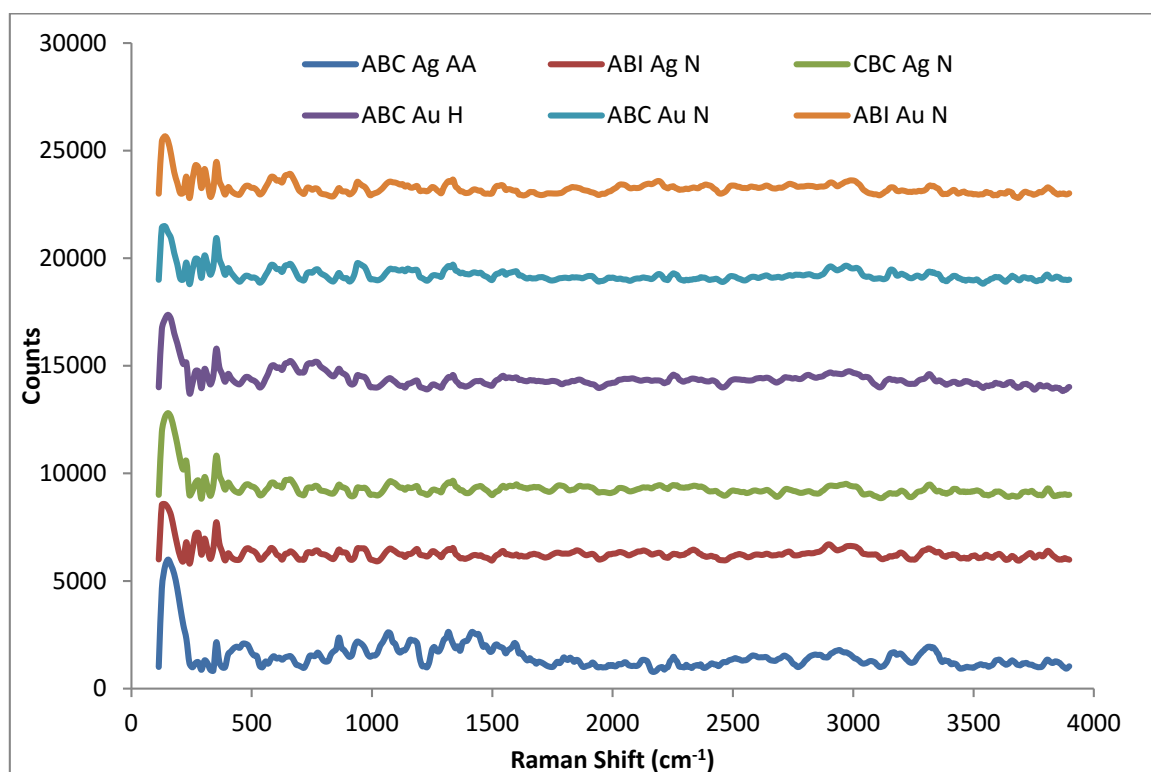
Figure 6.10: 1064nm Raman Spectra for NPs on filter paper with 1mM MBT. Spectra offset for clarity.

When the NP microemulsions with 1mM MBT were tested with 1064nm Raman (Fig. 6.11), the results showed similar spectra as that observed by the NP microemulsion controls. Ag and Au NPs within the ABC microemulsion system showed an additional peak for S-H stretch. The S-H stretch would indicate that MBT has not attached to the NP surface. However, its presence does indicate

MBT. Potentially the SERS peaks for MBT are being masked by the strong microemulsion constituent peaks.
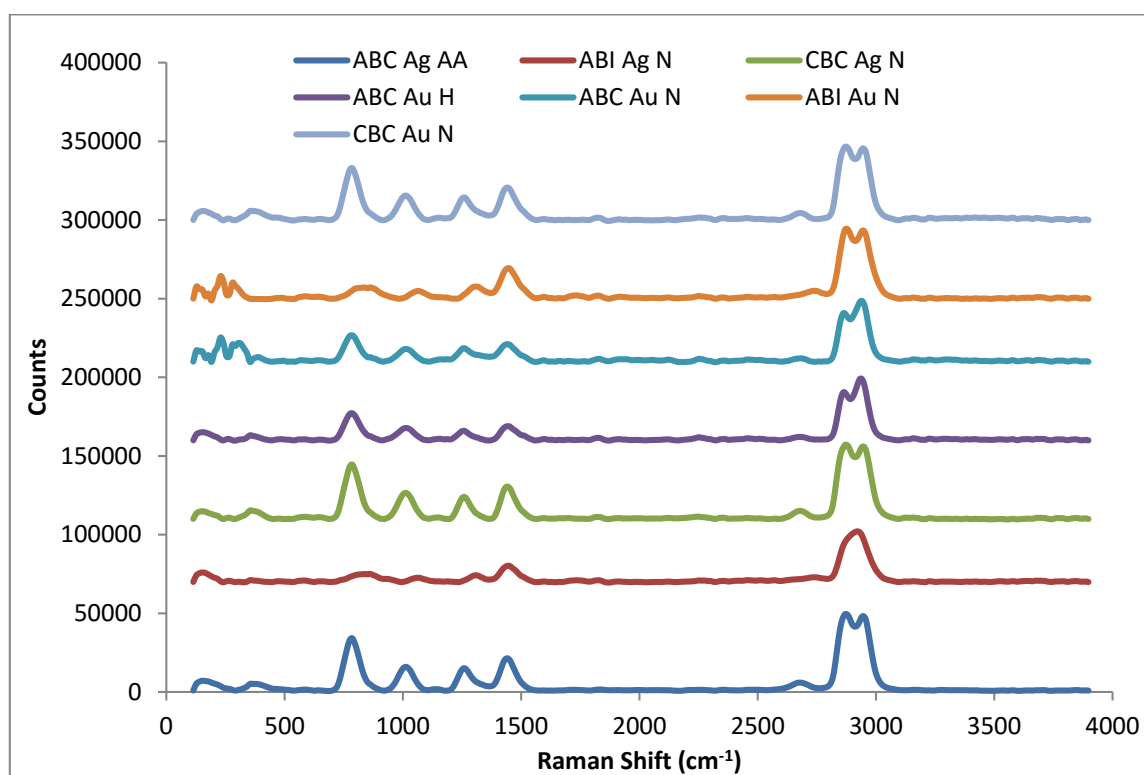
Figure 6.11: 1064nm Raman Spectra for NPs within microemulsion solutions with 1mM MBT. Spectra offset for clarity.

The 514nm Raman spectra for separated NPs on filter paper, Figure 6.12a, shows SERS peaks for MBT with Ag NPs from ABC AA and ABI N. Ag NPs from the ABI system showed the highest enhancement. With further analysis, Table 6.5, all NP separated systems except for Au NPs from ABC Au H provided a peak for C-S stretch around 1094cm^{-1}. All 3 Ag NP systems also provided a carbon ring stretch peak, which was not shown in the control spectra and therefore can be used for supporting the presence of MBT on the SERS substrates. When comparing these results for separated NPs on filter paper using 1064nm Raman (Fig. 6.12b), did not show SERS peaks for MBT with the exception of Au NPs separated from ABI N microemulsions.
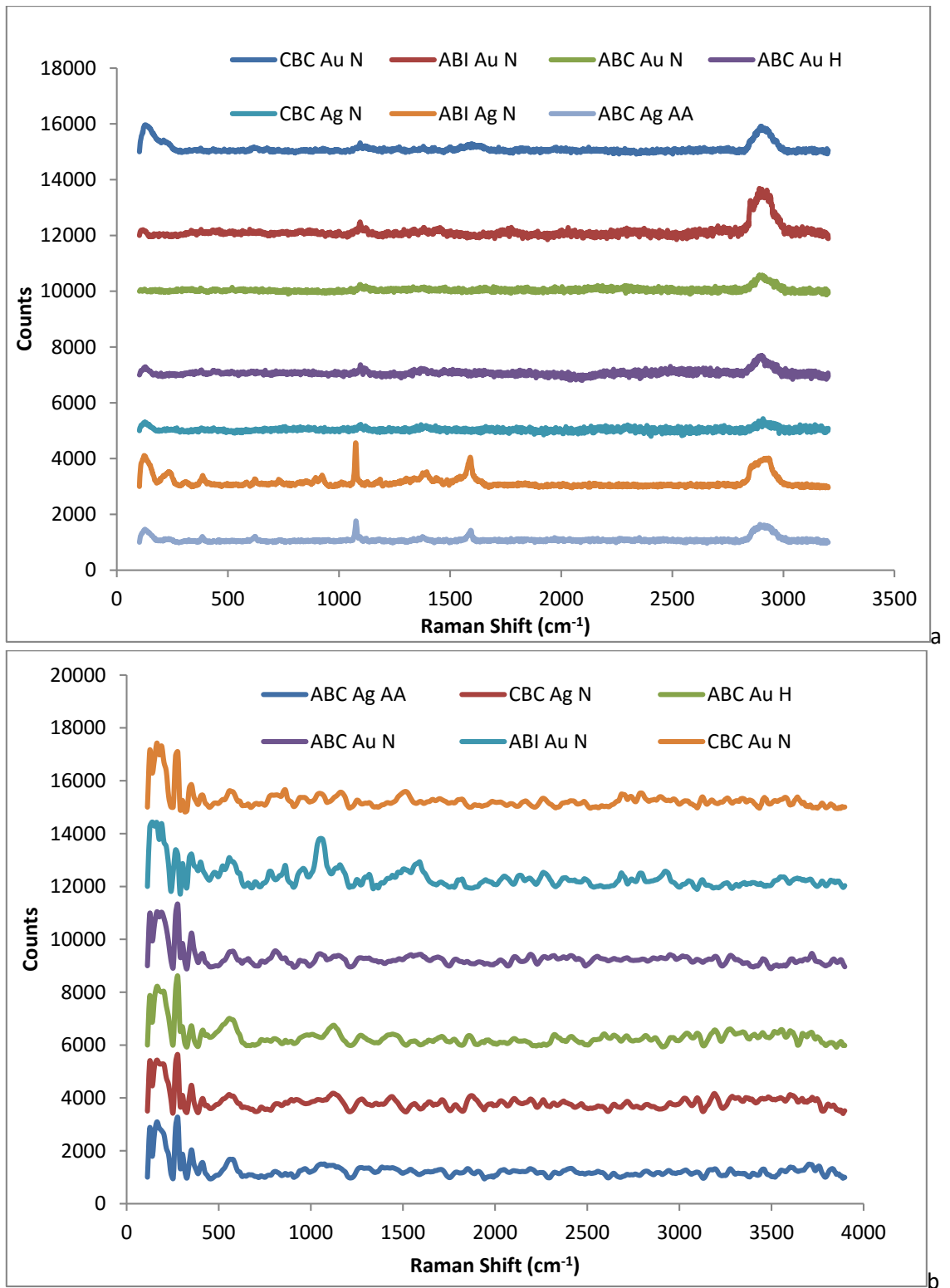
Figure 6.12: Separated NPs on filter paper with 1mM MBT using a) 514nm Raman and b) 1064nm Raman. Spectra offset for clarity.

Table 6.5: 514nm Raman Peaks (cm^{-1}) and corresponding bonds for MBT on Separated NPs on filter paper with 1mM MBT

ABC Ag AA	ABI Ag N	CBC Ag N	ABC Au H	ABC Au H	ABI Au N	CBC Au N	Peak Assignment
1076.6	1076.4	1076.3		1095.5	1094.0	1095.1	*C-S stretch*
1588.2	1592.7	1591.0					*Carbon Ring stretch*

When the separated NP solutions with 1mM MBT were tested with 1064nm Raman, the spectra, Figure 6.13 did not show any visible characteristic MBT peaks that could be differentiated from the background peaks present.
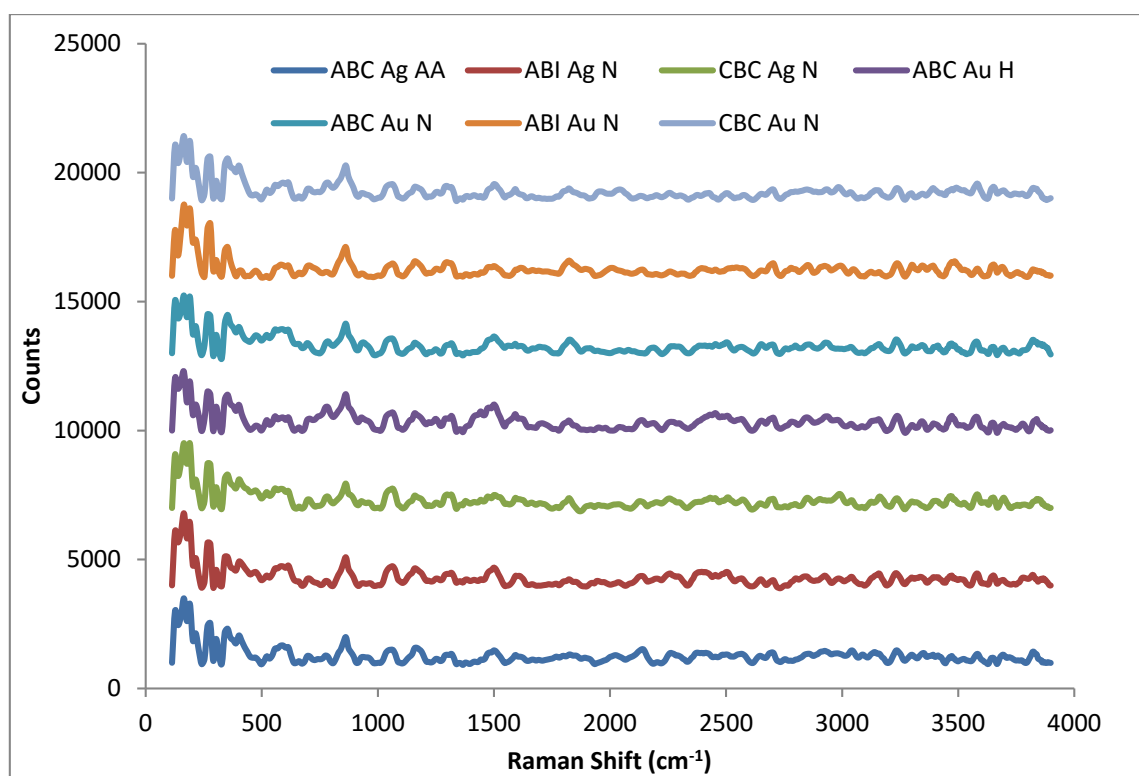
Figure 6.13: 1064nm Raman Spectra for separated NP solutions with 1mM MBT. Spectra offset for clarity.

6.5. Chapter Summary

This chapter summarises the separation of NPs from microemulsions and their characterization. Thereafter, the short-listed NPs of varied sizes and shapes, both within and separated from microemulsions, were tested for their ability to function as SERS substrates.

The NPs are stable within microemulsion, however the microemulsion constituents, particularly the surfactant can mask or prevent efficient SERS spectra for the analyte of interest. Therefore the NPs were separated from the microemulsions using an optimised separation method with water phase disruption. Centrifugation and phase disruption using anti-solvents was initially tested as a methodology for NP separation, however they were ruled out due to their inefficiency in separation. The separated NPs had similar sizes and shapes in general compared with their microemulsion counterparts.

The efficacy of the SERS substrates with 1mM MBT was tested with 514nm and 1064nm Raman. Due to instrumentation difficulties with 514nm Raman, NPs within microemulsion and water were incorporated onto filter paper for testing ease. Liquids were able to be tested with 1064nm Raman, however due to the high power output of the portable instrumentation a fluidic chip was prepared for immersing the NPs on filter paper in deionised water as without doing so the NPs on filter paper were shown to burn.

The results showed a significant divide in preference of particular metal types with either 514nm or 1064nm. Ag NPs on filter paper were shown to have MBT SERS efficacy with 514nm Raman whereas Au NPs showed better efficacy with 1064nm Raman. The intensity of the peaks however was weak due to the longer wavelength used. Au NPs from ABI N on filter paper, which had an average NP size of 16.3nm with increased anisotropically shaped rods and squares and Au NPs from ABC N microemulsion on filter paper which had square, triangle and hexagon morphologies with an average size of 29.5nm showed MBT enhancement with 1064nm Raman. For Ag NPs, from ABI N microemulsion on filter paper showed the highest MBT enhancement with

514nm Raman and had an average size of 7.8nm with large sharper NPs present within the solution, therefore the size of the NPs was not as significant as the anisotropy for SERS enhancement.

When the NPs were tested within solution with 1064nm Raman, MBT signal with ABC microemulsion systems was seen. Due to SERS being a surface layer technique the presence of surfactant upon the surface and high signal for solvents, was theorised as masking the signal of MBT for some of the systems. The separated NPs in water also did not show MBT peaks, which could be due to the lack of hot-spots within the solution. However, when these separated NP particles were placed on filter paper, they gave better results compared to the NPs deposited directly from microemulsions on filter paper, confirming that the presence of microemulsion constituents could mask the access of the NP surface for MBT.

To conclude, the hypothesis of metallic NPs of large size (>30nm) with anisotropic shapes, would provide SERS activity within solutions was disproved. Instead the NPs when placed on filter paper, were shown to give SERS spectra for MBT.

Chapter 7: SERS Substrate Design: NPs on electrospun membranes

7.1.   Introduction

Electrospinning is a simple and cost-effective technique, which uses an electric field to initiate the spinning of a polymer from solution into solid nanofibers on to a grounded collector to form nanostructured fibroporous mesh. The large surface area to volume ratio and porosity of such electrospun membranes is beneficial for the SERS substrate design. NPs, when coated on the electrospun fibres' surface, a large surface area per unit volume is generated for SERS interrogation. One such design was reported to result in increased hot-spot formation, thus, enabling a noted increase in SERS enhancement by 50 times compared to other SERS substrate designs (Lee et al, 2011).

The aim of this chapter was to develop NPs incorporated insoluble electrospun membranes (the third SERS substrate design category). Specifically, methods were optimized to electrospin PAA and EG based insoluble electrospun membranes, to covalently graft with Au or Ag NPs developed in this study (Chapter 4 & 5) on the electrospun fibre surface, to characterize the developed SERS substrates for their morphology, chemical and physical properties; as well as their efficacy as SERS substrates using MBT as the model Raman active molecule, and 514nm and 1064nm Raman spectrometers.

7.2.   Insoluble PAA-EG electrospun membranes

The equipment used for electrospinning the PAA-EG fibres was designed and built in-house, and it has humidity and temperature control features. The method used for electrospinning PAA-EG membranes was modified from that reported by Meng et. al. 2015.

7.2.1. Electrospinning Parameters

An electrospinning machine having controlled temperature and humidity was made with assistance from AC solutions ltd, as detailed in chapter 3. Control of temperature and humidity was essential for electrospinning PAA. A 4% (w/v) solution of PAA and EG at 88:12 weight ratio in ethanol

was prepared and incubated at 4°C for 72 hours before being used for electrospinning. The conductivity of this solution was poor (1µS) (Table 7.1), and hence did not form a polymer jet up on electrospinning. The polymer particles require an optimum conductivity to align and break the surface tension of the solution to form a polymer jet, which is critical for the electrospinning process (Lukas et al, 2009). To make the PAA-EG solution in ethanol electrospinnable, a small quantity of 1M H_2SO_4 was added, thus increasing its conductivity (Table 7.1). Addition of 25µl per ml of 1M H_2SO_4 to the PAA-EG solution increased the conductivity to about 581µS, which was optimal for electrospinning, as evident under light microscopy (Fig. 7.1). A higher conductivity of 950µS, when 50µl per ml of 1M H_2SO_4 was added to the PAA-EG solution, caused residual charge on the polymer particles preventing them from reaching the collector and forming a web-like structure between the spinneret needle and the collector. Electrospinning of PAA-EG fibres was achieved using the parameters: 4% polymer (88:12 percent weight ratio of PAA to EG) solution aged for 72h at 4°C; activation with addition of 25µl of 1M H_2SO_4 per 1ml polymer solution, just before electrospinning; 22 gauge flat-tipped needle as the spinneret; a distance of 20cm distance between spinneret and needle; 0.8ml/hr flow rate; 15kV voltage; with humidity below 10% and temperature <10°C.

Electrospinning requires the polymer of interest to be dissolved in an appropriate solvent, to provide a solution that has enough conductivity, viscosity and surface tension to be electrospun. However once these electrospun membranes are produced if the membrane is placed in contact with the same solvent, the integrity of the electrospun membrane is lost (dissolves). As the desired SERS substrate is to have a robust design for use ex-vivo in analytical testing, the electrospun membranes were required to be insoluble, to minimise problems to stability if used as a universal substrate design. Following electrospinning, the PAA-EG membranes were heated at 130°C for 30 minutes to facilitate crosslinking between the PAA polymer chains with the bifunctional crosslinker EG. The H_2SO_4, added just before electrospinning, is also said to have an important role in the catalysis of the crosslinking of PAA with EG (Meng et. al. 2015). Crosslinking was confirmed by the fact that the crosslinked membranes were insoluble both in ethanol and deionised water.

Table 7.1: Conductivity of PAA-EG electrospinning solution at different stages of preparation.

Electrospinning Solution	Conductivity (µS)
4% PAA (w/v) in ethanol	1
4% PAA and EG (at 88:12 v/v ratio) (w/v) in ethanol	1
4% PAA and EG (at 88:12 v/v ratio) (w/v) in ethanol plus 50µl per ml of 1M H₂SO₄	950
4% PAA and EG (at 88:12 v/v ratio) (w/v) in ethanol plus 25µl per ml of 1M H₂SO₄	581
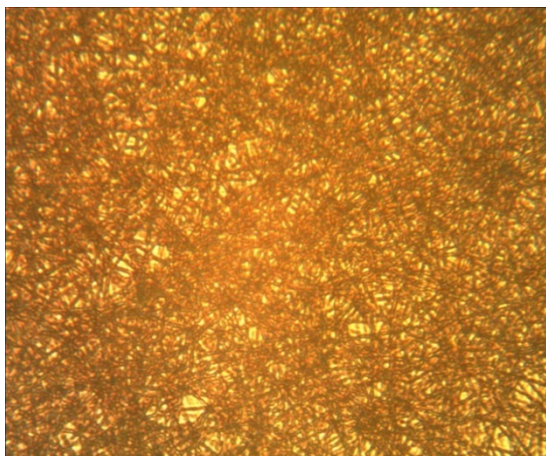
Figure 7.1: Light microscope image showing the electrospun PAA-EG fibrous membrane; 2 minutes spinning time with addition of 25µl per ml of 1M H_2SO_4; 60x magnification.

The electrospinning time was varied: 10, 20, 40, 60 and 120 minutes to obtain PAA-EG membranes of different thicknesses. Circular 8mm discs of the electrospun membranes were cut using a biopsy punch and used for weight and thickness measurements. The results in Figure 7.2, show that both the weight (R^2=0.8738, range: 0.35 to 0.68mg) and thickness (R^2=0.9428, range: 15.54 to 40.63µm) follow a linear increasing trend with increasing time of deposition. The 40 minute deposition time that produced membranes of thickness about 16.73 µm was chosen for further studies.

7.2.2. Characterisation of the Insoluble Electrospun PAA-EG Membranes

SEM images were recorded for the insoluble electrospun PAA-EG membranes and the typical fibroporous structure for electrospun membranes with random fibre orientation was observed (Fig. 7.3a). Image J software was then used to measure the fibre diameter. The fibre diameter

distribution histogram is shown in Figure 6.3b and it ranged between 187-447nm with an average

fibre diameter of 330.51nm.
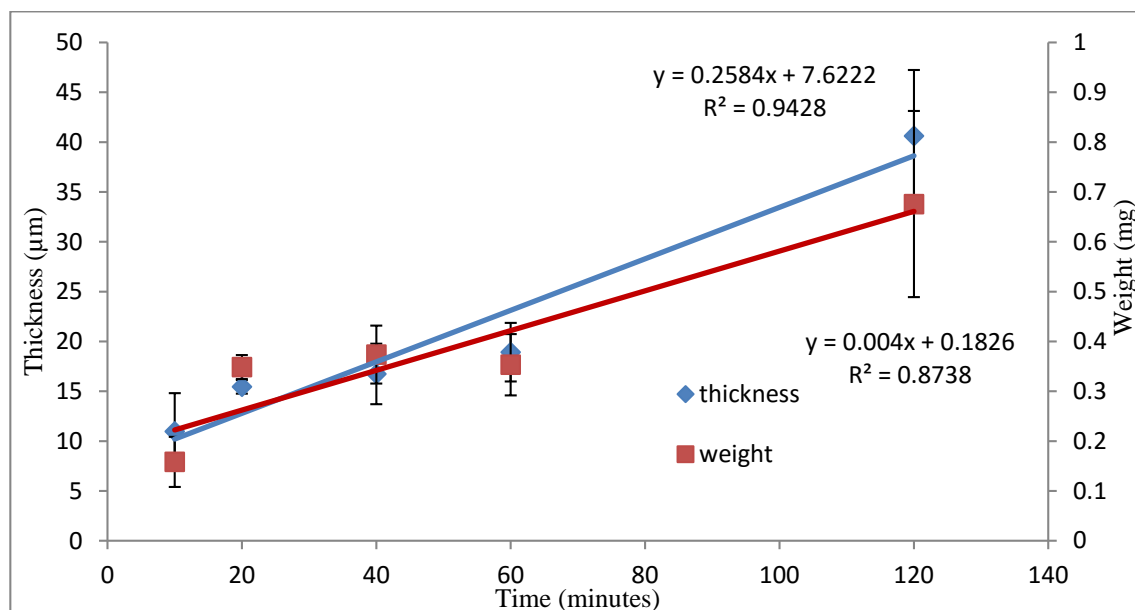
Figure 7.2: Scatter graph to show the thickness and weight of electrospun PAA-EG fibres after cross-linking at deposition times 10, 20, 60 and 120 minutes. Standard error, n=5.
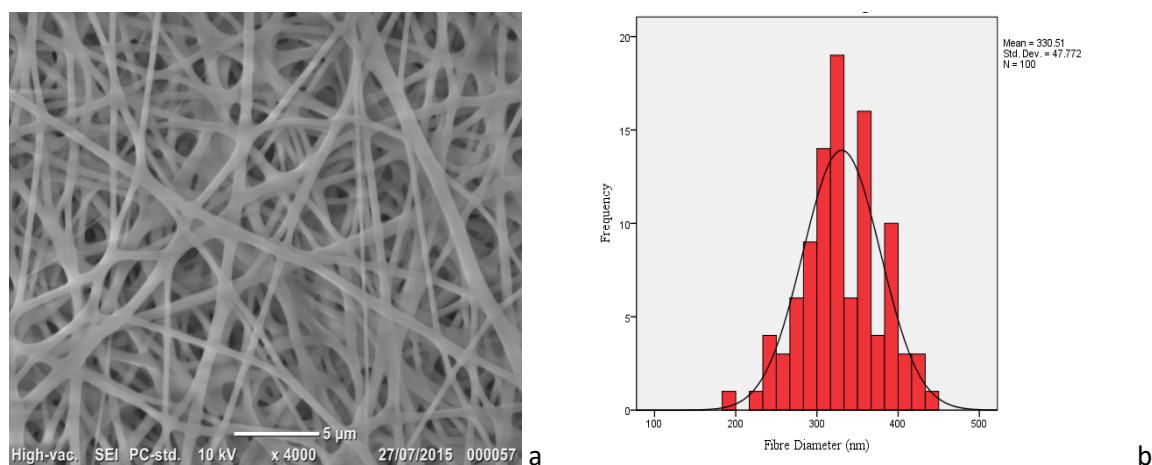
Figure 7.3: 40 minutes electrospun PAA-EG fibre morphology shown with a) SEM x4000 magnification and b) correlating fibre diameter histogram.

To determine the efficiency of the cross-linking reaction, FTIR spectra of the insoluble PAA-EG

membrane and compared with its precursors, PAA and EG. The FTIR spectra and their

corresponding peak assignment table are presented in Figure 7.4. and Table 7.2 respectively. It was

evident from the FTIR spectral data that the PAA-EG fibres were efficiently cross-linked as the

typical EG peaks of 3293cm^{-1} representing the O-H stretch, and the sharp doublet at 2935.46 and

2873.52cm^{-1} for antisymmetric and symmetric –CH$_2$ stretch were absent in the crosslinked PAA-EG

membrane's spectra (Fig. 7.4). Further, a broad peak ranging between 2700 and 3300cm^{-1} indicating the carboxylic acid peak on PAA and a slight shift in the carbonyl stretching vibration at 1695 to 1698cm^{-1} as well as a decrease in its intensity indicates the completion of crosslinking between PAA and EG. An additional indicator that PAA-EG was efficiently cross-linked is the presence of a peak for C-H out-of-plane deformations and CH$_2$ out-of-plane wag at 872.12 and 798.89cm^{-1} which correlate the corresponding sharp peaks in the EG spectrum.
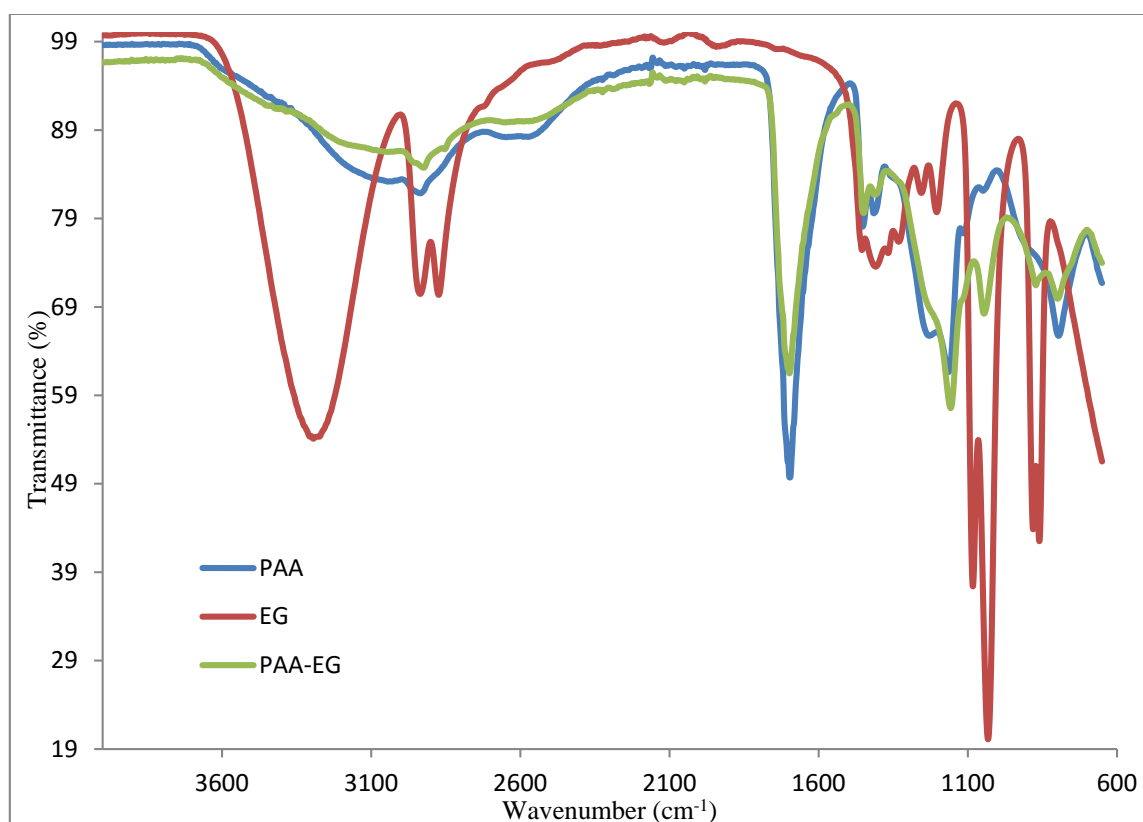
Figure 7.4: FTIR graph to show the cross-linking of PAA-EG electrospun membranes when compared to its precursor constituents.

7.3. Surface Modification of PAA-EG electrospun membranes with Cysteamine

For the fabrication of nanoparticle incorporated insoluble PAA-EG electrospun membranes, the membrane's surface was first modified by covalently grafting cysteamine. The amine groups on cysteamine was reacted with the remaining carboxyl groups on PAA-EG membrane, using zero-length carbodiimide crosslinking, resulting in a thiolated surface on the fibres of the electrospun membranes. The thiol groups were then utilized to coat Au and Ag NPs on the insoluble electrospun

173

membranes through the spontaneous reaction between the thiol groups with Au or Ag metal to form covalent linkages (Au-S / Ag-S).

Table 7.2: FTIR peaks (cm^{-1}) of PAA, EG and cross-linked PAA-EG electrospun membrane with their corresponding peak assignments.

PAA	EG	PAA-EG	Peak Assignment
	3293.6		*O-H stretch*
2934.4	2935.5	2924.4	*-CH antisymmetric and symmetric stretch or -OH stretch*
	2873.5		*in carboxylic acids*
2650.8			*O-H stretching*
	2117.7		*C≡C stretch*
2050		2050.9	*X=C=Y stretch (allenes, ketenes, isocyanates,*
			isothiocyanates)
1981.1	1943.4	1981.1	*C=C=C antisymmetric stretch*
1695.5		1698.3	*C=O stretch or COO- peak*
1452.7	1454.8	1449.2	*CH2 scissors vibration or CH3 symmetric deformation*
1415.7	1408.6	1410	*In-plane OH bending (carboxylic acids)*
	1367		*CH3 deformations*
	1331.6		*COO- symmetric stretch*
1229.1	1255.9	1157.5	*C-O-C stretch*
1164.5	1204.4		
1115.1	1083.1		
	1032.3	1045.7	*C-O stretch*
795.9	881.3	872.1	*CH out-of-plane deformation or CH2 out-of-plane wag*
	860.3	798.9	

The efficiency of the surface modification was characterised with FTIR as shown in figure 6.5 and the corresponding peak assignments presented in Table 6.3. The absence of the broad carboxylic acid peak between 2700cm^{-1} and 3300cm^{-1} and the carboxyl peak at 1695cm^{-1}; and the appearance of the 1716cm^{-1}, 1633cm^{-1}, and 1549cm^{-1}, representing carbonyl stretch, amide I (mainly C=O stretch) / H-O-H stretch, and amide II (N-H bend in plane, and C-N stretch) respectively were indicative of the successful grafting of cysteamine on the surface of the electrospun fibres.

The base cysteamine hydrochloride spectrum showed multiple other peaks. A large broad range of peaks between 2337.2 to 2841.5cm^{-1}, which correlate with NH stretching modes present within the structure and CH stretching modes when attached to N. The spectrum also show a large range of peaks between 632 to 1608.9cm^{-1}, these correlate with peaks for NH$_2$ deformation, 1608.9 and 1584.8cm^{-1}, NH$_3^+$ deformation, 1503.9cm^{-1}, CH$_2$ scissors vibration, 1469.1 and 1455.9cm^{-1}, different C-N stretching interactions and significantly C-S stretch at 758.3, 748.9 and 660.6cm^{-1} as

well as C-Cl stretch of the hydrochloride component of the cysteamine hydrochloride solid at 632.2cm^{-1}. A majority of these peaks observed in the FTIR spectrum of cysteamine hydrochloride were absent and some shifted on the PAA-EG-Cyste spectrum as described above, further reiterating the successful grafting of cysteamine on the PAA-EG membrane surface.
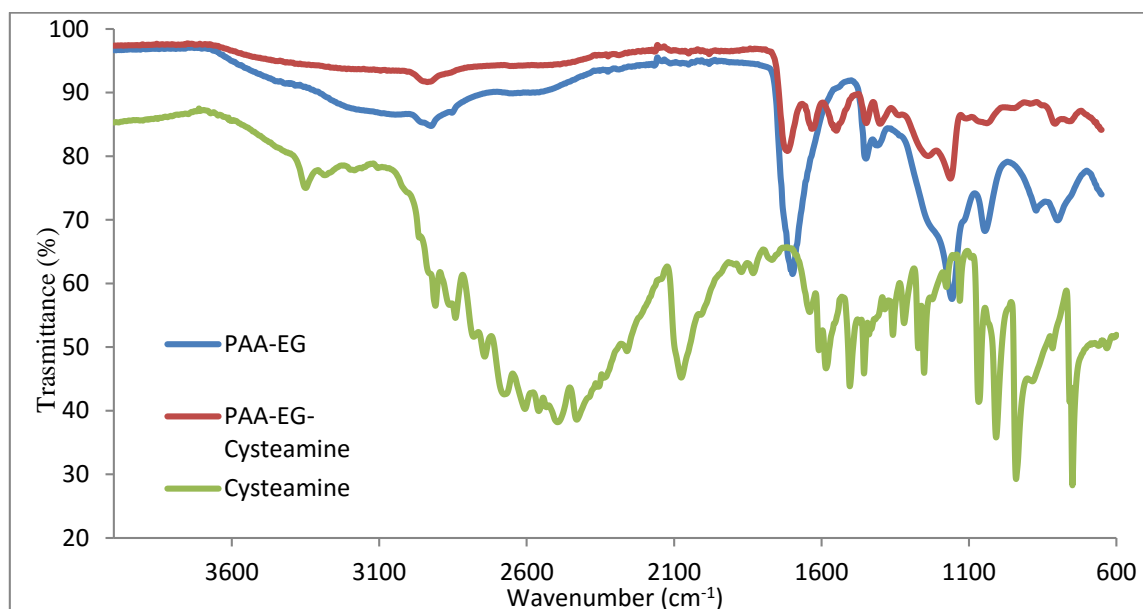
Figure 7.5: FTIR graph to show the spectra of PAA-EG-Cysteamine in relation to spectra of PAA-EG electrospun membrane and its constituent precursor Cysteamine.

Table 7.3: FTIR peaks (cm^{-1}) for PAA-EG, PAA-EG-Cysteamine and Cysteamine hydrochloride and corresponding chemical bonds.

PAA-EG	PAA-EG-Cysteamine	Cysteamine hydrochloride	Peak Assignment
		3349.4	*NH$_2$ antisymmetric stretch*
		3284.4	
		3184.2	*NH$_2^+$ antisymmetric stretch*
2924.4	2937	2909.5	*CH antisymmetric and symmetric stretching*
		2841.6	*CH stretching modes attached to an O or an N*
		2779.7	
		2742.5	
		2676	*NH stretching modes*
		2605.9	
		2533	
		2495.6	
		2430.1	
		2359.6	
		2337.2	
		2559.1	*S-H stretch*
		2083	*N=N=N antisymmetric stretch*
2050.9	2050.7		*X=C=Y stretch*
1981.1	1981		*C=C=C antisymmetric stretch*
1698.3	1716	1871.4	*C=O stretch*

175

		1831.7 1768.5 1640	
	1633.3		*Amide I (mainly C=O stretch) or H-O-H bending*
	1549.5		*Amide II (N-H bend in plane, and C-N stretch)*
		1608.9 1584.8	*NH$_2$ deformation (broad band)*
		1504	*NH$_3$+ deformation*
		1469.1 1455.9	*CH$_2$ scissors vibration*
1449.2	1448.1	1385.4	*CH$_3$ antisymmetric deformations*
1410			*In plane OH bending (in carboxylic acids)*
		1357.8	*NO$_2$ antisymmetric stretch*
		1319.9	*N=N-O symmetric stretch*
	1402 1238.2 1039.5	1271.8 1252.1 1176.4 1066.9	*C-N stretch*
	1162.8	1148.7 1130.8	*C-C-N bending*
1157.5			*C-O-C antisymmetric stretch*
1045.7			*C-O stretch*
		940.1	*C-C stretching*
872.1	807.5	884.7 816.5	*CH$_2$ out-of-plane wag or CC stretching*
798.9			*CH out of plane deformation*
		758.3 748.9 660.6	*C-S stretch*
		632.2	*C-Cl stretch*

The morphology of the PAA-EG-Cyste fibre structure was observed under SEM (Fig. 7.6). The average fibre diameter increased significantly to 1040nm (range: 454 to 1797nm) compared to 330nm (range: 187-447nm) observed with PAA-EG membranes. This could be due to the alteration in the surface characteristics, particularly the replacement of –COOH groups with –SH groups. This allows interaction between neighbouring fibres through hydrogen bonding, as evident from the absence of the FTIR peaks for the free –SH groups (2559.1cm^{-1}), which could cause conjoining of the neighbouring fibres, thus the larger fibre diameters.
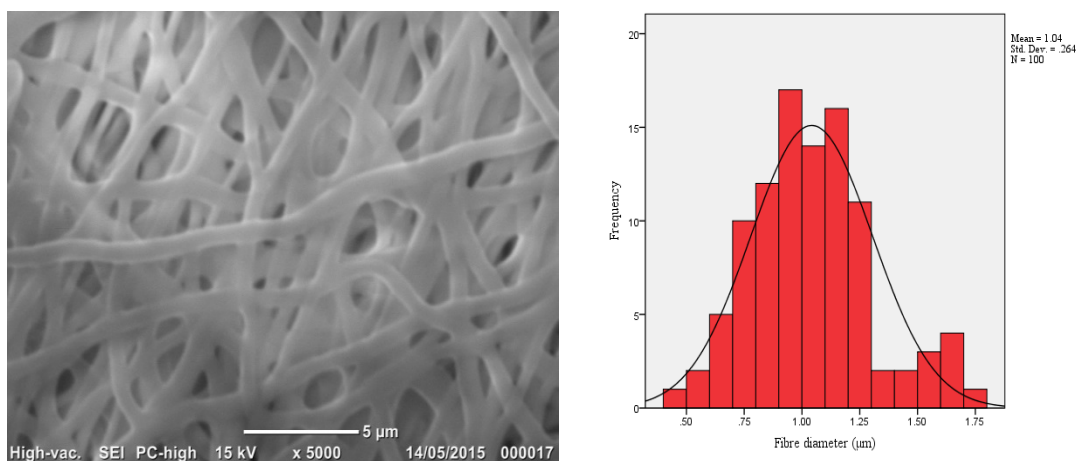
Figure 7.6: a) SEM image at x5000 magnification and b) correlating fibre diameter histogram for PAA-EG-Cysteamine membrane.

7.4. NPs on electrospun membranes

Au and Ag NPs from shortlisted microemulsion system detailed in chapter 4 and NP separated systems detailed in chapter 5 were used for addition of NPs onto PAA-EG-Cyste electrospun membranes. A maximum of 20 membranes (8mm diameter discs) per 10ml vial were immersed in one of the respective shortlisted solutions for 24 hours and then the membranes were removed, with observable indications in colour change, signifying NPs had bound onto the electrospun discs. The different colours exhibited by the NPs on the electrospun membranes was an initial indicator that the NPs on the surface had presumably maintained their integrity of size and shape as the scattering of light for the same colour was shown. The NPs were also shown to fully cover the membranes and were efficiently bound to the thiol groups as the membranes were cleaned in deionised water an average of 3 times until a clear liquid solution was present in which the NP-membranes remained. The NPs morphology on the membranes was then analysed with the use of TEM, whereby the PAA-EG membranes were saturated with 2.78M sucrose solution, cryogenically frozen and then slices of the membrane were cut using a cryostat for fibres thin enough to be observed using TEM, Figure 7.7. The TEM images firstly show that NPs have successfully bound to the PAA-EG-cyste electrospun membrane surface. Secondly it shows that depending on the system different size and shape morphologies as well as distribution are present upon the surface.

For Ag NPs from ABI Ag N microemulsions, Figure 7.7a&b, a dense coating of Ag NPs, of small spherical morphology are present upon the PAA-EG surface with a NP size range between 1.7-9.2nm and an average NP size of 4nm present. When compared with the original NP microemulsion system, chapter 4, the shape of the NPs has not altered from that seen within the microemulsion solution. For Au NPs from ABI Au N microemulsions, Figure 7.7c&d, a large aggregated Au NP is shown upon its surface, with sparse distribution of the Au NPs. The size range observed with TEM was between 8.1-68.5nm with an average size of 30.99nm present.

For NP separated Ag NPs from ABI Ag N, Figure 6.8e&f, show a uniform distribution of Ag NPs upon the PAA-EF surface with NPs which have a more elongated shape and a size range between 2.6-61.1nm, average size 18.1nm. For NP separated Au NPs from ABC Au N, Figure 7.7g&h, the NPs on the fibre surface show a dense covering in some regions of the fibre with small anisotropic shaped Au NPs of octagonal to diamond like morphologies present. The NPs size range on the fibre was between 2.9-47.5nm with an average size of 12.1nm. When compared with the original NP separated solution the size range is shown to decrease for NP separated Au NPs from ABI Au N microemulsion systems, Figure 7.7i& j, the NPs are shown to have two different morphologies, that of small spherical NPs and larger, anisotropic shaped NPs sparsely distributed on in different areas on the fibre surface. The size range of the NPs is shown to be between 3.8-38.5nm with an average size of 11.5nm. In conclusion, NPs were successfully attached to the PAA-EG fibre and the NPs maintained their size and shape integrity.

a

b
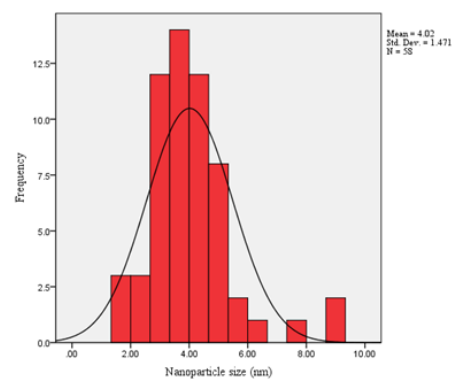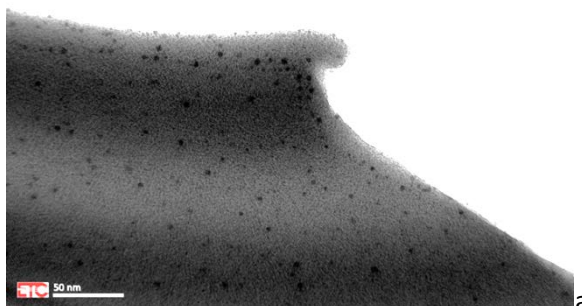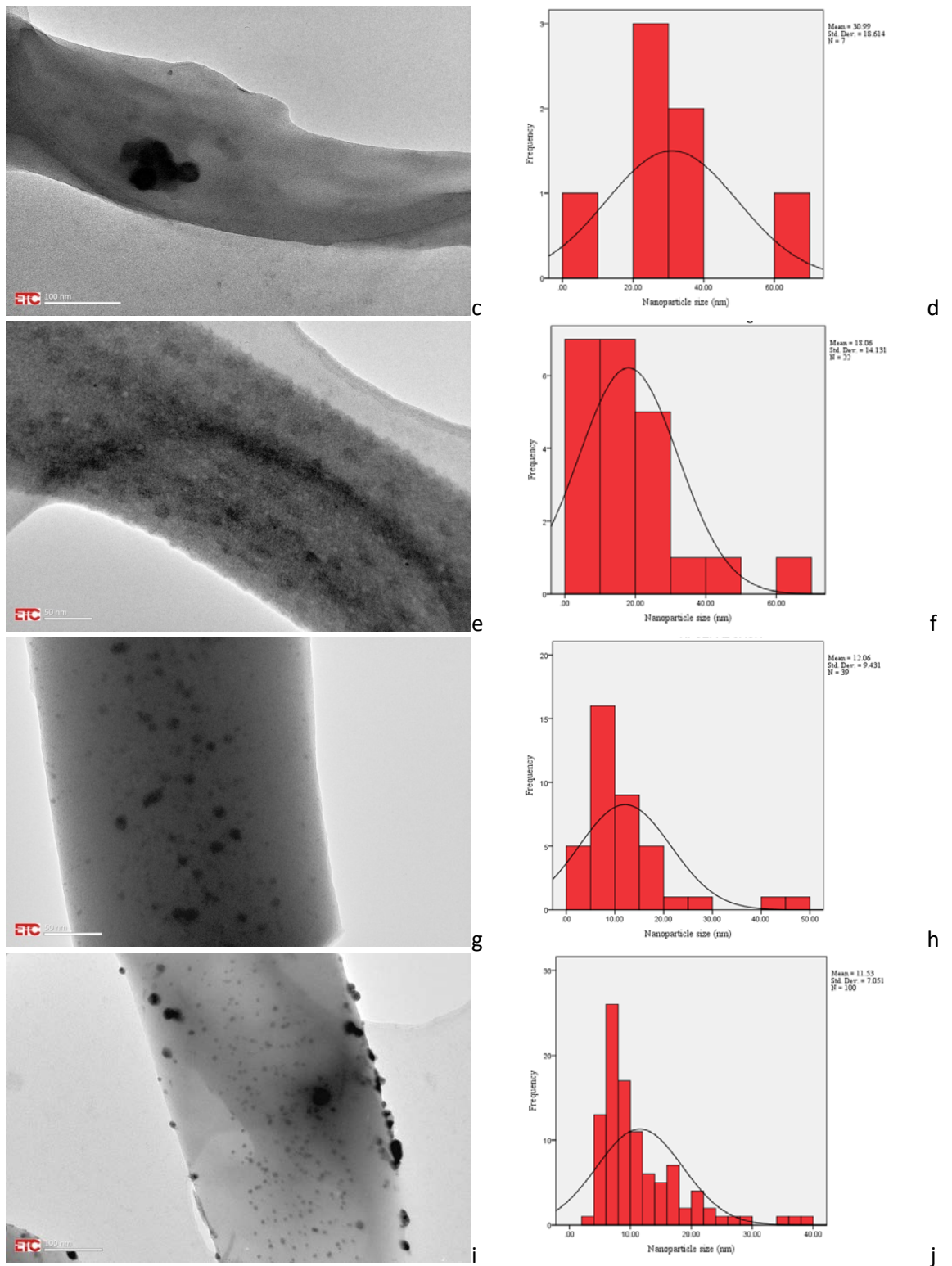
Figure 7.7: TEM images and correlating nanoparticle size histograms for a& b) AgNPs from AOT/But/IPM reduced by NaBH$_4$ microemulsion system, c&d) AuNPs from AOT/But/IPM reduced by NaBH$_4$ microemulsion system, e&f) NP separated AgNPs from AOT/But/IPM reduced by NaBH$_4$ microemulsions, g&h) NP separated AuNPs from AOT/But/Cyclo reduced by NaBH$_4$ microemulsion system and i&j) NP separated AuNPs from AOT/But/IPM reduced by NaBH$_4$ microemulsion system.

7.5. SERS for NPs on electrospun membranes

The NPs on electrospun membranes were tested using both 514nm and 1064nm Raman, with enhancement evaluated using 1mM MBT. For 1064nm testing, a closed chip design was prepared and membranes were hydrated with deionised water within the chambers for testing, since the high power of the 1064nm Raman laser caused the dry samples to burn. Testing them in a wet state potentially dissipated the heat generated by the incident high power laser light on the Au and Ag NPs allowing the recording of SERS spectra on the 1064nm Raman spectrometer.

7.5.1. Controls

SERS spectra for the base NP incorporated electrospun membranes were recorded using both 514nm and 1064nm Raman spectrometers (Fig. 7.8). With the base PAA-EG-Cyste membrane, we did not see any notable Raman peaks for 514nm, while for 1064nm Raman we saw a peak at 573cm^{-1} for C-S stretch. Ag NPs on PAA-EG-Cyste membranes particularly from ABC Ag AA and ABI Ag N systems showed high intensity peaks at around 1365cm^{-1} and 1587cm^{-1} for CH$_3$ symmetric deformation and COO^{-} symmetric stretch in the 514nm SERS spectra as shown in Figure 7.8a. All the Au NP incorporated electrospun membrane variants did not show any peaks within the range of 150cm^{-1} to 2900cm^{-1} in 514nm Raman. With 1064nm Raman, Ag and Au NPs from ABC and ABI microemulsions showed hydrocarbon and carbonyl peaks indicating small residues of surfactant on the surface. In general the intensity shown with 1064nm Raman was low for all SERS substrates.

When the NPs were separated from the microemulsion systems and placed on the electrospun membranes, the SERS spectra using both 514nm and 1064nm Raman spectrometers showed little to no SERS peaks, indicating that surfactant has been effectively removed by the washing treatments (Fig. 7.8c).
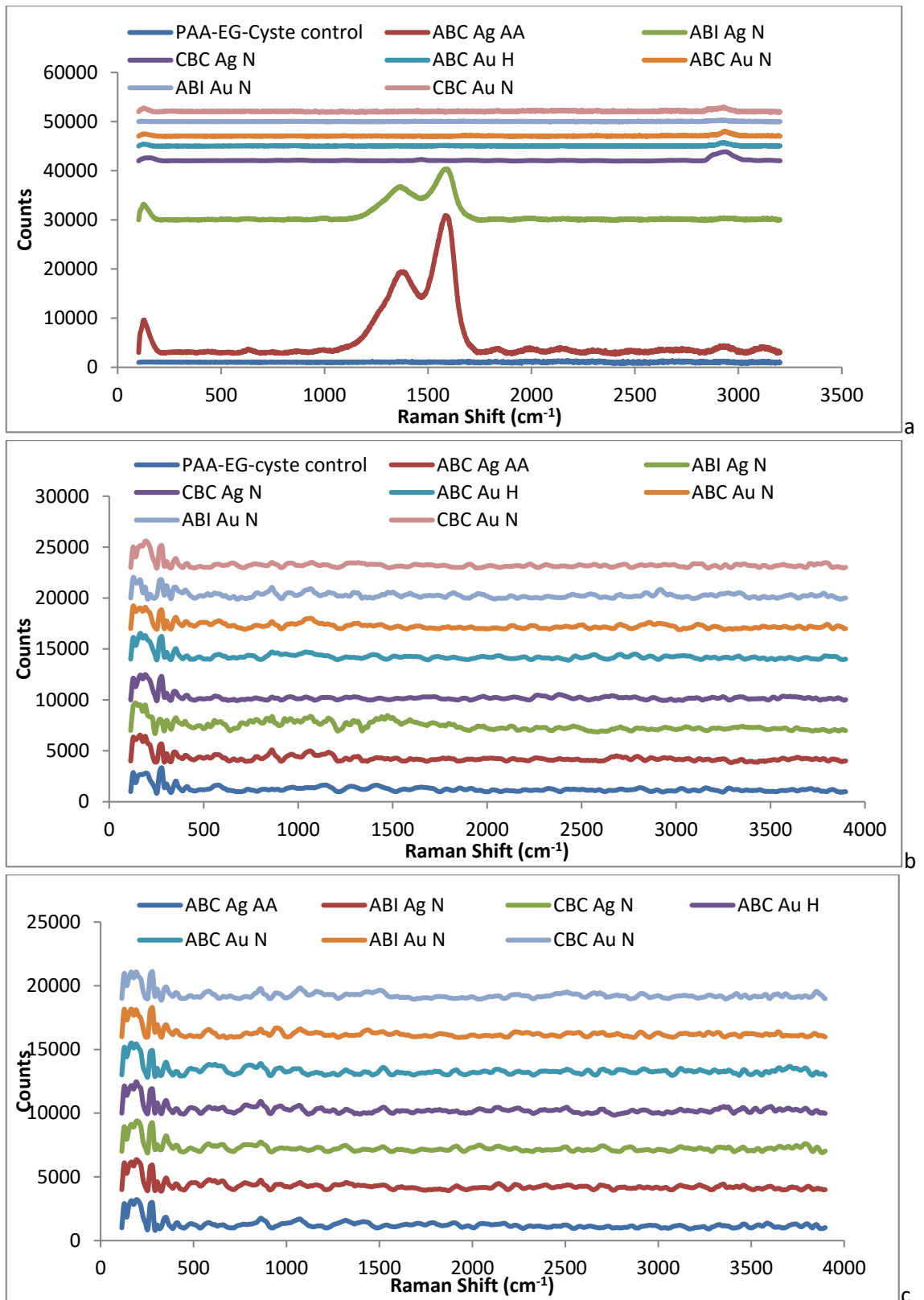
Figure 7.8: NP on membrane controls for a) NPs from microemulsions on electrospun membranes with 514nm Raman, b) NPs from microemulsion on electrospun membranes with 1064nm Raman and c) Separated NPs from microemulsions on electrospun membranes with 1064nm Raman. Spectra offset for clarity.

Table 7.4: 514nm Raman peaks (cm^{-1}) and corresponding bonds for the NPs from shortlisted microemulsions coated on electrospun membranes

PAA-EG-Cyste	ABC Ag AA	ABI Ag N	CBC Ag N	ABC Au H	ABC Au N	ABI Au N	CBC Au N	Peak Assignment
	130.2	129.6	149.4	124.9	126.9		130.1	Lattice vibrations
	634.7							O-C-O bend
	1365.5	1354.6						CH$_3$ symmetric deformation or COO- symmetric stretch
			1467.1					CH$_2$ scissors vibration
	1587.6	1587.2						COO- symmetric stretch
	1833.6							C=O stretch
	1971.3							C=C=C antisymmetric stretch
			2925.8	2926.9 2930.2	2935.6	2917.7	2930.8	CH antisymmetric stretch and symmetric stretch or O-H stretch

Table 7.5: 1064nm Raman peaks (cm^{-1}) and corresponding bonds for NPs from microemulsions coated on electrospun membranes

PAA-EG-Cyste	ABC Ag AA	ABI Ag N	CBC Ag N	ABC Au H	ABC Au N	ABI Au N	CBC Au N	Peak Assignment
275	274.4	307.2	274.9	274.6	274.7	303.8	274.2	Metal-O stretch or CC bend
573.3	571.9	558						C-S stretch
	857.9	861.8				857.5		CH out-of-plane deformation
	1165.6	1066.9			1056.9	1056.5		C-O stretch
		1476.6						CH$_2$ scissors vibration
						1488.1		Ring stretch
						1963.8		C=C=C antisymmetric stretch
					2856.3			CH antisymmetric stretch and symmetric stretch or O-H stretch

7.5.2. MBT enhancement

To test the SERS efficacy of the NP incorporated electrospun membranes, the substrates were immersed in 1mM MBT solution for 24 hours, after which they were washed 3 times in deionised water on a shaker to remove any excess MBT that was not covalently bound to the NPs and tested with Raman.

With 514nm Raman, Ag NPs from ABI Ag N and CBC Ag N microemulsion systems showed SERS peaks for MBT, C-S stretch (1076cm^{-1} and 1183cm^{-1}) and ring stretch (1576cm^{-1}). Ag NPs from CBC Ag N showed the highest enhancement (Fig. 7.9a & Table 7.6). With 1064nm Raman as shown in Figure 7.9b, the results were less visibly definitive, with Au NPs from ABC Au N, providing small peaks that appear to correspond with MBT peak characteristics. Upon further analysis (Table 7.7), all the NP SERS substrates with the exception of Au NPs from CBC Au N, provided peaks that correlated with MBT in the spectra.

For separated NPs incorporated on PAA-EG-Cyste electrospun membranes with 1mM MBT (Fig. 7.10, and Tables 7.8 & 7.9), SERS peaks for MBT were seen only for Ag NPs separated from ABI Ag N and ABC Ag AA microemulsions, under 514nm Raman spectrometer. On the other hand, under 1064nm Raman, only Au NPs separated from ABC Au N and ABI Au N microemulsions showed SERS peaks for MBT. From these results, it was evident that there is a preference of Ag NPs for 514nm Raman, and of Au NPs for 1064nm Raman, which can be attributed to the respective metal resonance wavelengths. The NP separated Au NP incorporated on PAA-EG-Cyste showed higher enhancement compared to their counterparts in microemulsions.
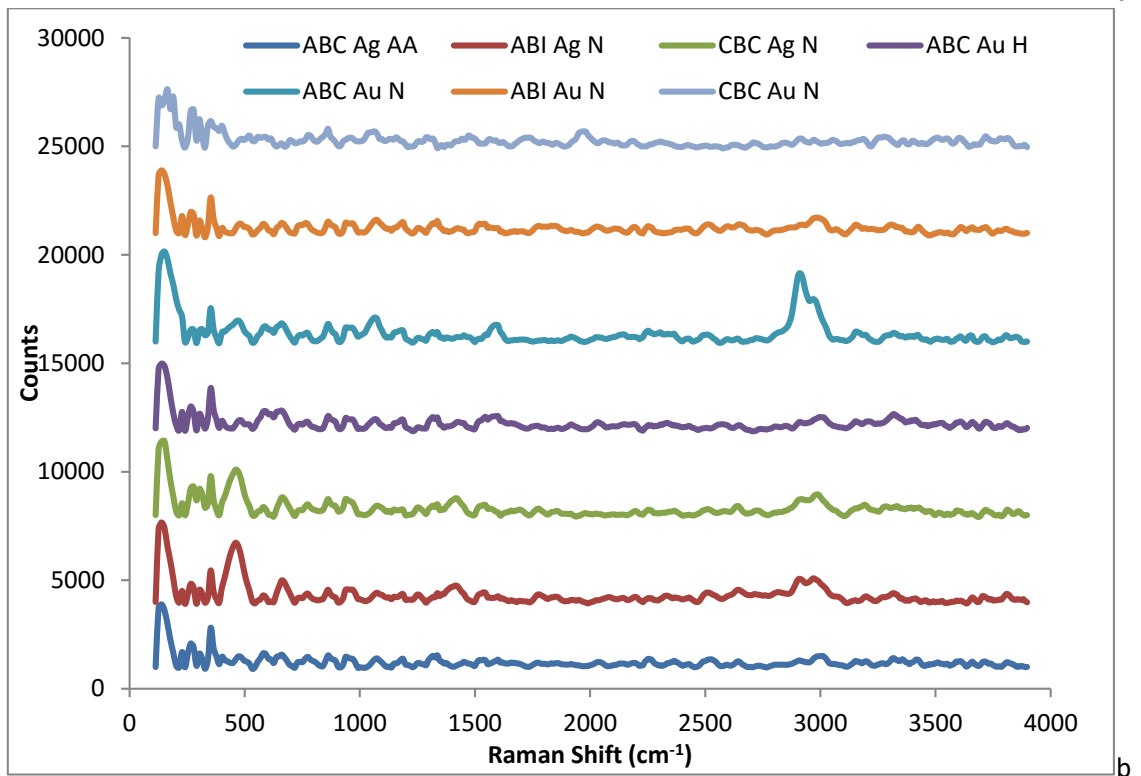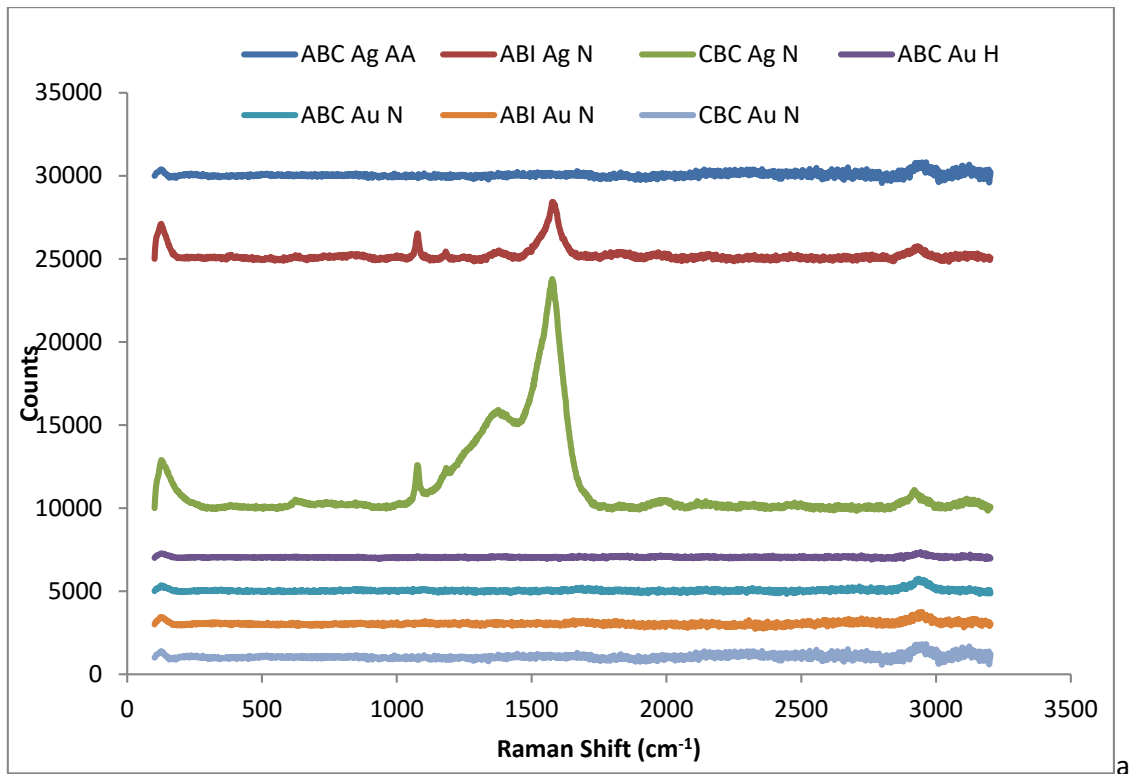
Figure 7.9: NPs from microemulsions on PAA-EG-Cyste electrospun membranes with 1mM MBT a) 514nm Raman Spectra and b) 1064nm Raman Spectra. Spectra offset for clarity.

Table 7.6: 514nm Raman peaks (cm^{-1}) and corresponding bonds related to MBT for NPs from microemulsions on PAA-EG-Cyste membrane with 1mM

MBT.

ABC Ag AA	ABI Ag N	CBC Ag N	ABC Au H	ABC Au N	ABI Au N	CBC Au N	Peak Assignment
							Ring breathing mode
	1076.1	1076.8					*C-S stretch*
	1180.3	1183.5					*C-S stretch*
							Ring stretch
	1581.1	1576.3					*Ring stretch*

Table 7.7: 1064nm Raman peaks (cm^{-1}) and corresponding bonds related to MBT for NPs from microemulsions on PAA-EG-Cyste membrane with 1mM

MBT.

ABC Ag AA	ABI Ag N	CBC Ag N	ABC Au H	ABC Au N	ABI Au N	CBC Au N	Peak Assignment
585	578.9	578.9	594.2	588	581.9		*C-S stretch*
1072.3	1052.6 1071.7	1073.9	1066.7	1066.9	1071.1		*C-S stretch*
1182.2			1181.7	1181	1182.4		*C-S stretch*
	1539.2	1539.8	1593.6	1586.8			*Ring stretch*
			2574.5				*S-H stretch*
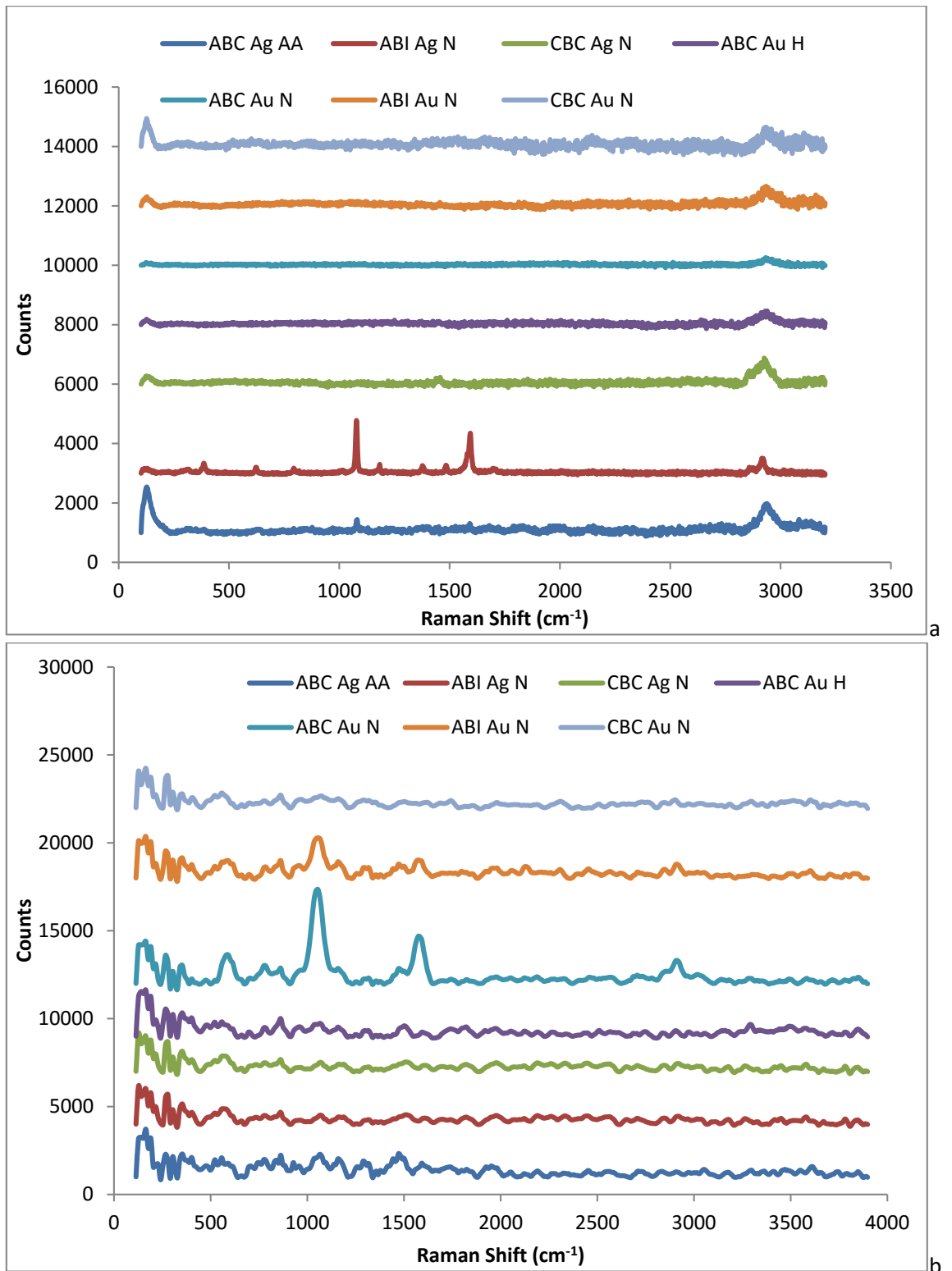
Figure 7.10: Separated NPs from microemulsions on PAA-EG-Cyste electrospun membranes with 1mM MBT a) 514nm Raman Spectra and b) 1064nm Raman Spectra. Spectra offset for clarity.

Table 7.8: 514nm Raman peaks (cm^{-1}) and corresponding bonds related to MBT for separated NPs from microemulsions on PAA-EG-Cyste membranes

with 1mM MBT.

ABC Ag AA	ABI Ag N	CBC Ag N	ABC Au H	ABC Au N	ABI Au N	CBC Au N	Peak Assignment
1079.6	1077.7						*C-S stretch*
	1183.3						*C-S stretch*
1591.4	1592.6						*Ring stretch*

Table 7.9: 1064nm Raman peaks (cm^{-1}) and corresponding bonds related to MBT for separated NPs from microemulsions on PAA-EG-Cyste membranes

with 1mM MBT.

ABC Ag AA	ABI Ag N	CBC Ag N	ABC Au H	ABC Au N	ABI Au N	CBC Au N	Peak Assignment
	572.3	569.9			582.5	559.5	*C-S stretch*
				779.1			*C-S stretch*
				1577.3	1575.3		*Ring stretch*

7.6. Chapter Summary

This chapter presented the preparation and characterization of the third category of the SERS substrate design, namely, Ag and Au NPs incorporated on insoluble electrospun membranes. The rationale for this design was that the electrospun membranes provide a fibroporous nanostructure, which inherently provides large surface area per unit volume for SERS detection using Raman spectroscopy. In particular, we designed insoluble electrospun membranes and modified their fibre surface to incorporate NPs developed in the study (Chapters 5 & 6). For a robust SERS substrate design, it was essential to make the electrospun membranes insoluble in common solvents such as water and ethanol.

The rationale behind preparing insoluble electrospun membranes was to maintain the integrity of the electrospun fibre morphologies when in the presence of solvent it would typically dissolve in, therefore limiting their applicability. This can be prevented through cross-linking of the polymer. There are two main methods to achieve cross-linking; during electrospinning and after electrospinning. For the cross-linking during electrospinning, the rate of reaction between the polymer and the cross-linker is required to be slow. The problem with this method is the solution has to be aged to an appropriate viscosity for it to be electrospinnable, judging the duration for which could be difficult. The other method for cross-linking after electrospinning can be done in two ways. First is to electrospun the polymer by itself and then expose the membrane to a cross-linking agent. An example for such method is the electrospinning of gelatin or collagen and post production exposure to glutaraldehyde vapours (Wang et al, 2014) or immersion in the glutaraldehyde solution. The immersion in the cross-linking solution could be deleterious to the integrity of the fibrous structure of the electrospun membranes. The second method involves the electrospinning of the polymer along with its cross-linker, after which the membrane is heated to facilitate the reaction between the cross-linker and polymer molecules. This method maintains the integrity of the inherent fibro-porous structure of the electrospun membranes. Hence we chose this method for preparing insoluble electrospun membrane in this study.

The polymer used in this study was PAA and the bifunctional cross-linker was EG. A 4% solution of PAA and EG at 88:12% ratio, was first electrospun, and thereafter the electrospun membrane was heat at 130°C for 30 minutes to facilitate the condensation reaction between the -COOH on PAA and -OH on EG to form ester linkages. In this study, a lot of work went into the optimisation of the electrospinning of PAA-EG fibres. A key problem that we needed to address was that of the temperature of the feed polymer solution. The in-house electrospinning box although with humidity and temperature control did not encapsulate the syringe pump that feeds the polymer solution into the electrospinning box, which was detrimental to electrospinning. We needed to maintain the temperature of the feed-solution outside the box to <10°C for the electrospinning to work.

The optimised parameters were: 4% polymer (88:12 percent weight ratio of PAA to EG) solution aged for 72h at 4°C; activation with addition of 25µl of 1M H_2SO_4 just before electrospinning; 22 gauge flat-tipped needle as the spinneret; a distance of 20cm distance between spinneret and needle; 0.8ml/hr flow rate; 15kV voltage; with humidity below 10% and temperature <10°C. This produced PAA-EG fibres that deposited uniformly on the flat plate collector. The smooth fibres had an average diameter of 330nm (range 187-447nm) and the membrane thickness increased with increasing electrospinning time. The crosslinking of the PAA chains in the electrospun fibres with the bifunctional cross-linker EG was confirmed using FTIR. The typical –OH peak of the EG monomer was absent in PAA-EG membrane, while then carbonyl peak on the PAA chains ($1695cm^{-1}$) decreased in intensity, as well as shifted to a longer wavelength ($1698cm^{-1}$) confirming the formation of ester linkages. The presence of free –COOH groups on the PAA chains was also evident from the broad carboxylic acid peak between $2700cm^{-1}$ and $3300cm^{-1}$.

In order to coat the electrospun PAA-EG fibres with Ag or Au NPs, we modified their surface by covalently attaching cysteamine to provide free thiol groups with which metallic Au and Ag NPs have high affinity to form Ag-S or Au-S covalent bonds. Zero-length crosslinking using carbodiimide chemistry, was utilized to form amide linkages between the –COOH groups on PAA and the –NH_2

groups on cysteamine to generate the PAA-EG-Cyste membranes. This grafting of cysteamine on the PAA-EG fibres was confirmed using FTIR, evident from replacement the carboxyl (1695cm^{-1}) and carboxylic acid peaks (2700cm^{-1} to 3300cm^{-1}) of the free –COOH groups on PAA with the carbonyl stretch (1715cm^{-1}), amide I (1633cm^{-1}) and amide II (1549cm^{-1}) peaks of the amide linkage between PAA and cysteamine. Under SEM, the average fibre diameter was 1040nm which was about 3 times bigger than the PAA-EG fibres. The increase could be due to the conjoining of neighbouring fibres due to hydrogen bonding of the hydrogen on –SH groups.

Shortlisted Au and Ag NPs either within microemulsions or separated from the microemulsion were then coated onto the PAA-EG-Cyste membranes by immersion of the membranes within the respective NP solutions for 24 hours. The colour of the membranes resembled that of the NP solution, indicating that NPs had successfully bound, indicating that the size and shape of the NPs had not been altered after attachment. TEM was used to characterise the NPs on electrospun membranes. The TEM results showed that the NPs could be either evenly spaced on the fibre surface (Ag NPs from ABI Ag N microemulsion) or aggregated into clusters (Au NPs from ABI Au N microemulsion). The sizes of the NPs incorporated on the fibre were similar to that in the original microemulsion solutions. Essentially the TEM results showed that Ag NPs and Au NPs were successfully grafted onto the surface of the PAA-EG-Cyste membranes.

All the shortlisted NPs on electrospun membrane were then tested with both 514nm and 1064nm Raman for their base Raman spectra. The base PAA-EG-Cyste membranes did not show any peaks with 514nm Raman, while with 1064nm Raman a C-S stretch (543cm^{-1}) peak was shown. Hydrocarbon and carbonyl peaks were observed for Ag and Au NPs from ABI and ABC microemulsions, indicating that the NP surface was contaminated with the surfactant. In the case of the NP separated from the microemulsion the carbonyl and hydrocarbon peaks were absent or minimal within the Raman spectra, indicating the effective cleaning of the NPs.

To investigate their efficacy as SERS substrates, all the NP coated electrospun membranes were tested with 1mM MBT. SERS spectra for MBT were obtained with 514nm and 1064nm Raman

for some of the NP on electrospun membrane SERS substrate variants. The MBT SERS spectra provided 3 prominent peaks; C-S stretch at 543cm^{-1} and 1076cm^{-1} and ring stretch at 1593cm^{-1}. With 514nm Raman, Ag NPs from CBC Ag N and ABI Ag N microemulsions and NP separated Ag NPs from ABI Ag N coated on PAA-EG-Cyste membranes showed prominent characteristic MBT peaks. With 1064nm Raman, Au NPs from CBC Au N microemulsion and Au NPs separated from ABC Au N and ABI Au N microemulsions coated on PAA-EG-Cyste electrospun membranes gave prominent MBT peaks. There is a clear preference by the laser wavelengths for SERS enhancement of particular metal types of the SERS substrates, with Ag NPs giving better results with 514nm Raman and Au NPs with 1064nm.

Chapter 8: SERS Substrate Enhancement

8.1.   Introduction

SERS substrates were prepared with a focus on using simpler methodologies that were less time and energy intensive. As such, SERS substrate designs from three main design categories were prepared: roughened Ag wire through chemical etching, Au and Ag NPs from microemulsions and Ag and Au NPs on insoluble electrospun membranes. SERS substrates designed from each category gave positive results with 1mM MBT using two different laser wavelengths 514nm and 1064nm.

Currently SERS substrates commercially available are expensive and work at a narrow wavelength ranges. The preparation of SERS substrates that show resonance with a wider array of wavelengths is highly beneficial for providing additional information of molecular structure, as different bonds typically vibrate with higher preference at certain wavelengths. With the use of SERS, bonds that would not usually resonate with enough intensity at certain wavelengths, have now the potential to be observed within the visible and near infrared spectrum. Improved design of SERS substrates would solve a bottleneck in providing simple, reliable signal for multiple analytes within mixed solutions, which at the moment would require multiple SERS substrates to be optimised at multiple wavelengths (Zhang et al, 2015).

The aim of this study was to compare the different SERS substrate designs fabricated within the project, that had shown desirable SERS enhancement of 4-Methylbenzenethiol (MBT). As well as compare with three commercially available SERS substrates; P-SERS (purchased from Stellarnet) and Ag and Au SERStrate (purchased from Silmeco ltd.). The significance of the different commercial SERS substrates with 1mM MBT, using 514nm and 1064nm Raman, highlighted the restrictions of the current commercial SERS substrates. After which the SERS substrates that showed the highest enhancement or optimised qualities were further evaluated with different concentrations of MBT to calculate their limit of detection (LOD). Equipment used for testing SERS substrates within this chapter were 514nm and 1064nm Raman instrumentation.

8.2. Short-listed SERS substrates

The SERS substrate designs that showed the most promise from previous chapters with 1mM MBT and therefore evaluated further within this chapter were detailed in Table 8.1.

Table 8.1: Shortlisted SERS substrates from three design categories detailed in previous chapters.

SERS substrate Design Category	SERS substrate
Chemically etched Silver (Ag) Wire	• Non-heated, 30s NH$_4$OH + 10s HNO$_3$ Ag Wire [30sA10sH Ag wire]
Nanoparticles (NPs) within microemulsion solutions	• Ag NPs in ABC reduced with AA [ABC Ag AA] • Au NPs in ABC reduced with H [ABC Au H] • Au NPs in ABC reduced with N [ABC Au N]
NPs from microemulsion systems on filter paper	• Ag NPs from ABC AA • Ag NPs from ABI reduced with N [ABI Ag N]
Separated NPs from microemulsions on filter paper	• Ag NPs separated from ABC AA • Ag NPs separated from ABI N • Au NPs separated from ABI reduced with N [ABI Au N]
NPs from microemulsions on electrospun membranes	• AgNPs from ABI N • Ag NPs from CBC reduced with N [CBC Ag N] • Au NPs from ABC reduced with N [ABC Au N]
Separated NPs from microemulsions on electrospun membranes	• Ag NPs from ABI N • Au NPs from ABC N

8.2.1. Comparison of short-listed SERS substrates with 1mM MBT

When the Raman spectra for the shortlisted solid SERS substrates were compared at 514nm (Fig. 8.1a), and 1064nm (Fig. 8.1b), the results indicated a clear divide for the majority of the SERS substrates with preferential resonance with one of the two wavelengths. For 514nm Raman spectra, Figure 8.1a, all of the Ag NP SERS substrates provided characteristic MBT peaks, whereas Au NP substrates showed no visible enhancement. Ag NPs from CBC Ag N on electrospun membranes showed the highest enhancement of signal, with chemically etched Ag wire providing the most peaks, particularly for MBT bonds, Table 8.2. When comparing the peak values, in Table 8.2 with the control MBT spectra for 514nm Raman, the results showed that Ag NPs on paper, Ag NPs from CBC Ag N on electrospun membrane and separated Ag NPs on electrospun membrane showed the closest peak values to that shown for control MBT peaks.

When the 1064nm Raman results for SERS substrates with 1mM MBT, Figure 8.1b, were compared, it showed the depletion of observable peaks for characteristic MBT spectra for the majority of SERS substrates, with the exception of chemically etched Ag wire and NP separated Au NPs from ABC Au N on electrospun membrane. NP separated Au NPs on electrospun membrane provided similar enhancement to that shown by chemically etched Ag wire. Upon further data analysis, Table 8.3, it was shown that all the Au NP substrates with 1064nm Raman presented peaks for MBT bonds, therefore support of the preference certain wavelengths have for resonance with SERS substrate metal type was highlighted. Corresponding MBT peaks were also shown for Ag NPs on electrospun membrane and when separated on paper, the presence of closer proximity of the Ag NPs using the electrospun membrane or removal of surfactant for the separated NPs was shown to be advantageous for improving SERS substrate resonance with wavelengths it is not preferable to. Chemically etched Ag wire showed the most promise, with SERS substrate characteristics showing definitive SERS enhancement of MBT with both 514nm and 1064nm Raman, therefore one could say it encompasses broadband SERS substrate characteristics which are highly desirable for future commercial SERS substrates. When the peak values for MBT solid using 1064nm Raman were compared with the SERS substrates, chemically etched Ag wire was the only substrate that had peak values within a close distance to what was shown for the MBT solid.
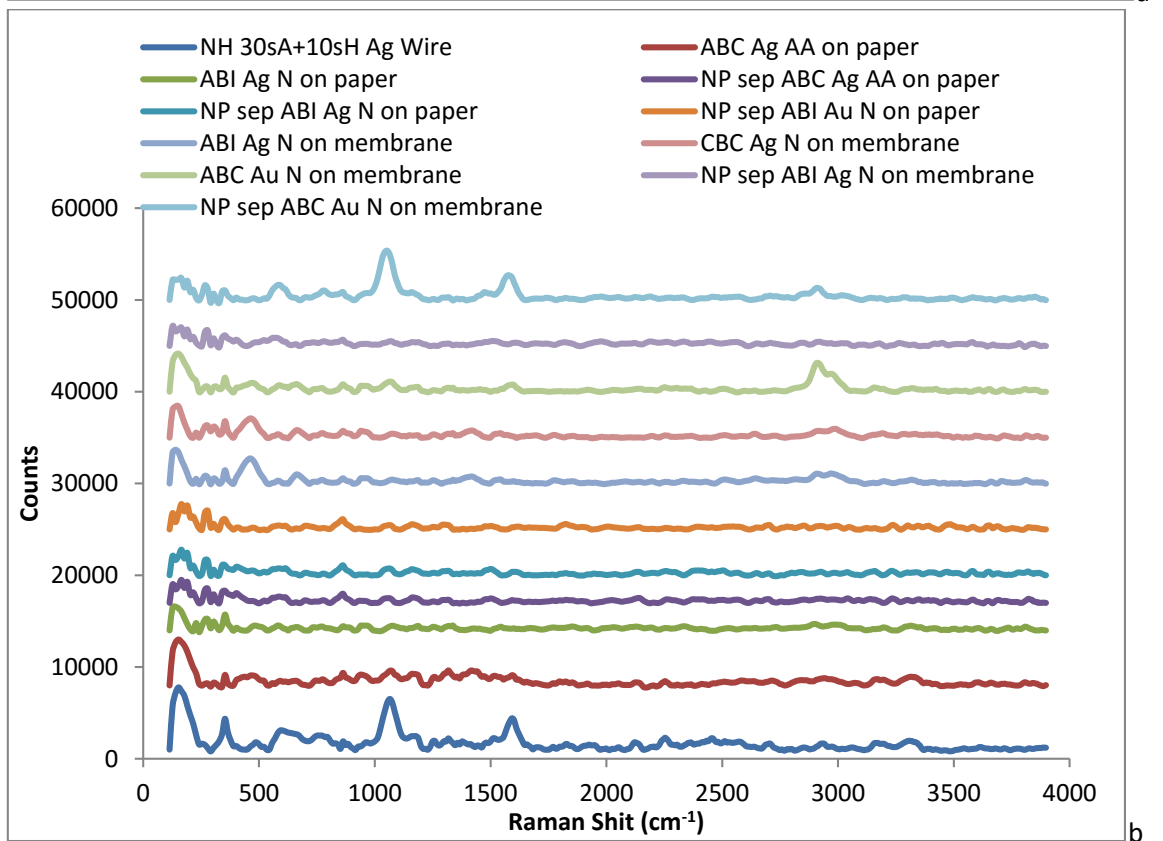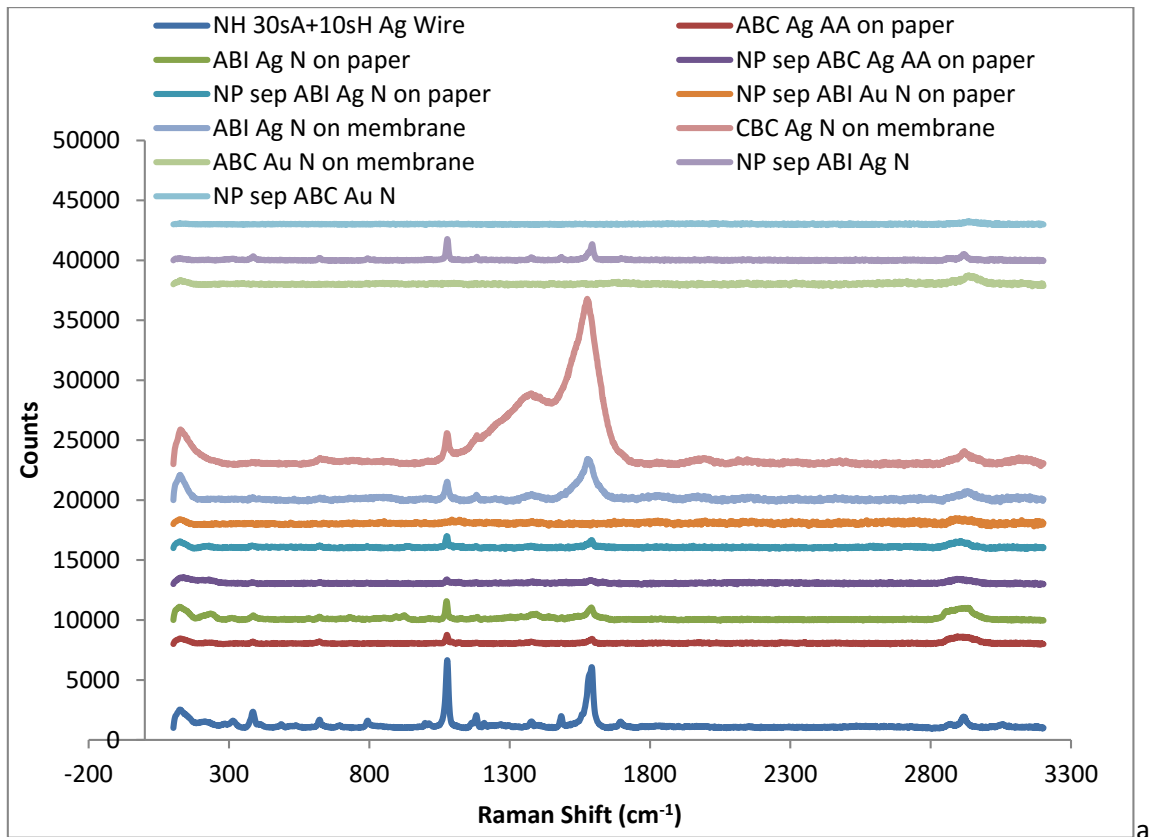
Figure 8.1: Comparison of fabricated SERS substrates that showed best 1mM MBT enhancement within their categories with a) 514nm Raman and b) 1064nm Raman. Spectra offset for clarity.

Table 8.2: 514nm Raman Peaks (cm^{-1}) correlating to significant MBT bonds for MBT solid and fabricated shortlisted SERS substrates with 1mM MBT

MBT solid	Ag Wire	NPs on paper		Separated NPs on paper			NPs on electrospun membrane			Separated NPs on membrane		Peak Assignment
	NH 30s A+10sH	ABC Ag AA	ABCl Ag N	ABC Ag AA	ABI Ag N	ABI Au N	ABI Ag N	CBC Ag N	ABC Au N	ABI Ag N	ABC Au N	
	622.4 696.4		584.5									*C-S stretch*
1183.9 1096.6	1077.4	1079.2	1186	1076.6	1076.4	1094	1076.1 1180.3	1076.8 1183.5		1077.7 1183.2		*C-S stretch*
1596.8	1483.7 1587.4	1593.5	1588.9	1588.2	1592.7		1581.1	1576.3		1592.6		*Carbon Ring stretch*
2561.9												*S-H stretch*

Table 8.3: 1064nm Raman Peaks (cm^{-1}) correlating to significant MBT bonds for MBT solid and fabricated shortlisted SERS substrates with 1mM MBT

MBT solid	Ag Wire	NPs on paper		Separated NPs on paper			NPs on electrospun membrane			Separated NPs on membrane		Peak Assignment
	NH 30s A+10sH	ABC Ag AA	ABCl Ag N	ABC Ag AA	ABI Ag N	ABI Au N	ABI Ag N	CBC Ag N	ABC Au N	ABI Ag N	ABC Au N	
598.7	595.9 626.1 757.1			564.1		569.7	578.9	578.9	588	572.3	582.5	*C-S stretch*
1085.7	1062.5					1055.5	1052.6 1071.7	1073.9	1066.9 1181		1050.9	*C-S stretch*
1592.1	1591.5						1539.2	1539.8	1586.8		1575.3	*Carbon Ring stretch*
2567.9												*S-H stretch*

For shortlisted liquid SERS substrates, Figure 8.2 shows NPs within microemulsions, the results do not visibly show peaks characteristic for MBT as they are masked behind strong microemulsion component peaks, particularly solvent peaks. However upon further analysis, Table 8.4, the results for these 3 NP microemulsion systems showed the presence of an S-H bond related to enhancement of MBT. The Ag NPs within ABC Ag AA, showed a peak for S-H closest to that observed by the MBT control spectra and therefore although 1064nm Raman is more preferable to Au NP SERS substrates, the characteristics of this Ag NP system are desirable as an efficient SERS substrate.
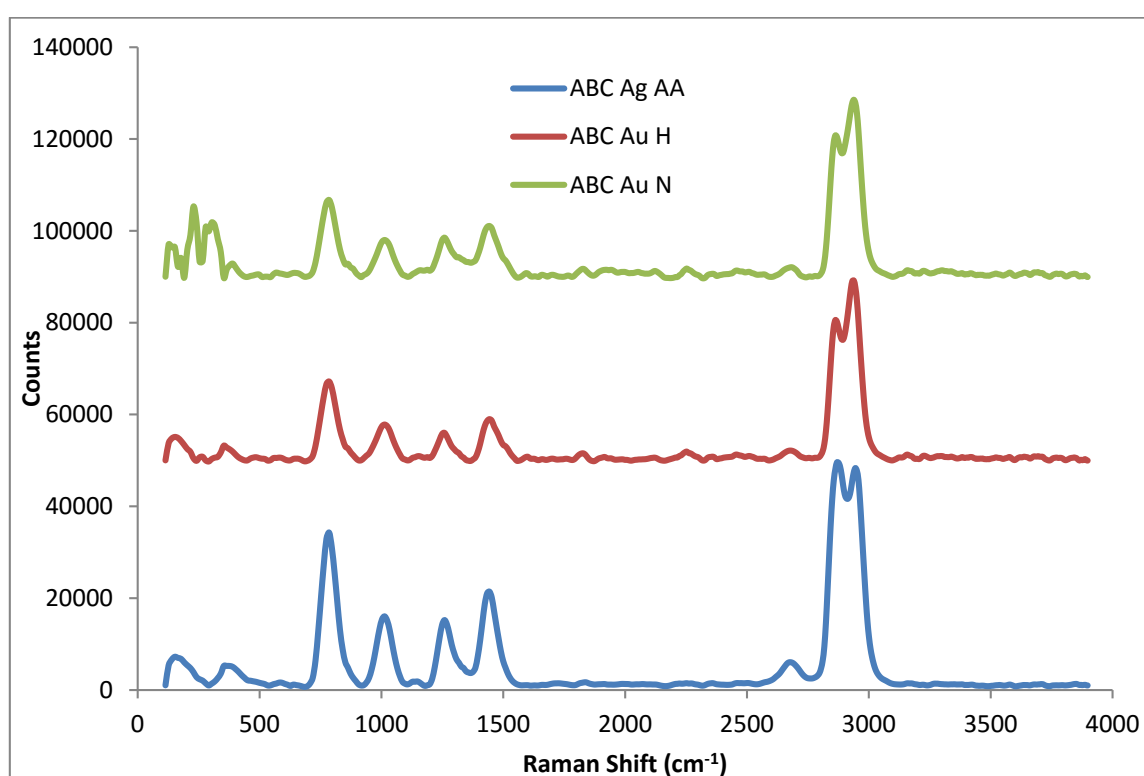
Figure 8.2: 1064nm Raman for shortlisted NPs within microemulsions with 1mM MBT.
Table 8.4: 1064nm Raman peaks (cm^{-1}) with related bond for MBT with shortlisted NPs within microemulsions.

MBT Solid	ABC Ag AA	ABC Au H	ABC Au N	Peak Assignment
2567.9	2596.6	2461.4	2467.5	*S-H stretch*

8.2.2. Enhancement Factor

For evaluation of the efficacy of the SERS substrates, the enhancement factor (EF) was calculated for fabricated SERS substrates in relation to their enhancement of 1mM MBT. The EF can be calculated in many ways, with different research groups concentrating on different aspects of

the SERS substrate qualities. For this study the analytical chemistry point of view was taken for calculating EF. This addressed the simple question of how much more signal is produced for the SERS substrate compared to the normal Raman signal under identical experimental conditions (Le Ru et al, 2007). For this, control spectra of 1mM MBT on filter paper, electrospun PAA-EG-Cyste membrane and within solution were taken with 514nm Raman and 1064nm Raman (Fig. 8.3). The results showed that compared with the solid MBT with these wavelengths, when on substrates with no SERS enhancement, definitive MBT peaks were not present visibly within the spectra. Upon further analysis, this lack of MBT signal was supported with lack of peaks present within the spectra that related with MBT, with the exception of 1mM MBT on filter paper with 514nm Raman, which showed a peak with a value that correlated with a C-S stretch at $1093.7 cm^{-1}$. These results generally support the presence of SERS enhancement of the SERS substrates shortlisted due to the implementation of peaks that correlate with 1mM MBT that are not present within the Raman spectra.

To calculate the EF of the shortlisted SERS substrates, equation 8.1 was used, where a ratio between I_{SERS}, which is the intensity for a significant peak within the SERS spectra in relation to C_{SERS} which is the concentration of the analyte within the SERS spectra is compared with the ratio between I_{RS} for the intensity of the same peak within the Raman spectra in relation to the C_{RS} which is the concentration of the analyte within the Raman spectra;

$$\mathrm{AEF} = \frac{I_{\mathrm{SERS}}/c_{\mathrm{SERS}}}{I_{\mathrm{RS}}/c_{\mathrm{RS}}}.$$

Equation 8.1: Equation to calculate the enhancement factor of the SERS substrate in relation to Raman scattering (*RS*), *I* is the intensity of the signal and *C* is the concentration of the molecule. (Le Ru & Etchegoin, 2009)
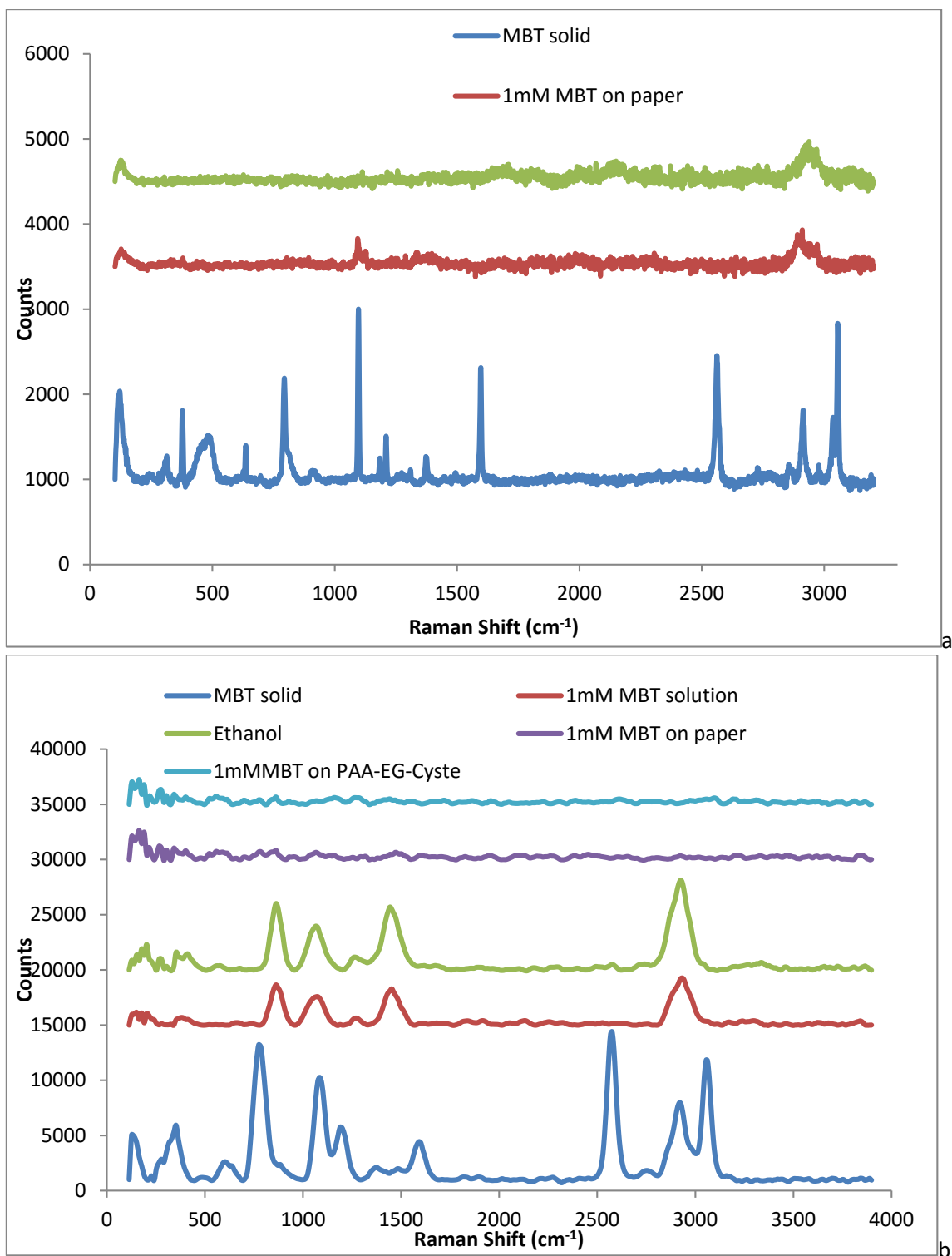
Figure 8.3: Raman Spectra for control MBT and 1mM MBT in solution, on filter paper and on PAA-EG-Cyste electrospun membrane using a) 514nm Raman and b) 1064nm Raman. Spectra offset for clarity.

The shortlisted SERS substrate EF was calculated, using a peak that reliably correlated with MBT using 514nm and 1064nm Raman and this value was compared with correlating Raman peak intensity of the same bond with the solid MBT control within the respective Raman spectra.

The results in Table 8.5, show the optimised EF values from averaged SERS spectra for each fabricated SERS substrate design. The EF values given when 514nm Raman is used was between 5.2-114.9, with Ag NPs from ABI Ag N on filter paper showing the lowest EF and chemically etched Ag wire (NH, 30s NH_4OH+10s HNO_3) showed the highest EF. For each SERS substrate design category, the EF range was tighter, with NPs on filter paper from microemulsions and separated systems showing a range from 5.2-35.9. NP separated Au NPs from ABI Au N showing the highest EF. This result is quite interesting as typically 514nm Raman has been shown to have preference to resonate Ag metal configurations at a higher intensity compared to Au metal motifs. Therefore the size, shape and distribution of these Au NPs are highly desirable for a SERS substrate that encompasses broadband characteristics. When comparing the EF for the NPs taken from microemulsions or separated before addition onto filter paper, the results show that there is no trend with increased EF with microemulsion separation as Ag NPs from the ABC Ag AA system on filter paper showed higher EF, 15.3 compared with its separated NP configuration on filter paper, 7.7, whereas Ag NPs from ABI Ag N on filter paper, increased in EF when within its separated NP configuration from 5.2 to 20.9 respectively. For NPs on electrospun membranes the EF range was higher than that observed on filter paper, 31.2-51.5 supporting the increased hot-spot formation produced to reduced distance of the NPs caused by the nanofiber morphology. The results showed Ag NPS from CBC Ag N on membrane had the highest EF and that Ag NPs from ABI Ag N on membrane when attached from the microemulsion solution or NP separated solution, EF increased with NPs attached after separation from 31.2 to 35.1 respectively. Therefore as with the filter paper with this NP system, separation appears to be increasing SERS substrate EF qualities and therefore the surfactant layer around the NPs may be a hindrance for firstly binding to the electrospun membrane or filter paper and reducing electromagnetic intensity due to the coating, as SERS is a surface layer technique.

Table 8.5: Enhancement Factor of C-S stretch of MBT for 514nm SERS peaks (cm^{-1}) with shortlisted SERS substrates

SERS substrate + 1mM MBT	SERS Peak Value	Chemical Bond	I_{SERS}	C_{SERS}	I_{RS}	C_{RS}	EF
NH 30sA+10sH Ag wire	1077.4	C-S stretch	5828.4	0.001	2000.8	0.039452	**114.9**
ABC Ag AA on filter paper	1079.2	C-S stretch	776.6	0.001	2000.8	0.039452	**15.3**
ABI Ag N on filter paper	1186	C-S stretch	265.7	0.001	2000.8	0.039452	**5.2**
NP sep ABC Ag AA on filter paper	1076.6	C-S stretch	388.7	0.001	2000.8	0.039452	**7.7**
NP sep ABI Ag N on filter paper	1076.4	C-S stretch	1058.8	0.001	2000.8	0.039452	**20.9**
NP sep ABI Au N on filter paper	1094	C-S stretch	382	0.001	2000.8	0.039452	**35.9**
ABI Ag N on membrane	1076.1	C-S stretch	1579.8	0.001	2000.8	0.039452	**31.15**
CBC Ag N on membrane	1077.7	C-S stretch	2611.3	0.001	2000.8	0.039452	**51.5**
NP sep ABI Ag N membrane	1077.7	C-S stretch	1778.4	0.001	2000.8	0.039452	**35.1**

Table 8.6: Enhancement Factor of MBT for 1064nm SERS peaks (cm^{-1}) with shortlisted SERS substrates

SERS substrate + 1mM MBT	SERS Peak Value	Chemical Bond	I_{SERS}	C_{SERS}	I_{RS}	C_{RS}	EF
NH 30sA+10sH Ag wire	1062.5	C-S stretch	3423.5	0.001	9261.9	0.039452	**14.6**
ABC Ag AA microemulsion	2596.6	S-H stretch	5268	0.001	13426.3	0.039452	**15.5**
ABC Au H microemulsion	2461.4	S-H stretch	1324.8	0.001	13426.3	0.039452	**3.9**
ABC Au N microemulsion	2467.5	S-H stretch	1352.9	0.001	13426.3	0.039452	**4**
NP sep ABI Au N on filter paper	1055.5	C-S stretch	1818.6	0.001	9261.9	0.039452	**7.7**
ABI Ag N on membrane	1071.7	C-S stretch	426.1	0.001	9261.9	0.039452	**1.8**
CBC Ag N on membrane	1073.9	C-S stretch	434.7	0.001	9261.9	0.039452	**1.9**
ABC Au N on membrane	1066.9	C-S stretch	1104.3	0.001	9261.9	0.039452	**4.7**
NP sep ABC Au N membrane	1050.9	C-S stretch	5381.5	0.001	9261.9	0.039452	**22.9**

The 1064nm EF results, Table 8.5, show lower EF values overall compared with 514nm Raman, which supports that with longer wavelengths, intensity of signal decreases. The EF range for the shortlisted SERS substrates was between 1.8-22.9, with Ag NPs from ABI Ag N on electrospun membrane showing the lowest EF and NP separated Au NPs from ABC Au N on electrospun membrane showing the highest EF. For chemically etched Ag wire, EF had decreased from 114.9 with 514nm results to 14.56 with 1064nm wavelength, therefore the Ag wire morphological structure resonates more preferably with 514nm Raman, however as 1064nm does not preferentially resonate with Ag metal, the results are very positive for the use of Ag wire as a broadband SERS substrate.

As 1064nm Raman is able to test liquids easily compared with the 514nm Raman instrumentation, the NP microemulsion systems EF was able to be calculated. The results show that Ag NPs from ABC Ag AA, have the highest EF at 15.45and the Au NPs within microemulsion solution with MBT had similar EF values of 3.9 for both. Therefore Ag NPs within solution have shown higher preferential for enhancement of MBT within the solution with 1064nm wavelength compared with the expected Au NPs. The configuration of the Ag NPs, distribution, size and shape is thus of interest for deciphering its beneficial effects as a SERS substrate within solution.

For NPs on filter paper only NP separated systems provided enhancement with 1064nm Raman, with Ag NPs from ABC Ag AA showing higher EF at 17 compared with Au NPs at 7.8, therefore yet again the morphological structure of Ag NPs plays a more critical role than the typical preferred resonance of the wavelength with a metal type. For NPs on electrospun membrane the EF range was from 1.8-22.9, with both the highest and lowest EF shown within this SERS substrate design category, and as with 514nm there is an increase in EF for Ag NPs from the ABI Ag N system when separated and placed on electrospun membrane, from 1.8 to 3.8 respectively.

The EF results for both 514nm and 1064nm Raman highlight firstly the difference in EF with the wavelength used for the same SERS substrates, also that the EF of the shortlisted SERS substrate is

more dependent on the morphological characteristics of the substrate compared with the metal used, with Ag SERS substrates and Au SERS substrates showing high EF values with wavelengths it is typically not preferential with.

8.3. Commercial SERS substrates

Two commercial SERS substrates were purchased for comparison with the shortlisted SERS substrates fabricated within our lab. These commercial SERS substrates were of two different designs;

- P-SERs (Diagnsotic anSERS inc, USA) (Fig. 8.4a), an inkjet-printed Au NP clustered SERS substrate on cellulose paper, with noted enhancement qualities between 633 nm ≤ λ ≤ 1064 nm, 785 nm being optimal.

- SERStrate (Slimleco, Denmark) (Fig. 8.4b), silicon nanopillars coated with either Ag or Au, with noted enhancement qualities at 514nm, 532nm, 633nm, 780-785nm.
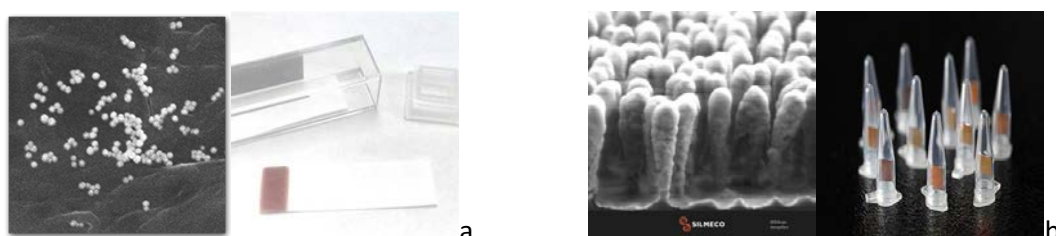
Figure 8.4: Commercial SERS substrates a) P-SERS and b) SERStrate

The control 514nm and 1064nm Raman spectra were taken for these commercial SERS substrates (Fig. 8.5). The spectra showed that for 514nm Raman, Figure 8.5a, Ag SERStrate shows high intensity peaks, with a sharp peak for C-C=O bend at 518cm^{-1}. The peaks present within the spectra seem to be contaminants from air being enhanced by the Ag nanopillars, as the correlated bonds for the peaks, Table 8.7, show carbonyl, hydrocarbon, nitrile and azo compounds enhancement. One could say the high enhancement shown by this substrate would signify increased sensitivity and high potential SERS enhancement of the substrate. For the Au

configuration of SERStrate no peaks were present within the spectra, therefore the enhanced spectra shown by Ag SERStrate is caused predominately by the metal used, and the morphological structure to a lower extent as Au SERStrate with the same morphological structure did not resonate with the wavelength. For P-SERS, there was little resonance as well with the 514nm Raman, with only 3 peaks present within the spectra, for lattice vibrations and hydrocarbon bonds.

The control spectra for 1064nm Raman, Figure 8.5b, does not visibly show definitive differences between the three commercial SERS substrates; however upon further analysis, Table 8.8, Ag SERStrate shows the highest number of peaks, for metal-O stretch, hydrocarbons and nitrogen bonds. The presence of increased enhancement with the 1064nm Raman spectra, a wavelength not preferential for Ag substrates, shows promise for this substrates use as a broadband SERS substrate, not highlighted within the commercial documentation. For P-SERS only one significant peak is present within the spectra, for CH out-of-plane deformation. The lack of presence of peaks with the control, would indicate that the SERS substrate may not be as efficient for SERS enhancement. For Au SERStrate, peaks are now present within the spectra, which is typical for the 1064nm wavelength preference for gold metal. The difference between P-SERS and Au SERStrate may highlight the importance of substrate morphology as well as metal used, with Au SERStrate having a more effective morphology for resonance with 1064nm.
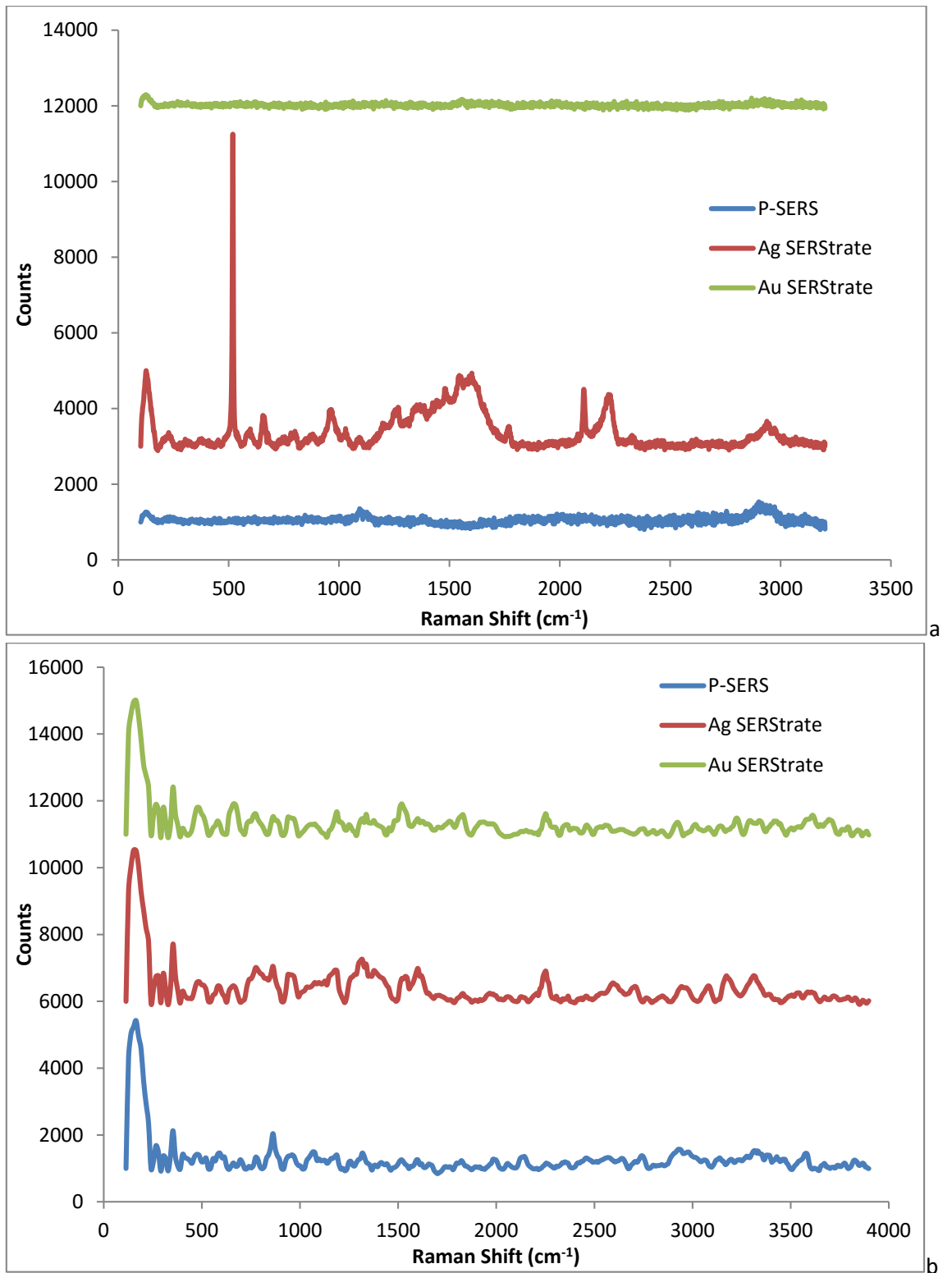
Figure 8.5: Control Raman Spectra for commercial SERS substrates, a) 514nm Raman and b) 1064nm Raman. Spectra offset for clarity.

Table 8.7: 514nm Raman shift peaks (cm^{-1}) and corresponding bonds for commercial SERS substrate controls

P-SERS	Ag SERStrate	Au SERStrate	Peak Assignment
132.2	129.2		*Lattice vibrations*
	518.9		*C-C=O bend*
	655.3		*C-O-H bend*
	964.9		*=CH out-of-plane deformation*
1093.8	1270.1		*C-O-C antisymmetric stretch*
	1544.9		*Ring stretch*
	1770.7		*C=O stretch*
	2109.4		*N=N=N antisymmetric stretch*
	2221.9		*C≡N stretch*
2895.4	2938.4		*CH antisymmetric and symmetric stretch or OH stretch*

Table 8.8: 1064nm Raman shift peaks (cm^{-1}) and corresponding bonds for commercial SERS substrate controls

P-SERS	Ag SERStrate	Au SERStrate	Peak Assignment
	354.4	354.1	*Metal-O stretch or CC bend*
		480.7	*Metal-O stretch or C-O-C bend*
		661.5	*O-C=O bend*
862	779.9 862.5		*CH out-of-plane deformation*
	942		*CH2 out-of-plane wag*
	1181.4	1186.6	*C-O stretch*
	1311.8		*N=N=O symmetric stretch*
		1517.4	*Ring stretch*
	1599.4		*COO- antisymmetric stretch*
	2247.4		*N=C=O antisymmetric stretch*
	3171.3		*NH3+ antisymmetric stretch*

When these commercial SERS substrates were immersed with 1mM MBT following the same protocol used for the in-house made shortlisted SERS substrates, the 514nm and 1064nm Raman was then taken and results are shown in Figure 8.6. The 514nm results (Fig. 8.6a), showed only Ag SERStrate showing strong SERS enhancement with visibly definitive MBT characteristic peaks within the spectra. For the Au SERStrate and P-SERS spectra, no visible characteristic peaks were seen, however upon further analysis, Table 8.9, P-SERS showed a peak at 1093cm^{-1} which correlated with a C-S stretch band for MBT. For Ag SERStrate MBT peaks for C-S stretch and Ring stretch were identified. When 1064nm Raman was used, Figure 8.6b, visibly definitive peaks characteristic for MBT were now shown by the Au SERStrate and P-SERS, whereas for Ag SERStrate, multiple large peaks were present, which masked the MBT characteristics spectra. Upon further

analysis, Table 8.10, P-SERS provided peaks for C-S stretch and Ring stretch with the closes peak values to that observed by the MBT solid. Ag SERStrate did provide peaks for C-S stretch and S-H stretch, which neither of the Au substrates showed and Au SERStrate which showed the highest definitive enhancement of MBT peaks. Although multiple characteristic peaks are present for MBT the lack of peaks that correlate with MBT bonds, is hypothetically being caused by the SERS effect, which causes the peaks within the spectra to shift from that observed with Raman, this shift causes some bonds to be out of the range detailed within their frequency libraries and therefore within this study may not be deemed reliable enough for further analysis.

The EF factor was calculated for these commercial SERS substrates with 1mM MBT for both 514nm and 1064nm Raman, using the C-S stretch peak within the spectra as was done for the fabricated SERS substrates, Table 8.10. The results showed that for 514nm Raman, the EF range for all the commercial SERS substrates was between 6.8- 219.7. With Ag SERStrate showing the highest EF value observed from the commercial as well as the shortlisted SERS substrates fabricated in-house. For 1064nm Raman, the EF range was much lower between 6.1-67.5, with Ag and Au SERStrates showing similar EF values, higher than that of P-SERS. The commercial SERS substrates highlight the preference of the metal used by the wavelength in the case of Au SERStrate however it also highlights as with chemically etched Ag wire that if the roughness of the surface is within a certain threshold, SERS enhancement with wavelengths not typically favoured for that metal can be accomplished. P-SERS shows similar EF values as that of the fabricated NP on filter paper, whereas SERStrate, the more expensive substrate showing optimised SERS enhancement, with values not dissimilar to chemically etched Ag wire with 514nm Raman.
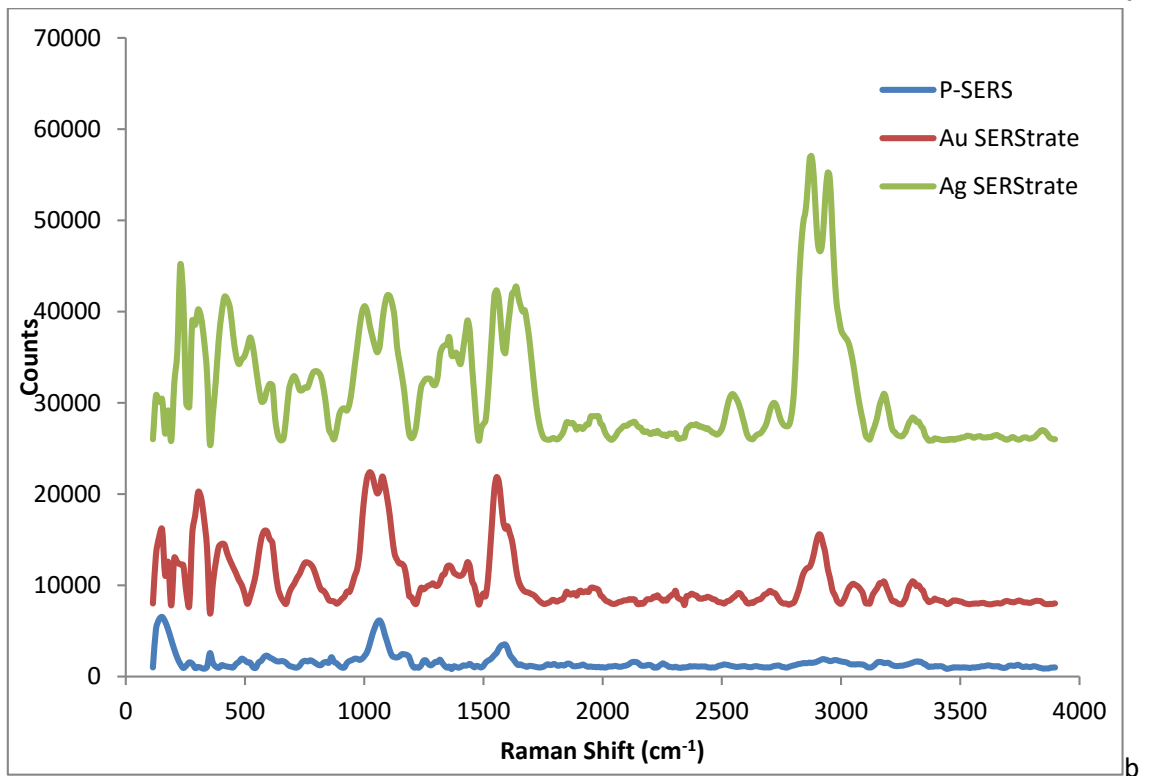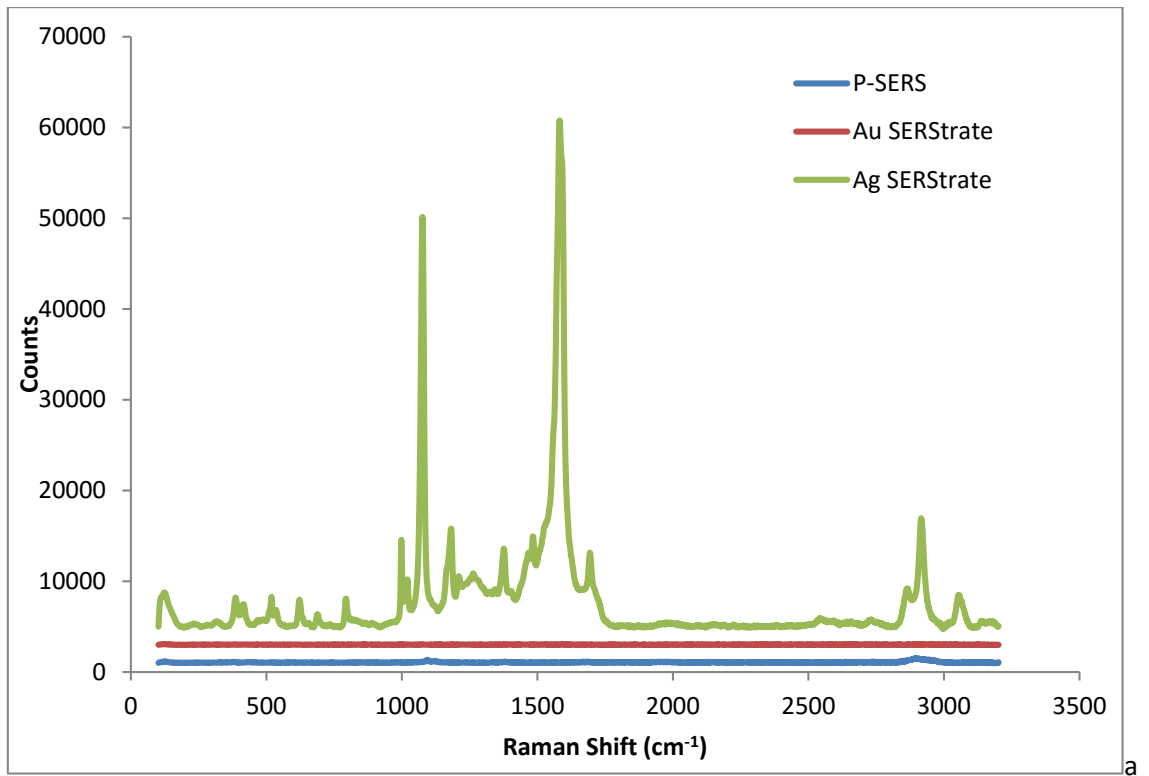
Figure 8.6: SERS spectra for commercial SERS substrates with 1mM MBT with a) 514nm Raman and b) 1064nm Raman. Spectra offset for clarity.

208

Table 8.9: 514nm Raman Shift peaks (cm^{-1}) corresponding to definitive MBT bonds for commercial SERS substrates with 1mM MBT

MBT solid	P-SERS	Ag SERStrate	Au SERStrate	Peak Assignment
1096.6 1183.9	1093.9	1179.5		*C-S stretch*
1596.8		1584.6		*Ring stretch*

Table 8.10: 1064nm Raman Shift peaks (cm^{-1}) corresponding to definitive MBT bonds for commercial SERS substrates with 1mM MBT

MBT solid	P-SERS	Ag SERStrate	Au SERStrate	Peak Assignment
598.7	588.9		578.1	*C-S stretch*
1085.7	1175.1	1100.2		*C-S stretch*
1592.1	1581.9		1560	*Ring stretch*
2567.9		2549.2		*S-H stretch*

Table 8.11: EF values for C-S stretch for commercial SERS substrates with 1mM MBT using 514nm and 1064nm Raman.

SERS substrate	Wavelength (nm)	SERS Peak Value	I_{SERS}	C_{SERS}	I_{RS}	C_{RS}	EF
P-SERS	514nm	1093.9	346.1	0.001	2000.8	0.039452	**6.8**
	1064nm	1175.1	1425.3	0.001	9261.9	0.039452	**6.1**
Ag SERStrate	514nm	1179.5	11144.1	0.001	2000.8	0.039452	**219.7**
	1064nm	1100.2	15853.1	0.001	9261.9	0.039452	**67.5**
Au SERStrate	1064nm	1049	15775.4	0.001	9261.9	0.039452	**67.2**

8.4. Quantitative Characteristics of the SERS substrates

The fabricated SERS substrates as well as the commercial P-SERS were further tested at MBT concentrations from 1aM to 1M to determine their quantitative characteristics including the limit of detection. Initially, we looked at quantifying the effect of increasing concentration of MBT on the increase in the absolute intensity of the C-S stretch peak (at about 1094cm^{-1}). However, the increase in C-S stretch peak intensity was inconsistent, which could be due to differences in the spectral acquisition conditions for the different samples. To overcome the inter sample spectral differences, we did a ratio of absolute peak intensities for ~1096cm^{-1} (C-S stretch) to ~1563cm^{-1} (ring stretch) on individual spectra. The peak ratios did normalize the effects of spectral acquisition conditions as

highlighted by the linear trends of increasing peak intensity ratios observed for the different SERS substrate designs developed in this study.

Ag wire SERS substrate gave SERS spectra for MBT using both 514nm and 1064nm Raman spectrometers (Fig. 8.7). However the limits of detection were different. LOD was down to 1aM using 514nm laser wavelength, while that with 1064nm laser wavelength was 1nM. The R^2 on the linear regression curves were similar for both laser wavelengths (R^2 of 0.75 and 0.92 for 514nm and 1064nm respectively). The 1nM LOD for 1064nm Ag wire SERS substrate with MBT compared to 1aM LOD for that observed with 514nm Raman, can be attributed to the lower SERS enhancement for longer wavelength lasers. Ag NPs on filter paper (Fig. 8.8) or electrospun membrane (Fig. 8.9) gave similar LOD values of 0.01µM with 514nm Raman. Effectively these substrates can be used for quantitative SERS detection.

For dry NPs on filter paper, electrospun membranes or with P-SERS, with 1064nm Raman, the substrates were being burnt. Hence we needed to test them within a microfluidic chip in a wet state, to obtain meaningful spectra. The resulting spectral intensity was much lower for detection of MBT and therefore were inconsistent for quantification of MBT. The best results were seen for Au NPs on electrospun membrane, where the LOD was 0.1µM (Fig. 8.10). With Ag NPs on filter paper or electrospun membranes and P-SERS the results were inconsistent.
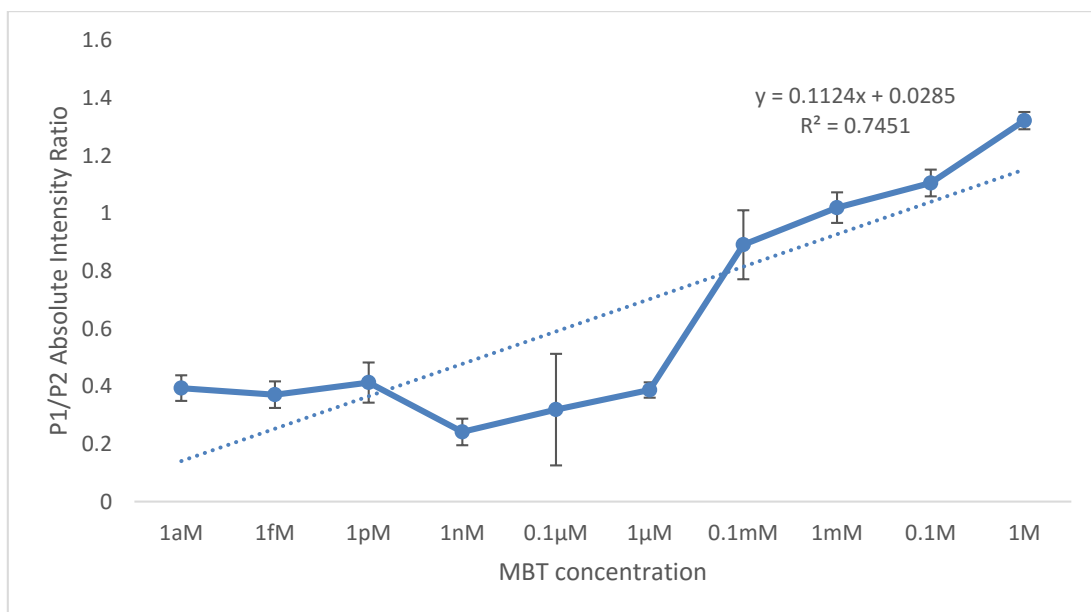
a
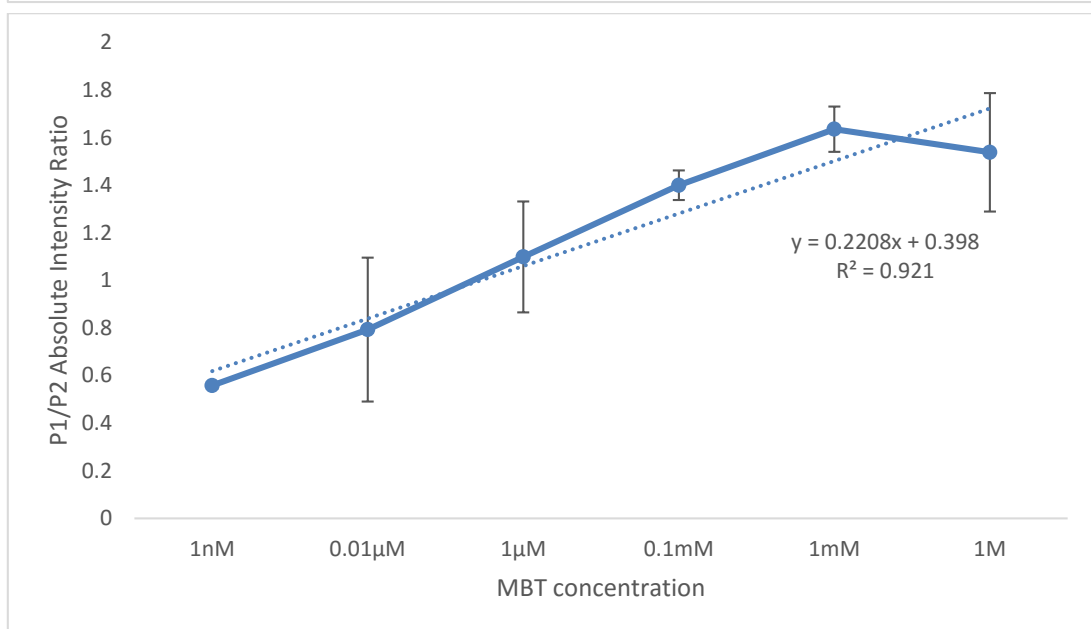
b

Figure 8.7: Linear regression curves for MBT on Ag wire SERS substrate using a) 514nm and b) 1064nm Raman spectrometers; where P1 is peak 1 around 1096cm^{-1} representing C-S stretch and P2 is peak 2 around 1563cm^{-1} representing the ring stretch vibration. Standard error shown, n=6.
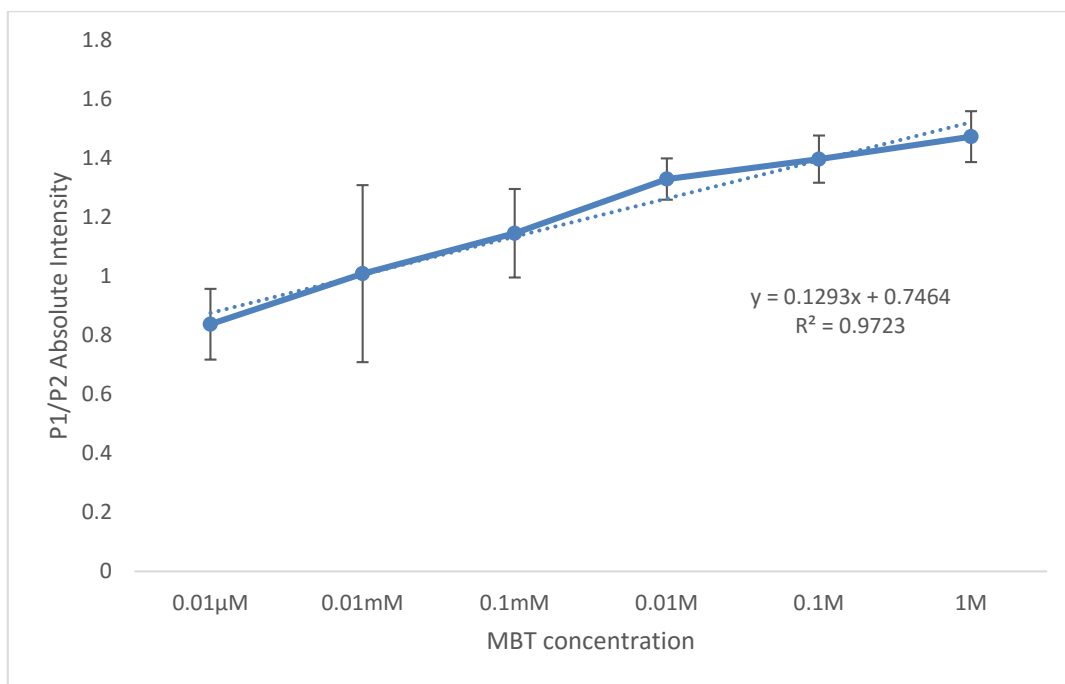
Figure 8.8: Linear regression curves for MBT on Ag NPs on filter paper using 514nm Raman spectrometer; where P1 is peak 1 around 1096cm^{-1} representing C-S stretch and P2 is peak 2 around 1563cm^{-1} representing the ring stretch vibration. Standard error shown, n=6.
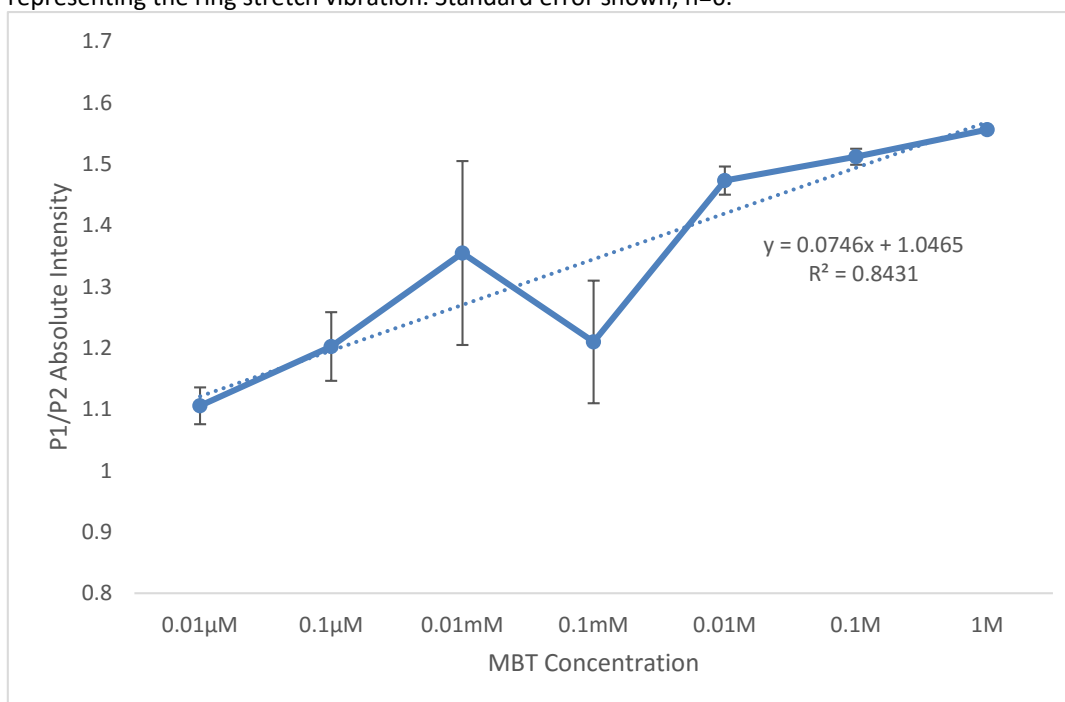
Figure 8.9: Linear regression curves for MBT on Ag NPs on electrospun membranes using 514nm Raman spectrometer; where P1 is peak 1 around 1096cm^{-1} representing C-S stretch and P2 is peak 2 around 1563cm^{-1} representing the ring stretch vibration. Standard error shown n=6.
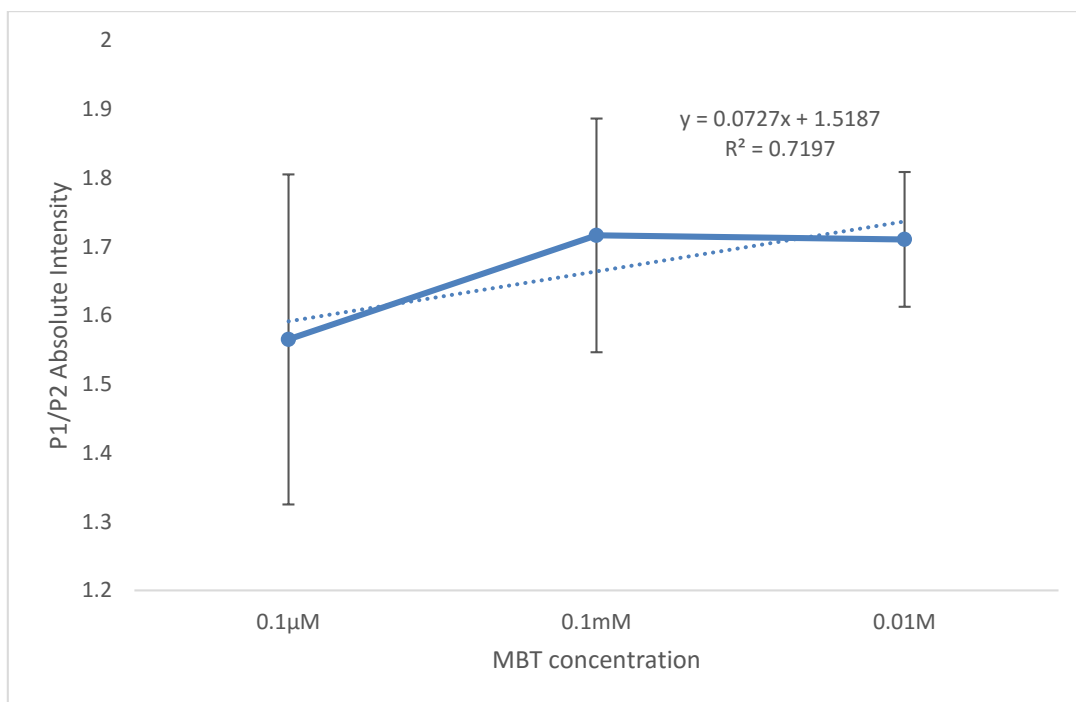
Figure 8.10: Linear regression curves for MBT on Au NPs on electrospun membranes using 1064nm Raman spectrometer; where P1 is peak 1 around 1096cm^{-1} representing C-S stretch and P2 is peak 2 around 1563cm^{-1} representing the ring stretch vibration. Standard error shown, n=6.

8.5. Chapter Summary

In this study, optimised SERS substrates from each design category were compared with one another as well as with two commercial SERS substrate designs; P-SERS, inkjet printed Au NPs on cellulose paper and SERStrate, Au and Ag film on silicon pillars using mask less lithography. The results for 514nm Raman firstly for the SERS substrates designed within the 3 design categories, with 514nm Raman showed that Ag NPs from CTAB/But/Cyclo reduced with NaBH$_4$ on electrospun membrane had the visible enhancement of MBT, whereas chemically etched Ag wire showed the most peaks corresponding to MBT spectra. For 1064nm Raman results, NP separated Au NPs from AOT/But/Cyclo reduced with NaBH4 on electrospun membranes showed the highest enhancement of MBT within the spectra, with chemically etched Ag wire, 30s NH$_4$OH+ 10s HNO$_3$, showing similar intensities in MBT peaks. For the commercial SERS substrates, Ag SERStrate, showed the highest enhancement of MBT with 514nm Raman, with P-SERS showing little visible MBT spectra but corresponding peaks upon further analysis and Au SERStrate shows no MBT enhancement. When the commercial substrates were tested with 1064nm Raman, Au SERStrate showed the highest MBT

enhancement of peaks, with P-SERS showing more definitive MBT peaks within the spectra compared with the 514nm spectra and Ag SERStrate showing MBT peaks, however they were masked within the 1064nm spectra so characteristic peaks were not easily visibly defined. From these results the SERS substrates fabricated and commercial SERS substrates were compared in relation to their enhancement factor (EF). The results showed that with 514nm Raman, Ag SERStrate had the highest EF of 219.7, with fabricated in-house SERS substrates showing highest EF for chemically etched Ag wire at 114.9 EF. P-SERS had a similar EF value as that of NPs on filter paper, particularly of NPs added to the filter paper while still in the microemulsions, when NPs were separated EF value was shown to increase from 5.2 to 35.9 respectively. NPs on electrospun membranes were shown to have higher EF values compared to NPs on filter paper with an increase from 35 to 51.5, taking maximum EFs from each design category with 514nm Raman. Therefore the proximity of the NPs upon the surface is of importance for controlling hot-spot formation and thus increased SERS enhancement as the NP size and shape, particularly for Ag NPs remained typically unaltered after separation, when compared with Au NPs. The 1064nm Raman results showed that Au SERStrate now have SERS enhancement characteristics for 1mM MBT with an EF value of 67.2, which was similar to the Ag SERStrate counterpart which although within the spectra visibly appeared more noisy for MBT determination and one may assume was burning with the laser wavelength, showed an EF of 67.5. P-SERS showed similar EF values for both 514nm and 1064nm of around 6. Among the fabricated SERS substrates NP separated Au NPs on electrospun membrane showed the highest EF of 22.9. The preference of 1064nm Raman for Au metal compared with Ag metal was highlighted by the SERS enhancement of Au SERS substrate motifs of both the commercial and fabricated designs, however structural alteration was shown to also be of importance for EF with Au NPs on filter paper not presenting as high an EF as Au NPs on electrospun membrane. The promising EF values of chemically etched Ag wire and Ag SERStrate, highlight the importance surface morphology, as with controlled roughness, wavelength preference can be subdued to provide a SERS substrate with broadband characteristics. All three SERS substrate

designs, chemically etched Ag wire, NPs on filter paper and NPs on electrospun membranes were also highlighted for their quantification characteristics with MBT. With chemically etched Ag wire showing a concentration range down to 1aM and a linearity of R^2 0.74 with 514nm Raman, with 1064nm Raman the concentration range was higher with a limit of detection at 1nM and a linearity of R^2 0.92. For Ag NPs on filter paper and electrospun membranes the limit of detection was similar at 0.01µM with R^2 of 0.97 and 0.84 respectively with 514nm Raman. When Au NPs on electrospun membrane were tested for their quantitative behaviour with MBT using 1064nm Raman was shown to have a higher LOD of 0.1µM and R^2 of 0.72. Ag SERS substrates fabricated can thus be shown as having an optimised structures for SERS efficacy, particularly with 514nm Raman. Chemically etched Ag wire provided the best results for SERS substrate efficacy with MBT, with high EF values and low LOD values with high linearity with both 514nm and 1064nm Raman. Therefore the Ag SERS substrate was taken for use as the SERS substrate for proof-of-concept work with the use of diabetes biomarkers.

Chapter 9: Diabetes Biomarker detection using SERS

9.1. Introduction

The incorporation of SERS within a lab-on-a-chip device for diagnostics and monitoring would be highly beneficial due to its high sensitivity, rapid detection time, ability for equipment miniaturisation, minimal sample requirement, little to no sample preparation and multiplexing capability. However as of yet it has not been implemented within the field, due to lack of repeatability and reliability, caused by hot-spot irregularity, high cost of SERS substrates and minimal data regarding the use of SERS for repeatable biomolecule detection, noted for diabetes mellitus (Alvarez-Pueblo & Liz-Marzan, 2012; Barman et al, 2012; Dingari et al,2012; Lyandres et al, 2007). There is a high need for improved diagnostics and monitoring within disease diagnosis, particularly for Diabetes Mellitus, with research highlighting that with improved detection & monitoring, the problems faced by diabetes would be reduced or even prevented (Baynes & Dominczak, 2009). Multiple biomolecules have been highlighted as providing increased information for diabetes care, with glucose and HbA$_{1C}$ providing information on glycaemic control for 24 hours to 6-8 weeks respectively. The use of an additional biomarker, glycated albumin is noted to provide information of glycaemic control for 2-3 weeks, enabling a more extensive snapshot for diabetes treatment. As well improving the ability of these biomarkers to overcome limitations for individual patients who could cause false positives or negatives with individual biomarkers, detailed in chapter 2.

The aim of this study was to provide proof-of-concept for the use of our optimised SERS substrates for selective detection of diabetes biomarkers; glucose, Haemoglobin, HbA$_{1c}$, Albumin and glycated albumin. For testing these biomolecules, chemically etched Ag Wire; 30s NH$_4$OH+10s HNO$_3$ was used to evaluate the use of different SERS morphologies for affinity of the biomolecules to the surface.

The equipment used within this chapter was FTIR and Raman in 514nm and 1064nm configurations. For protein detection only 514nm Raman was used as it was found that due to the high power output of the 1064nm laser, the proteins were burning.

9.2. Diabetes Biomolecules Control Spectra

As with MBT tests, control spectra for glucose and the protein biomarkers were taken using FTIR and Raman when possible. FTIR is a complementary technique to Raman, which provides molecular information of bonds. However due to difficulty of FTIR for miniaturisation as well as the types of samples that can be processed, most notably the difficulty with assessment of liquids, the use of SERS is more desirable for use within a lab on a chip device.

9.2.1. Glucose

Solid glucose control spectra using FTIR and both Raman instruments, Figure 9.1, supported that the peaks present with both FTIR and Raman were complimentary to one another, with high intensity peaks shown for both Raman wavelengths for bonds that had weak transmittance with FTIR and vice versa. The Raman spectra highlighted higher intensity peaks for glucose with 514nm Raman compared to 1064nm Raman. The FTIR results for glucose, Figure 9.1a, showed multiple sharp peaks at lower wavenumbers associated with carbonyl bonds, and with increasing wavenumber, sharp peaks at lower transmittance for hydrocarbon peaks with a broad peak around 3204cm^{-1} for O-H stretch. When compared with the Raman results, Figure 9.1b, showed sharp peaks with high intensity, especially with regards to the use of 514nm for hydrocarbon peaks, as well as for multiple smaller intensity peaks below 1500cm^{-1}, which was for additional hydrocarbon bond movements as well as carbonyl bonds, detailed in Table 9.1.
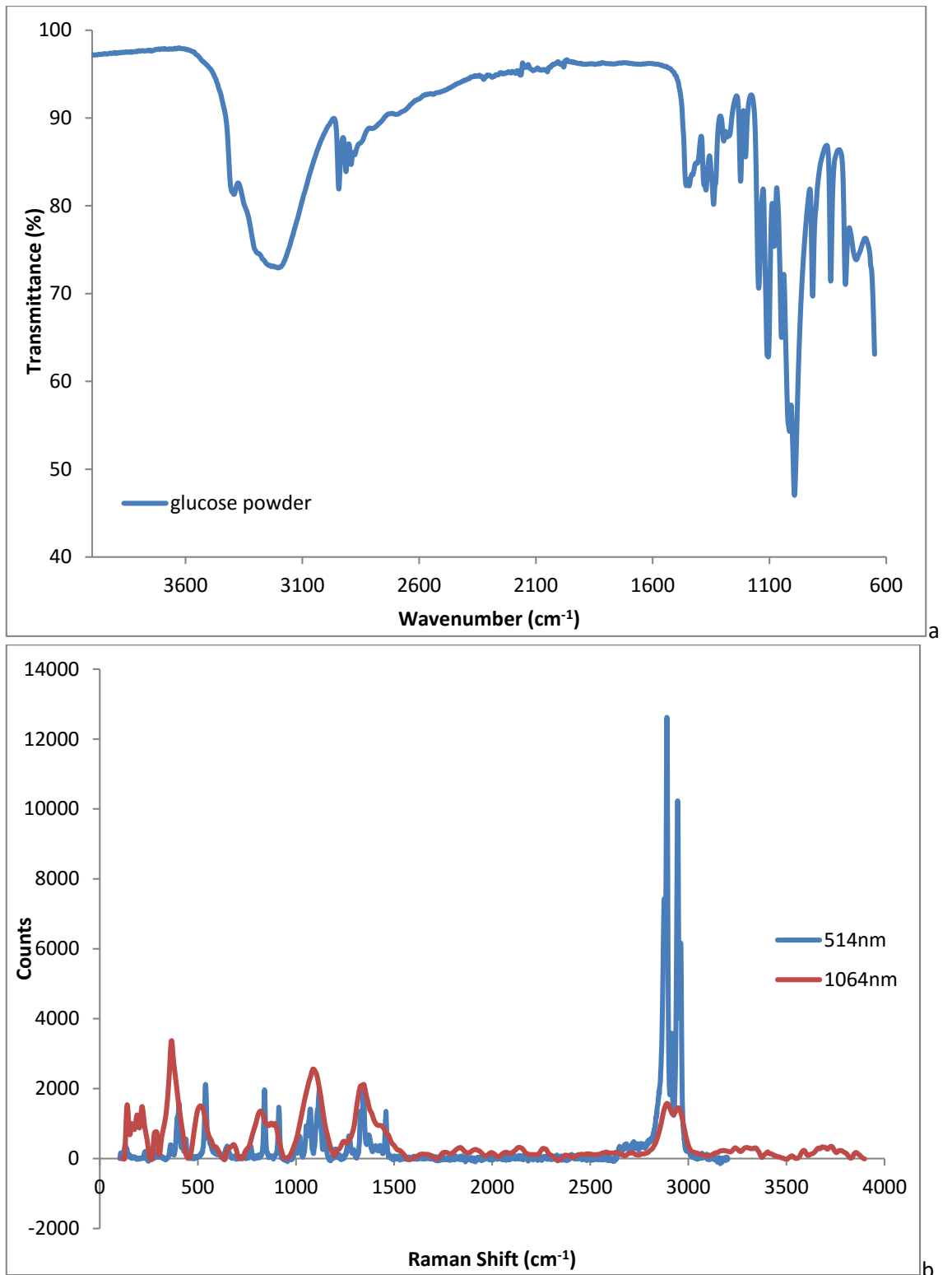
Figure 9.1: Molecular spectra for solid glucose control using a) FTIR and b) Raman 514nm and 1064nm.

When the 1064nm Raman spectra for solid glucose control was compared with concentrations of glucose dissolved in deionised water at concentrations of 3mM and 30mM, the results showed, that at that at the higher concentration of glucose there were more peaks that correlated to similar bonds with the control glucose solid, compared to 3mM glucose, which showed little presence of peaks above the background noise. The glucose peaks within solution that correlated with the glucose solid were for CC bend around 353cm^{-1}, CH out-of-plane deformation at around 800cm^{-1} and carbonyl C-O stretch at around 1075cm^{-1}. Additional peaks for both solutions correlated with bonds shown by 514nm Raman and FTIR, for CH$_2$ scissor vibration with 3mM glucose and O-H stretch from 30mM glucose respectively. This highlights that the free movement of glucose within the liquid state compared with solid state causes scattering of different bonds, therefore for a SERS substrate that is within solid form compared to within solution the presence of bonds could theoretically be different.
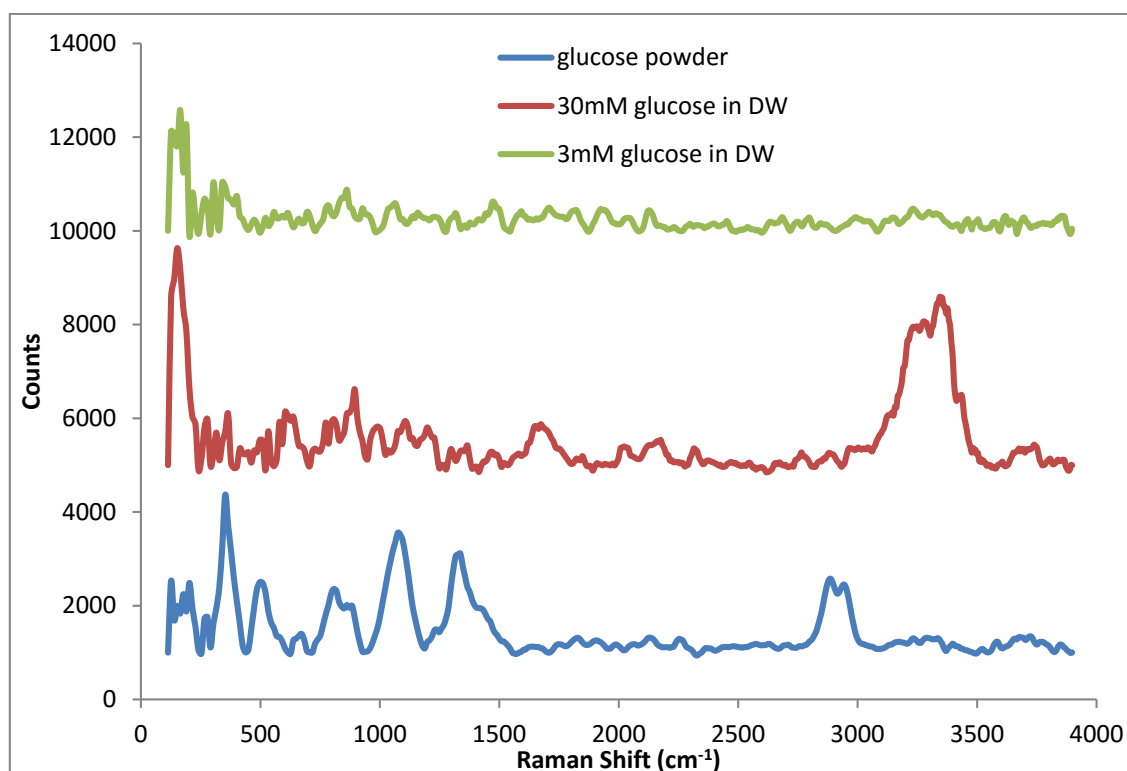
Figure 9.2: 1064nm Raman spectra for control glucose solid and glucose concentrations in deionised water at 3mM and 30mM. Spectra offset for clarity.

Table 9.1: Control glucose peak and associated bonds for solid and concentrations within deionised water using FTIR and Raman 514nm and 1064nm

FTIR Glucose Powder	514nm Glucose Powder	1064nm Glucose Powder	1064nm 30mM Glucose in DW	1064nm 3mM Glucose in DW	Peak Assignment
	360.9 402.8	353.7	354.7	349.6	*CC bend*
		498.5			*C-O-C bend*
	539.3				*Ring deformation*
			593.1		*O-C-O bend*
	649	659.9			*O-H out-of-plane deformation*
728.8					*CH_2 rocking*
	770.4 839.4	813	780.2 861.8	862.2	*CH out-of-plane deformation*
915.35	913.137				*CH_2 out-of-plane wag*
993.08					*=CH out-of-plane deformation*
1014.4	1019.9 1071.2 1148.7	1075.3	1068.3 1157.1	1058.6	*C-O stretch*
1078.9 1202.7 1223.7	1202.4 1269.6				*C-O stretch or C-O-C antisymmetric stretch*
	1343.8	1330.1			*COO- symmetric stretch*
1372	1370.2				*CH_3 symmetric deformation*
1444.6					*CH_3 antisymmetric deformation*
1456.9	1458.3			1477.5	*CH_2 scissors vibration*
			1622.9		*C=C stretch*
2051.1					*Several bands from overtone and combinations bonds*
2891.4 2913.4 2944.1	2890.7 2945.6	2911.9			*CH antisymmetric and symmetric stretch*
3204.7			3255.7		*O-H stretch*
3392.6					*OH stretch*

9.2.2. Proteins

The protein biomarkers of interest for diabetes mellitus detection were HbA$_{1c}$ and glycated Albumin. To test these concentrations, typically a ratio is calculated in relation to their non-glycated protein forms. Therefore a difference in spectra was required for difference between the two forms. As proteins have a lower melting point than glucose, with 1064nm Raman it was observed that due to the high power output of the instrumentation, protein samples burned before sufficient scans could take place, even with improvised designs and within liquid. Therefore FTIR was used for assessment of control spectra.

For the study of diabetes biomarkers with SERS, bovine samples of the biomolecules were used for most of the testing as an alternative to the human samples, due to technical problems for experiments regarding availability of consumables, therefore a comparison between the bovine and human forms was highlighted in Figure 9.3 to compare any differences present within the spectra that would be unsatisfactory for detection further along. In Figure 8.3a, the FTIR spectra for haemoglobin (Hb) shows similar peaks for both configurations, with human Hb having higher transmittance of bonds compared with the bovine alternative. Upon further analysis, Table 8.2, the results show similar bonds for the majority of the peaks present, with an additional bond for bovine Hb at 1084cm^{-1} for C-O-C stretch, whereas for human Hb, additional peaks for further bonds with nitrogen such as C-N stretch and NH3^{+} antisymmetric stretch are shown at 1241cm^{-1} and 3060cm^{-1} respectively. The presence of the Amide I and Amide II bands for both Hb motifs, shows that the FTIR spectra has picked up the presence of a protein. For albumin, Figure 9.3b, the spectra also similar peaks for the bovine and human configurations, with bovine serum albumin showing higher transmittance on this occasion when compared to the human alternative. An additional C-OC stretch at 1081cm^{-1} is also shown for the bovine albumin as for bovine Hb that was not present within the human forms. Also as with the human Hb, the human albumin also shows additional peaks for nitrogen bonds such as NH3^{+} deformation at 1516cm^{-1}, shown in Table 9.2.
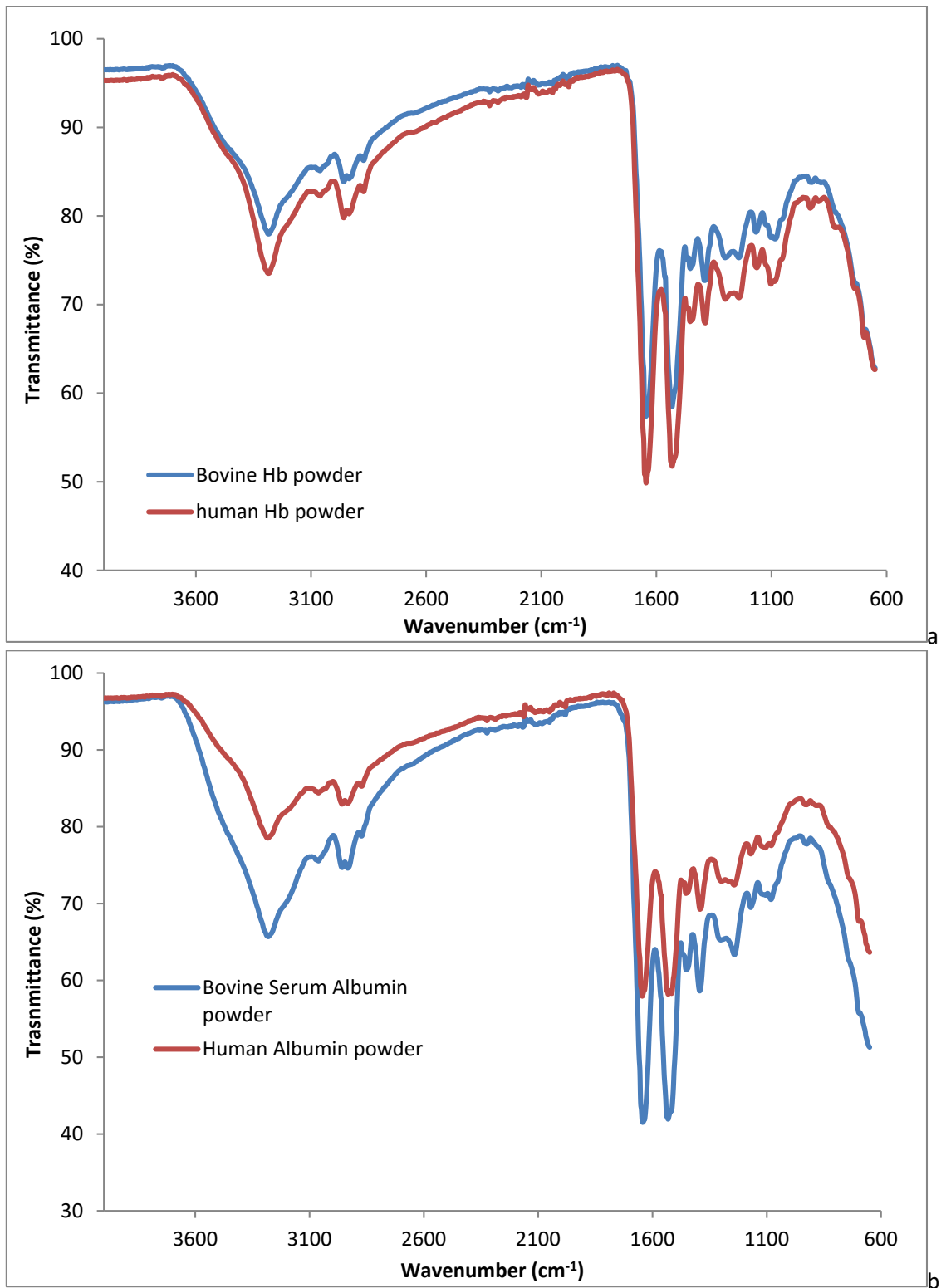
Figure 9.3: FTIR spectra of human and bovine alternatives for a) Haemoglobin and b) Albumin

When the protein and its glycated form were compared, Figure 9.4, the results showed visibly similar peaks within the spectra for both glycated and non-glycated forms, with transmittance of peaks for Hb and HbA_{1c}, Figure 9.4a, showing similar values. Whereas for glycated and non-glycated albumin, Figure 9.4b the transmittance of non-glycated albumin was visibly higher than that of its

glycated counterpart. Upon further data analysis, Table 9.2, HbA_{1c} shows additional bonds at 981cm^{-1}, 1079cm^{-1} and 2166cm^{-1} for =CH out-of-plane deformation, C-O-C stretch and N≡C stretch respectively. Whereas Hb shows an additional peak at 2324.64cm^{-1} for P-H stretch, these slight alternatives in bonds present could be useful for qualitative determination between the two forms. For Albumin and glycated albumin, Figure 9.3b, there are multiple peak differences shown upon further data analysis, Table 9.2, with glycated albumin showing peaks at 1077cm^{-1}, 1299cm^{-1}, 1649cm^{-1} and 2050cm^{-1} for C-N stretch, N-O stretch, C=O stretch and combination bonds overtone respectively. The non-glycated albumin also show peaks not present within the glycated form at 1242cm^{-1}, 1516cm^{-1}, 2163cm^{-1} and 3061cm^{-1} for C-N stretch within this band, NH3^{+} deformation, N≡C stretch and NH3^{+} antisymmetric stretch. One presumes that with the addition of glucose as supported by the difference in bonds for both HbA_{1c} and glycated albumin there is conformational change within the protein structure causing alteration in bond movement. These characteristics with SERS would essentially be enhanced due to SERS highlighted ability within literature for single molecule detection.

When the proteins were compared with one another with FTIR, Figure 9.5, all the spectra, due to protein structures showed similar FTIR results, upon further analysis, Table 9.2, Hb configurations showed peaks for CH out-of-plane deformation not present within the albumin alternatives, with each individual protein configuration presenting an individual peak that was not present within the other spectra. Such as within the HbA_{1c} spectra, a peak at 981cm^{-1} for =CH out-of-plane deformation is only present for this protein motif whereas for glycated albumin a peak at 1077cm^{-1} for C-N stretch is only present there.
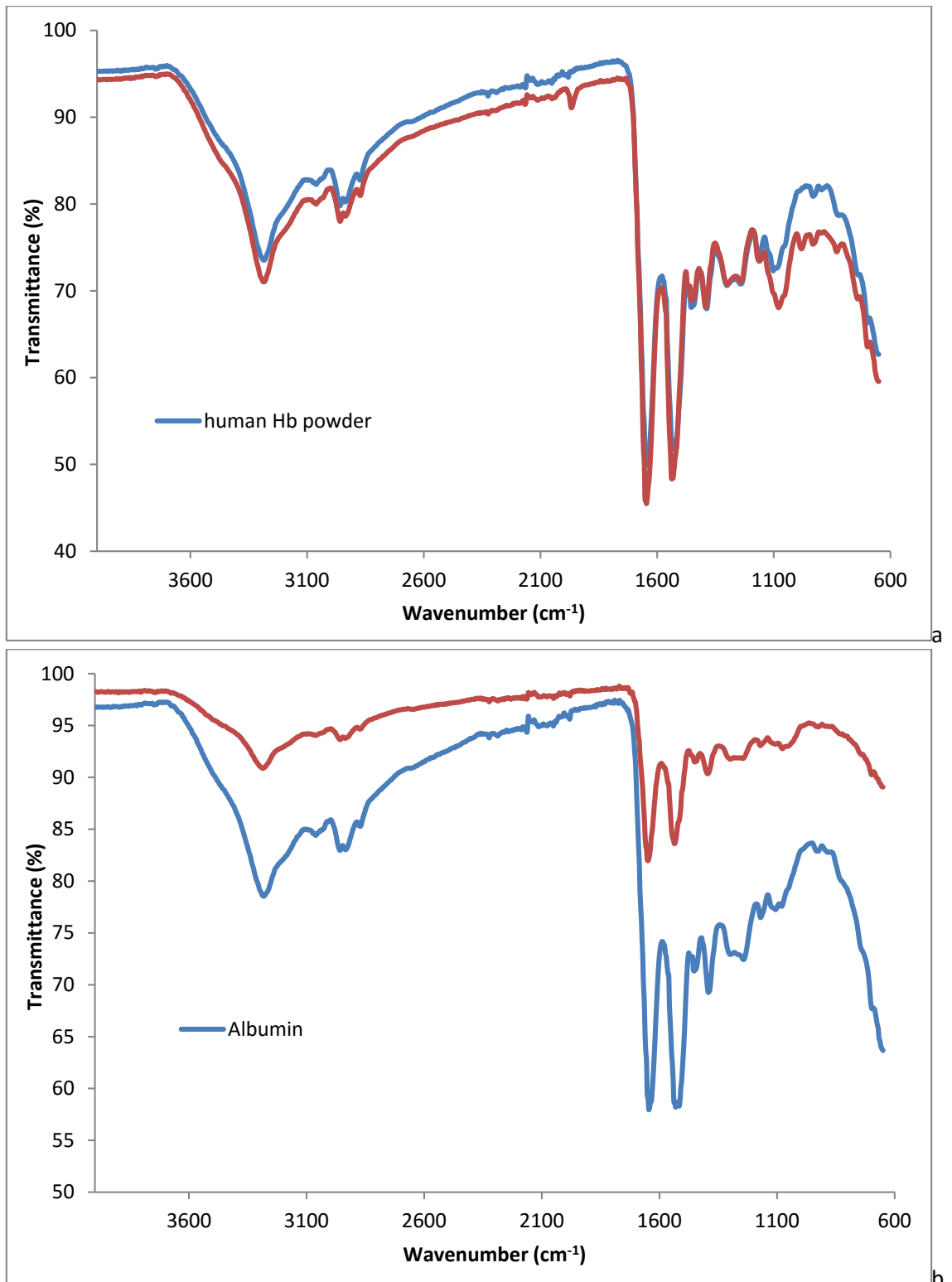
Figure 9.4: FTIR spectra for a) Hb and HbA$_{1c}$ and b) Albumin and glycated Albumin
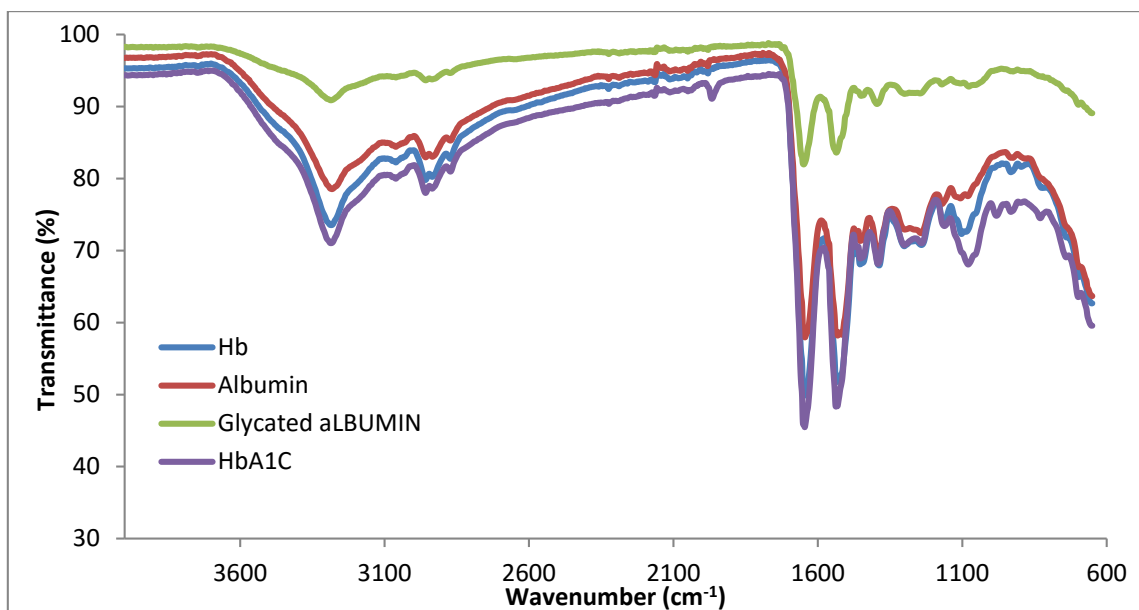
Figure 9.5: FTIR spectra for Hb, Albumin and their glycated forms.

When the 514nm Raman spectra for Hb and Albumin were taken the results showed lack of any characteristic peaks for the molecules. This which supported within literature, as 514nm wavelength is noted as not typically resonating with bonds within biomolecules compared to longer wavelengths (AZO materials, 2015). Therefore, SERS enhancement of these biomolecules with this wavelength would be advantageous in supporting the applicability of SERS within biosensors.
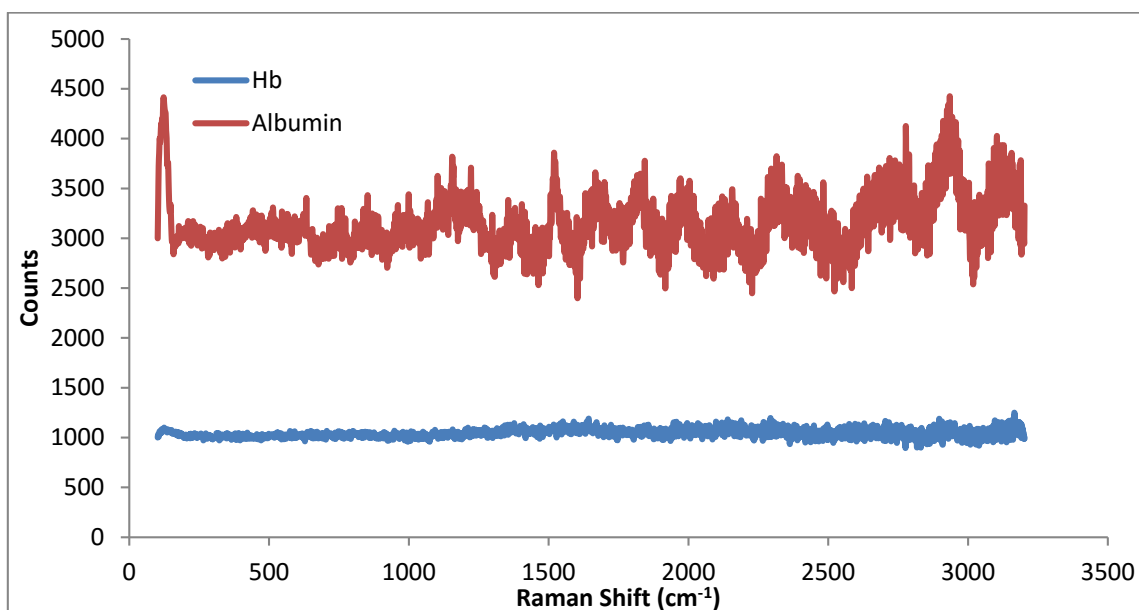
Figure 9.6: 514nm Raman Spectra for Hb and Albumin control.

Table 9.2: Control peaks and correlating bonds for Protein Hb and Albumin and their glycated forms with FTIR

Bovine Hb	Human Hb	Human HbA1C	Bovine Serum Albumin	Human Albumin	Human Glycated Albumin	Peak Assignment
697.8	698.5	698.6 830.1				CH out-of-plane deformation
924.3	896 932	931.9	925	925.1		CH_2 out-of-plane wag
		981.9				=CH out-of-plane deformation
					1077.3	C-N stretch
1084.5		1079.5	1081.7			C-O-C stretch
	1102.7			1106.5		C-C-N bend
1167.4	1163.8	1161.8	1170.4	1169.9	1170.7	C-O-C antisymmetric stretch
	1241.5	1240.7	1241.5	1242.8		C-N stretch (aromatic amines)
1242.3 1301.3	1300.8	1300.6			1299.9	N-O stretch
1390.8	1387.4	1392.6	1393.4	1391.9	1395.3	CH_3 deformations
1453	1453.7	1453.1	1452.5	1453.7	1450.2	CH_2 scissors vibration or N=N-O antisymmetric stretch
				1516.2		$NH3^+$ deformation
1532	1531.6	1537.8		1531.4	1536	NO_2 antisymmetric stretch (Amide II band)
1644.9	1644.9	1645.5	1642.8		1649.1	C=O stretch (Amide I band)
				1644.6		C=N stretch
					2050.1	Several bands from overtone and combination bonds
2113.8	2112.6	2112.4	2111.9	2113.8		N=N=N antisymmetric stretch
		2166.5		2163.2		N≡C stretch
	2324.6					P-H stretch
2871.7 2958	2872 2935.2 2958.3	2872 2958	2872.6 2933.4 2958.4	2957.8	2957.5	CH antisymmetric and symmetric stretch or OH stretch
	3060.8	3061	3061.2	3061.1		$NH3^+$ antisymmetric stretch (amino acids)
3284.4	3284.5	3285.9	3281	3282.1	3285.8	NH stretch

9.3. SERS enhancement of Diabetes Biomolecules

For assessing SERS enhancement with the diabetes biomarkers, chemically etched 30s NH$_4$OH+ 10s HNO$_3$ non-heated Ag wire was used, as it provided strong enhancement with both Raman wavelengths as well as being quicker to fabricate and more robust than the other SERS substrate designs.

9.3.1. Glucose

For SERS enhancement of glucose, 30mM concentration was prepared in three different mediums; deionised water, PBS buffer and synthetic saliva, to assess the ability of SERS enhancement of glucose within increasingly more complex solutions. The results with 514nm Raman (Fig. 9.7), showed that glucose firstly is enhanced on the Ag wire surface and secondly that depending on the medium the enhancement of the molecular bonds is altered. 30mM glucose in deionised water is shown to have the highest SERS enhancement of glucose with synthetic saliva showing minimal enhancement. Therefore, increased complexity of the medium does hinder SERS enhancement. Despite claims made within literature that SERS is able to be used with little to no sample preparation, for the implementation of SERS substrates within a lab on a chip design, sample processing would be required, for minimising saturation of the surface with multiple contaminants, preventing the enhancement of the target analyte.
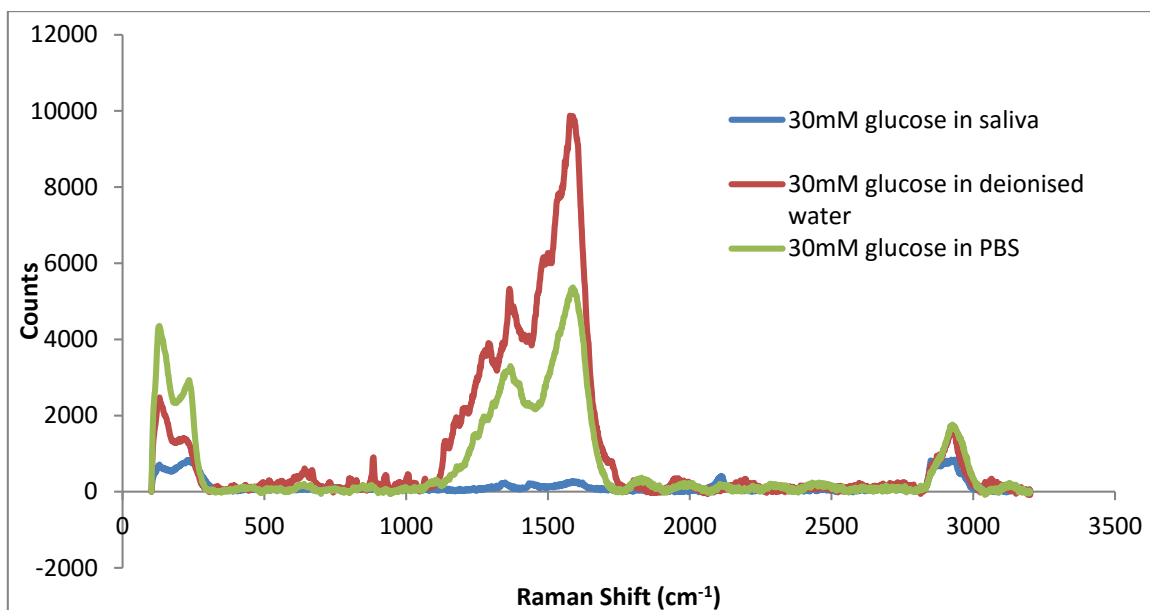
Figure 9.7: 514nm Raman spectra for SERS enhancement of 30mM glucose in deionised water, PBS buffer and synthetic saliva on chemically etched Ag wire SERS substrate.

For continued experiments with glucose, deionised water was used as the medium, for proof-of-concept work regarding the ability of SERS substrates for enhancing biomolecular signal with wavelengths not attuned or developed for these characteristics. As well as providing support for the use of SERS substrates as an ideal biosensor component within a lab on a chip device.

The problem previously faced within literature for the use of SERS substrates for detection of analytes, was that due to hot-spot irregularity there was a variation in enhancement and signal produced on the substrate, and therefore the technique had low repeatability and reliability. With the use of chemically etched Ag wire, it was shown with 3 samples as an example that the SERS enhancement of glucose (Fig. 9.8), remained generally similar for each SERS substrate with the biomolecule; however there still were samples that showed increased intensity of signal. These occurrences were typically minimal and therefore the surface of the Ag wire can be pronounced as providing an increased uniform hot-spot distribution, which is a very promising direction for the preparation of a new generation of SERS substrates.
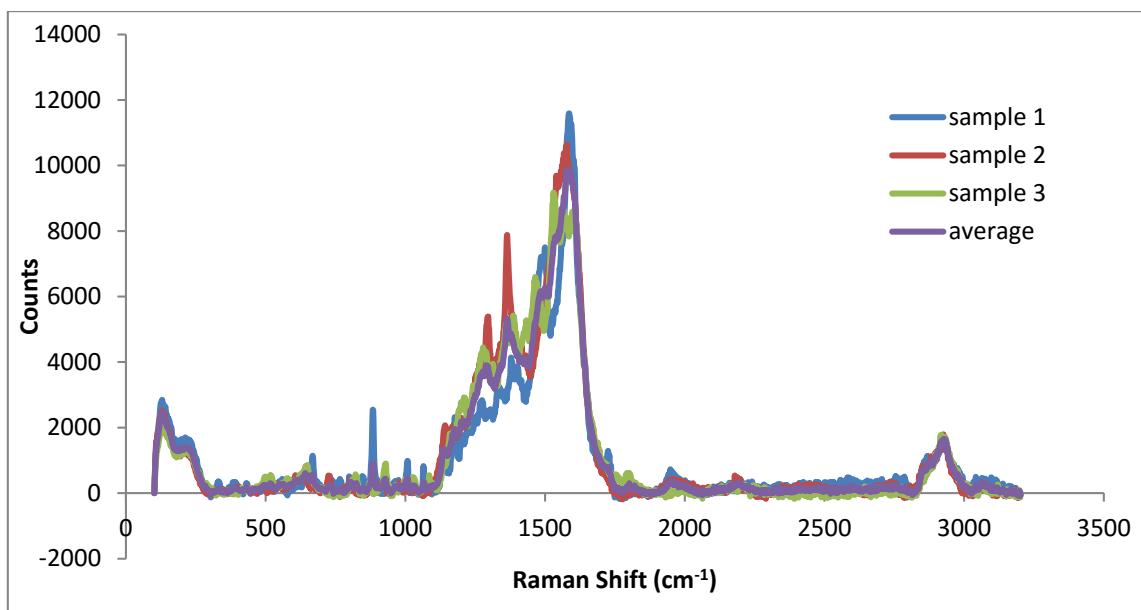
Figure 9.8: 514nm Raman for 30mM glucose in deionised water on SERS Ag wire substrates.

When 30mM glucose on chemically etched Ag wire was tested with both 514nm and 1064nm Raman (Fig. 9.9), the results showed a clear difference in SERS enhancement of glucose. The 514nm wavelength provided increased SERS enhancement of the glucose on the Ag wire, whereas the 1064nm wavelength did not visibly show definitive glucose peaks. Upon further analysis, Table 9.3, both wavelengths did show enhancement of glucose on Ag wire, with 1064nm Raman with glucose showing additional peaks not present within the 1064nm control glucose spectra. However, these peaks correlated with both the FTIR and 514nm Raman control. Therefore, one could support that SERS has provided enhancement of glucose signal. Two peaks appear distinctive for both 514nm and 1064nm Ag wire with 30mM glucose, these were for CH_2 out-of-plane wag and C-O stretch at around 915cm^{-1} and 1223cm^{-1} respectively. Additional peaks were present for both 514nm and 1064nm Raman as mentioned previously with 514nm SERS providing peaks that correlated closely with the control and FTIR spectra, whereas 1064nm SERS spectra provided additional peaks especially within the 1500-2700cm^{-1} range.
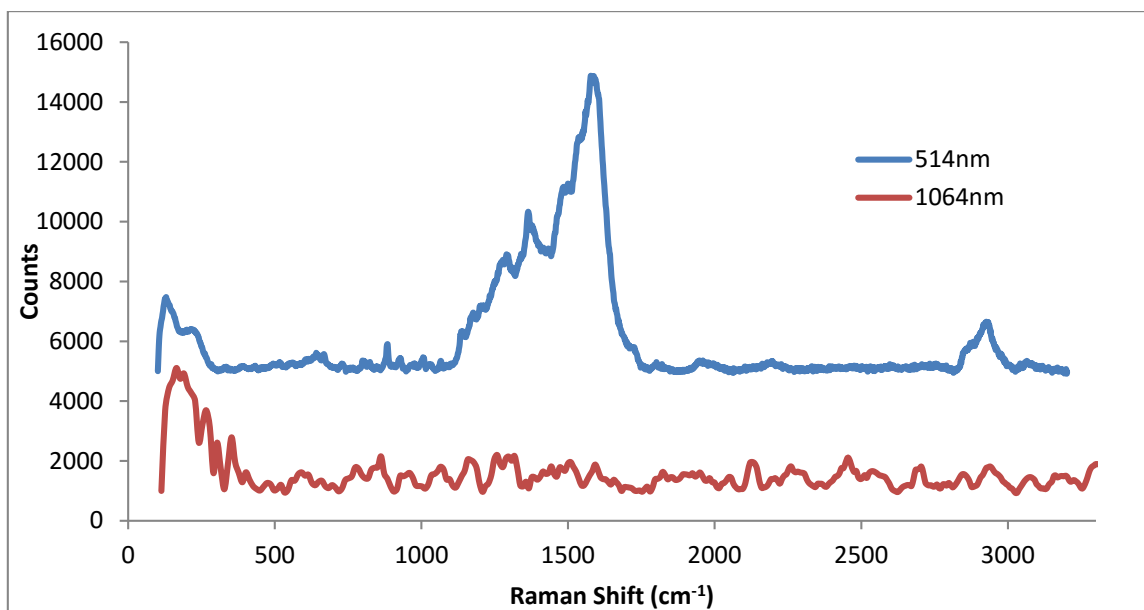
Figure 9.9: SERS spectra of 30Mm glucose on chemically etched Ag wire SERS substrate using 514nm and 1064nm Raman. Spectra offset for clarity.

Table 9.3: Raman and FTIR peaks (cm^{-1}) and corresponding bonds for glucose controls and 30mM glucose on chemically etched Ag wire

Ag wire control	FTIR Glucose control	514nm Glucose control	514nm Ag wire+ 30mM glucose in DW	1064nm Glucose control	1064nm Ag wire+ 30mM glucose in DW	Peak Assignment
133.7			130.3			*Lattice vibrations*
392.7		360.9 402.8		353.7	354.2	*Metal-O stretch or CC bend*
				498.5		*C-O-C bend*
		539.3			590.8	*O-C-O bend*
		649	649.7	659.9		*O-H out-of-plane deformation*
	728.8					*CH$_2$ rocking*
811.4		770.4				*CH out-of-plane deformation*
	915.4	**839.4 913.1**	**882.7 928.5**	**827.5**	**861.2**	**CH$_2$ out-of-plane wag**
1042.6	1043.4 1078.8	1019.9 1071.2 1117.7	1007.6 1065.9 1137.1	1075.3	1067.6 1163.7	*C-O stretch*
			1176.9			*C-O-C antisymmetric stretch*
	1202.7 1223.7	**1202.4 1269.6**	**1290**		**1255.5**	**C-O stretch or C-O-C antisymmetric stretch**
					1317.1	*COO- symmetric stretch*
1346.4	1372	1343.8 1370.2	1364.7	1330.1		*CH$_3$ deformations*
1430.1						*In-plane OH bending*
	1444.6					*CH$_3$ antisymmetric deformation*
	1456.9	1458.3				*CH$_2$ scissors vibration*
			1486.1		1508.9	*Ring stretch*
1587.9			1589.7		1592.3	*COO- antisymmetric stretch*
			1729.4		1823.5	*C=O stretch*
					2128.9	*C≡C stretch*
					2696.7	*Overtone of CH bend*
2929.4	2890.7 2945.6	2890.7 2945.6	2924	2911.9	2940.4	*CH$_3$, CH$_2$, antisymmetric and symmetric stretching respectively or O-H stretch.*
					3314	*O-H stretch*

9.3.2. Hb & HbA$_{1c}$ SERS

Bovine Hb was dissolved in PBS solution, rather than deionised water, due to solubility issues with regards to the latter. As with glucose, a concentration within the typical physiological range observed was taken for qualitative detection with chemically etched Ag wire SERS substrates, this was 2.77mM. The Ag wires were immersed in fresh solution for 24 hours after which they were removed and washed three times before drying in ambient conditions for testing with 514nm Raman. The results shown in Figure 9.10 for 2.77mM bovine Hb on Ag wire, highlight firstly that Hb molecular signal has been enhanced, compared with its control spectra at the same wavelength. The sharp peaks within the 1000-1700cm^{-1} range show enhancement of C-N bonds, carbonyl bonds and hydrocarbon bonds, detailed in in Table 9.4, with bands for Amide II and III shown within the spectra at 1638cm^{-1} and 1396cm^{-1} respectively.
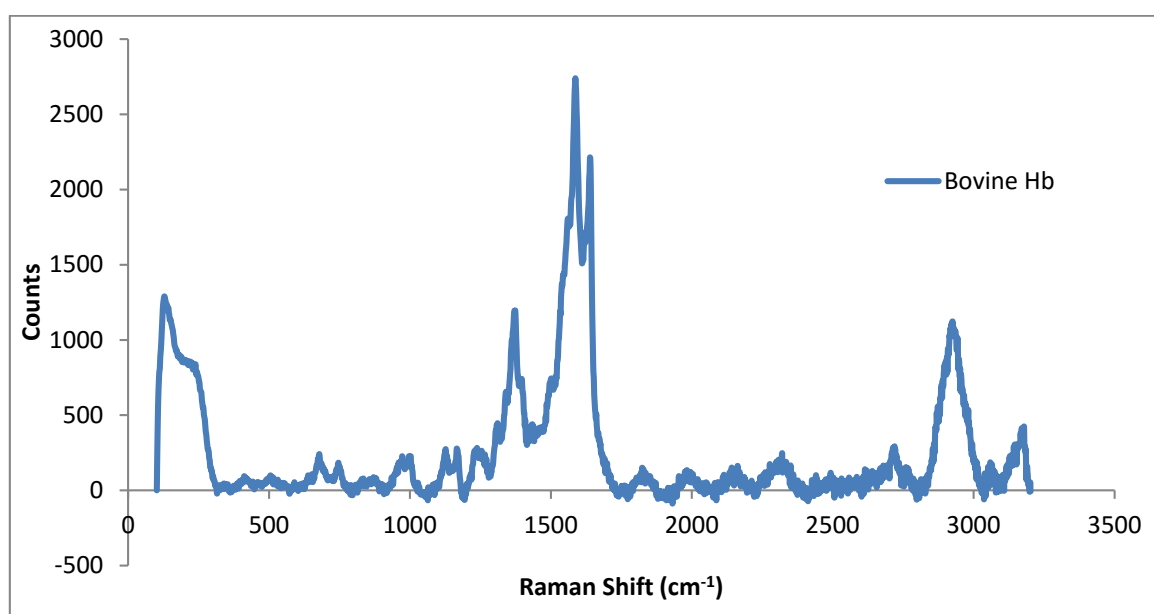
Figure 9.10: 514nm Raman for 2.77mM bovine Hb on Ag wire SERS substrate

As SERS successfully showed enhancement of Hb with 514nm Raman, comparison was made with human Hb and HbA$_{1c}$. For testing, 1M concentrations of each biomolecule configuration was dissolved in PBS buffer, after which following the same protocol, Ag wire SERS substrate was immersed within the solutions for 24 hours and then cleaned and dried before testing. The results (Fig. 9.11) show that there is a threshold concentration for the detection of bovine Hb on the Ag wire surface. As the definitive peaks, shown at 2.77mM have depleted at the higher concentration,

232

therefore the Ag wire may have become saturated preventing efficient scattering of molecules upon the surface. For human Hb and HbA_{1c} as the molecular weights are lower than the bovine alternative, spectra for the biomolecules can still be observed. For both human Hb and HbA_{1c} similar peaks are shown within the same ranges and so visibly could not be accurately differentiated. Table 9.4 highlights three peaks which were present for HbA_{1c} and not Human Hb, at around $1372cm^{-1}$, $1561cm^{-1}$ and $3149cm^{-1}$, for C-N stretch (Amide III band), NH deformation (Amide II band) and $NH3^+$ antisymmetric stretch (amino acids) respectively. The addition of glucose to the N-terminus of the Beta-chains in haemoglobin, cause a slight conformational change within the structure causing the allowed movement of bonds that were previously obstructed within Hb and did not resonate with the 514nm wavelength. One should highlight that the orientation of the biomolecules on the SERS substrate also play a part for the peaks that can be scattered and present spectra for the biomolecule, shown by the diminished peaks of Bovine Hb as the surface becomes to saturated. Upon this SERS surface however, these three peaks can be used for differentiation between Hb and HbA_{1c}.
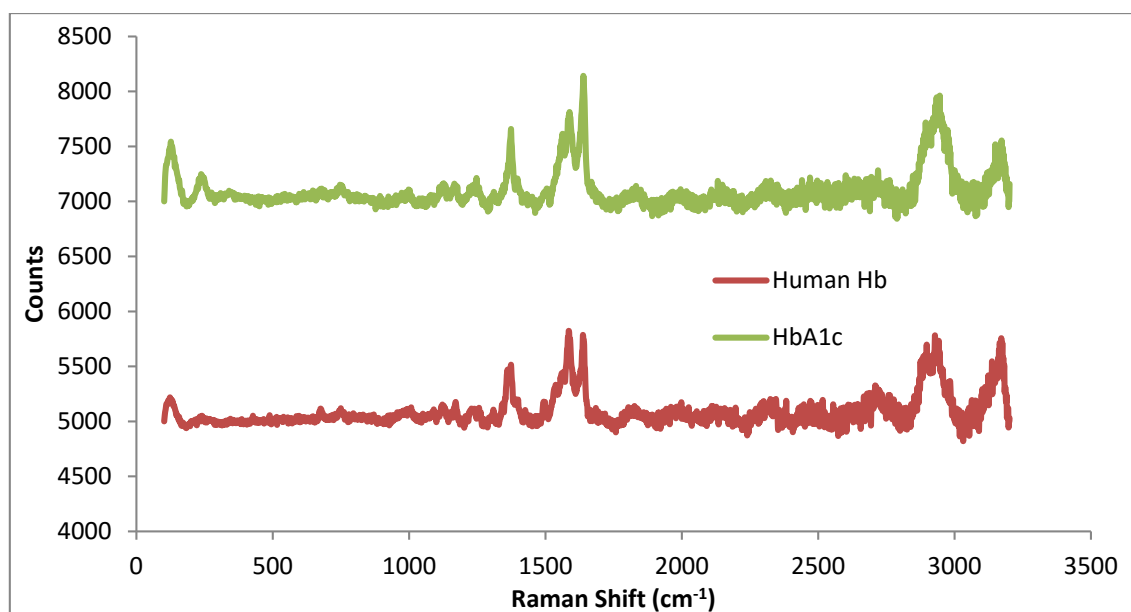
Figure 9.11: 514nm Raman for 1M Hb form bovine and human configurations as well as human HbA_{1c}. Spectra offset for clarity.

Table 9.4: 514nm Raman Peaks (cm^{-1}) and associated bonds for Hb and HbA$_{1c}$ on SERS substrate Ag wire compared with control FTIR and wire

Ag wire control	Hb bovine		Human Hb		Human HbA$_{1c}$		Peak Assignment
	FTIR control	SERS Ag wire	FTIR control	SERS Ag wire	FTIR control	SERS Ag wire	
133.7		132		122.8		126.9	*Lattice vibrations*
392.7						240	*Metal-O stretch or CC bend*
		678.3		677.3			*C-O-H bend*
811.4	697.8	745.8	698.5	749.4	698.6 830.1		*CH out-of-plane deformation*
	924.3		896 932		931.9		*CH2 out-of-plane wag*
					981.9		*=CH out-of-plane deformation*
1042.6							*C-O stretch*
	1084.5				1079.5		*C-O-C stretch*
		1126.2	1102.7	1128.2			*C-C-N bend*
	1167.4	1167	1163.8	1170	1161.8		*C-O-C antisymmetric stretch or C-C-N bend*
		1245.1	1241.5		1240.7		*C-N stretch (aromatic amines)*
	1242.3 1301.3		1300.8		1300.6		*N-O stretch*
		1310.4		1314.1		1310.6	*N=N-O symmetric stretch*
		1370.4		1366.9			*NO2 symmetric stretch or CH3 symmetric deformation*
1346.4							*CH3 deformations*
	1390.8	**1396.8**	**1387.4**		**1392.6**	**1372.5 1396.9**	***C-N stretch (Amide III band)***
1430.1							*In-plane OH bend*
	1453		1453.7		1453.1		*CH2 scissors vibration or N=N-O antisymmetric stretch*
				1492.8			*NH3+ deformation*
	1532		1531.6	1536.3	1537.8		*NO2 antisymmetric stretch (Amide II band)*

						1561.4	**NH deformation (Amide II band)**
1587.8		1586.3		1585.3		1587.4	NH2 deformation or COO- antisymmetric stretch
		1638.6		1638.2		1639	NH deformation (Amide II band)
	1644.9		1644.9		1645.5		C=O stretch (Amide I band)
							C=N stretch
	2113.8		2112.6		2112.4		N=N=N antisymmetric stretch
					2166.5		N≡C stretch
			2324.6				P-H stretch
2929.4	2871.7 2958	2925	2872 2935.2 2958.3	2898	2872 2958	2894.3	CH antisymmetric and symmetric stretch or OH stretch
			3060.8		**3061**	**3149.4 3172.7**	**NH3+ antisymmetric stretch (amino acids)**
	3284.4		3284.5		3285.9		NH stretch

1

2

3   **Table 9.4.** continued

9.3.3. Albumin & Glycated Albumin SERS

Bovine serum albumin was initially used for biomarker SERS tests with chemically etched Ag wire at a 0.5g/dL concentration within deionised water. For the SERS enhanced spectra of bovine serum albumin (Fig. 9.12), the Raman peaks show definitive protein characteristics as highlighted with Hb previously. It also shows success in producing efficient signal with a wavelength not preferred for testing with the use of SERS. The spectra shows sharp peaks within the 1100-1600cm^{-1} range, which are associated as with Hb for nitrogen bonds, carbonyl bonds and hydrocarbon bonds, with peaks present within the Amide II and III bands at 1558cm^{-1} and 1368cm^{-1} respectively, Table 9.5.
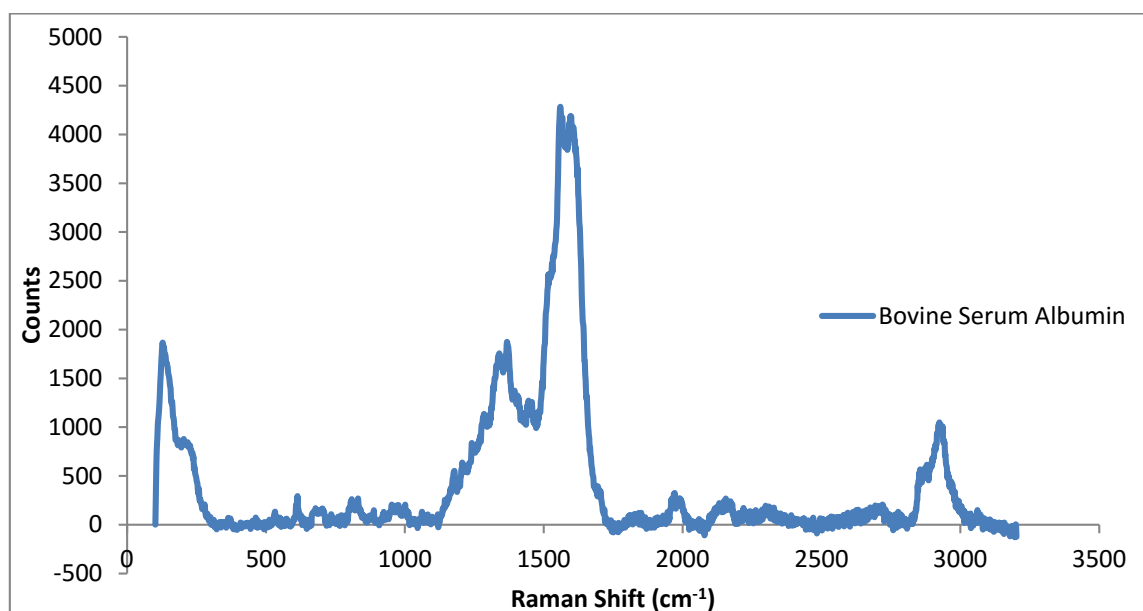
Figure 9.12: 514nm Raman for 0.5g/dL Bovine Serum Albumin in deionised water on chemically etched Ag wire SERS substrate.

As Albumin was shown to be enhanced with the SERS substrate, 0.05g/dL concentrations of human Albumin and glycated Albumin were prepared in deionised water for SERS testing with chemically etched Ag wire. The results (Fig. 9.13), showed a visually definitive difference between the protein and its glycated configuration, with fewer peaks at lower intensity present within the glycated albumin spectra compared with albumin. Upon further analysis, Table 9.5, additional peaks present for glycated albumin compared with albumin show only a peak for a C-O stretch at 1020cm^{-1}, however the use of that peak for determination of glycated albumin is unreliable as there

is a peak within that range for the control Ag wire as well, albeit at a higher Raman-shift value. For determination between the protein motifs, one could use a subtractive technique, as there are additional peaks present for albumin that are not present within the glycated form, highlighted at; $1373cm^{-1}$, $1421cm^{-1}$ and $1592cm^{-1}$ for NO_2 symmetric stretch, C-N stretch and NH_2 deformation respectively. The SERS results also highlight the presence of additional peaks present with 514nm Raman that are not present within the FTIR controls, as they are complimentary techniques this would be presumed and therefore SERS is providing a complimentary spectra to FTIR for these proteins.
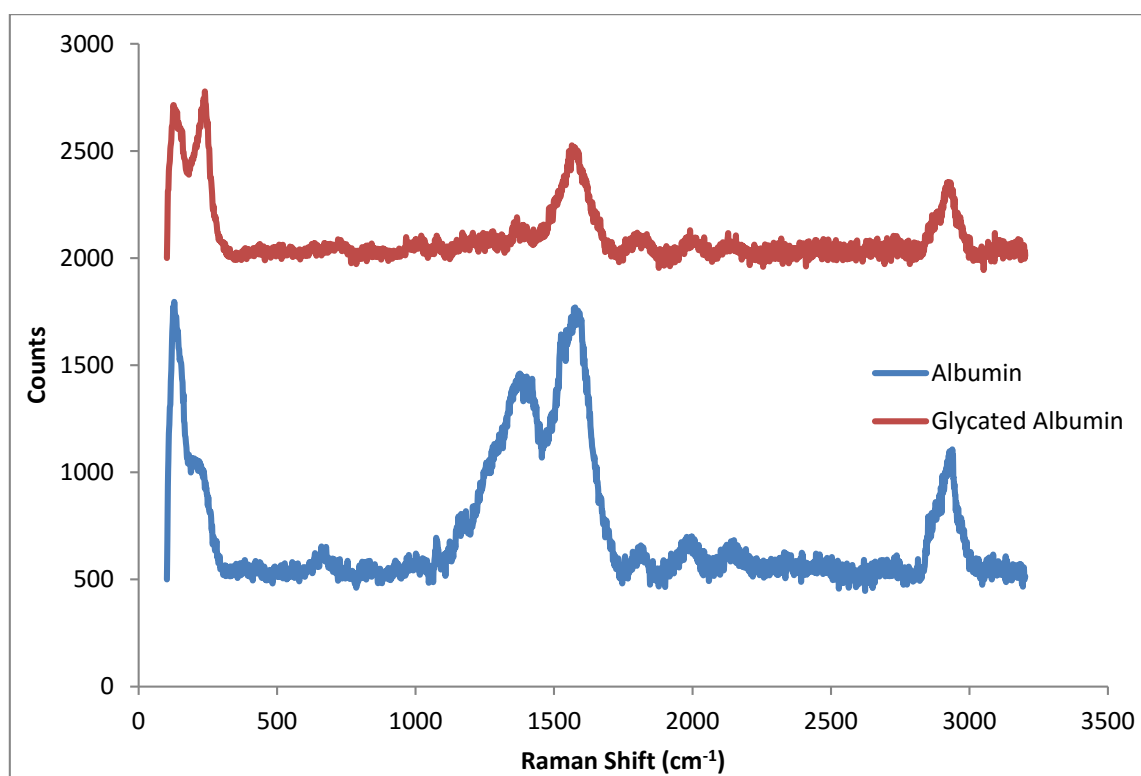
Figure 9.13: 514nm Raman for 0.05g/dL human albumin and glycated albumin with chemically etched Ag wire SERS substrate. Spectra offset for clarity.

Table 9.5: Peaks (cm^{-1}) and correlated bonds using 514nm Raman and FTIR for control and SERS spectra of Albumin and glycated albumin with chemically etched Ag wire SERS substrate.

Ag wire control	Bovine Serum Albumin		Human Albumin		Glycated Albumin		Peak Assignment
	FTIR control	SERS Ag wire	FTIR control	SERS Ag wire	FTIR control	SERS Ag wire	
133.7		132.5		130.8		128.7	*Lattice vibrations*
392.7						238	*Metal-O stretch of CC bend*
		613.1					*N-C=O bend*
811.4							*CH out-of-plane deformation*
		831.2					*NH2 wag*
	925		925				*CH2 out-of-plane wag*
1042.6						**1020.5**	***C-O stretch***
				1074.7	1077.3		*C-N stretch*
	1081.7						*C-O-C stretch*
			1106.5				*C-C-N bend*
	1170.4	1177.3	1169.9		1170.7		*C-O-C antisymmetric stretch or C-C-N bend*
	1241.5		1242.8				*C-N stretch (aromatic amines)*
		1284.7			1299.9		*N-O stretch*
		1339.7					*COO- symmetric stretch*
1346.4		1368.1				1366.3	*CH3 deformations of C-N stretch (Amide III band)*
				1373.3			***NO2 symmetric stretch***
	1393.4		1391.9		1395.3		*CH3 deformations*
				1421.1			***C-N stretch***
1430.1							*In-plane OH bend*
		1445					*CH3 antisymmetric deformation*

	1452.5		1453.7		1450.2		CH2 scissors vibration or N=N-O antisymmetric stretch
			1516.2				NH3+ deformation
			1531.4	1531.5	1536		NO2 antisymmetric stretch (Amide II band)
		1558.1				1558.1	NH deformation (Amide II band)
1587.9				**1592.3**			**NH2 deformation (Amide II band) or COO- antisymmetric stretch**
		1612.8					NH3+ deformation (amino acids)
	1642.8				1649.1		C=O stretch (Amide I band)
			1644.6				C=N stretch
					2050.1		Several bands from overtone and combination bonds
	2111.9		2113.8				N=N=N antisymmetric stretch
			2163.2				N≡C stretch
							P-H stretch
2929.4	2872.6 2933.4 2958.4	2929.5	2957.8	2932.5	2957.5	2947	CH antisymmetric and symmetric stretch or OH stretch
	3061.2		3061.1				NH3+ antisymmetric stretch (amino acids)
	3281		3282.1		3285.8		NH stretch

Table 9.5: continued.

9.3.4. Diabetes Biomarkers with chemically etched Ag wire SERS substrate

When the diabetes biomarkers SERS spectra with 514nm laser wavelength were compared with one another (Fig. 9.14), there were visible differences between glucose, albumin configurations and Hb configurations. With the peak intensities present for the biomolecules showing higher intensity peaks for glucose at its maximum physiological concentration compared with bovine albumin and bovine Hb which also were at their maximum concentrations found within blood. The difference in intensity could be due to the size of the biomolecule attaching to the SERS surface. As SERS is a surface layer technique, smaller biomolecule's such as glucose can cover the surface with a higher number of glucose molecules present compared with albumin and Hb. Therefore, the concentration of the biomolecule and coverage of the SERS substrate is of importance for signal intensity given. For the human forms which were not at their maximum physiological concentrations, the graph shows similarity of peaks present within the spectrum for the protein classes.

For qualitative SERS detection of biomolecules with chemically etched Ag wire SERS substrate, Table 9.6, details their individual fingerprints. The results show that glucose has 3 signature bonds present that the other biomarkers do not have, these were at; 649cm^{-1}, 882cm^{-1}, 928cm^{-1} and 1486cm^{-1} for O-H out-of-plane deformation, CH$_2$ out-of-plane wag and ring stretch. When comparing these peaks with the SERS spectra (Fig. 9.14), the CH$_2$ out-of-plane wag peak shows the most promise as a sharp small intensity peak is present that is not visibly seen with any of the other biomolecule spectra. For Albumin, the bovine configuration is shown to have more peaks present than the human variation; this could however be due to the concentration difference used for SERS testing. As FTIR supports that bovine and human albumin is relatively the same, one could highlight that there are 4 peaks present for albumin that differentiate it from glucose and Hb. These were at 613cm^{-1}, 1445cm^{-1} and 1612cm^{-1} [1] for N-C=O bend, CH$_3$ antisymmetric deformation and NH3$^+$ deformation. For further tests when comparing the peak ranges and bonds with the spectra, two peaks one at 1445cm^{-1} and 1612cm^{-1} show the most promise for visible determination of the protein. When differentiating albumin from its glycated counterpart, as detailed previously the loss

of peaks present within the glycated protein form could be determinative of its presence instead of albumin. There is however a bond that both HbA$_{1c}$ and glycated albumin show at around 237cm^{-1} for CC bend that is not present within any of the other biomolecular spectra. Therefore, separation of Hb from albumin on a lab on a chip device would provide a determinative peak for selective determination of the glycated forms of the protein from there non-glycated forms. For Hb, selective peaks for Hb are also shown and not present within the other biomolecule spectra at 678cm^{-1} and 1245cm^{-1} for C-O-H bend, C-O stretch or C-O-C antisymmetric stretch. As with albumin and glycated albumin, HbA$_{1c}$ could be determined through the reductive process between Hb peaks not present within the HbA$_{1c}$ spectra. HbA$_{1c}$ also shows an individual peak at around 3149cm^{-1} for NH3$^+$ antisymmetric stretch that is not present within any of the other spectra. The ability to differentiate between the SERS spectra detailed above is an essential characteristic if the SERS substrates are to be used within a lab on chip design for biomedical purposes.
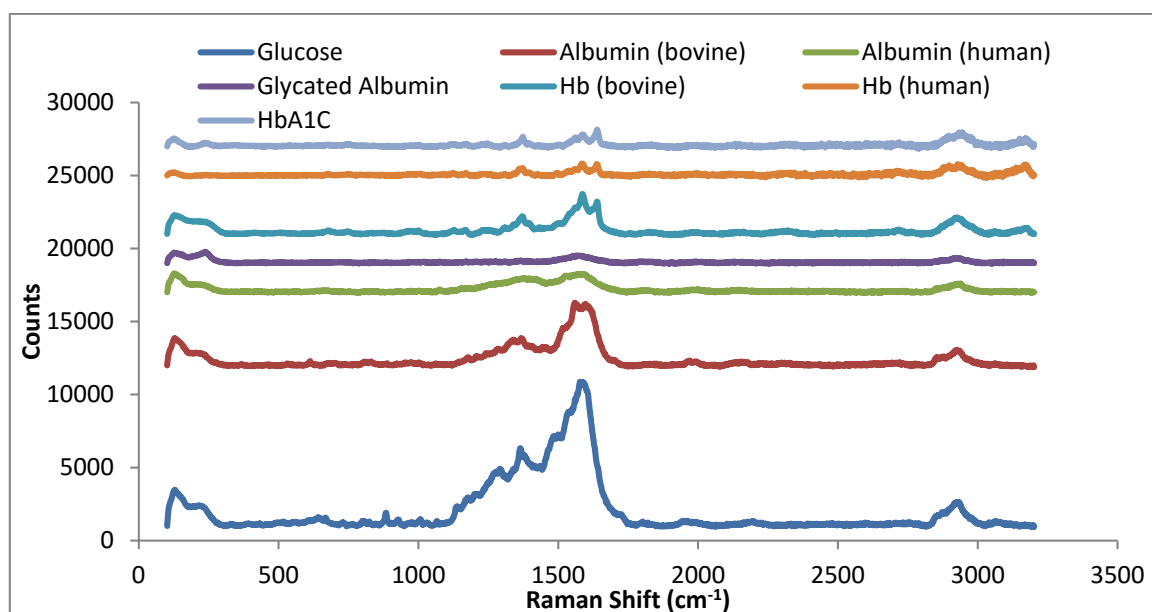
Figure 9.14: 514nm SERS spectra for diabetes biomarkers; glucose, albumin and Hb and there glycated configurations from bovine and human samples with chemically etched Ag wire SERS substrates. Spectra offset for clarity.

Table 9.6: 514nm SERS peaks (cm^{-1}) and correlated bonds for diabetes biomarkers; glucose, Albumin, Hb and their glycated versions from Bovine and Human samples on chemically etched Ag wire SERS substrates.

Glucose	Albumin (bovine)	Albumin (human)	Glycated Albumin (human)	Hb (bovine)	Hb (human)	HbA$_{1c}$ (human)	Peak Assignment
130.3	132.5	130.8	128.7	132	122.8	126.9	*Lattice vibrations*
			238			240	*Metal-O stretch or CC bend*
	613.1						*N-C=O bend*
649.7							*O-H out-of-plane deformation*
				678.3	677.3		*C-O-H bend*
	831.2			745.8	749.4		*CH out-of-plane deformation or NH2 wag*
882.7 928.5							*CH2 out-of-plane wag*
1007.6 1065.9 1137.1		1074.7	1020.5	1126.2	1128.2		*C-O stretch or C-N stretch*
1176.9	1177.3			1167	1170		*C-O-C antisymmetric stretch or C-C-N bend*
				1245.1			*C-O stretch or C-O-C antisymmetric stretch*
1290	1284.7						*N-O stretch or C-O stretch*
				1310.4	1314.1	1310.6	*N=N-O symmetric stretch*
	1339.7						*COO- symmetric stretch*
1364.7	1368.1	1373.3	1366.3	1370.4	1366.9	1372.5	*CH$_3$ deformations or NO2 symmetric stretch*
		1421.1		1396.8		1396.9	*C-N stretch*
	1445						*CH3 antisymmetric deformation*
1486.1							*Ring stretch*
					1492.8		*NH3+ deformation*
		1531.5			1536.3		*NO2 antisymmetric stretch (Amide II band)*

	1558.1		1558.1			1561.4	*NH deformation (Amide II band)*
1589.7	1598.4	1592.3		1586.3	1585.3	1587.4	*NH2 deformation (Amide II band) or COO- antisymmetric stretch*
	1612.8						*NH3+ deformation (amino acids)*
				1638.6	1638.2	1639	*NH deformation (Amide II band)*
2924	2929.5	2932.5	2947	2925	2898	2894.3	*CH$_3$, CH$_2$, antisymmetric and symmetric stretching respectively or O-H stretch.*
						3149.4 3172.7	*NH3+ antisymmetric stretch (amino acids)*

Table 9.6: continued.

9.4. Quantitative measurement of Diabetes Biomarkers with SERS

To provide support that SERS can work for analytical measurement of these diabetes biomarkers, different concentrations of glucose, bovine Hb and bovine Albumin were used. For glucose, concentrations at the maximum physiological range of 30mM were prepared in deionised water and dilutions of this stock solution to 3mM, 0.3mM and 0.03mM concentration were tested with chemically etched Ag wire. For bovine Hb, the maximum physiological concentration noted within literature was of 2.77mM and therefore as with glucose, dilutions by the power of 10 were carried out to prepare 0.277mM, 0.0277mM, 0.00277mM and 0.000277mM for testing. Bovine serum albumin (BSA) was tested under that same protocol, where the maximum concentration of the protein which is typically given in g/dL was 5g/dL corresponding to 750mM was prepared and dilutions of this concentration up to 0.075mM were made. As with MBT, initially individual peaks definitive for the diabetes biomarker were tested, however it was observed that with these analytes as well, the spectra required normalisation and therefore two specific peaks present for the biomolecule were used with their absolute intensity as a ratio and the results provided linear regression plots expressing linearity of the Ag wire SERS substrate for quantitative detection of the diabetes biomarkers. Due to different concentration ranges used and the molecules being of different sizes, the SERS spectra, Figure 9.15, highlights different LOD and standard curve characteristics.

Glucose was tested with both 514nm and 1064nm Raman spectrometers, however the results of glucose with 1064nm Raman could be deemed unreliable as the peaks were not definitive above the background noise within the spectra. Further optimisation with the 1064nm Raman instrumentation is thus required for SERS assay development. For 514nm Raman, as with MBT, a peak ratio between a COO- antisymmetric stretch peak ($\sim$1589cm^{-1}) and CH$_3$ and CH$_2$ antisymmetric stretch ($\sim$2923cm^{-1}) was used to normalise the SERS spectra for quantitative calculations. The results in Figure 9.15a show a LOD of 0.3mM glucose on Ag wire SERS substrate, with an R^2 of 0.85.

For bovine Hb the linearity was lower with an R^2 of 0.71, however with a lower LOD of 0.0277Mm. The two peaks taken for the Peak 1 to Peak 2 ratio was of the NH_2 deformation (Amide II band) stretch (~1586cm^{-1}) and the NH deformation (Amide II band) stretch (~1639cm^{-1}). For BSA, the results showed the highest linearity with an R^2 of 0.99 and a LOD of 0.075mM within a similar range to the Hb protein LOD concentration. The two peaks used for peak 1 to peak 2 ratio were NH_2 deformation (Amide II band) stretch (~1598cm^{-1}) and CH_3 and CH_2 antisymmetric stretch (~2929cm-1). As the peaks used are quite similar to that used for glucose, there is a need for the biomarkers to be separated before SERS testing.

a

b
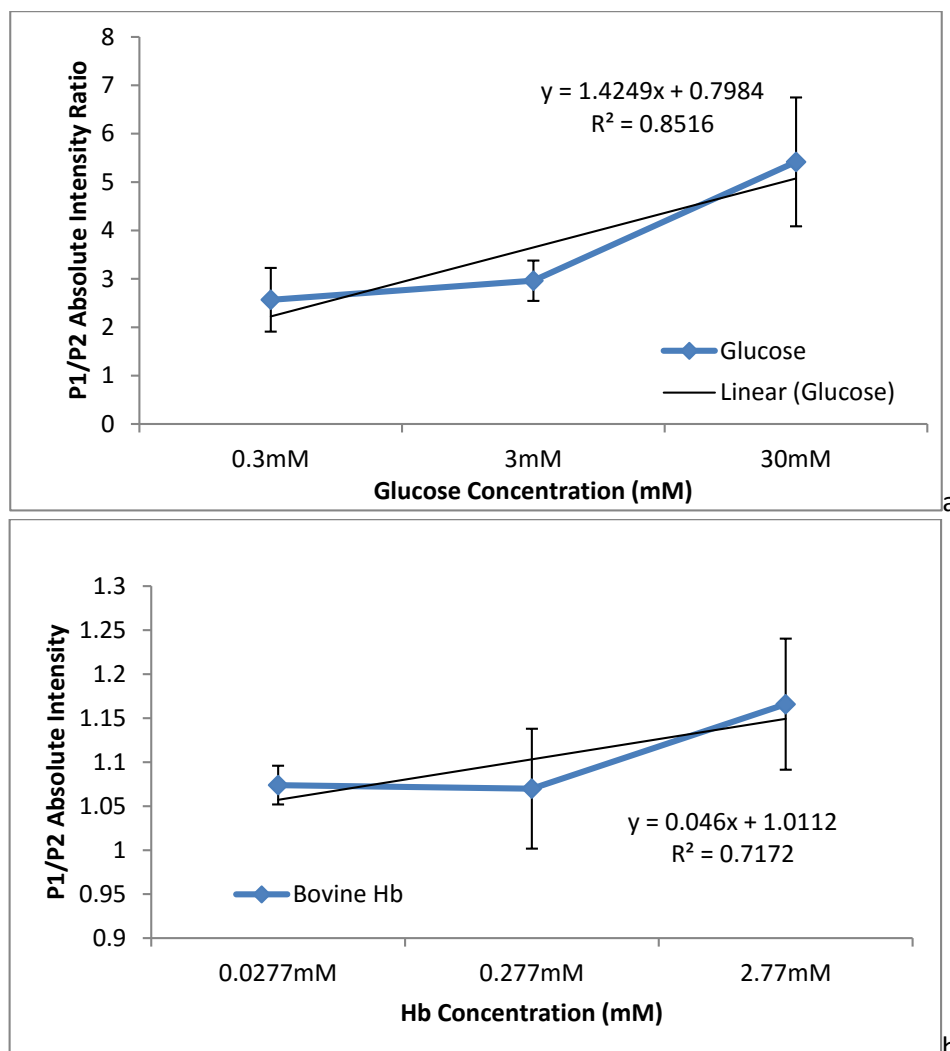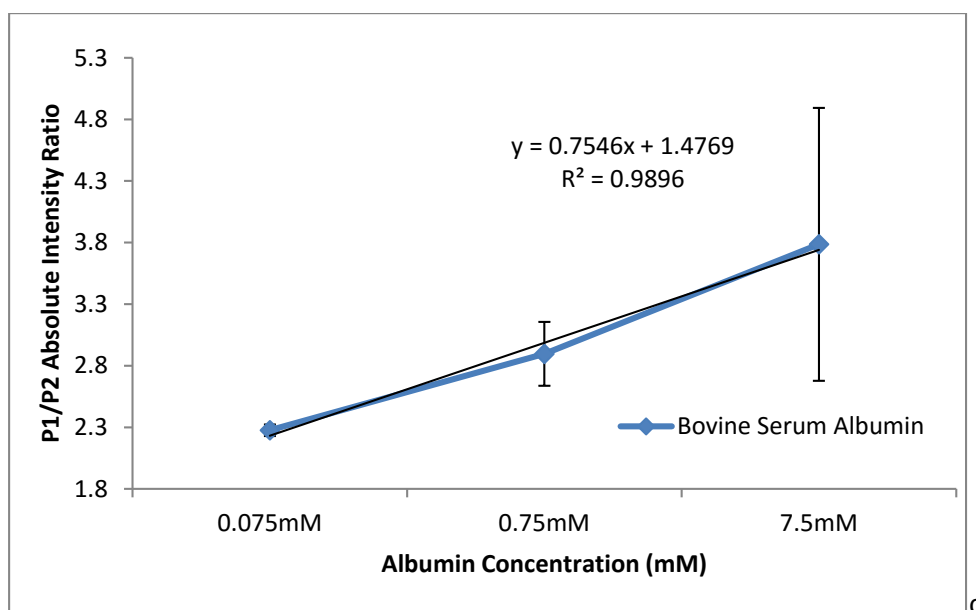
Figure 9.15: Linear regression graphs for 514nm SERS results using roughened Ag wire SERS substrates with a) glucose, b) Hb and c) BSA using a peak 1 (P1) to peak 2 (P2) ratio of absolute intensity. Standard error shown, n=6 minimum.

9.5. Chapter Summary

In this study, the SERS substrate chemically etched Ag wire, 30s NH_4OH+10s HNO_3, was taken forward for proof-of-concept work for its use and the use of SERS for selective detection of biomarkers related to improved diagnostics and monitoring of diabetes mellitus. Glucose and the proteins Haemoglobin (Hb), albumin as well as their glycated forms, HbA_{1c} and glycated Albumin, from human and bovine lines was used for testing. The control spectra for the biomolecules were characterised using FTIR and both Raman wavelengths and it was found that with the 1064nm Raman due to the high power output of the portable laser the protein biomolecules were burning, despite dissolving within solution to dissipate heat, therefore 514nm was predominately used for SERS substrate assessment with the protein biomolecules. The control Raman showed no enhancement of protein biomolecules and therefore when tested with chemically etched Ag wire, there was definitive success in providing evidence of protein enhancement with a wavelength not attuned for resonance with these bonds.

The results for glucose on Ag wire using 514nm and 1064nm laser wavelengths, showed 2 peaks that indicated the presence of glucose, CH_2-wag and C-O stretch. When the proteins were tested

on chemically etched Ag wire, as previously mentioned, characteristic spectra for Amide bands were shown within the spectra for Hb, Albumin and their glycated forms. The results indicated a concentration sensitivity of the spectra as at higher concentrations used for Hb within the molar range compared with the millimolar range, the spectra showed diminished peaks, therefore the spectra was shown to have become overly saturated. An issue observed when comparing the SERS spectra of glucose within different solutions, deionised water, PBS and synthetic saliva. Increased complexity, caused decreased peak intensity, therefore despite the lack of requirement for assay development in regards to protein attachment, separation of the molecule of interest from the complex medium is necessary within a lab on a chip device, for reliable results. When the diabetes biomarkers were compared with one another, it showed successful differentiation of spectra for the different molecules as definitive peaks were observed for each molecule, supporting the role of SERS as providing fingerprint analysis of molecules; for glucose a peak at 882cm^{-1} for CH$_2$ out-of-plane wag showed the most promise for selective identification of the molecule, for Hb peaks at 678cm^{-1} and 1245cm^{-1} for C-O-H bend, C-O stretch or C-O-C antisymmetric stretch were shown and for HbA$_{1c}$ a reductive process of the two could be undertaken between difference in Hb and HbA$_{1c}$ spectra as well as the use of a peak at 3149cm^{-1} for NH3^{+} antisymmetric stretch that was not present within any of the other spectra. For Albumin peaks at 613cm^{-1}, 1445cm^{-1} and 1612cm^{-1} for N-C=O bend, CH$_3$ antisymmetric deformation and NH3^{+} deformation could be used and for its glycated form as with HbA$_{1c}$, a reductive strategy between the protein and its glycated form could be used as well as a peak at 237cm^{-1} for C-C bend.

For quantitative detection of biomarkers related to diabetes, glucose, bovine Hb and BSA were used. A peak ratio between two significant peaks for each biomolecule was taken to calculate an absolute intensity ratio at the different concentrations. It showed that SERS detection of glucose with 514nm Raman was within the concentration range of 0.3-30mM with an R^2 of 0.85. Hb had a concentration range of 0.027-2.77mM with an R^2 of 0.71 and BSA had a concentration range between 0.075-750mM with an R^2 of 0.99. Thus this study highlighted that SERS could be useful for

the detection of diabetes biomarkers: glucose, Hb and Albumin. Further studies would require testing them in complex media such as blood and saliva.

Chapter 10: Summary & Conclusions

10.1. Introduction

Surface enhanced Raman Spectroscopy (SERS) is a technique that is gaining increased interest for multiplexed detection of wide variety of analytes, in medical diagnostics, environmental monitoring, food and agriculture, forensics and defence applications (Sur et al, 2008; Sharma et al, 2012). The method provides rapid detection, can test solids, liquid or gases (wide applicability), can detect multiple molecules in a single sample (multiplexing), can have much lower limits of detection compared to the gold standard methods (e.g. HPLC, Elisa, Electrochemical, immunoassays, fluorescence, and calorimetric methods), requires small sample volumes (<100µl) and the instrumentation can be miniaturised to suit lab on a chip design for point of care testing.

Despite the huge promise, the SERS-based detection is yet to reach wide-spread acceptance as a routine analytical tool, especially in medical diagnostics. The main bottleneck for this is the optimisation of SERS substrates for specific analytes (Alverez-Pueblo& Liz-Marzan, 2012, Zhang et al, 2013; Lin et al, 2009). Current commercially available SERS substrates are quite expensive (£6 to £40 per test), have short shelf life, have efficacy within a narrow laser wavelength range (typically in the visible range), and are time consuming and energy intensive to manufacture (Lin et al, 2009, Le Ru & Etchegoin, 2009; Zhang et al, 2013).

The aim for this project was to evaluate new SERS substrate design that are rapid to produce, while requiring minimal energy, thus minimizing the cost of production. Additionally, SERS being a molecular resonance spectroscopy, its efficacy in the detection of specific classes of molecules depends on the wavelength of the laser light source and the choice of plasmonic material (e.g Au, Ag, or Cu). Hence, in this study, we investigated the use of Au and Ag as the plasmonic materials, and three different SERS substrate design categories, namely 1) roughened planar Ag surface, 2) Au and Ag NPs (in solution or coated on solid supports – cellulose based filter paper), and 3) nanostructured electrospun membranes coated with Au or Ag NPs. Their efficacy as SERS substrates

were first tested using a Raman active molecule – namely, 4-methylbenzenethiol (MBT), and thereafter optimized substrates was carried forward for testing efficacy in the detection of diabetes biomarkers. Two commercial SERS substrates, namely P-SERS and SERStrates supplied by StellarNet Inc., and SILMECO ltd., were used as controls.

10.2. Summary

Specifically, we looked at three different SERS substrate design categories, each of which were rapid and less energy intensive to produce: 1) roughened planar Ag surface, 2) Au and Ag NPs (in solution or coated on solid supports – cellulose based filter paper), and 3) nanostructured electrospun membranes coated with Au or Ag NPs.

In the design of roughened planar metal SERS substrates, roughening of the solid metal is typically achieved using electrochemical oxidation and reduction cycles, or chemical etching. The former is time and energy intensive, while the latter is simple, rapid and achieved at room temperature. Hence, we utilized chemical etching treatments in the preparation of roughened Ag planar surfaces. Specifically, NH_4OH and/or HNO_3 treatments with or without post chemical etching heat treatment, were utilized to make roughened planar Ag metal based SERS substrates. The roughness obtained by the different chemical etching treatments were in the microscale, consisting of valleys and peaks (maximum peak to valley distance ranging between 10 and 16μm). HNO_3 treatments produced sharper peaks with a flake-like morphology as observed under SEM, whereas NH_4OH treatment resulted in a smoothening of the surface. The SERS enhancement is dependent on the proximity of the peaks (surface) upon the Ag surface. Hence, we hypothesised that the rougher the surface the higher would be the SERS enhancement. The samples treated with NH_4OH followed by HNO_3 in general produced the higher roughness. 30s NH_4OH+2m HNO_3 treated Ag wires had the highest roughness as indicated by the R_q (RMS) roughness of 1.95±0.41μm, indicated the closest proximity of neighbouring peaks. However, when tested for SERS efficacy with 514nm and 1064nm Raman spectrometers, it was not the roughest surface that showed the highest SERS

efficacy; instead, it was the 30s NH$_4$OH + 10s HNO$_3$ treated sample having an R$_q$ of 1.40±0.30μm, indicating that there is an optimum proximity range for the peaks (surface features), wherein the best SERS enhancement was observed. Post chemical etching heat treatments did not improve the SERS enhancement, which could be due to smoothening of the surface roughness and oxidation of the surface resulting from the heat treatments in air.

The SERS enhancement efficacy of the different Ag wires was tested by treating them with 1mM MBT (a Raman active molecule). The covalent grafting of MBT on the Ag SERS substrates, through the spontaneous reaction of the thiol group on MBT with Ag metal, was confirmed by the presence of C-S stretch (598cm^{-1}, 1085cm^{-1}) and C-C ring stretch (1592cm^{-1}) peaks and the absence of the free S-H stretch (2561cm^{-1}) peaks on the SERS spectra, recorded using 514nm and 1064nm laser Raman spectrometers. Enhancement factor (EF) was determined by taking the prominent MBT peak (1085cm^{-1}) within the SERS spectra and comparing with the corresponding peak intensity within the control solid MBT spectra. The peak intensity in the control MBT spectrum was normalized with its concentration and then correlated with the corresponding SERS concentrations. The 30s NH$_4$OH + 10s HNO$_3$ treated Ag wires showed highest EF with 514nm with MBT at 114.9.

The second SERS substrate design was the use Au and Ag NPs having controlled size and shape. Traditional bottom-up methods typically use reduction of metal salt in deionised water, the process is time consuming (hours to weeks) and energy intensive (requires heat). We employed microemulsion synthesis, wherein inverse micelles act as nanoreactors that facilitate rapid synthesis (seconds to minutes) at room temperature. It is well known that large sized NPs (≥30nm) having anisotropic shape (non-spherical), provide improved SERS activity. In order to achieve NPs of desired size and shape, we looked into 7 different microemulsion system parameters, namely surfactant, co-surfactant, solvent, precursor concentration, reducing agent, W number and electrolyte. The formation of Au and Ag NPs was characterised with UV-Vis spectroscopy and TEM. Initially NP synthesis was carried out using a simple microemulsion system AOT/Water/IPM,

wherein the metal salts were reduced by hydrazine hydrate (AI H). Irrespective of the changes in the concentrations of the precursors, reducing agent or W number (water content), the NPs remained predominately spherical and of small size (~10nm), which could be attributed to the rigidity of the inverse micelles between the AOT and IPM molecules. Cosurfactant, Butanol, was added to the microemulsion system (ABI), to improve fluidity of the microemulsions. This proved beneficial for increasing the size of the NPs (34.9nm, Au NPs), but the shape was not uniform. As a result we looked into changing the solvent. Long chained IPM was changed to short-chained cyclohexane. This resulted in an increase in size as well as shape. Ag NPs had an octagonal shape, but the size was <30nm (21.1nm). Hence we looked at changing the reducing agent. Specifically, AA and $NaBH_4$ were tested. AA was too mild a reducing agent to reduce $HAuCl_4$. Ag NPs produced with AA had a size of 37.9nm and uniform conjoined morphology as observed under TEM. The results highlighted that with a milder reducing agent, there would be a predicted alteration in the nucleation and growth stages within the microemulsions, with a larger growth stage, thus the morphology and increase size. When $NaBH_4$ was used, we saw the largest alterations in shape and size of Au and Ag NPs. Au NPs synthesised within ABC system using $NaBH_4$ produced cuboid shaped NPs of 16.3nm average size. Other shapes observed included triangles, hexagons and rods, but the size was <30nm. Next we changed the surfactant. Instead of anionic AOT, we used cationic CTAB, which we anticipated could have an effect on the NP size. The results supported that the cationic charge of CTAB increased the size of the NPs (Ag NPs, 32.7nm, Au NPs 43.9nm). The last microemulsion system parameter that we looked at was the use of electrolyte, NaCl. Electrolyte is known to cause aggregation of NPs but within microemulsions, they did not have a significant effect on the size, shape or aggregation. Based on these studies, we shortlisted 7 microemulsion systems (Table 10.1), 3 for Ag NPs and 4 for Au NPs. The rationale behind the anisotropic shape was that with sharp edges tangential to the metallic surface, surface plasmons can exit the surface, making SERS possible. Potentially the individual metallic NPs could act as SERS substrates, without the need for NP aggregation, as required for spherical NPs. In terms of NP sizes, it was observed that the

cationic surfactant CTAB caused a large size distribution of NPs compared to that observed with the

anionic surfactant - AOT (Table 10.1). Among the 7 NP systems chosen, the size distributions were

varied, to see which factor - size and/or shape was of importance for SERS enhancement.

Table 10.1: Shortlisted Au and Ag NPs for SERS substrate design.

Microemulsion System	Avg NP Size (Size Range), nm	Shape
Ag NPs in ABC AA	37.9 (12-59)	Conjoined
Ag NPs in ABI N	8 (1.8-34.5)	Elliptical
Ag NPs in CBC N	39.6 (4.2-443.4)	Irregular
Au NPs in ABC H	9.7 (3.1-43.8)	Irregular
Au NPs in ABC N	29.5(17.6-49)	Cuboids, Triangles, Hexagons, Rods
Au NPs in ABI N	16.3(5.4-49.7)	Octogons, Irregular and Rods
Au NPs in CBC N	39.9 (13.8-170.6)	Diamond, Irregular

To test the SERS efficacy of NPs within microemulsions, 1064nm Raman spectra was recorded

with 1mM MBT. Within the spectra there was strong microemulsion constituent peaks that

potentially were masking MBT enhancement, with the exception of ABC microemulsions, wherein

an S-H peak (around 2561cm^{-1}) was observed. This indicates that MBT is not binding onto the metal

surface and potentially being blocked by a surfactant layer on the surface of the NPs. To overcome

the issue of MBT signal being masked by microemulsion components, NPs were separated from the

microemulsion system using water phase disruption method. The separated NPs were dispersed in

deionised water and tested for MBT SERS efficacy using 1064nm Raman. The results did not show

any enhancement of MBT signal, potentially, the SERS signal was being attenuated by water. With

514nm Raman, liquid samples could not be tested due to instrumentation constraints. Hence, NPs

were coated onto filter paper from both the shortlisted microemulsion systems and NP separated

from the microemulsion systems. This substrate design was then tested with both 514nm and

1064nm Raman for SERS efficacy.

Ag NPs in ABC AA and ABI N, were the only two microemulsion systems, as well as their NP

separated forms coated on filter paper, that showed SERS spectra for MBT on both 514nm and

1064nm Raman spectrometers. They had EF of 15.3 and 5.2 respectively for Ag NPs within

microemulsions and 7.7 and 20.9 respectively for Ag NPs separated from the microemulsions for the 1094cm^{-1} peak of 1mM MBT. For 1064nm Raman, Ag NPs separated from ABC microemulsion and Au NPs separated from ABI showed SERS spectra for MBT, with EF values of 17 and 7.7 respectively. Effectively Ag NPs, particularly with the conjoined shape and size of 37.9nm showed the best enhancement for detection of MBT Ag NPs deposited on filter paper both within the microemulsions and the separated form.

In the third SERS substrate design category, metallic NPs were covalently attached onto nanostructured insoluble electrospun membranes. This was aimed at maximising the surface area available per unit volume for SERS detection. Commonly, lithography methods are used for the design of nanostructured planar SERS substrates. The technique as with the others is again labour intensive and expensive. Electrospinning is a simple methodology to prepare controlled nanofibers with large surface area per unit volume. Considering the depth of penetration of the laser beam (100μm), having a fibro-porous structure will provide a much larger surface area for analysis, which is unique to the NP coated electrospun membranes. The polymer used in this study was polyacrylic acid (PAA) 4% w/w cross-linked with 12% Ethylene glycol (EG) to produce insoluble electrospun membranes. The covalent grafting of NPs onto the electrospun fibre surface, was achieved first by surface modification using carbodiimide chemistry between amine groups on cysteamine with acid groups on PAA. The free thiol groups from cysteamine were then used to react with the Au and Ag NPs from microemulsion and NP separated solutions. The grafting was confirmed with the use of FTIR and TEM.

NPs on the electrospun surface were observed in two forms, either individual particles uniformly distributed on the fibre surface or aggregated into clusters, which we anticipated would serve as SERS substrates. The results showed not all the NP coated electrospun membrane variants gave SERS spectra for MBT. SERS enhancement was observed for Ag NPs from CBC N on PAA-EG showing highest MBT enhancement (EF 51.5) as well as with Ag NPs from ABI on membrane (EF

31.2) with 514nm Raman spectrometer. NP separated Ag NPs from ABI when tested with 514nm Raman, gave EF of 35.1, similar to its microemulsion counterpart. When Ag NPs from CBC and ABI were tested with 1064nm EFs were 1.8 and 1.9 respectively, while Au NPs from ABC N had an EF of 4.7. NP separated Ag NPs from ABI showed an EF of 3.8 and Au NPs from ABC N had an increased EF to its microemulsion counterpart of 22.9.

Of the three categories for SERS substrate designs prepared and tested for their efficacy for the detection of MBT, the roughened Ag wire substrates showed the best SERS enhancement (EF 114.93), when tested with 514nm Raman spectrometer. The corresponding EF for Ag wire with 1064nm Raman spectrometer was 14.6, which is about 10 times smaller compared with 514nm. This result is expected due to the SERS activity being inversely related to the 4th power of the wavelength. Metal type dependence is also shown for SERS enhancement with specific wavelengths, as Au NPs showed the best EF of 22.9 with the 1064nm laser. The resonance frequency of Au is known to be closer to longer wavelengths than Ag, hence the better EF compared to the corresponding Ag NPs.

When commercial SERS substrates were compared with the SERS substrates developed in this study, the results showed Silmeco Ag SERStrate had the highest enhancement with 514nm Raman (EF 219.7), while that observed with 1064nm was EF 67.5. Silmeco Au SERStrate on the other hand did not give any spectrum for MBT with 514nm Raman, but gave MBT enhancement with 1064nm Raman at a similar EF value to that of Ag SERStrate (EF 67.2). The other commercial substrate we tested, P-SERS, which is ink-jet printed Au colloid clusters on cellulose paper, showed significantly lower EF (6.8) when tested with 514nm Raman compared to Au NP coated filter paper (35.9). With 1064nm Raman, P-SERS (6.1) being within a similar range seen by NPs on filter paper. Again the effect of the laser wavelength on the SERS activity of the intra and inter metal types is evident with the commercial SERS substrate, as observed above with Ag and Au NP SERS substrates developed in this study.

As evident from the above discussed SERS enhancement tests for the three SERS substrate designs developed in this study as well as the commercial P-SERS, Ag and Au SERStrates, all substrates showed SERS enhancement for MBT. The EFs reported were specifically calculated for the C-S stretch peak (~1096cm^{-1}). Following on we further tested all the substrates, except the Silmeco Ag and Au SERStrate due to their prohibitive cost, for each of their LOD for MBT. We obtained MBT SERS spectra for concentrations as low as 1aM, 0.01μM, and 0.01μM respectively for Ag wire, Ag NPs on filter paper and Ag NPs on electrospun membranes. On the other hand, P-SERS an Au NP based SERS substrate did not give reliable spectra for MBT both on 514nm and 1064nm Raman spectrometers. The former might be due to the incompatibility of the metal with the laser wavelength 514nm. Similar result was also observed for Au NPs on filter paper as well as electrospun membranes. With 1064nm Raman spectrometer, the laser power was too high for dry filter paper, electrospun membranes and P-SERS, which caused the sample to burn. We used microfluidic chips with wetting of the above said substrates with deionised water to obtain meaningful spectra using 1064nm Raman spectrometer. However, the results were weak for the detection of MBT, potentially due to the attenuation of the SERS signal by the added water for wetting. Hence, for further testing in this study, we utilized the Ag wire SERS substrate, which could be tested on both 514nm and 1064nm Raman spectrometer, without damaging the SERS substrate. For the range of 1aM to 1M, the absolute intensity, peak height or peak area of the C-S stretch peak (~1096cm^{-1}) did not give a linear response. Hence, we did a ratio of peak heights ~1094cm^{-1} (C-S stretch) to ~1563cm^{-1} (ring stretch) to normalize the differences in spectral intensities due to the spectral acquisition conditions. There was a linear response for the peak height ratios for MBT concentration ranging from 1aM to 1M, with an R^2 of 0.75, using Ag Wire substrate and 514nm Raman spectrometer. However, the LOD using 1064nm Raman in the detection of MBT on Ag wire SERS substrates was 1nM and the R^2 of 0.92 for the detection range of 1nM to 1M. Thus, the efficacy of the Ag wire SERS substrates for quantitative detection using both 514nm and 1064nm Raman spectrometers was demonstrated.

Based on the best EF, we chose roughened Ag wire, roughened using 30s NH_4OH + 10s HNO_3 treatment, for proof-of-concept work for its use as SERS substrates for selective detection of diabetes biomarkers. Glucose and the proteins haemoglobin (Hb) and albumin as well as their glycated forms, HbA_{1c} and glycated Albumin, from both human and bovine sources were used for testing. Glucose could be tested with both 514nm and 1064nm Raman spectrometers. However, the proteins, due to their low melting point and despite attempts to modify testing with 1064nm Raman, could not be tested due to the high power of the 1064nm laser causing the protein to burn. FTIR and Raman was used for control spectra of glucose and the protein biomarkers, and it was observed that glucose could be effectively tested as solid with both 514nm and 1064nm with higher preference of peaks with 514nm Raman. Upon addition of these biomarkers to chemically etched Ag wire SERS substrate, SERS spectra were obtained for all variants. The SERS spectra was characterised and typical peaks related to the biomarker were established, with amide bands and amino acid group bonds present within the protein biomarker spectra. The biomarkers were then compared with one another and it was seen that each spectra were different to one another, with the ability to select peaks from the spectra that would determine that biomarkers presence.

Glucose, bovine Hb and bovine Albumin were then further tested on chemically etched Ag wire at concentrations diluted from their respective maximum physiological concentrations. All three biomarkers showed quantifiable measurements as absolute intensity varied with the concentration used. Shift in SERS spectral peaks were observed for calibration and limit of detection for each biomarker compared to their bulk (control) Raman spectra, which can be attributed to differences in their molecular orientation on the Ag wire SERS substrate surface. Similar to that with MBT, a peak ratio between a COO- antisymmetric stretch peak (~1589cm^{-1}) and CH_3 and CH_2 antisymmetric stretch (~2923cm^{-1}) was used to normalise the SERS spectra for quantitative calculations for glucose. For the range of 0.3 to 30 mM glucose concentration, the SERS detection using roughened Ag wire SERS substrates, showed an R^2 of 0.85. For bovine Hb, the two peaks taken for the Peak 1 to Peak 2 ratio were of the NH_2 deformation (Amide II band) stretch (~1586cm^{-1}) and the NH

deformation (Amide II band) stretch (~1639cm^{-1}), an R^2 was 0.71 for the detection range of 0.0277 to 2.77mM. For BSA, the results showed the best linearity with an R^2 of 0.99 for the detection range of 0.075 to 750mM, using the peak 1 to peak 2 ratio for NH_2 deformation (Amide II band) stretch (~1598cm^{-1}) to the CH_3 and CH_2 antisymmetric stretch (~2929cm^{-1}). Thus, the proof-of-concept for detection of glucose, Hb and BSA using the roughened Ag wire SERS substrate was demonstrated.

10.3. Conclusions

- Less time and energy intensive methods for fabrication of SERS substrates from the three SERS substrate design categories were developed.

- Flattened Ag wire was successfully etched using chemical treatments for uniform roughness, and the 30s NH_4OH + 10s HNO_3 treatment produced the optimum spacing between the flake-like surface features to produce the best SERS signal enhancements. They showed the best enhancement factors of 114 and 14 respectively on 514nm and 1064nm Raman spectrometers in the detection of 1mM MBT.

- Methods were optimized for preparation of Au and Ag NPs using microemulsions synthesis, and average sizes ranging between 7 and 40 nm, and shapes including, conjoined, elliptical, irregular, cuboids, triangles, hexagons, rods, octagons, and diamond, were achieved.

- Water based phase disruption method for separation of Au and Ag NPs from microemulsions were optimized, and the sizes and shapes of the NPs, in general, were maintained post separation.

- SERS efficacy assessments for Au and Ag NPs within microemulsions and water were carried out using 1064nm Raman, and failed to obtain reliable SERS spectra for 1mM MBT, potentially due to the dissipation of the SERS spectral signal by the large volume of solvents used to suspend the NPs. However, when deposited on filter papers, the Ag and Au NPs showed efficacy in the SERS detection of MBT, with EFs as high as 16.98 and 20.88 respectively with 514nm and 1064nm Raman spectrometers.

- Insoluble electrospun membranes based on PAA and EG were successfully fabricated using an in-house built electrospinning machine with controlled temperature and humidity. It was essential to maintain humidity and temperature below 10% and 10°C, as well as an optimal conductivity of the solution of around 581µS for electrospinning PAA-EG fibres.

- Carbodiimide chemistry was used to successfully graft cysteamine on the anionic surface of PAA-EG fibres, and thereafter, the spontaneous reaction of the metal NPs with the free thiol groups of cysteamine attached on the PAA-EG fibres, to prepared the Ag or Au NPs incorporated insoluble electrospun membrane based SERS substrates.

- The Ag and Au NPs incorporated insoluble electrospun membranes showed efficacy in the SERS detection of MBT with EFs as high as 51.49 and 22.92 respectively with 514nm and 1064nm Raman spectrometers.

- When compared with a similar commercial SERS substrate - PSERS, the Au NPs incorporated filter papers and insoluble elelctrospun membranes fabricated SERS substrates showed better enhancement factors for the detection of 1mM MBT.

- Chemically etched Ag wire SERS substrate was successful in proving proof-of-concept detection of the diabetes biomarkers – glucose, haemoglobin and albumin through the generation of standard curves for their respective clinically relevant linear detection ranges of 0.3-30mM, 0.027-2.77mM and 0.075-750mM.

10.4. Future directions

The experimental results achieved within this project are promising towards the development of cost-effective SERS substrates that are more robust, require simple equipment, can be miniaturised, long shelf-lives and broadband SERS characteristics. The ability to gain results with SERS substrates both with the 514nm and 1064nm wavelengths highlights a beneficial ability. Future work would be to address the efficacy of the different SERS substrate designs developed in this study in the detection of the diabetes biomarkers in more complex biological media, such as

blood and saliva. This technology can be expanded for detection of multiple other clinical analytes, including for drugs of abuse, cancer, and Alzheimer's diseases. The ultimate goal for this research is to integrate the SERS transduction method for detection of multiple clinical analytes on a single lab-on-chip platform. Furthermore, the due to their insolubility and tailorable surface chemistries, the developed PAA-EG membranes could find applications in solid-phase extraction, chromatography, as well as tissue engineering scaffolds.

Bibliography

Aguiree, F., Brown, a, Cho, N., & Dahlquist, G. (2013). IDF Diabetes Atlas. doi:10.1016/j.diabres.2009.10.007

Alvarez-Puebla, R. a., & Liz-Marzán, L. M. (2010). SERS-based diagnosis and biodetection. Small, 6(5), 604–610. doi:10.1002/smll.200901820

Alvarez-Puebla, R. a., & Liz-Marzán, L. M. (2012). Traps and cages for universal SERS detection. Chemical Society Reviews, 41(1), 43. doi:10.1039/c1cs15155j

Atkins, P., & De Paula, J. (Eds.). (2010). Physical Chemistry (9th Editio). W.H. Freeman Company and New York.

AtoID. (2015). AtoID - Raman spectroscopy solutions. Retrieved July 26, 2015, from http://atoid.com/shop/

Bahari. (2015). Maintaining A Healthy Lifestyle: How To Maintain A Normal Blood Sugar Level. Retrieved July 26, 2015, from http://baharimachoman.blogspot.co.uk/2010/10/how-to-maintain-normal-blood-sugar.html

Bandodkar, A. J., & Wang, J. (2014). Non-invasive wearable electrochemical sensors: A review. Trends in Biotechnology, 32(7), 363–371. doi:10.1016/j.tibtech.2014.04.005

Bantz, K., Meyer, A., Wittenberg, N., Im, H., Kurtulus, O., Lindquist, N., … Haynes, C. (2011). NIH Public Access. Phys Chem Chem Phys, 29(6), 997–1003. doi:10.1016/j.biotechadv.2011.08.021.Secreted

Barman, I., Dingari, N. C., Kang, J. W., Horowitz, G., Dasari, R. R., & Feld, M. S. (2012). Raman spectroscopy based sensitive and specific detection of glycated hemoglobin Raman spectroscopy based sensitive and specific detection of glycated hemoglobin. Biomedical Research.

Baynes, & Dominczak. (2005). Medical Biochemistry. 2nd Edition Second Edition. by Baynes & Dominiczak: Amazon.co.uk: Books. Retrieved July 26, 2015, from http://www.amazon.co.uk/Medical-Biochemistry-Edition-Edition-Dominiczak/dp/B008I1SWF8

Bell, S. E. J., & Sirimuthu, N. M. S. (2008). Quantitative surface-enhanced Raman spectroscopy. Chemical Society Reviews, 37(5), 1012–1024. doi:10.1039/b705965p

Burge, M. R. (2001). Lack of Compliance With Home Blood Glucose Monitoring Predicts Hospitalization in Diabetes. Diabetes Care, 24(8), 1502–1503. doi:10.2337/diacare.24.8.1502

Buszewski, B & Szultka, M. (2012). Past, Present, and Future of Solid Phase Extraction: A Review. Critical Reviews in Analytical Chemistry, 42(3), 198–213. doi:10.1080/07373937.2011.645413

Cao, M., Cheng, S., Zhou, X., Tao, Z., Yao, J., & Fan, L. J. (2012). Preparation and surface-enhanced Raman performance of electrospun poly(vinyl alcohol)/ high-concentration-gold nanofibers. Journal of Polymer Research, 19(1). doi:10.1007/s10965-011-9810-4

Cash, K. J., & Clark, H. a. (2010). Nanosensors and nanomaterials for monitoring glucose in diabetes. Trends in Molecular Medicine, 16(12), 584–593. doi:10.1016/j.molmed.2010.08.002

Chen, L., & Choo, J. (2008). Recent advances in surface-enhanced Raman scattering detection technology for microfluidic chips. Electrophoresis, 29(9), 1815–1828. doi:10.1002/elps.200700554

ChiLab, M. and M. L. (2015). Nano-biosensing for Healthcare - Chilab. Retrieved July 26, 2015, from http://areeweb.polito.it/ricerca/micronanotech/research-activities/Nano-biosensing

Chin, C. D., Linder, V., & Sia, S. K. (2012). Commercialization of microfluidic point-of-care diagnostic devices. Lab on a Chip, 12(12), 2118. doi:10.1039/c2lc21204h

Cialla, D., März, A., Böhme, R., Theil, F., Weber, K., Schmitt, M., & Popp, J. (2012). Surface-enhanced Raman spectroscopy (SERS): Progress and trends. Analytical and Bioanalytical Chemistry, 403(1), 27–54. doi:10.1007/s00216-011-5631-x

Clarke, S. F., & Foster, J. R. (2012). A history of blood glucose meters and their role in self-monitoring of diabetes mellitus. British Journal of Biomedical Science, 69(2), 83–93.

Climate Science Investigations South Florida - Energy: The Driver of Climate. (n.d.). Retrieved July 26, 2015, from http://www.ces.fau.edu/nasa/module-2/radiation-sun.php

De Almeida, P. D. V., Grégio, A. M. T., Machado, M. A. N., de Lima, A. A. S., & Azevedo, L. R. (2008). Saliva composition and functions: a comprehensive review. The Journal of Contemporary Dental Practice, 9(3), 72–80. Retrieved from http://www.ncbi.nlm.nih.gov/pubmed/18335122

Destrée, C., & B.Nagy, J. (2006). Mechanism of formation of inorganic and organic nanoparticles from microemulsions. Advances in Colloid and Interface Science, 123-126(SPEC. ISS.), 353–367. doi:10.1016/j.cis.2006.05.022

Diabetes UK. (2014). Diabetes-key-stats-guidelines-April2014-1, (March 2014).

Diagnostic anSERS. (2015). Sensitive, flexible SERS substrates | Diagnostic anSERS Inc. Retrieved July 26, 2015, from https://www.diagnosticansers.com/

Dingari, N. C., Horowitz, G. L., Kang, J. W., Dasari, R. R., & Barman, I. (2012). Raman spectroscopy provides a powerful diagnostic tool for accurate determination of albumin glycation. PLoS ONE, 7(2). doi:10.1371/journal.pone.0032406

Domènech, B., Bastos-Arrieta, J., Alonso, A., Macanás, J., Muñoz, M., & Muraviev, D. N. (2012). Bifunctional Polymer-Metal Nanocomposite Ion Exchange Materials. Ion Exchange Technologies, 35–72. doi:http://dx.doi.org/10.5772/51579

Eastoe, J., Hollamby, M. J., & Hudson, L. (2006). Recent advances in nanoparticle synthesis with reversed micelles. Advances in Colloid and Interface Science, 128-130(2006), 5–15. doi:10.1016/j.cis.2006.11.009

Ferretti, S., Paynter, S., Russell, D. a., Sapsford, K. E., & Richardson, D. J. (2000). Self-assembled monolayers: a versatile tool for the formulation of bio-surfaces. TrAC Trends in Analytical Chemistry, 19(9), 530–540. doi:10.1016/S0165-9936(00)00032-7

Fleischmann M, Hendra P.J, McQuillan A.J. Raman spectra of pyridine adsorbed at a silver electrode. Chemical Physics Letters, 1974, Vol 26(2), pp 163-166

Ganguli, A. K., Ganguly, A., & Vaidya, S. (2010). Microemulsion-based synthesis of nanocrystalline materials. Chemical Society Reviews, 39(2), 474–485. doi:10.1039/b814613f

García-Barrasa, J., López-de-Luzuriaga, J. M., & Monge, M. (2011). Silver nanoparticles: synthesis through chemical methods in solution and biomedical applications. Central European Journal of Chemistry, 9(1), 7–19. doi:10.2478/s11532-010-0124-x

Gene Quantification. (2015). lab-on-chip.gene-quantification.info. Retrieved from http://lab-on-chip.gene-quantification.info/

Germain, V., Li, J., Ingert, D., Wang, Z. L., & Pileni, M. P. (2003). Stacking faults in formation of silver nanodisks. Journal of Physical Chemistry B, 107(34), 8717–8720. doi:10.1021/jp0303826

Gilbert, De Magnete, 2013, Mottelay Fleury translated, Dover Publications Inc, New York

Gómez, M., & Lazzari, M. (2014). Reliable and cheap SERS active substrates. Materials Today, 17(7), 358–359. doi:10.1016/j.mattod.2014.08.001

Griffin, W, 1949, Classification of surface-active agents by 'HLB', Journal of the Society of Cosmetic Chemists, 1 (5): 311-26

Grunsby, R. (2012). Raman Spectroscopy An Overview. Retrieved July 26, 2015, from http://www.photonicsonline.com/doc/raman-spectroscopy-an-overview-0001

Guo, B., Han, G., Li, M., & Zhao, S. (2010). Deposition of the fractal-like gold particles onto electrospun polymethylmethacrylate fibrous mats and their application in surface-enhanced Raman scattering. Thin Solid Films, 518(12), 3228–3233. doi:10.1016/j.tsf.2009.10.148

Han, X. X., Ozaki, Y., & Zhao, B. (2012). Label-free detection in biological applications of surface-enhanced Raman scattering. TrAC - Trends in Analytical Chemistry, 38, 67–78. doi:10.1016/j.trac.2012.05.006

Hawkins, R. C. (2007). Laboratory turnaround time. The Clinical Biochemist. Reviews / Australian Association of Clinical Biochemists, 28(4), 179–194.

He, D., Hu, B., Yao, Q., Wang, K., & Yu, S. (2009). Large-Scale Synthesis of Flexible Free-Sensitivity : Electrospun PVA Nanofibers of Silver Nanoparticles. ACS Nano, 3(12), 3993–4002. doi:10.1021/nn900812f

Heuck, C.-C., Home, P. D., Reinauer, H., & Kanagasabapathy, a. S. (2002). Laboratory Diagnosis and Monitoring of Diabetes Mellitus. World Health Organisation, 1–26.

Hoelzel, W., Hoshino, T., & Miedema, K. (2002). Approved IFCC Reference Method for the Measurement of HbA 1c in Human Blood, 35(1), 78–89.

Hollamby, M. J., Eastoe, J., Chemelli, A., Glatter, O., Rogers, S., Heenan, R. K., & Grillo, I. (2010). Separation and purification of nanoparticles in a single step. Langmuir, 26(10), 6989–6994. doi:10.1021/la904225k

HORIBA. (n.d.). What laser wavelengths are used for Raman spectroscopy? - HORIBA. Retrieved July 26, 2015, from http://www.horiba.com/uk/scientific/products/raman-spectroscopy/raman-academy/raman-faqs/what-laser-wavelengths-are-used-for-raman-spectroscopy/

Huang, Z. M., Zhang, Y. Z., Kotaki, M., & Ramakrishna, S. (2003). A review on polymer nanofibers by electrospinning and their applications in nanocomposites. Composites Science and Technology, 63(15), 2223–2253. doi:10.1016/S0266-3538(03)00178-7

Jianrong, C., Yuqing, M., Nongyue, H., Xiaohua, W., & Sijiao, L. (2004). Nanotechnology and biosensors. Biotechnology Advances, 22(7), 505–518. doi:10.1016/j.biotechadv.2004.03.004

John Morris Scientific. (2015). ASPEC-C18-50mg-1ml @ www.johnmorris.com.au. Retrieved from http://www.johnmorris.com.au/Solid-Phase-Extraction-Automated/ASPEC-C18-50mg-1ml.aspx?pd=181238&CategoryID=1302

Kim, Y. B., Cho, D., & Park, W. H. (2009). Electrospinning of Poly(Dimethyl Siloxane) by Sol-Gel Method. Journal of Applied Polymer Science, 114, 3879–3874. doi:10.1002/app

Kiran, M. S., Itoh, T., Yoshida, K., Kawashima, N., Biju, V., & Ishikawa, M. (2010). Selective detection of HbA1c using surface enhanced resonance Raman spectroscopy. Analytical Chemistry, 82(4), 1342–1348. doi:10.1021/ac902364h

Kneipp, K. (2007). Surface-enhanced raman scattering. Physics Today, 60(11), 40–46. doi:10.1063/1.2812122

Kneipp, K., Kneipp, H., Itzkan, I., Dasari, R. R., & Feld, M. S. (2002). Surface-enhanced Raman scattering and biophysics. Journal of Physics: Condensed Matter, 14(18), R597–R624. doi:10.1088/0953-8984/14/18/202

Kowalczyk, B., Lagzi, I., & Grzybowski, B. a. (2011). Nanoseparations: Strategies for size and/or shape-selective purification of nanoparticles. Current Opinion in Colloid and Interface Science, 16(2), 135–148. doi:10.1016/j.cocis.2011.01.004

Larkin, P. J. (2011). "IR and Raman Spectroscopy - Principles and Spectral Interpretation." Vasa. doi:10.1016/b978-0-12-386984-5.10001-1

Le Ru, E., & Etchegoin, P. (Eds.). (2009). Principles of Surface Enhanced Raman Spectroscopy and related plasmonic effects (1st editio). Elsevier.

Lee, C. H., Tian, L., Abbas, A., Kattumenu, R., & Singamaneni, S. (2011). Directed assembly of gold nanorods using aligned electrospun polymer nanofibers for highly efficient SERS substrates. Nanotechnology, 22(27), 275311. doi:10.1088/0957-4484/22/27/275311

Li, W., Xu, P., Zhou, H., Yang, L., & Liu, H. (2012). Advanced functional nanomaterials with microemulsion phase. Science China Technological Sciences, 55(2), 387–416. doi:10.1007/s11431-011-4687-3

Lin, X. M., Cui, Y., Xu, Y. H., Ren, B., & Tian, Z. Q. (2009). Surface-enhanced raman spectroscopy: Substrate-related issues. Analytical and Bioanalytical Chemistry, 394(7), 1729–1745. doi:10.1007/s00216-009-2761-5

Little, R. R., Rohlfing, C. L., Hanson, S., Connolly, S., Higgins, T., Weykamp, C. W., … Roberts, W. L. (2008). Effects of hemoglobin (Hb) E and HbD traits on measurements of glycated Hb (HbA1c) by 23 methods. Clinical Chemistry, 54(8), 1277–1282. doi:10.1373/clinchem.2008.103580

Liu, Y., Sun, Y., Sun, K., Song, L., & Jiang, X. (2010). Recent developments employing new materials for readout in lab-on-a-chip. Journal of Materials Chemistry, 20(35), 7305. doi:10.1039/c0jm00576b

Lowe H. F. and Spindloe C. White light interferometric profilometry of surface structured glass for high power laser microtargets. Annual Report, Central Laser Facility, TFC, Rutherford Appleton Laboratory, Didcot, UK, Chapter 7 in Laser Science and Development, Target Fabrication 2006-2007

Lukáš, D., Sarkar, a., Martinová, L., Vodsed'álková, K., Lubasová, D., Chaloupek, J., … Komárek, M. (2009). Physical principles of electrospinning (Electrospinning as a nano-scale technology of the twenty-first century). Textile Progress, 41(2), 59–140. doi:10.1080/00405160902904641

Luppa, P. B., Müller, C., Schlichtiger, A., & Schlebusch, H. (2011). Point-of-care testing (POCT): Current techniques and future perspectives. TrAC - Trends in Analytical Chemistry, 30(6), 887–898. doi:10.1016/j.trac.2011.01.019

Lyandres, O., Glucksberg, M. R., Walsh, J. T., Shah, N. C., Yonzon, C. R., Zhang, X., & Van Duyne, R. P. (2007). Surface-Enhanced Raman Sensors for Metabolic Analytes. Biomedical Vibrational Spectroscopy, 221–241. doi:10.1002/9780470283172.ch10

MacPherson, M., & Ravichandrian, M. (2011). Lab-on-a-chip technology: the future of point- of-care diagnostic ability. University of Western Ontario Medical Journal, 80(1), 24–26.

Mattel G, Quagliano L.G, Pagannone M. Surface-Enhanced Raman Scattering (SERS) on silver surfaces activated by a simple chemical treatment, Europhys. Lett, 1990. Vol 11(14)pp373-378

McNay, G., Eustace, D., Smith, W. E., Faulds, K., & Graham, D. (2011). Surface-enhanced Raman scattering (SERS) and surface-enhanced resonance raman scattering (SERRS): A review of applications. Applied Spectroscopy, 65(8), 825–837. doi:10.1366/11-06365

Medicine, J. H. (2015). Alternative markers of glycemia: fructosamine, glycated albumin, 1,5-AG | Johns Hopkins Diabetes Guide. Retrieved July 26, 2015, from http://www.hopkinsguides.com/hopkins/view/Johns_Hopkins_Diabetes_Guide/547055/all/Altern ative_markers_of_glycemia:_fructosamine__glycated_albumin__1_5_AG

MedScape. (2015). Albumin: Reference Range, Interpretation, Collection and Panels. Retrieved July 26, 2015, from http://emedicine.medscape.com/article/2054430-overview

Meng, L., Klinkajon, W., K-hasuwan, P., Harkin, S., Supaphol, P., & Wnek, G. E. (2015). Electrospun crosslinked poly(acrylic acid) fiber constructs: towards a synthetic model of the cortical layer of nerve. Polymer International, 64(1), 42–48. doi:10.1002/pi.4793

MicroChemicals. (2013). Wet Chemical Etching, 4–7.

Myakonkaya, O., & Eastoe, J. (2009). Low energy methods of phase separation in colloidal dispersions and microemulsions. Advances in Colloid and Interface Science, 149(1-2), 39–46. doi:10.1016/j.cis.2009.03.001

Najjar, R. (1970). Microemulsions – A Brief Introduction. Development.

nanoComposix. (2015). nanoComposix · Plasmonic Nanoparticles. Retrieved July 26, 2015, from http://nanocomposix.com/pages/plasmonic-nanoparticles

Nazar, M. F., Myakonkaya, O., Shah, S. S., & Eastoe, J. (2011). Separating nanoparticles from microemulsions. Journal of Colloid and Interface Science, 354(2), 624–629. doi:10.1016/j.jcis.2010.11.017

Pileni, M. P. (2006). Reverse micelles used as templates: a new understanding in nanocrystal growth. Journal of Experimental Nanoscience, 1(1), 13–27. doi:10.1080/17458080500462075

Pileni, M.-P. (2003). The role of soft colloidal templates in controlling the size and shape of inorganic nanocrystals. Nature Materials, 2(3), 145–150. doi:10.1038/nmat817

Plus, M. T. A. (2007). Glycohemoglobin Whole Blood.

Polavarapu, L., & Liz-Marzán, L. M. (2013). Towards low-cost flexible substrates for nanoplasmonic sensing. Physical Chemistry Chemical Physics : PCCP, 15(15), 5288–300. doi:10.1039/c2cp43642f

Popp, J., & Kiefer, W. (2000). Fundamentals of Raman spectroscopy. Encyclopedia of Analytical Chemistry, 1–21. Retrieved from http://scholar.google.com/scholar?hl=en&btnG=Search&q=intitle:Fundamentals+of+Raman+spectroscopy#8

Prof.Xies group. (2015). UCLA semiconductor materials Lab. Retrieved July 26, 2015, from http://www.seas.ucla.edu/smrl/Graphene Plasmonic Hybrid System.html

R. Nagarajan. (2008). Nanoparticles: Synthesis, Stabilization, Passivation, and Functionalization. (R. Nagarajan & T. A. Hatton, Eds.) (Vol. 996). Washington, DC: American Chemical Society. doi:10.1021/bk-2008-0996

Rajesh, D., Mahendar, M., & Sunandana, C. S. (2013). Effect of etching on the optical, morphological properties of Ag thin films for SERS active substrates. Journal of Chemistry, 2013. doi:10.1155/2013/285431

Ramakrishna, S., Fujihara, K., Teo, W.-E., Teik-Cheng, L., & Ma, Z. (2005). An Introduction to Electrospinning and Nanofibers (World Scientific). World Scientific Publishing co. Retrieved from http://www.worldscientific.com/worldscibooks/10.1142/5894

Real Time Analyzers. (2015). SERS Vials. Retrieved July 26, 2015, from http://www.rta.biz/Content/SERS_Vials.asp

Reyes-Goddard, J. M., Barr, H., & Stone, N. (2005). Photodiagnosis using Raman and surface enhanced Raman scattering of bodily fluids. Photodiagnosis and Photodynamic Therapy, 2(3), 223–233. doi:10.1016/S1572-1000(05)00066-9

Rolinski E, Konieczny A, Sharp G. Influence of nitriding mechanisms on surface roughness of palsma and gas nitride/nitorcarfurized gray cast iron. Heat treating progress, March/April, 2007, 39-46. (magazine reference)

Roohk, H. V., & Zaidi, A. R. (2008). A review of glycated albumin as an intermediate glycation index for controlling diabetes. doi:10.1177/193229680800200620

Sanchez-Dominguez, M., Aubery, C., & Solans, C. (2011). New Trends on the Synthesis of Inorganic Nanoparticles Using Microemulsions as Confined Reaction Media. Smart Nanoparticles Technology, (Figure 1), 195–220. Retrieved from http://cdn.intechopen.com/pdfs/35424/InTech-New_trends_on_the_synthesis_of_inorganic_nanoparticles_using_microemulsions_as_confined_reaction_media.pdf

Scientific, H. (2012). Raman Spectroscopy for proteins Catalina DAVID Ph . D .– application scientist.

Sers, W. (2015). P - SERS TM Technology Technical Paper P-SERS TM — Trace detection overcoming the cost and usability limitations of traditional SERS technology, 1–8.

Sharma, B., Fernanda Cardinal, M., Kleinman, S. L., Greeneltch, N. G., Frontiera, R. R., Blaber, M. G., … Van Duyne, R. P. (2013). High-performance SERS substrates: Advances and challenges. MRS Bulletin, 38(08), 615–624. doi:10.1557/mrs.2013.161

Shchukin, D. G., & Sukhorukov, G. B. (2004). Nanoparticle synthesis in engineered organic nanoscale reactors. Advanced Materials, 16(8), 671–682. doi:10.1002/adma.200306466

Silberberg, M. (n.d.). Entropy Changes and the Third Law of Thermodynamics. Retrieved July 26, 2015, from http://2012books.lardbucket.org/books/principles-of-general-chemistry-v1.0/s22-04-entropy-changes-and-the-third-.html

Silmeco. (2015). SERS Substrates - Low cost and high performing SERS substrate, SERStrate, from Silmeco. Retrieved July 26, 2015, from http://www.silmeco.com/products/sers-substrate-serstrate/

Simmons, A Blake (San francisco, CA), Talin, Alec Albert (Livermore, C. (2009). US7608461.pdf.

Singh, V., Veerma, R., Singh, M., Javed, A., & Sharma, H. (2013). Topical non steroidal anti inflammatory drug (NSAIDs microemulsions: Rationale, review and future prospective. Asian Journal of Pharmaceutics, 7(1), 1. doi:10.4103/0973-8398.110929

Solanki, J. N., & Murthy, Z. V. P. (2010). Highly monodisperse and sub-nano silver particles synthesis via microemulsion technique. Colloids and Surfaces A: Physicochemical and Engineering Aspects, 359(1-3), 31–38. doi:10.1016/j.colsurfa.2010.01.058

Sperling, R. a, & Parak, W. J. (2010). Surface modification, functionalization and bioconjugation of colloidal inorganic nanoparticles. Philosophical Transactions. Series A, Mathematical, Physical, and Engineering Sciences, 368(1915), 1333–1383. doi:10.1098/rsta.2009.0273

Stedwell, C. N., & Polfer, N. C. (2013). Laser Photodissociation and Spectroscopy of Mass-separated Biomolecular Ions, 83. doi:10.1007/978-3-319-01252-0

Stiles, P. L., Dieringer, J. a, Shah, N. C., & Van Duyne, R. P. (2008). Surface-enhanced Raman spectroscopy. Annual Review of Analytical Chemistry (Palo Alto, Calif.), 1, 601–626. doi:10.1146/annurev.anchem.1.031207.112814

Sur, U. K., Sung, S. H., Stiles, P. L., Dieringer, J. a, Shah, N. C., & Van Duyne, R. P. (2008). Surface-enhanced Raman spectroscopy. Annual Review of Analytical Chemistry (Palo Alto, Calif.), 1(February), 601–26. doi:10.1146/annurev.anchem.1.031207.112814

Tang, C., Saquing, C. D., Harding, J. R., & Khan, S. a. (2010). In situ cross-linking of electrospun poly(vinyl alcohol) nanofibers. Macromolecules, 43(2), 630–637. doi:10.1021/ma902269p

TOSOH. (2015). Principles of Reversed Phase Chromotography. Retrieved from http://www.separations.eu.tosohbioscience.com/ServiceSupport/TechSupport/ResourceCenter/PrinciplesofChromatography/ReversedPhase/

Usković, V., & Drofenik, M. (2005). Synthesis of Materials Within Reverse Micelles. Surface Review and Letters, 12(02), 239–277. doi:10.1142/S0218625X05007001

Vandenabeele, P. (2013). Practical Raman Spectroscopy: An Introduction. John Wiley & Sons. Retrieved from https://books.google.com/books?hl=en&lr=&id=HjFi5eOUYvgC&pgis=1

Vangala, K., Yanney, M., Hsiao, C.-T., Wu, W. W., Shen, R.-F., Zou, S., … Zhang, D. (2010). Sensitive Carbohydrate Detection using Surface Enhanced Raman Tagging. Anal Chem, 82(24), 10164–10171. doi:10.1016/j.biotechadv.2011.08.021.Secreted

Vo-Dinh, T. (2014). Biomedical Photonics Handbook, Second Edition: Therapeutics and Advanced Biophotonics. CRC Press. Retrieved from https://books.google.com/books?id=nCMbBAAAQBAJ&pgis=1

Walker, P., & Tarn, W. H. (1991). Handbook of Metal Etchants. doi:10.1201/9781439822531

Wang, J., Yao, H. Bin, He, D., Zhang, C. L., & Yu, S. H. (2012). Facile fabrication of gold nanoparticles-poly(vinyl alcohol) electrospun water-stable nanofibrous mats: Efficient substrate materials for biosensors. ACS Applied Materials and Interfaces, 4(4), 1963–1971. doi:10.1021/am300391j

Wang, N., Burugapalli, K., Song, W., Halls, J., Moussy, F., Ray, A., & Zheng, Y. (2013). Electrospun fibro-porous polyurethane coatings for implantable glucose biosensors. Biomaterials, 34(4), 888–901. doi:10.1016/j.biomaterials.2012.10.049

Wang, W., Zhang, L., Tong, S., Li, X., & Song, W. (2009). Three-dimensional network films of electrospun copper oxide nanofibers for glucose determination. Biosensors and Bioelectronics, 25(4), 708–714. doi:10.1016/j.bios.2009.08.013

Whitehouse D. Surfaces and Their Measurement, Chapter 3, Hermes Penton Science, 2002.

WHO. (2015). WHO | Diabetes. Retrieved July 26, 2015, from http://www.who.int/mediacentre/factsheets/fs312/en/

Willets, K. a, & Van Duyne, R. P. (2007). Localized surface plasmon resonance spectroscopy and sensing. Annual Review of Physical Chemistry, 58(October), 267–297. doi:10.1146/annurev.physchem.58.032806.104607

World Health Organization. (2011). Use of glycated haemoglobin (HbA1c) in the diagnosis of diabetes mellitus: abbreviated report of a WHO consultation, (WHO/NMH/CHP/CPM/11.1), 25. doi:WHO/NMH/CHP/CPM/11.1

Wu, W., Liu, L., Dai, Z., Liu, J., Yang, S., Zhou, L., … Roy, V. a. L. (2015). Low-Cost, Disposable, Flexible and Highly Reproducible Screen Printed SERS Substrates for the Detection of Various Chemicals. Scientific Reports, 5(October 2014), 10208. doi:10.1038/srep10208

Xu, S., Sun, D., Liu, H., Wang, X., & Yan, X. (2011). Fabrication of Cu-doped cerium oxide nanofibers via electrospinning for preferential CO oxidation. Catalysis Communications, 12(6), 514–518. doi:10.1016/j.catcom.2010.11.021

Yang, E., Qin, X., & Wang, S. (2008). Electrospun crosslinked polyvinyl alcohol membrane. Materials Letters, 62(20), 3555–3557. doi:10.1016/j.matlet.2008.03.049

Yang, Q., Deng, M., Li, H., Li, M., Zhang, C., Shen, W., … Song, Y. (2015). Highly reproducible SERS arrays directly written by inkjet printing. Nanoscale, 7, 421–425. doi:10.1039/c4nr04656k

Yonzon, C. R., Haynes, C. L., Zhang, X., Walsh, J. T., & Van Duyne, R. P. (2004). A Glucose Biosensor Based on Surface-Enhanced Raman Scattering: Improved Partition Layer, Temporal Stability, Reversibility, and Resistance to Serum Protein Interference. Analytical Chemistry, 76(1), 78–85. doi:10.1021/ac035134k

Yoo, E.-H., & Lee, S.-Y. (2010). Glucose biosensors: an overview of use in clinical practice. Sensors (Basel, Switzerland), 10(5), 4558–76. doi:10.3390/s100504558

Yu, B., Moussy, Y., & Moussy, F. (2005). Coil-type implantable glucose biosensor with excess enzyme loading. Frontiers in Bioscience : A Journal and Virtual Library, 10(FEBRUARY 2005), 512–520. doi:10.2741/1547

Zaidi, A. R., Ali, O., Bernet, G., & Comstock, P. (2008). Epinex diagnostics inc., 10–25.

Zhang, C.-L., & Yu, S.-H. (2014). Nanoparticles meet electrospinning: recent advances and future prospects. Chemical Society Reviews, 43(13), 4423–48. doi:10.1039/c3cs60426h

Zhang, X., Chen, Y. L., Liu, R.-S., & Tsai, D. P. (2013). Plasmonic photocatalysis. Reports on Progress in Physics. Physical Society (Great Britain), 76(4), 046401. doi:10.1088/0034-4885/76/4/046401

Zielinska-Jurek, A., Reszczynska, J., Grabowska, E., & Zaleska, A. (2012). Nanoparticles Preparation Using Microemulsion Systems. Microemulsions - An Introduction to Properties and Applications, 229–250. doi:0.5772/2300